Applications of Electromagnetic Phenomena in Periodic Structures

A THESIS

SUBMITTED TO THE DEPARTMENT OF ELECTRICAL AND ELECTRONICS ENGINEERING

AND THE GRADUATE SCHOOL OF ENGINEERING AND SCIENCE

OF BILKENT UNIVERSITY

IN PARTIAL FULFILLMENT OF THE REQUIREMENTS

FOR THE DEGREE OF

DOCTOR OF PHILOSOPHY

By

Atilla Özgür Çakmak

August 2012

I certify that I have read this thesis and that in my opinion it is fully adequate, in scope and in quality, as a thesis for the degree of Doctor of Philosophy.

Prof. Dr. Ekmel Özbay (Supervisor)

I certify that I have read this thesis and that in my opinion it is fully adequate, in scope and in quality, as a thesis for the degree of Doctor of Philosophy.

Prof. Dr. Levent Gürel

I certify that I have read this thesis and that in my opinion it is fully adequate, in scope and in quality, as a thesis for the degree of Doctor of Philosophy.

Assoc. Prof. Dr. Vakur B. Ertürk

I certify that I have read this thesis and that in my opinion it is fully adequate, in scope and in quality, as a thesis for the degree of Doctor of Philosophy.

Assoc. Prof. Dr. M. Özgür Öktel

I certify that I have read this thesis and that in my opinion it is fully adequate, in scope and in quality, as a thesis for the degree of Doctor of Philosophy.

Assoc. Prof. Dr. Sefer Bora Lişesivdin

Approved for the Graduate School of Engineering and Science:

Prof. Dr. Levent Onural

Director of Graduate School of Engineering and Science

ABSTRACT

APPLICATIONS OF ELECTROMAGNETIC PHENOMENA IN PERIODIC STRUCTURES

Atilla Özgür Çakmak

Ph.D. in Electrical and Electronics Engineering

Supervisor: Prof. Dr. Ekmel Özbay

August, 2012

The field of Electromagnetics encompasses several research areas and finds itself applications in all frequency ranges starting from very low frequencies up to optical wavelengths. Periodic structures offer a vast research area in Electromagnetics. Amongst these periodic configurations metamaterials and photonic crystals have been investigated in this study. Metamaterials (MTMs) are artificial materials which are carefully engineered to give outstanding electromagnetic responses, e.g. negative phase velocity, negative refraction. On the other hand, Photonic Crystals (PhCs) offer band stopping and full reflection at certain wavelengths and they are highly favored due their particular properties. PhCs are even commercially available nowadays in optical communication.

In the first part of the study, we have been concentrated on the enhanced transmission through subwavelength apertures with the incorporation of the MTMs. Resonators that are inspired from the MTM research field are placed in the vicinity of the subwavelength apertures such that a near-field electromagnetic wave localization at the output side can be observed. The considered subwavelength apertures have poor transmission figures on the order of 1/10,000 (in terms of intensity) on the average throughout the investigated frequency band, which dramatically limits the propagation. We show that once the subwavelength resonators are allowed to interact with such subwavelength

apertures, astonishingly high transmission enhancement figures (typically ranging from 30 *dB* up to 50 *dB*) can be attained, which in turn results in electromagnetic wave localization in the near-field.

On top of these single aperture related studies, we investigated the propagation of the electromagnetic waves in aperture arrays. We explicitly distinguish the working mechanisms of the presently studied aperture arrays which also cause a transmission enhancement below the cutoff frequency of the regarding apertures. The transmission enhancement has been shown to be accompanied by the left handed propagation, which is a characteristic of the MTMs. We show that both right and left handed transmission channels can be opened simultaneously in these periodically stacked aperture arrays.

Alternatively, we have worked on the graded-index PhCs (GRIN PhCs) in order to tailor the course of the propagating electromagnetic waves. It has been demonstrated that modified Gauss-Hermite modes are available in GRIN PhCs similar to the those in conventional homogenous GRIN structures that are already in use in the field of optics. The underlying physics of the propagation has been discussed and a focusing lens has been proposed, which is based on the GRIN PhCs. The proposed lens has been shown to provide improved input and output coupling figures for the waveguide configurations. The input coupling efficiency has been boosted by a factor of 8 *dB*, while the GRIN PhC at the output side of the waveguide achieved a collimated beam with 7 degrees of half power beam width according to the results of the far-field measurements.

Lastly, PhC based gratings have been utilized to search for an optical diode. It has been shown that such a PhC grating can offer an extremely good contrast (on the order of 1000) between the intensities of the electromagnetic waves that are approaching from different sides of the proposed design. The working mechanism of the optical diode has been shown to rely on the gratings that opened higher order diffraction channels as the zeroth order diffractions are suppressed.

Keywords: Photonic Crystals, Metamaterials, subwavelength aperture

ÖZET

PERİYODİK YAPILARDA BELİREN ELEKTROMANYETİK FENOMENLERİN UYGULAMA SAHALARI

Atilla Özgür Çakmak

Elektrik Elektronik Mühendisliği Doktora

Tez Yöneticisi: Prof. Dr. Ekmel Özbay

Ağustos, 2012

Elektromanyetizma çok geniş bir araştırma sahasını kapsar ve çok düşük frekanslardan optik dalgaboylarına kadar kendisine uygulama sahaları bulur. Elektromanyetizma içinde de periodik yapılar geniş bir araştırma sahası sunarlar. Mevcut periodik araştırma sahaları içinden Fotonik Kristaller ve Metamalzemeler bu tez kapsamında incelenmiştir. Metamalzemeler yapay malzemeler olup, olağandışı elektromanyetik yanıtlar vermek üzere dikkatle düzenlenirler. Metamalzemelerin gösterdikleri bu olağandışı durumlara örnek olarak eksi faz hızı ve negatif kırılım gösterilebilinir. Diğer taraftan da Fotonik Kristaller belirli bantları durdurma ve tamamen yansıtma kabiliyeti gösterme bakımından araştırmalarda yoğunlukla talep görürler. Hatta Fotonik Kristaller günümüzde optik haberleşme ünitelerinde kullanılmak üzere ticari değer taşıyan ürünlere dönüştürülmüşlerdir.

Tez çalışmalarının ilk kısmında dalgaboyundan küçük, metamalzeme iliştirilmiş yarıkların iyileştirilmiş geçirgenlik özellikleri ile ilgileneceğiz. Metamalzeme çalışma sahasından esinlenilen rezonatör yapıları dalgaboyundan küçük yarıkların yakınlarına yerleştirildiğinde elektromanyetik dalgaların yarığın hemen dışında lokalize olduğunu gözlemleyebiliriz. Bahsi geçen yarıklar ilgilenilen çalışma bandı içerisinde aslen ortalama onbinde bir gibi geçirgenlik

sunarken (elektrik alan şiddeti biriminden) yarık içerisinden yayılımı da çok ciddi şekilde sekteye uğratmaktadırlar. Biz dalga altı rezonatörlerimizle dalga altı yarıklarımızı etkileşime soktuğumuzda şaşırtıcı derecede (tipik olarak 30-50 *dB* civarında) ilk duruma nazaran yüksek geçirgenlikler elde edebiliyoruz. Bu etki de dalga altı açıklığının çıkış tarafında elektromanyetik dalgaların lokalizasyonu ile eşzamanlı gerçekleşmekte.

Bu tek yarık tabanlı çalışmaların üzerine düzenli yarık dizinlerindeki elektromanyetik dalga yayılımlarını da inceledik. İncelenilen yarık dizinlerinin farklı çalışma mekanizmalarını net bir şekilde ortaya koyduk. Bu farklı mekanizmalar yarıkların geçirgenlik dalgaboyu öncesinde yüksek şiddetlerde iletime olanak vermekteydi. Bu farklı durumlarda dahi iyileştirilen geçirgenliğin metamalzemelerin karakteristik özelliği olan sol el yayılım özellikleri ile birlikte ortaya çıktığını gözlemledik. Sol ve sağ el geçirgenlik bantlarının eş zamanlı olarak bu art arda sıralanmış periodik yarık dizinlerinde açılabilineceğini gösterdik.

Elektromanyetik dalgaların izledikleri yolları uyarlamak için alternatif olarak dereceli kırılım indeksli Fotonik Kristalleri ile de çalıştık. Bu dereceli kırılım indeksli Fotonik Kristal yapılarında geleneksel dereceli kırılım indeksi optiğini hatırlatır şekilde modifiye edilmiş Gauss-Hermite modlarına rastladık. Elektromanyetik dalgaların bu yapılarda ilerleyişini tartıştıktan sonra bir lens uygulaması önerdik. Önerilen lensin Fotonik Kristal dalgaklavuzları ile birlikte kullanımında bu dalgaklavuzları için iyileştirilmiş giriş ve çıkış bağlaşım katsayılarına yol açtığını gösterdik. Girişteki iyileşme 8 *dB* kadar ölçülürken, dalgaklavuzunun çıkışında da hizaya sokulmuş (kolimasyon), yarı güç dalga açıklığı 7 dereceye indirgenmiş elektromanyetik dalgayı uzak alan ölçümlerinde gözlemleyebiliyoruz.

Son olarak da Fotonik Kristal tabanlı ızgaraları kullanarak optik bir diyot ortaya çıkarmaya çalıştık. Bu ızgaraların Fotonik Kristalin tek yüzüne uygulanması durumunda Fotonik Kristale farklı iki yönden yaklaşan dalganın geçirgenlik katsayıları arasında çok yüksek seviyede kontrast (1000 civarında)

elde edilebilineceğini gösterdik. Önerilen optik diyotun Fotonik Kristal ızgaralarının sıfırıncı difraksiyon seviyesini bastırırken, yüksek difraksiyon seviyelerine olanak tanıması yoluyla çalıştığını kanıtladık.

Anahtar sözcükler: Fotonik Kristaller, Metamalzemeler, dalgaboyu altı açıklık

Acknowledgement

I am honored to present my sincere gratitude to my supervisor Prof. Dr. Ekmel Özbay for his endless support, guidance, motivation and encouragement during this research. It was a life time experience and such a great honor to work with him.

I would like to thank to Prof. Dr. Levent Gürel, Assoc. Prof. Dr. Vakur B. Ertürk, Assoc. Prof. Dr. Mehmet Özgür Oktel and Assoc. Prof. Dr. Sefer Bora Lişesivdin for being in my thesis committee. I am grateful for their valuable time and comments for evaluating this thesis.

Assist. Prof. Dr. Cem Öztürk from my previous university (Sabancı University) had lightened up my interest in Photonics, Optics in my first graduate years. Richard Feynman emphasizes the simplicity and quotes that someone can only master a scientific issue as long as s/he can find methods to explain it in the most comprehensible and *simple* way. Accordingly, I have had the opportunity to take courses from three outstanding lecturers (of course, outstanding is a very subjective adjective here) Prof. Dr. Ali Alpar (Sabancı University), Prof Dr. Abdullah Atalar (Bilkent University) and Prof. Dr. Levent Gürel (Bilkent University). They have been and they are still going to be my role models in my future experiences in effectively conveying the scientific information.

I have to also thank once again to Prof. Dr. Ayhan Altıntaş, Prof. Dr. Levent Gürel and Assoc. Prof. Dr. Vakur B. Ertürk for teaching me the fundamentals of electromagnetics almost from scratch.

At this stage, I have to express my gratitude to Dr. Andriy E. Serebryannikov (Hamburg University of Technology) and Assoc. Prof. Dr. Hamza Kurt (TOBB University). Working with them cannot be just described merely as a collaboration. They have been the key persons who have shaped and guided my thesis work together with my supervisor Prof. Dr. Ekmel Özbay. I

have learnt a great deal of information especially about Photonic Crystals from them. Furthermore, this thesis helped me to get to know a lifelong friend, Dr. Andriy E. Serebryannikov and his family.

I would like to thank to all the former and present personnel of the Nanotechnology Research Center (NANOTAM) for being good friends, understanding and making life easier. I have had the great opportunity to work side by side with Dr. Koray Aydın, Dr. Hümeyra Çağlayan, Dr. Kamil Boratay Alıcı, Dr. Zhaofeng Li, Ms. Damla Ateş, Mr. M. Deniz Çalışkan, Mr. Mehmet Özgür and especially Assoc. Prof. Dr. Kaan Güven whose support I had always felt at the beginning of my thesis work. Mrs. Nursel Aşıcı and Mrs. Gamze Seğmenoğlu have always helped me with every little social detail in NANOTAM.

Moreover, I have gotten acquainted with a very special friend, Dr. Evrim Colak on this occasion. Dr. Evrim Colak will always be a dear and a passionate friend who is always trying to come up with the optimum answers to make the life easy for everyone around him. I have to acknowledge Mr. Semih Çakmakyapan at this point, who has always been so kind and understanding. I will never forget the fruitful discussions with Dr. Serkan Bütün, Mr. Özgür Kazar, Mrs. Neval Cinel and Mr. Ahmet Emin Akosman.

I also thank Dr. Rohat Melik, Dr. Sedat Nizamoğlu, Dr. Evren Mutlugün, Dr. İbrahim Murat Soğancı, Mr. Can Uran, Mrs. Özge Özel, Mr. Tuncay Özel, Mr. Emre Sarı, Ms. Gülis Zengin, Ms. Aslı Ünlügedik and all other friends with whom I have shared the offices in Bilkent Advanced Research Labs.

I would also like to mention the names of our night watchmen, Mr. Hasan Deli and Mr. Doğan Keller. We have spent countless sleepless nights at NANOTAM.

Mosf of all, I am indebted to my parents and Fatma Pir Çakmak for their love, encouragement and support. I am grateful for their patience and voluntary love. Then again, there are those who are not aware of their own contribution to this thesis. My life in Ankara would never be this joyful and beautiful without

the help of my beloved grandmother and aunts who have devoted their time for my sake. I dedicate this work to the endless love and trust of my parents, wife and relatives.

Contents

List of Figures

List of Tables

Chapter 1

Introduction

The title of my thesis covers an immensely broad research field. Periodic structures are popularly used in the field of electromagnetics. Yet, I will be *confining* my focus on metamaterials and photonic crystals with the intention of intelligently guiding the light by making use of the peculiar properties that come into play in these aforementioned periodic structures.

Controlling the flow of light has been an everlasting ambition and a necessity for human being on the surface of earth. We can immediately borrow a legend from the history books. One way or another curious people are certainly acquainted with the famous story of the parabolic reflectors that Archimedes was supposed to build. The story conveys the significance of these mirrors during the heroic defense of Syracuse against Roman ships. Yet, we do not have to go back to the ancient Greeks or Roman times in order to seek an evidence for the quest of humanoids to master the light. It can be speculated that the humanoids have tried to come up with intelligent ideas to make use of the light for their advantage ever since the first attempts to control the fire.

Metamaterials, which popped up in the last century, can be listed merely as one of the outcomes of this pursuit. The name, meta-material, comes from the Greek prefix “beyond, after”, meaning that the material at hand is something well beyond the ordinary materials. There is no solid consensus on the definition of the metamaterials. However, they can be defined as artificial materials with unusual electromagnetic properties. Then again, an unusual property might not be that unusual for someone else. Even if we circumvent this issue, the problem related to the ambiguous definition of the artificial medium awaits us ahead. Actually, there is nothing that outstanding about the building blocks and the governing electromagnetics in metamaterials. As we are going to be discussing the succeeding chapters, the very propaganda of presenting metamaterials as a

totally new, separate research field may produce unwanted consequences. However outstanding properties metamaterials may exhibit, they should always be viewed within the context of the classical electromagnetics (assuming that we are staying outside of the nano scales where the classical electromagnetic theories may cease to be applicable).

Veselago is known to be the father of the research field of metamaterials. He was the first one to approach the left-handed materials in a systematic manner in his seminal paper back in 1967 [1]. Nevertheless, the possibility of a negative refraction had already been speculated as early as 1940s by Mandelshtam [2]. Mandelshtam had also given examples of structures with negative group velocities [3]. Sivukhin in 1957 contemplated a medium with simultaneous negative permittivity and permeability [4]. Silin discussed the negative refraction in connection with the slow-wave structures in 1959 [5]. Furthermore, the backward wave transmission lines, which we are going to be studying in the upcoming chapters, were already known in 1940s and were used by authors, for instance Brillouin [6]. Yet, Veselago was the first person to conduct a systematic study that gave birth to today's metamaterials and he did not stop there. He predicted the most fundamental properties of such a media if it were to exist, i.e. negative refraction, inverse Doppler shift and reversal of Cerenkov radiation.

There has been no real effort to realize Veselago's left-handed medium till the realization by Smith *et al.* [7,8]. The resonant type resonators were found to yield negative permeability whereas continuous wires were shown to act like a negative permittivity medium after the investigations of Pendry at the turn of the century [9,10]. It is interesting to note that very similar resonators were reported within the context of chiral loops in 1980s and 90s [11]. Moreover, variants of the split ring resonators (the most commonly used subwavelength resonator) were presented in the textbook by Schelkunoff and Friis in 1952 [12].

Today, the research field of metamaterials is quite well established. For the time being, it will be very unfair and I will not be citing a single work or a

paper corresponding to the current leading actors that are shaping the research field of metamaterials. Nonetheless, in a very broad sense the main spirit of the metamaterial based research can be caught by simply dedicating a couple hours to the internet search for any educated eye. Then, it can be argued that the researchers are utilizing metamaterials in order to design lenses that are not limited by diffraction. Transformation optics makes the cloaking possible with metamaterials. The research field of metamaterials is nowadays on the road to be merged with quantum nanoplasmonics. Metamaterials are functionalized for photovoltaic applications in light trapping. It is very likely for the browser to come across with the phrases like nanoantennas and metasurfaces mentioned together with metamaterials. The field of metamaterials is in a transition stage and it looks very likely that it will be joined with other overlapping research areas.

Hence, in this thesis Chapter 2 will be devoted to the fundamentals of electromagnetics of metamaterials. The left-handedness of the metamaterials, their dispersive characteristics, the negative phase velocity, the boundary problem in metamaterials and the origins of the negative refraction will be discussed here. Chapter 3 will present a brief idea about the negative permittivity, permeability and split ring resonators as subwavelength resonators. Planar metamaterials that are in the form of cutwires will also be covered in this chapter. The chapter will be concluded by lying couple of antenna oriented application fields for metamaterials. Chapter 4 will address the problem of transmission through single and multiple subwavelength apertures. The theoretical background for such systems will be taken into consideration.

Chapter 5 will be the first chapter in which the original work and results (not the theoretical background) are presented. First, the split ring incorporated subwavelength aperture and its transmission characteristics will be introduced. The possibility of further increasing the transmission figures with connected split ring resonators will be investigated. The localized fields at the exit side of the subwavelength aperture and the subwavelength focusing capabilities of the

resonator attached subwavelength aperture system will be analyzed. In the second part of the chapter, the interest will be mainly focused on the transmission through aperture arrays. The hybrid unit lattice fishnet configurations, their underlying physics entailing the electromagnetic wave propagation will be studied. Later on, the hybrid unit lattice configurations are stacked in a wedge shaped arrangement in order to study the negative refraction.

In the second part of the thesis, photonic crystals will be studied. Particularly, the graded-index photonic crystals and the photonic crystals with gratings will be studied. The photonic crystal work has been boosted up in the second half of the 80s, especially after the pioneering paper by Yablonovitch *et al.* [13]. Since then, the theory of photonic crystals has been expanded and well equipped with the efforts of the research community. The products of the research field have already been made commercially available. Couple of such examples includes light emitting diodes [14], gas/chemical sensors [15], fibers [16] and lasers [17].

Chapter 6 is dedicated to the theoretical background of the photonic crystals. In the following chapter (Chapter 7), the course of the propagating electromagnetic wave has been carefully tailored inside the photonic crystal. The graded-index photonic crystal will be exploited for lensing purposes. The out coupling properties of the graded-index materials will also be considered. Meanwhile, the coupling scenarios to the gratings in photonic crystals will be argued within the framework of the unidirectional transmission.

We give our final remarks and possible future directions of this study in Chapter 8.

We provide brief information on the used simulation tools in Appendix A.

The copyright pages are also attached to the end of the thesis

Chapter 2

Fundamental Electromagnetics In Metamaterials

This chapter is dedicated to the discussions of the fundamental electromagnetics entailed in metamaterials. The chapter undertakes the responsibility of thoroughly confronting some of the basic notions that are already well-established inside the metamaterial community. These ideas are so much repeated over that it might be hard for the researchers to come back to the fundamentals, which in turn brings a disadvantage for the newcomers, like me. Yet, it is still worthwhile to return to the ground breaking ideas of the metamaterials of the last century, when they were either disregarded or highly challenged due to their counter-intuitive specialties. Likewise, the chapter starts with an introduction towards the famous left-handedness of the metamaterials, continues with a transmission-line based approach for the analysis of the backward waves in metamaterials and argues the compulsory dispersive characteristics of the loss-free metamaterials. Finally, the chapter is concluded with the theoretical background for the negative refraction, transfer matrix method and the retrieval algorithms.

2.1 What is left about metamaterials?

We start by laying out Maxwell's equations for the most general case with the aid of the duality:

$$\nabla \times \overline{E}(r,t) = -\frac{\partial \overline{B}(r,t)}{\partial t} - \overline{M}(r,t) \tag{2.1}$$

$$\nabla \times \overline{H}(r,t) = \frac{\partial \overline{D}(r,t)}{\partial t} + \overline{J}(r,t) \tag{2.2}$$

$$\nabla \cdot \overline{B}(r,t) = \rho_m(r,t) \tag{2.3}$$

$$\nabla \cdot \overline{D}(r,t) = \rho_e(r,t) \tag{2.4}$$

where $\overline{E}(r,t)$ and $\overline{H}(r,t)$ are the electric and magnetic field intensities, respectively. Furthermore, $\overline{D}(r,t)$ and $\overline{B}(r,t)$ are the electric and magnetic flux densities, correspondingly. $\overline{M}(r,t)$ is the fictitious magnetic current density, whereas $\overline{J}(r,t)$ is the electric current density. Lastly, $\rho_m(r,t)$ and $\rho_e(r,t)$ are the electric and (fictitious) magnetic charge densities, respectively. The constitutive equations relate the electric and magnetic fields with the electric and magnetic flux densities in the following way:

$$\overline{D}(r,t) = \varepsilon_0 \overline{E}(r,t) + \overline{p} \tag{2.5}$$

$$\overline{B}(r,t) = \mu_0 \overline{H}(r,t) + \overline{m} \tag{2.6}$$

where ε_0 and μ_0 are the free space permittivity and permeability values, respectively. Equations (2.5) and (2.6) might look appropriate for a more general case without (an)isotropy. However, we are still assuming that the presently examined medium is nondispersive, which will become very important within the context of the quest for a negative index medium. Moreover, $\overline{p}$ and $\overline{m}$ are the electric and magnetic polarizabilities of the currently studied medium. They are defined in the subsequent equations:

$$\overline{p} = \varepsilon_0 \overline{\overline{\chi_{ee}}}\,\overline{E}(r,t) + j\sqrt{\varepsilon_0 \mu_0}\,\overline{\overline{\chi_{me}}}\,\overline{H}(r,t) \tag{2.7}$$

$$\overline{m} = \mu_0 \overline{\overline{\chi_{mm}}}\,\overline{H}(r,t) - j\sqrt{\varepsilon_0 \mu_0}\,\overline{\overline{\chi_{em}}}\,\overline{E}(r,t) \tag{2.8}$$

where $\overline{p}$ and $\overline{m}$ can also be perceived as the combination of the induced dipole moments inside the studied zone. $\overline{\overline{\chi_{ee}}}$ and $\overline{\overline{\chi_{mm}}}$ are the electric and magnetic susceptibility tensors. Besides, $\overline{\overline{\chi_{em}}}$ and $\overline{\overline{\chi_{me}}}$ are the cross-polarization susceptibility tensors. They are related as $\overline{\overline{\chi_{me}}} = -(\overline{\overline{\chi_{em}}})^T$ by making use of

Onsager relation. They are strategically important for the investigation of the subwavelength resonators in the upcoming chapters since the induced dipole moments in such subwavelength resonators will yield a cross-polarized scenario which renders the bianisotropic nature in those cases. Once we let alone the bianisotropy for the time being, the constitutive relations in Eqs. (2.5) and (2.6) become

$$\overline{D}(r,t) = \overline{\overline{\varepsilon}}\,\overline{E}(r,t) = \varepsilon_0(1+\overline{\overline{\chi_{ee}}})\overline{E}(r,t)\,, \tag{2.9}$$

$$\overline{B}(r,t) = \overline{\overline{\mu}}\,\overline{H}(r,t) = \mu_0(1+\overline{\overline{\chi_{mm}}})\overline{H}(r,t)\,. \tag{2.10}$$

If we drop the matrix formalism and make an intuitive reduction, we may describe the space-invariant relative permittivity and permeability of the examined medium as $\varepsilon_r \equiv (1+\overline{\overline{\chi_{ee}}})$ and $\mu_r \equiv (1+\overline{\overline{\chi_{mm}}})$, respectively. Of course, these expressions can be written by taking account of the inherent losses, $\varepsilon_r = \varepsilon' - j\varepsilon''$ and $\mu_r = \mu' - j\mu''$. Now, let us assume harmonic fields and sources of the form

$$\overline{F}(r,t) = \mathrm{Re}\left[\overline{F}(r)e^{j\omega t}\right] \tag{2.11}$$

while making use of the $+j\omega t$ convention. Then, Maxwell's equations in Eqs. (2.1) to (2.4) simplify to be

$$\nabla\times\overline{E}(r) = -j\omega\mu_0\mu_r\overline{H}(r) - \overline{M}(r)\,, \tag{2.12}$$

$$\nabla\times\overline{H}(r) = j\omega\varepsilon_0\varepsilon_r\overline{E}(r) + \overline{J}(r)\,, \tag{2.13}$$

$$\nabla.\overline{H}(r) = \frac{\rho_m(r)}{\mu_0\mu_r}\,, \tag{2.14}$$

$$\nabla.\overline{E}(r) = \frac{\rho_e(r)}{\varepsilon_0\varepsilon_r}\,. \tag{2.15}$$

Every propagating wave can be described in terms of plane wave components in Fourier Optics. Thus, it is reasonable to consider the propagation

of a plane wave $\overline{E}(r) = \overline{E_0} e^{-j\bar{k}\cdot\bar{r}}$ in a medium without sources ($\overline{M} = \overline{J} = 0$). If we assume that the considered plane wave has an electric field in *y* direction and the propagation is along *z*-axis (wave vector, *k*), the magnetic field is easily found out to lie on –*x*-axis from Eq. (2.12). The results of the regarding simple exercise are generalized for the plane waves:

$$\bar{k} \times \overline{E}(r) = \omega \mu_0 \mu_r \overline{H}(r) \tag{2.16}$$

$$\bar{k} \times \overline{H}(r) = -\omega \varepsilon_0 \varepsilon_r \overline{E}(r) . \tag{2.17}$$

Consequently, the propagation of the plane wave describes a Right-Handed (RH) system, as shown in Fig. 2.1(a), for the conventional constitution parameters ($\mu_r, \varepsilon_r > 0$). The real question is what happens if both of these parameters get negative values at the same time ($\mu_r, \varepsilon_r < 0$)? Then, the propagation is now described with a Left-Handed (LH) system, which is exhibited in Fig. 2. 1(b).

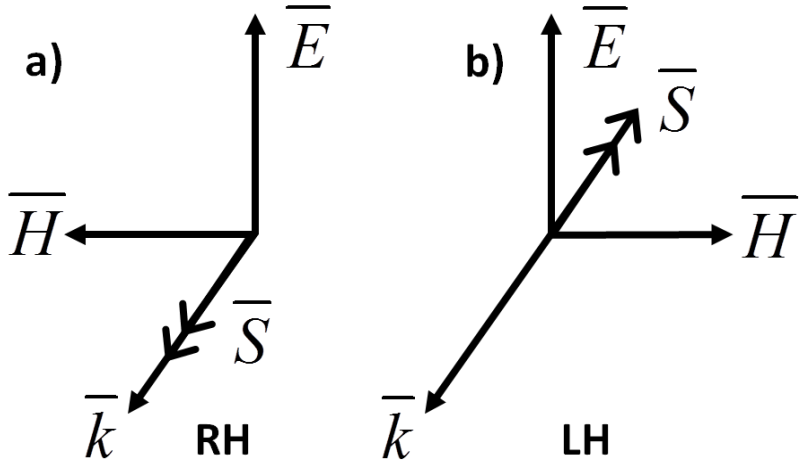

Figure 2.1: The directions of the electric field, magnetic field, wave vector and Poynting vector for (a) a conventional (RH) medium and (b) a LH medium.

The Poynting vector, $\overline{S}(r)$, represents the flow of the electromagnetic energy density and is defined as

$$\overline{E}(r) \times \overline{H}^{*}(r) = \overline{S}(r) \tag{2.18}$$

for the harmonic fields. The most significant observation in Fig. 2.1 is that the simultaneous negativity of the constitution parameters produce antiparallel $\bar{S}(r)$ and $\bar{k}$. Hence, backward waves are supported in LH medium. The details of the backward waves will be outlined in the next section with a transmission-line based approach. It is apparent even at this stage that the negativity of just one of these parameters is going to result in non-propagating (evanescent) modes, since they do not form a RH or a LH system.

2.2 A transmission-line based approach to the one-dimensional (1-D) metamaterials

One of the most practical ways of visualizing backward waves is to exploit the transmission line (TL) theory. For the moment, let us stick to the conventional TL theory and assume that the TL includes distributed inductance and capacitance continuously throughout its total length. We will also work with the lossless case for simplicity. Then, the conventional TL is shown in Fig. 2.2(a).

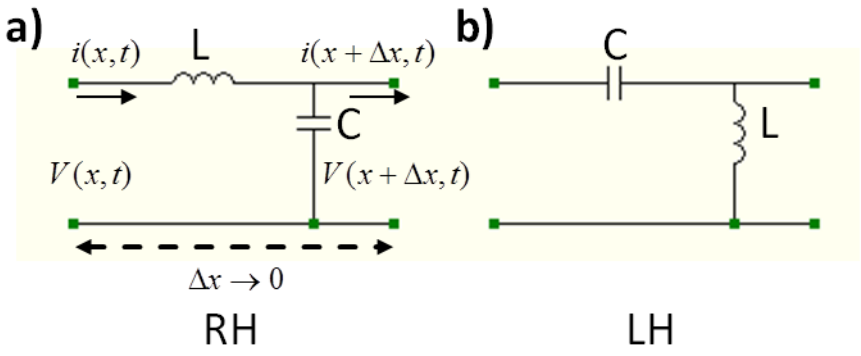

Figure 2.2: TL models for (a) a conventional (RH) medium and (b) a LH medium.

For this infinitesimal length ($\Delta x \to 0$), TL is decomposed into an *LC*-network whose inductance and capacitance are defined for per unit length. Then, Krichhoff's voltage and current laws dictate

$$V(x,t) = \frac{\partial i(x,t)}{\partial t} L\Delta x + V(x+\Delta x,t) \tag{2.19}$$

$$i(x,t) = \frac{\partial V(x+\Delta x,t)}{\partial t} C\Delta x + i(x+\Delta x,t) \tag{2.20}$$

where $V(x,t)$ and $i(x,t)$ are the voltage and current values at the input port, respectively. If we carry out the algebra,

$$\frac{V(x,t) - V(x+\Delta x,t)}{\Delta x} \Rightarrow \frac{\partial V(x,t)}{\partial x} = L\frac{\partial i(x,t)}{\partial t} \tag{2.21}$$

$$\frac{i(x,t) - i(x+\Delta x,t)}{\Delta x} \Rightarrow \frac{\partial i(x,t)}{\partial x} = C\frac{\partial V(x,t)}{\partial t} \tag{2.22}$$

are found. These two equations bear a strong resemblance to Eqs. (2.1) and (2.2). After all, an analogy between the voltage, current waves and the electric, magnetic fields can be developed, respectively. Accordingly, the same analogy entails a relationship between the inductance, capacitance and the permeability, permittivity. Again for harmonic fields the voltage equation boils down to

$$\frac{dV(x)}{dx} = j\omega L i(x) = Z_s i(x) \tag{2.23}$$

$$\frac{di(x)}{dx} = j\omega C V(x) = Y_p Vx) \tag{2.24}$$

where Z_s and Y_p are the series and parallel impedance values in the network. Hence,

$$\frac{d^2V(x)}{dx^2} = -k^2 V(x) \tag{2.25}$$

$$\frac{d^2 i(x)}{dx^2} = -k^2 i(x) \tag{2.26}$$

where k is the propagation constant of the voltage wave forms inside the TL. Actually, they yield the same formulas as Helmholtz equations do for the electromagnetic fields in source free regions. Equations (2.25) and (2.26) are known as the Telegrapher's equations and the solutions to these equations are in the form of

$$V(x) = V^+ e^{-jkx} + V^- e^{jkx} \tag{2.25}$$

$$i(x) = \frac{1}{Z_0}(V^+ e^{-jkx} - V^- e^{jkx}) \tag{2.26}$$

where Z_0 is the characteristic impedance of the TL. V^+ and V^- are to be determined from the boundary conditions. The propagation constant (dispersion relation) of the conventional TL for the lossless case becomes

$$k = -j\sqrt{Z_s Y_p} = \omega\sqrt{LC}\,. \tag{2.27}$$

Subsequently, the phase (v_p) and group (v_g) velocities for the transmitted signal can be written as

$$v_p = \frac{\omega}{k} = \frac{1}{\sqrt{LC}} > 0\,, \tag{2.28}$$

$$v_g = \frac{\partial\omega}{\partial k} = v_p = \frac{1}{\sqrt{LC}} > 0\,. \tag{2.29}$$

The results are not surprising for this 1-D problem. The group and phase velocities are equal to each other and both positive for the conventional (RH) TL in Fig. 2.2(a). The Poynting vector's direction that is expressed in Eq. (2.18) is the same as the defined v_g for this 1-D problem. Consequently, the TL model in Fig. 2.2(a) obeys the RH regulations while v_p and v_g are along the same direction.

On the other hand, a LH system can be built by simply interchanging the places of L and C in Fig. 2.2(b). Such a change assigns the propagation constant as

$$k = -j\sqrt{Z_s Y_p} = -\frac{1}{\omega\sqrt{LC}}\,. \tag{2.30}$$

Thus,

$$v_p = \frac{\omega}{k} = -\omega^2\sqrt{LC} < 0 \tag{2.31}$$

$$v_g = \frac{\partial\omega}{\partial k} = (\frac{\partial k}{\partial\omega})^{-1} = \omega^2\sqrt{LC} > 0\,. \tag{2.32}$$

In contrast to the RH TL case, LH TL line has the group and phase velocities in opposite directions as it was depicted in Fig. 2.1(b). The group velocity is always positive, such that the medium does not violate the causality. However, the backward waves' phase velocity inside the LH medium advances in opposite direction to the Poynting vector.

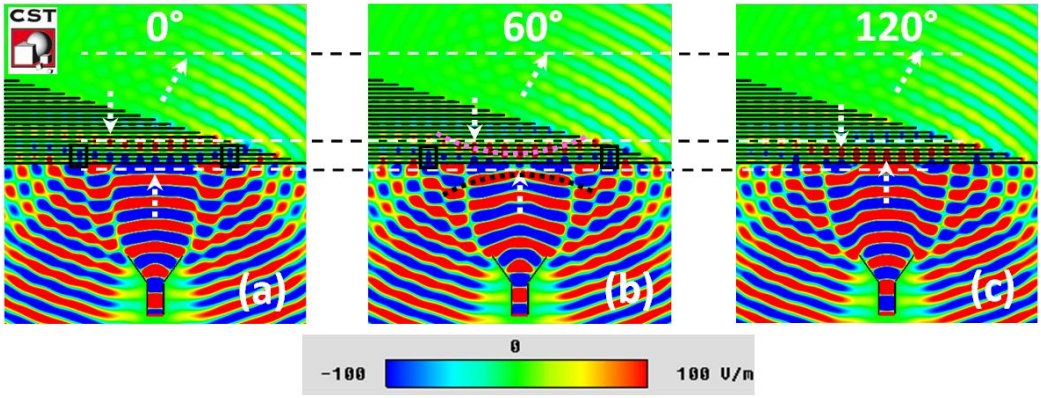

Figure 2.3: The phase advance inside the LH medium. The phase of the propagating waves inside the LH medium is illustrated as (a) 0, (b) 60 and (c) 120 degrees.

This situation can be visualized in Fig. 2.3. The incident wave is launched in the simulation tool (CST®) by modeling the horn antenna. The LH medium is in the shape of a wedge. As the electromagnetic waves are exiting the surface of the wedge configuration, the phase advances in the opposite direction. Thus, the wave fronts of the propagating waves approach the input surface of the wedge. The phenomenon is explained in the following way. Once we adapt the $+j\omega t$ convention, the plane waves that can be monitored on the screen are in the form

$$\overline{E}(r,t) = \mathrm{Re}\left[\overline{E_0} e^{-j\bar{k}\cdot\bar{r}} e^{j\omega t}\right] = \overline{E_0}\cos(\omega t - \bar{k}\cdot\bar{r})\,. \tag{2.33}$$

Consequently, the wave fronts must satisfy the condition:

$$\omega t - \bar{k}\cdot\bar{r} = Const. \tag{2.34}$$

In the simulation environment, the time advance is modeled with an incremental phase input that is also shown in Fig. 2.3. This input phase is 0, 60 and 120 degrees. Thus, the wavefront approaches to the input side of the wedge

configuration as Eq. (2.34) implies. In other words, while ωt is increasing, the compensation is done by decreasing $\bar{k} \cdot \bar{r}$ product.

2.3 Negative refractive index: Is the theory bullet proof?

Finally, we come to the result that the multiplication of the constitutive parameters gives the refractive index of the medium.

$$n = \pm\sqrt{\varepsilon_r \mu_r} \tag{2.35}$$

The outcome of Eq. (2.35) is very important because a whole new quadrant (3rd quadrant in Fig. 2.4), which was otherwise unknown to the electromagnetic community, is now opened. The studied medium supports propagating waves only if it is categorized under the 1st or 3rd quadrants in Fig. 2.4. Such a material has either double positive (DP) or negative (DN) constitutive parameters. As the results of Sec. 2.1 implies, the LH medium supports backward-propagating waves in comparison to the RH medium with the usual forward-propagating waves. The categorization of the backward or forward waves rely on the result of $\bar{S} \cdot \bar{k}$. The angle between these two vector quantities does not have to be restricted to 0 and 180 degrees, as we have studied in the previous chapters. More generally, anisotropy both in LH and RH media brings deviations and different angle orientations. However, the isotropic cases have been investigated because of the simplicity in Fig. 2.4.

The 2nd and 4th quadrants are dedicated to the materials with single negative (SN) constitutive parameters. Plasmas and ferrites are some of the examples that first come to the mind, respectively for the 2nd and 4th quadrants. Since the propagation constant of the planes waves, $k = k_0 n$, it is apparent that SN media can only support evanescent modes, as it is outlined in this simplified example. Therefore, these quadrants are opaque to the incident waves.

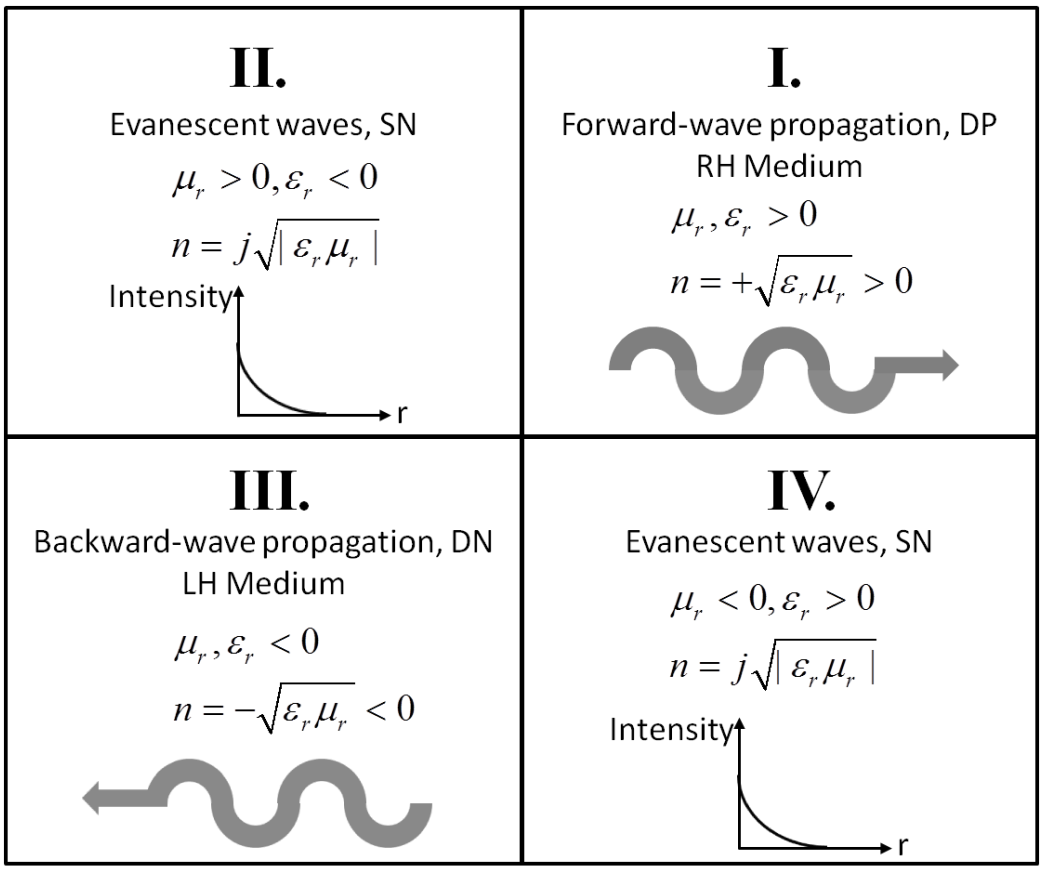

Figure 2.4: Four quadrants of the plane wave propagation. The categorization is based on the sign of the constitutive parameters.

Under the light of these discussions, now let us consider the example portrayed in Fig. 2.5. Slabs of RH (upper) and LH (lower) media inserted on top of the ground plane can be perceived as TLs. Hence, a TL transforms the load impedance to the input port and is commonly employed in matching scenarios.

$$Z(x) = \frac{V(x)}{i(x)} = Z_0 \frac{V^+ e^{-jkx} + V^- e^{jkx}}{V^+ e^{-jkx} - V^- e^{jkx}} = Z_0 \frac{1 + \Gamma e^{2jkx}}{1 - \Gamma e^{2jkx}} \tag{2.36}$$

where $\Gamma = V^-/V^+ = (Z_L - Z_0)/(Z_L + Z_0)$ is the reflection coefficient due to the impedance termination at the end of the TL and Z_L is the load impedance. The RH and LH slabs are both put on top of the ground plane with $Z_L = 0$.

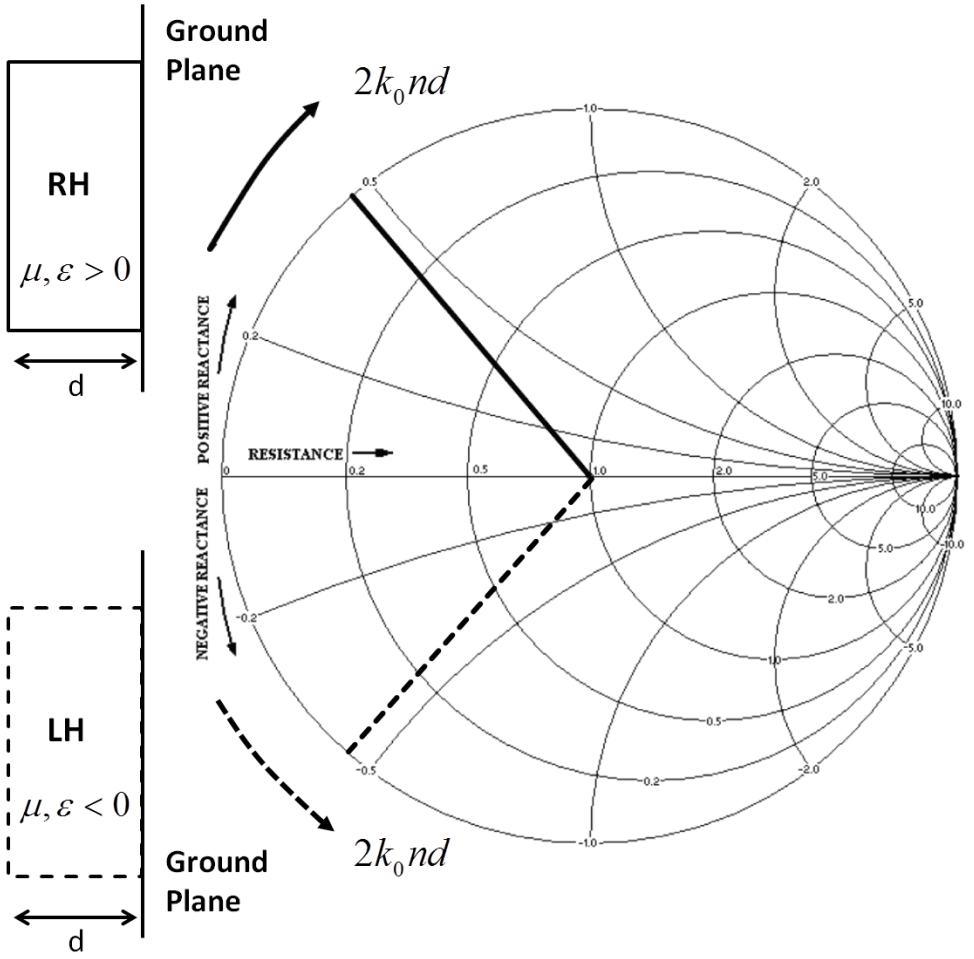

Figure 2.5: RH (upper) and LH (lower) media with the same thickness, d, are covering the ground plane. The Smith Chart on the right hand side shows the representative impedance matching scenarios.

Then, $\Gamma = -1$ and matching can be achieved to the succeeding layers. Smith Charts are used for such purposes. As for this example, a phase term will be added to the reflection coefficient of the shorted load impedance, which is $2k_0nd$. Here k_0 is the propagation constant in free space, n is the refractive index and d is the thickness of the slab, respectively. This additional phase term will cause a clockwise shift towards the generator in the conventional RH medium. On the other hand, the shift will be in the opposite direction, namely in the counter-clockwise direction, for the LH medium such that the slab will produce a negative reactance term (in the capacitive half plane). Yet, as good as this may sound things look bad for the LH medium once we remind ourselves Foster's

reactance theorem. Foster's reactance theorem tells that the reactance (X) of a lossless, passive, two terminal network must increase monotonically ($\partial X/\partial\omega > 0$). However, in our case for the lossless LH medium with n, the additional phase term, $2k_0nd = 2\omega nd / c$, progresses in the counter-clockwise direction yielding a smaller reactance value (X) for the network. Then, the challenging question arises whether the existence of the negative refractive index is at stake or we may have missed a point in our consideration. Fortunately, the latter is true specifically for the LH medium. The details of these speculations will be discussed in the next section. Nevertheless, the LH medium looks to be a promising candidate aside from the current debate for matching purposes when we refocus on Fig. 2.5. The characteristic wave impedances ($\eta = E/H$) of air and LH medium are not necessarily equal to each other. Hence, this fact turns out to be an advantage for fully matching the input impedance due to the mismatch of the characteristic impedances of the corresponding media. In such cases, the origin of the constant standing wave ratio circles also move away from the origin of the Smith Chart.

2.4 Non-dispersive metamaterials?

Unfortunately, members of the metamaterial community have a tendency to disregard or forget the Kramers-Kronig relations while considering the LH media. Because it makes the analysis very practical and simple. Hence, it is not impossible to come across with dispersion free negative refractive index expressions (indefinitely from daylight to DC) in the literature, whose validity is not questioned. The LH media are bound to be dispersive, which creates extra restrictions on the constitutive parameters. Accordingly, we will have to return to the original Maxwell's equations. The divergence of the Poynting vector in time domain is defined as

$$\nabla \cdot \overline{S}(r,t) = \nabla \cdot (\overline{E}(r,t) \times \overline{H}(r,t)) . \tag{2.37}$$

By making use of the divergence theorem, the expression becomes

$$\int_V \nabla \cdot \overline{S}(r,t)dV = \oint_s \overline{S}(r,t) \cdot \overline{ds} = \int_V \nabla \cdot (\overline{E}(r,t) \times \overline{H}(r,t))dV \,. \qquad (2.38)$$

With the help of the following vector identity

$$\nabla.(\overline{E}(r,t) \times \overline{H}(r,t)) = \overline{H}(r,t) \cdot (\nabla \times \overline{E}(r,t)) - \overline{E}(r,t) \cdot (\nabla \times \overline{H}(r,t)), \quad (2.39)$$

and going back to Eqs. (2.1) and (2.2)

$$\nabla \times \overline{E}(r,t) = -\frac{\partial \overline{B}(r,t)}{\partial t} - \overline{M}_s(r,t) - \sigma_m \overline{H}(r,t) \qquad (2.40)$$

$$\nabla \times \overline{H}(r,t) = \frac{\partial \overline{D}(r,t)}{\partial t} + \overline{J}_s(r,t) + \sigma_e \overline{E}(r,t) \qquad (2.41)$$

where $\overline{M}_s(r,t)$ and $\overline{J}_s(r,t)$ are the (fictitious) magnetic and electric currents generated by the sources, respectively. Conversely, if we have electric and (fictitious) magnetic conductors inside the investigated space, additional currents will be induced in the form of $\sigma_e \overline{E}(r,t)$ and $\sigma_m \overline{H}(r,t)$, respectively. If we carry out the algebra,

$$\oint_s \overline{S}(r,t) \cdot \overline{ds} = -\int_V (\overline{E}(r,t) \cdot \overline{J_s}(r,t) + \overline{H}(r,t) \cdot \overline{M_s}(r,t))dV - \sigma_e \int_V |\overline{E}(r,t)|^2 dV \ldots$$

$$\ldots - \sigma_m \int_V |\overline{H}(r,t)|^2 dV - \int_V \overline{H}(r,t) \cdot \frac{\partial \overline{B}(r,t)}{\partial t} dV - \int_V \overline{E}(r,t) \cdot \frac{\partial \overline{D}(r,t)}{\partial t} dV \quad (2.42)$$

This rather long equation in Eq. (2.42) is very important, because it points to the conservation of energy inside volume, *V*. It is called the Poynting's theorem, for which the first term on the left hand side of the equation in Eq. (2.42) determines the power flow out of the volume with a total surface of *s*, as shown in Fig. 2.6. The first term on the right hand side of Eq. (2.42) is associated with the power done by the sources in volume *V*. The second and the third terms are the dissipated power in the conductors inside the volume. The last term contains both the absorbed and stored electromagnetic energy inside the volume. Hence, the power out of the surface is equal to the difference between the generated and the dissipated power inside the volume.

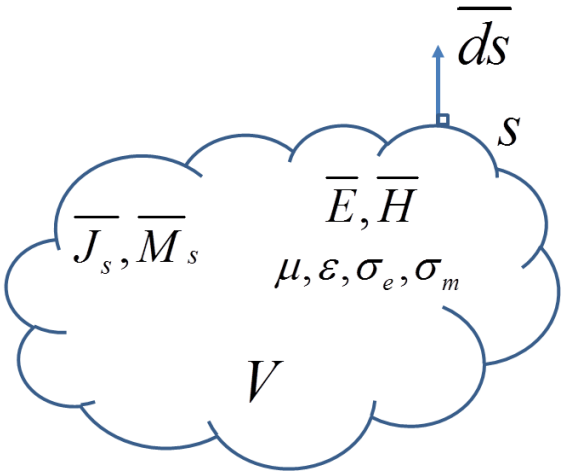

Figure 2.6: Volume, *V*, with a total surface of *s* encapsulates sources ($\overline{M}_s(r,t)$, $\overline{J}_s(r,t)$), electromagnetic fields ($\overline{E}(r,t)$, $\overline{H}(r,t)$).

For the dispersive media, the electric and magnetic flux densities are related to the fields with a convolution.

$$\overline{D}(r,t) = \varepsilon(t) * \overline{E}(r,t) = \int_{-\infty}^{t} \varepsilon(t-t')\overline{E}(r,t)dt', \tag{2.43}$$

$$\overline{B}(r,t) = \mu(t) * \overline{H}(r,t) = \int_{-\infty}^{t} \mu(t-t')\overline{H}(r,t)dt'. \tag{2.44}$$

At least for the linear and anisotropic negative refractive index medium

$$\overline{D}(r,\omega) = \varepsilon(\omega)\overline{E}(r,\omega), \tag{2.45}$$

$$\overline{B}(r,\omega) = \mu(\omega)\overline{H}(r,\omega). \tag{2.46}$$

At this point, we will assume that the fields are slowly varying in order to derive a useful expression. Then, the fields are quasi harmonic with a mean frequency of ω_0.

$$\overline{F}(r,t) = \mathrm{Re}\left[\overline{F}'(r,t)e^{j\omega_0 t}\right] = \mathrm{Re}\left[\overline{F}\right] = \frac{\overline{F} + \overline{F}^*}{2} \tag{2.47}$$

In case of the absence of the sources and conductors Eq. (2.42) turns into

$$\left\langle \oint_s \overline{S}(r,t)\cdot\overline{ds} \right\rangle = -\frac{1}{4}\left\langle \int_V (\overline{H}\cdot\frac{\partial \overline{B}^*}{\partial t} + \overline{H}^*\frac{\partial \overline{B}}{\partial t})dV + \int_V (\overline{E}\cdot\frac{\partial \overline{D}^*}{\partial t}\ldots \right.$$

$$\left. \ldots + \overline{E}^*\frac{\partial \overline{D}}{\partial t})dV \right\rangle \qquad (2.48)$$

which gives the time averaged power flow out of the surface. All the other terms bringing $2j\omega_0 t$ terms vanish when averaged over time[1]. If we expand the quasi-harmonic fields as a Fourier series

$$\overline{D} = \left[\sum_{\omega'} \overline{D_{\omega'}} e^{+j\omega' t}\right] e^{j\omega_0 t} = \sum_{\omega'} \overline{D_{\omega'}} e^{+j(\omega'+\omega_0)t} \ldots$$

$$\ldots = \sum_{\omega'} \varepsilon(\omega'+\omega_0)\overline{E_{\omega'}} e^{+j(\omega'+\omega_0)t} \qquad (2.49)$$

where only the terms with $\omega' << \omega_0$ prevail. A very similar expansion can also be handled for $\overline{B}$. Then the terms in Eq. (2.48) can be calculated as

$$\frac{\partial \overline{D}}{\partial t} = \sum_{\omega'} \varepsilon(\omega'+\omega_0)\times j(\omega'+\omega_0)\times \overline{E_{\omega'}} e^{+j(\omega'+\omega_0)t}. \qquad (2.50)$$

Using the Taylor expansion around ω_0

$$\varepsilon(\omega)\times j\omega = \varepsilon(\omega_0)\times j\omega_0 + \frac{d(\varepsilon(\omega)\times j\omega)}{d\omega}\Big|_{(\omega=\omega_0)} \times(\omega-\omega_0)\ldots$$

$$\ldots \Rightarrow \varepsilon(\omega'+\omega_0)\times j(\omega'+\omega_0)\ldots$$

$$\ldots \approx \varepsilon(\omega_0)\times j\omega_0 + \frac{d(\varepsilon(\omega)\times j\omega)}{d\omega}\Big|_{(\omega=\omega_0)} \times(\omega') \qquad (2.51)$$

Accordingly, when we arrange Eq. (2.50)

$$\frac{\partial \overline{D}}{\partial t} = \sum_{\omega'} [\varepsilon(\omega_0)\times j\omega_0 \times \overline{E_{\omega'}} \times e^{+j(\omega'+\omega_0)t} + \ldots$$

[1] Actually, terms like $\left\langle |\overline{E}'|^2 e^{2j\omega_0 t} \right\rangle$ does not automatically give zero as in the case of the harmonic fields due to the time dependence of $\overline{E}'$. Nevertheless for slowly varying fields the time averaged value gets comparably small.

$$\ldots \frac{d(\varepsilon(\omega)\times j\omega)}{d\omega}|_{(\omega=\omega_0)} \times(\omega')\times \overline{E_{\omega'}} \times e^{+j(\omega'+\omega_0)t}]\ldots$$

$$\ldots = \varepsilon(\omega_0)\times j\omega_0 \times e^{+j\omega_0 t} \times \sum_{\omega'} \overline{E_{\omega'}} e^{+j\omega' t} + \ldots$$

$$\ldots \frac{d(\varepsilon(\omega)\times j\omega)}{d\omega}|_{(\omega=\omega_0)} \times e^{+j\omega_0 t} \times \sum_{\omega'} \omega' \overline{E_{\omega'}} e^{+j\omega' t} \qquad (2.52)$$

Hence, Eq. (2.47) reminds us

$$\frac{\partial \overline{D}}{\partial t} = j\omega_0 \varepsilon(\omega_0)\overline{E}'(r,t)e^{+j\omega_0 t} + \frac{d(\varepsilon(\omega)\omega)}{d\omega}|_{(\omega=\omega_0)} \frac{\partial \overline{E}'(r,t)}{\partial t} e^{+j\omega_0 t} \ldots$$

$$\ldots = j\omega\varepsilon(\omega)\overline{E} + \frac{d(\varepsilon(\omega)\omega)}{d\omega}\frac{\partial \overline{E}'(r,t)}{\partial t} e^{+j\omega t} \qquad (2.53)$$

when we drop the ω_0 subscript. Again a very similar formula can be derived for $\frac{\partial \overline{B}}{\partial t}$. Then, if we insert them to the main equation (Poynting's theorem) in Eq. (2.48)

$$\left\langle \oint_s \overline{S}(r,t)\cdot \overline{ds} \right\rangle = -\frac{1}{4}\left\langle \int_V (-\overline{H}\cdot j\omega\mu^*(\omega)\overline{H}^* + \overline{H}\cdot \frac{d(\mu^*(\omega)\omega)}{d\omega}\frac{\partial \overline{H}'^*(r,t)}{\partial t} e^{-j\omega t})dV + \ldots \right.$$

$$\ldots \int_V (-\overline{E}\cdot j\omega\varepsilon^*(\omega)\overline{E}^* + \overline{E}\cdot \frac{d(\varepsilon^*(\omega)\omega)}{d\omega}\frac{\partial \overline{E}'^*(r,t)}{\partial t} e^{-j\omega t})dV + \cdots$$

$$\ldots \int_V (\overline{H}^*\cdot j\omega\mu(\omega)\overline{H} + \overline{H}^*\cdot \frac{d(\mu(\omega)\omega)}{d\omega}\frac{\partial \overline{H}'(r,t)}{\partial t} e^{+j\omega t})dV + \cdots$$

$$\left. \ldots \int_V (\overline{E}^*\cdot j\omega\varepsilon(\omega)\overline{E} + \overline{E}^*\cdot \frac{d(\varepsilon(\omega)\omega)}{d\omega}\frac{\partial \overline{E}'(r,t)}{\partial t} e^{+j\omega t})dV \right\rangle \qquad (2.54)$$

Equation (2.54) offers the general picture for the energy conservation. Now, we are going to consider a special case without the losses. Hence, $\mu = \mu^*$ and $\varepsilon = \varepsilon^*$ for this case. Thus, all the terms in Eq. (2.54) without the derivatives

cancel out. We are left with the following special formula (simplified) that can also apply for the RH media.

$$\left\langle \oint_s \overline{S}(r,t)\cdot\overline{ds} \right\rangle = -\frac{1}{4}\left\langle \int_V \left(\frac{d(\mu\omega)}{d\omega}\frac{\partial(H\cdot\overline{H}^*)}{\partial t} + \frac{d(\varepsilon\omega)}{d\omega}\frac{\partial(\overline{E}\cdot\overline{E}^*)}{\partial t}\right)dV \right\rangle \quad (2.55)$$

We have used the property that

$$\overline{E}\cdot\frac{\partial\overline{E}'^*(r,t)}{\partial t}e^{-j\omega t} + \overline{E}^*\cdot\frac{\partial\overline{E}'(r,t)}{\partial t}e^{+j\omega t} = \ldots$$

$$\ldots\overline{E}(r,t)e^{+j\omega t}\frac{\partial\overline{E}'^*(r,t)}{\partial t}e^{-j\omega t} + \overline{E}^*(r,t)e^{-j\omega t}\frac{\partial\overline{E}'(r,t)}{\partial t}e^{+j\omega t} = \ldots$$

$$\ldots\frac{\partial|\overline{E}(r,t)|^2}{\partial t} = \frac{\partial|\overline{E}|^2}{\partial t} \quad (2.56)$$

After all this algebra we have arrived at the Poynting's theorem for source free media with no losses (in terms of conductance and absorption due to the imaginary parts of the constitution parameters).

$$W = -\left\langle \oint_s \overline{S}(r,t)\cdot\overline{ds} \right\rangle == \frac{\frac{1}{4}\int_0^{\frac{2\pi}{\omega}}\int_V \left(\frac{d(\mu\omega)}{d\omega}\frac{\partial(|\overline{H}|^2)}{\partial t} + \frac{d(\varepsilon\omega)}{d\omega}\frac{\partial(|\overline{E}|^2)}{\partial t}\right)dVdt}{\frac{2\pi}{\omega}} \quad (2.57)$$

where W is the time averaged internal electromagnetic energy in the volume, V. For the dispersion-free medium it boils down to the well-known stored electromagnetic power equation.

$$W = \frac{\int_V(\mu|\overline{H}|^2 + \varepsilon|\overline{E}|^2)dV}{4} \quad (2.58)$$

For the RH medium $W > 0$ is always satisfied for the lossless, non-dispersive case (Of course, this is an abstraction. Losses, however small, accompany in real life problems). Thus, the electromagnetic waves evolve inside the volume even after the sources outside the volume are shut down. The

same thing must be also true for Eq. (2.57). Once $W > 0$, the divergence of the Poynting vector must attain a negative value as it is indicated in Fig. 2.7. Accordingly these dispersive relations must be satisfied.

$$\frac{d(\omega\varepsilon)}{d\omega} > 0, \tag{2.59}$$

$$\frac{d(\omega\mu)}{d\omega} > 0. \tag{2.60}$$

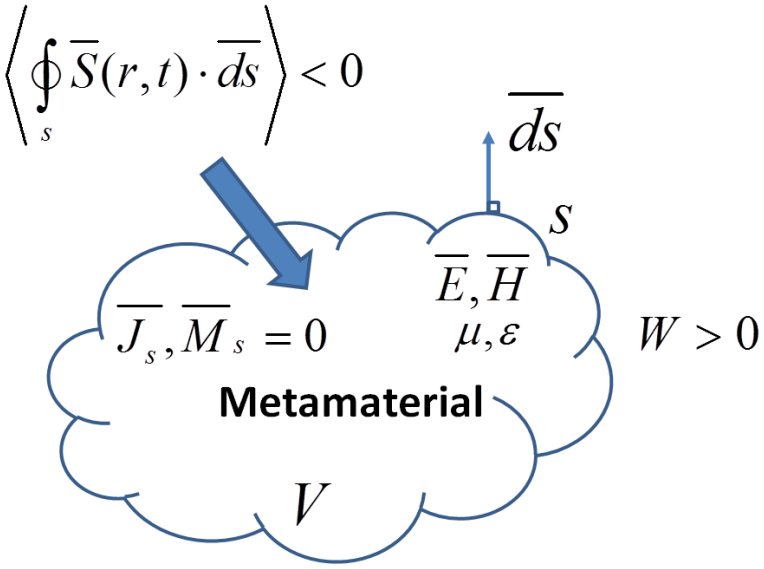

Figure 2.7: The energy conservation restrictions for a volume, *V*.

Therefore, the constitutive parameters (ε and μ) can get negative values. They can have simultaneous negative values, as well. However, the LH medium must be dispersive for the lossless case. It cannot have non-dispersive features. Hence, this hypothetical case cannot be assumed as a simple non-dispersive slab as in the case of the misguiding proposals in the research community. Furthermore, the derivative of the constitutive parameters must be always positive (for the loss-free case, with no dominant absorption inside the LH medium) in accordance with the Foster's reactance theorem that we have just discussed in the last section. In summary, a LH medium can exist, but the researcher must be very careful in analyzing and modeling this medium.

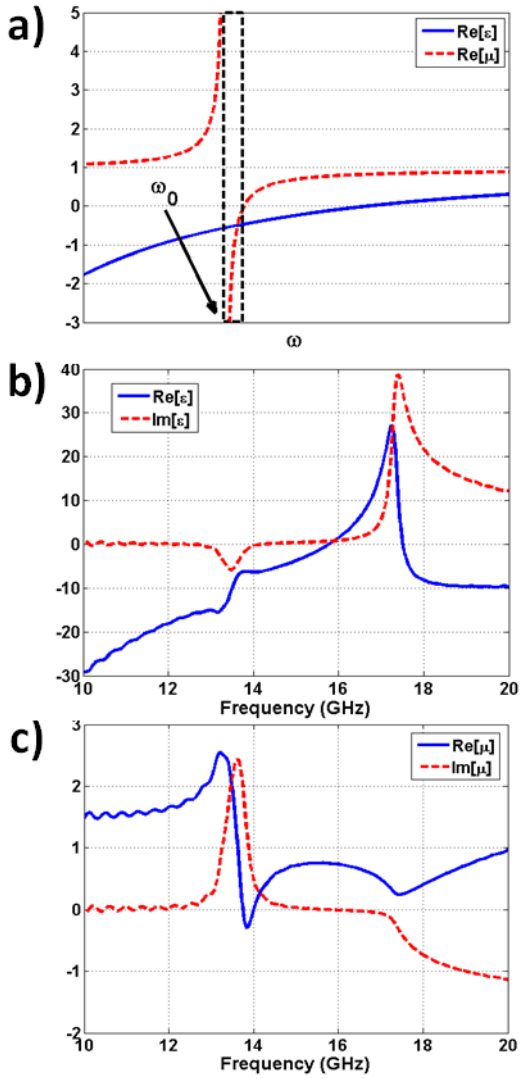

Figure 2.8: (a) The loss-free case for the permittivity (blue line) and permeability (dashed red line) vs. frequency. (b) The retrieved effective permittivity for the metamaterial. Real part (blue line) and imaginary part (dashed red line). (c) The retrieved effective permeability for the metamaterial. Real part (blue line) and imaginary part (dashed red line).

Actually, Eq. (2.54) presents the general case. As we have underlined, the stored electromagnetic energy can be expressed as in the case of the simplified version in Eq. (2.57) only for the lossless scenario. And the conditions that are given in Eq. (2.59)-(2.60) are merely applicable for this special case. The lossess are always evident, however small, in the metamaterials. Then, the conditions of Eq. (2.59)-(2.60) are no longer directly applicable. Nevertheless, we have worked with the loss-free case due to its

simplicity in analyses. Let us compare what these equations imply and compare it with the real life problem.

The researchers need low loss (ideally loss-free) metamaterials. But the loss free case must be subject to dispersion and the operational band of the metamaterial, where both of the constitutive parameters get negative values gets limited by a finite band.

The constitutive parameters are given in Fig. 2.8 for the loss-free case and the metamaterial (real life) problem. Once the losses are ignored, the effective permittivity and permeability values are portrayed in Fig. 2.8(a). The hypothetical problem has a magnetic resonance around ω_0. Thus, the conditions in Eq. (2.59)-(2.60) are satisfied over the band (dashed frame in Fig. 2.8(a)) in order not to violate the energy stability issues (the same conditions would also need to be satisfied for the RH medium as well, they are not solely appropriate for the LH medium). On the other hand, the retrieved parameters have a finite slope around the magnetic resonance unlike the loss-free case and the conditions in Eq. (2.59)-(2.60) are no longer meaningful with the incorporation of the losses. For a very limited region where the losses tend to get smaller values (only a very narrow region around 14 GHz) the real life problem may resemble the case in Fig. 2.8(a). Thus, this is the main reason why the researchers have grown an interest for the analysis of the loss-free metamaterials such as in Ref. 18. The simplified results of the loss-free problem might enable one to predict the results for certain bands (not the entire band) with low losses. The working band of the metamaterials for which both of the constitutive parameters are assigned to negative values, the losses might become bearable and the metamaterial might allow significant transmission (as one can see, not necessarily the example depicted in Fig. 2.8). Then, the loss-free problem might be projected to the real life problem or at least an analogy might be formed. However, such bold moves still have to be grounded and must be carried out with the utmost care.

It should be noted that the energy conservation conditions for the dispersive medium can also be written as $d(\omega\varepsilon_r)/d\omega + \mu_r / \varepsilon_r d(\omega\mu_r)/d\omega > 0$ in the absence of the losses, where ε_r and μ_r are the real parts of the permittivity and permeability, respectively. Then, this limitation is only valid as long as both of these parameters are positive or negative, simultaneously. Otherwise (when only one them is negative), the structure at hand would be opaque and it would be absorbing the incoming electromagnetic energy. Consequently, the energy conservation would not be a problem as in the case of the metamaterials. This is the region that is approximately between 14 GHz – 16 GHz in Fig. 2.8(b) and (c).

All in all, the derivations from Eq. (2.47) to Eq. (2.57) and the assumption of working with quasi-static fields are not mandatory to arrive at Eq. (2.59)-(2.60). Instead of the treatment given above Kramers-Kronig relations already provide the same conditions given in Eq. (2.59)-(2.60) for the lossless case [19]. One has to calculate the Kramers-Kronig integrals for the lossy metamaterial in order to determine boundaries of the bands in which the metamaterial can be effectively considered roughly loss free such that the conditions in Eq. (2.59)-(2.60) can be approximately applicable.

We have studied the energy conservation in metamaterials and associated it with the Foster's reactance theorem in passive one port network. Such a one to one correspondence can be established by assuming that the total area depicted in Fig. 2.7 (*s*) constitutes the total interaction area of the metamaterial with the outside world. This could be imagined by inserting the metamaterial inside a perfect conductor as in the case of Ref. 20 and connecting the metamaterial with the outer world through the specified area (*s*). Under those conditions, the problem boils down to the conventional one port network and Foster's reactance theorem can be immediately equated to the Poynting's theorem regarding the energy conservation. As a final remark, the researchers have also found out ways to relieve the dispersive restrictions on loss-free metamaterials. By adding active elements into the unit lattice of the metamaterial, the Foster's reactance

theorem could be violated while non-dispersive, relatively broadband negative constitutive parameters are achieved [21].

2.5 What is wrong with the negative group velocity?

With the emergence of the dispersive negative refractive index materials, the negative group velocities and negative group delays have been subject to investigations in a greater depth. Frankly, the heart of these regarding discussions is beyond the scope of this work. Yet, I feel obliged to just make a small remark about the notion of the negative group velocity from the limited number of papers that I have been able to cover. First of all, the negative group velocity (the negativity of the dispersion relation, $\partial\omega/\partial k$) may either mean a fast electromagnetic wave or antiparallel group and phase velocities inside the medium. We have, so far, been able to clarify the latter case in details in the previous chapters. The backward propagating waves do actually have negative phase velocities rather than a negative group velocity. Unfortunately, the concepts are carelessly used interchangeably in the research community. On the other hand, a fast light manifests itself in plasmonic structures, for which the light can be coupled in between the interfaces of the lossy materials. These mentioned plasmonic structure fall into the 2^{nd} quadrant in Fig. 2.4. Thus, we have evanescent waves inside the configuration. Such structures seem to be amplifying the input signal at first glance. However, a careful analysis reveals that they do not violate the causality, i.e., the electromagnetic waves do not go faster than light.

The tricky part is that cases when the direction of the group velocity and Poynting vector definitions do not mean the same thing. The electromagnetic waves always travel to the expected directions, however the wave packets may behave in counterintuitive ways, which result in negative group velocity. The present author of this work is aware of such cases, yet none of these scenarios have been encountered throughout the thesis writing. Hence, a relatively

acceptable reduction has been made to confine the interest by assuming that the group velocity does not extend beyond the definition of the Poynting's vector for the studied cases.

When we return back to the definition of the group velocity, $v_g = \partial\omega/\partial k$, we can face such dispersive media with $\partial n/\partial\omega < 0$. Does this automatically point to negative group velocity? Not necessarily, because the dispersion relation has to be sorted out carefully in the following way.

$$n = \frac{ck}{\omega} \Rightarrow \frac{dn}{d\omega} = \frac{-ck}{\omega^2} + \frac{c}{\omega}\frac{dk}{d\omega} \Rightarrow \frac{d\omega}{dk} = \frac{c}{n + \omega\dfrac{dn}{d\omega}} \tag{2.61}$$

Such a relation in the refractive index does not automatically lead to the negative group velocity.

2.6 Boundary conditions between a LH and a RH media

One of the most highly disputable issues regarding the LH medium is the boundary conditions. The discussion stems from the fact that the LH media are artificially constructed by carefully engineering the dispersive characteristics of the fundamental blocks. Hence, the actual boundaries of such structures are far more complicated than their homogenized counterparts. We are going to take a look at such structures in the following chapter. Even though the researchers are fond of sticking to the effective medium representations and attacking the problem as a homogenized slab problem, the boundaries of the structured metamaterials should be examined with care. I should still emphasize that such treatments involving an effective medium have not failed all together in the literature and founded a basis for the understanding of the refractions, diffractions and reflections from the surfaces of the LH media.

For the time being, let us assume a weakly dispersive homogenized LH slab stacked onto the RH medium, as shown in Fig. 2.9. Then, the boundary problem comprises the following well-known equations.

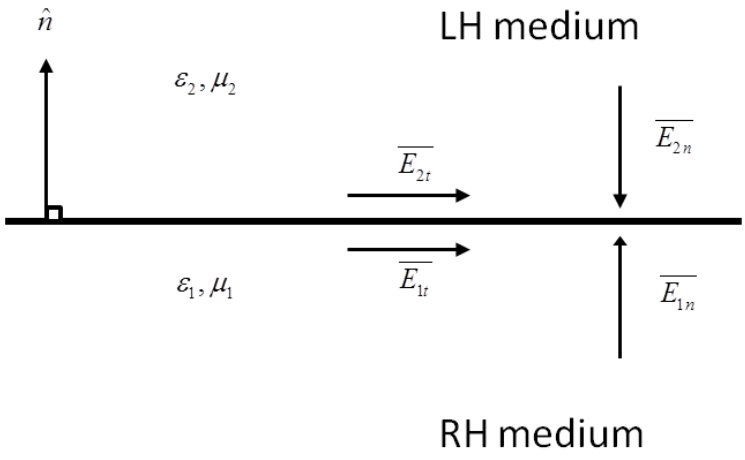

Figure 2.9: Boundary conditions between a RH and a LH media.

$$\hat{n} \cdot (\overline{D_2} - \overline{D_1}) = \rho_{es} \tag{2.62}$$

$$\hat{n} \cdot (\overline{B_2} - \overline{B_1}) = \rho_{ms} \tag{2.63}$$

$$\hat{n} \times (\overline{E_2} - \overline{E_1}) = -\overline{M_s} \tag{2.64}$$

$$\hat{n} \times (\overline{H_2} - \overline{H_1}) = \overline{J_s} \tag{2.65}$$

After having set the right hand sides of the above equations to zero (assuming no charge densities or surface currents at the boundary), it is evident that the normal components inside the two media are antiparallel to each other, whereas the tangential components are in parallel. The antiparallel normal components originate from the sign change of the constitutive parameters at the boundary.

2.7 Negative refraction

Negative refraction is a direct consequence of the boundary equations (Eq. 2.62-2.65). Plane waves are TEM waves for which both the electric and magnetic fields are perpendicular to the propagation direction. However, for the

impinging fields the classification is done with respect to the plane of incidence. TE (TM) waves are those whose magnetic (electric) field components are on the same plane with the incident plane. The definitions are also getting quite more confusing in the literature. Because, the same TE field turns into a TM wave with a reasoning that the electric field is on the same plane with the propagation direction. This is very unfortunate. We are going to be adapting these conventions that are commonly used (frankly quite misleadingly) in the literature. The detailed illustration regarding the TE/TM distinction is shown in Fig. 2.10.

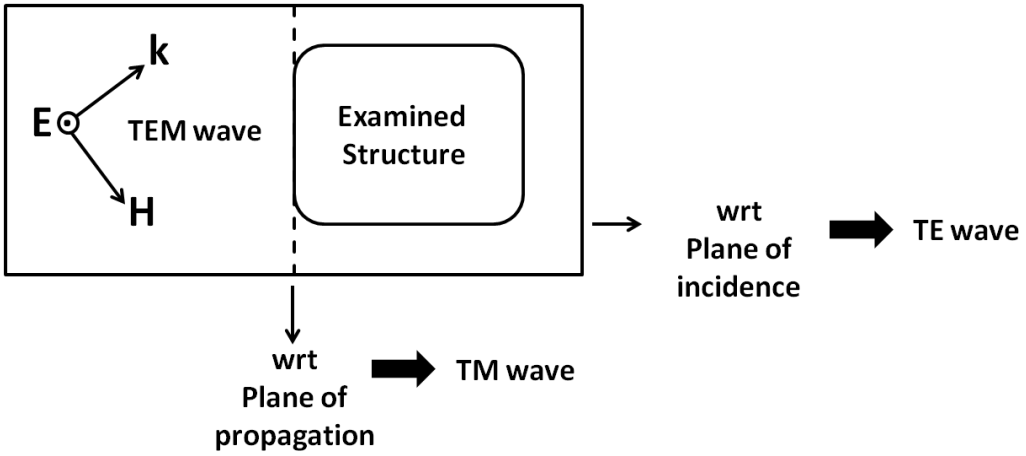

Figure 2.10: Originally a plane wave, TEM wave is defined with respect to the propagation and incident planes as TM and TE, respectively.

If we consider a plane wave $\overline{E_i}e^{-j\bar{k}\cdot\bar{r}}$ impinging on a boundary with an incident angle, then the tangential components have to be preserved. Let us assume that for this plane wave the electric field component is along *z*-axis and the plane of incidence lies on *y*-*z* plane. Then, the tangential component of the electric field at the boundary will give

$$E_i e^{-jk_{iy}y} + E_r e^{-jk_{ry}y} = E_t e^{-jk_{ty}y} \tag{2.66}$$

at $x = 0$ (the plane of incidence is located at this place), for which E_r and E_t are the reflected and transmitted field amplitudes, respectively. Thus, Eq. (2.66) has to be conserved for all and *y* values along the boundary. This can only be achieved when

$$k_{iy} = k_{ry} = k_{ty} \Rightarrow k_i Sin\theta_i = k_r Sin\theta_r = k_t Sin\theta_t \qquad (2.67)$$

which is called the phase matching condition at the boundary. The wavevectors, k_i and k_r reside inside the same medium so that $k_i = k_r \Rightarrow \theta_i = \theta_r$. The incident and reflected angles are the same. Another output of the phase matching condition gives way to what is known as Snell's law.

$$k_i Sin\theta_i = k_t Sin\theta_t \Rightarrow \frac{\omega}{v_i} Sin\theta_i = \frac{\omega}{v_t} Sin\theta_t \Rightarrow n_i Sin\theta_i = n_t Sin\theta_t \qquad (2.68)$$

The same phenomenon can also be analyzed in *k*-plane. Two different cases have been investigated. In the first one, a RH medium is adjacent to another RH medium. The circles in Fig. 2.11(a) have a definite radius equal to ω/v, where v is the speed of the electromagnetic wave inside the medium. For this particular example, the incident wave reaches the boundary that is along $\overline{k_y}$ from the higher index medium (with a circle that has a larger radius) and gets transmitted into the lower index medium. The circles depicted in Fig. 2.11 have also been named as Ewald circles. They present the dispersion relation for the isotropic medium. The phase matching condition manifests itself in the form of the construction line. The tangential components of the transmitted and incident waves have to be matched to each other. The construction line crosses the inner circle at two points. Given that the emerging field's Poynting vector is along +*x*, the transmitted field must also be propagating towards +*x* direction. Hence, the problem of choosing amongst the two crossed points is solved. The direction of the group velocity of the transmitted or in other words refracted field is drawn perpendicular to the tangential of the crossing point. The isotropy dictates that the phase velocity and group velocity are parallel to each other and the angle between the two is equal to zero. The last remark is about the total internal reflection. If the electromagnetic wave emerged at the boundary with a greater incidence angle, the construction line would not cross the inner circle. Thus, the total internal reflection would be observed.

On the other hand the refraction mechanism between a RH and LH media is depicted in Fig. 2.11(b). The inner circle corresponds to the medium with a negative refractive index. The 2nd medium has the opposite sign of refractive index with regards to the 2nd medium in Fig. 2.11(a). The significant difference is that the other crossing point is now used in order to obey the causality. The reason behind this selection is again related with the direction of the group velocity. The group velocity has to be drawn in the opposite direction for the negative index medium in comparison to the case in Fig. 2.11(a). The negative refractive index medium's circles (or dispersion contours) shrink inwards in contrast to the positive refractive index medium as the frequency is increased (since $\overline{v_g} = \overline{\nabla_k} \cdot \omega(\overline{k})$. Hence, the negative refraction occurs in accordance with Eq. (2.68) in the latter case.

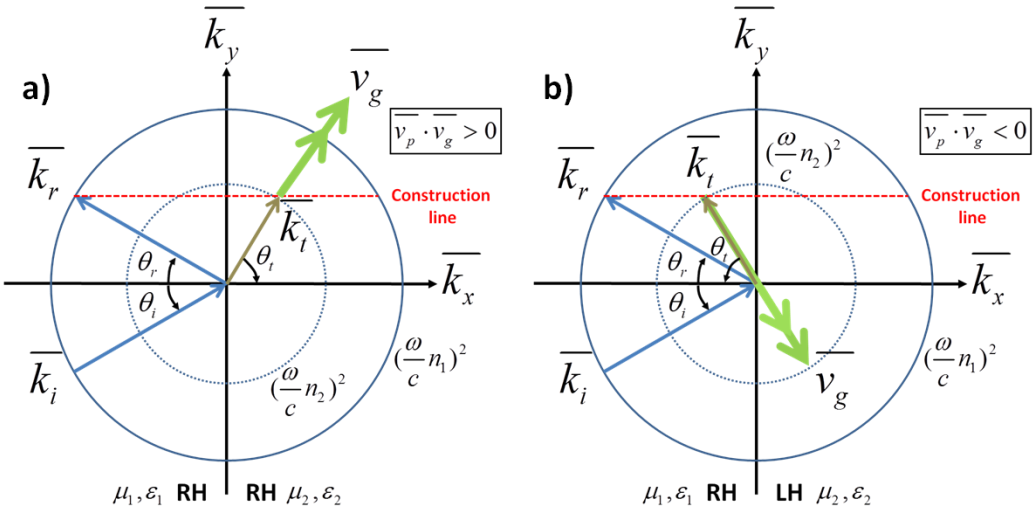

Figure 2.11: The refraction mechanism is shown in *k*-plane for (a) RH-RH and (b) RH-LH interfaces. The positive and negative refraction is depicted in (a) and (b), respectively.

2.8 Negative refraction or diffraction? A story of the contest between the believers and skeptics

As soon as the idea of a negative refractive index became relevant with the periodic materials that are going to be discussed in the following chapter, a huge dispute has also been initiated between the believers and skeptics in the

field of electromagnetics. The main motivation behind the debate could be attributed to the fact that such a periodic medium that demonstrates effective negative refractive index would definitely find profound application fields. Rather convincing experiments have been carried out by several research groups in the field of metamaterials clearly demonstrating the negative refraction, which would automatically lead to subwavelength imaging. Yet, many of these results were open to discussion typically because the transmitted results experienced large losses, the negative refraction could be observed solely in the near field and some of the periodic structures' dimensions were not engineered to stay in the effective homogeneity limit.

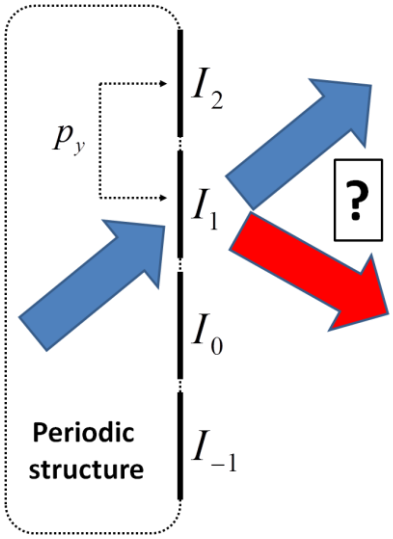

Figure 2.12: The dilemma of the refraction direction for a periodic structure.

It is well known in microwave engineering that an effective homogeneity limit can be reached when the lattice spacing between the alternating unit cells of the periodic structure is much less than the operational wavelength. Precisely speaking, $\lambda / 4 > p$ is accepted as this limit, where p is the lattice size. An exemplary refraction phenomenon has been demonstrated in Fig. 2.12. Despite the objection of the believers of the negative refraction, some of the persistent skeptics associated the phenomenon with possible diffractions and surface waves. After all, such periodic structures are nothing but a mixture of conductors and dielectrics. Electromagnetics entailing the inspection of such

configurations should be still valid. The depicted periodic structure in Fig. 2.12 can be perceived as an antenna array with induced dipoles at its surface. Accordingly, the radiation of such an antenna array can be arranged in different angular directions. Thus, for the simplest case of the uniform excitation,

$$\overline{E} \sim AF(p_y)g(r)[\hat{\theta} f_\theta + \hat{\phi} f_\phi] \tag{2.69}$$

defines the relation between the far-field electric field and the single dipole radiation, where *AF* is the array factor and directly determined by the element separation along *y*-axis for the exhibited case in Fig. 2.12, *g(r)* brings a phase term, f_ϕ, f_θ are the vector current moments of the induced surface current of the single element. An endfire or a broadside radiation patterns could be attained and the angular domain could be swept if the incident wave is somehow coupled and radiated by the surface elements.

Likewise, the diffractions coming from the periodic gratings can also alter the route of the incoming electromagnetic wave such that a negative refraction can be mimicked. Gratings with $\lambda/2 < p_y$ are known to support backward waves in photonic crystals.

As a result, the negative refraction at the output should be studied with care. One of such examples that I have encountered in my own studies has been pictured in Fig. 2.13 in which a wedge shaped structure is subject to the illumination from a horn antenna. The details of this structure will be given in the next chapters. For the sake of discussing the negative refraction this particular example has been attached. The periodicity of the unit elements at the interface were on the order of $\lambda/2 \leq p_y$. First of all, the observed negative refraction was ascribed to the involvement of the higher diffraction orders. The results of Fig. 2.14 assured that the higher orders ($+1^{st}$ and -1^{st} diffraction orders) were not coming into the picture within the frequency range of interest. The yellow zone in Fig. 2.14 demonstrated the acceptable solutions to the $\sin^{-1}$ problem, which should reside inside ± 1. Later on, it was suspected that the losses inside the wedge structure produced the seemingly negatively refracted

beam at the output by giving rise to an asymmetric effective aperture at the exit interface of the wedge configuration. Further inspections also approved the existence of the high losses inside the wedge configuration. Nevertheless, the wedge was also shown to support backward waves [see Fig. 2.3] and the combined effects of the dispersion due to the geometry of the prism and inherent losses affected the negative refraction, but did not terminate it totally. These aforementioned effects played a role in the shifting of the radiated beam on the exit surface of the wedge. It was successfully shown in the simulations that the output beams did not couple to a surface wave and the negative refraction was not the consequence of such a coupling. The negatively refracted beams went through losses but could still be detected at the outer boundaries of the Fresnel zone (at $z = 1$ m) for certain design parameters, which reinforced our conclusions about the negative refraction.

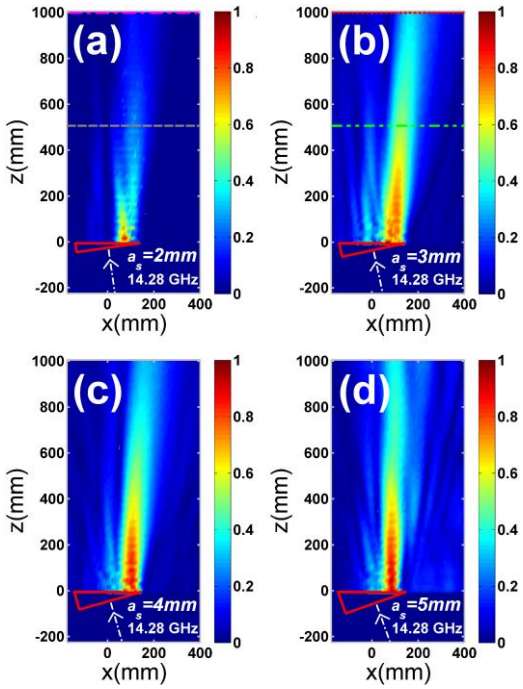

Figure 2.13: The experimental results of the negative refraction with a wedge structure for different inter lattice separations along the propagation direction. (a) $a_s = 2$ **mm, (b)** $a_s = 3$ **mm, (c)** $a_s = 4$ **mm and (d)** $a_s = 5$ **mm.**

In the end, I would humbly suggest to those who are in search for the negative refraction with periodic configurations to reserve their seat between the

true believers and persistent nonbelievers in order to approach with skepticism towards their results. A single type of scanning measurement, as in the case of the previous example, may present clues about the negative refraction but it does not have to be immediately sufficient for us to jump to sudden conclusions regarding the appearance of the negative refraction. Working with a periodicity, $\lambda / 2 > p_y$ is much safer owing to the fact that the course of the refracted beams are more difficult to be manipulated. Yet, systematic, thorough investigations are very likely to be needed.

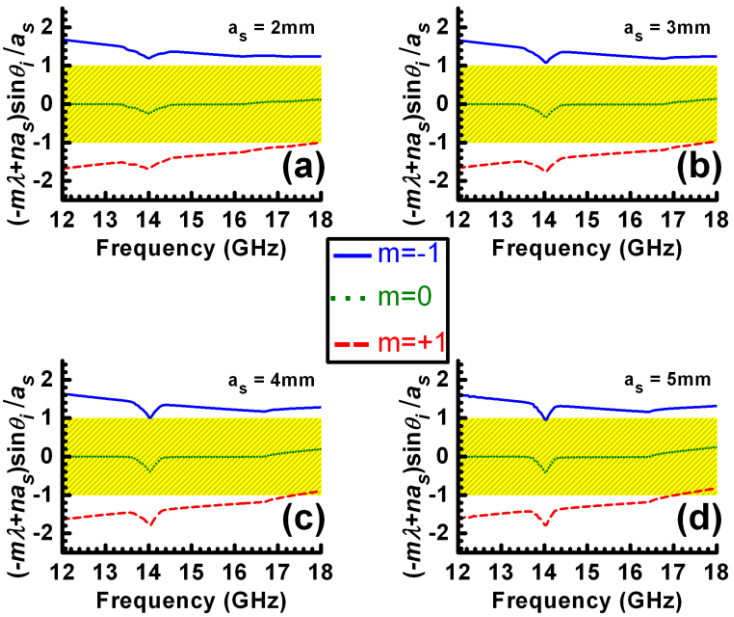

Figure 2.14: The effects of the higher diffraction orders at the exit of the wedge configuration, again for (a) $a_s = 2$ mm, (b) $a_s = 3$ mm, (c) $a_s = 4$ mm and (d) $a_s = 5$ mm.

2.9 Transfer matrix method and retrieval analyses

In this section, we are going to briefly discuss the transfer matrix method that is commonly employed in the calculations of the periodically cascaded structures. Conversely, the retrieval analyses serve the purpose of gathering information about the effective constitutive parameters of the complicated periodic configurations.

2.9.1 Transfer matrix method

If we examine Fig. 2.15 and try to come up with the Transfer Matrix Method (TMM) parameters of the simple TL,

$$E_{1+} = E_{2+}e^{+jkl},\ E_{1-} = E_{2-}e^{-jkl} \tag{2.70}$$

where l is the length of the TL. The above equation has been written by relying on Eq. (2.25) and (2.26). Then, the propagation matrix becomes

$$\begin{bmatrix} E_{1+} \\ E_{1-} \end{bmatrix} = \begin{bmatrix} e^{jkl} & 0 \\ 0 & e^{-jkl} \end{bmatrix} \begin{bmatrix} E_{2+} \\ E_{2-} \end{bmatrix}. \tag{2.71}$$

The total electric and magnetic fields at the ports can be expressed in the following way, just as in the case of Eq. (2.25) and (2.26).

$$E_1 = E_{1+}e^{-jkz} + E_{1-}e^{jkz} \tag{2.72}$$

$$H_1 = \frac{1}{\eta}[E_{1+}e^{-jkz} - E_{1-}e^{jkz}] \tag{2.73}$$

where $\eta = E/H$ is again the wave impedance that we had defined previously. Accordingly, the following relation can be established

$$\begin{bmatrix} E_1 \\ H_1 \end{bmatrix} = \begin{bmatrix} 1 & 1 \\ 1/\eta & -1/\eta \end{bmatrix} \begin{bmatrix} E_{1+} \\ E_{1-} \end{bmatrix}. \tag{2.74}$$

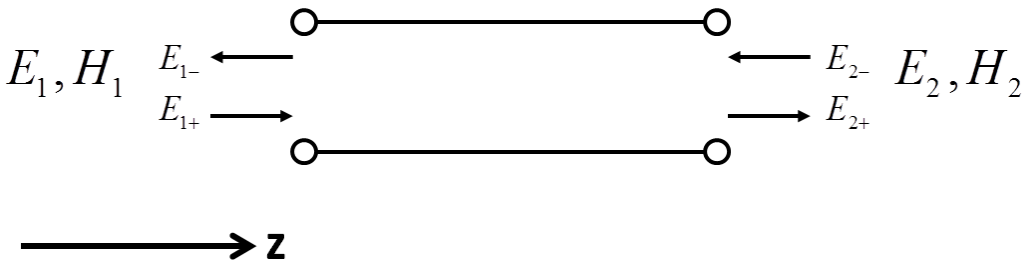

Figure 2.15: The TMM adaption of the simple TL

Hence, by making use of the following equation

$$\begin{bmatrix} E_1 \\ H_1 \end{bmatrix} = \begin{bmatrix} 1 & 1 \\ 1/\eta & -1/\eta \end{bmatrix} \begin{bmatrix} e^{jkl} & 0 \\ 0 & e^{-jkl} \end{bmatrix} \begin{bmatrix} 1 & 1 \\ 1/\eta & -1/\eta \end{bmatrix}^{-1} \begin{bmatrix} E_2 \\ H_2 \end{bmatrix} \tag{2.75}$$

which is equal to

$$\begin{bmatrix} E_1 \\ H_1 \end{bmatrix} = \begin{bmatrix} \cos kl & j\eta \sin kl \\ \dfrac{j \sin kl}{\eta} & \cos kl \end{bmatrix} \begin{bmatrix} E_2 \\ H_2 \end{bmatrix}, \begin{bmatrix} E_1 \\ H_1 \end{bmatrix} = \begin{bmatrix} A & B \\ C & D \end{bmatrix} \begin{bmatrix} E_2 \\ H_2 \end{bmatrix}. \quad (2.76)$$

Actually, TMM method comes handy for the cascaded systems and it works with the ABCD parameters of the system that the microwave engineers are already accustomed with. Thus, a conversion from the ABCD to S parameters yields the total transmission and reflection of the cascaded configuration.

$$T = S_{21} = \frac{2(R_{01}R_{02})^{1/2}}{AZ_{02} + B + CZ_{01}Z_{02} + DZ_{01}}, \quad (2.77)$$

$$R = S_{11} = \frac{AZ_{02} + B - CZ_{01}^{*}Z_{02} - DZ_{01}^{*}}{AZ_{02} + B + CZ_{01}Z_{02} + DZ_{01}}, \quad (2.78)$$

where R_{01} and R_{02} are the real parts of the seen impedances at the input and output terminals, respectively, likewise Z_{01} and Z_{02} are the impedance values at the corresponding terminals. These equations are for the most general case. If we assume that the cascaded network is inserted in between two dielectrics of the same kind, i.e., $R_{01} = R_{02} = Z_{01} = Z_{02} = Z$ Eq. (2.77) and (2.78) turns into a simplified version that I have also used in my research.

2.9.2 Retrieval method

The retrieval methods were first proposed at the turn of the century and since then several more complicated methods that can also be valid for thicker structures involving bianisotropy have been offered by the researchers for the varying angle of incidence. We are going to be discussing just the fundamentals of the retrieval analysis here that can be suitable specifically for 1-D metamaterials and 2-D metamaterials with small anisotropy. The results of the retrieval analysis are highly controversial. Many papers have discussed the validity of the retrieval codes. Basically, I have to make clear that we are not after the absolute value of the effective constitutive parameters in this work.

Such a detailed analysis is way beyond the scope of this thesis. The retrieval analyses that are employed in this work are assumed to be electrically thin structures that are causing small phase changes between the input and output ports. Furthermore, the essence of the retrieval analyses is merely to provide a fast recognition of the negative constitutive parameters.

The retrieval analysis is appropriate when the S parameters of the structure under test are collected in phasor format. Then, the investigated structure is aimed to be replaced with a simple slab with effective constitutive parameters such that it will give the same transmission and reflection parameters as the original structure gives. Retrieval approximations help us in converting the rather complicated electromagnetic response of the structures into plain slabs with effective parameters.

Hence, in order to do this we have to make use of Eq. (2.76). The ABCD parameters of a slab are given. With the given S parameters we are going to do just the reverse engineering of the problem we have attacked in the previous section.

$$\cos(k_0 nl) = A \Rightarrow n = \frac{\cos^{-1}(A)}{k_0 l} \tag{2.79}$$

$$B = j\eta \sin(k_0 nl),\ C = j\sin(k_0 nl)/\eta \Rightarrow \sqrt{B/C} = \eta \tag{2.80}$$

Thus, Eq. (2.79) and (2.80) shows that the refractive index and wave impedance of the slab can be retrieved once the ABCD parameters are known. Likewise, we can sort out the ABCD parameters from S parameters.

$$A = \frac{(Z_{01}^{\ *} + S_{11}Z_{01})(1 - S_{22}) + S_{12}S_{21}Z_{01}}{2S_{21}(R_{01}R_{02})^{1/2}} \tag{2.81}$$

$$B = \frac{(Z_{01}^{\ *} + S_{11}Z_{01})(Z_{02}^{\ *} + S_{22}Z_{02}) - S_{12}S_{21}Z_{01}Z_{02}}{2S_{21}(R_{01}R_{02})^{1/2}} \tag{2.82}$$

$$C = \frac{(1 - S_{11})(1 - S_{22}) - S_{12}S_{21}}{2S_{21}(R_{01}R_{02})^{1/2}} \tag{2.83}$$

Similarly, these equations are valid for the non-symmetric structures that are stacked in between different dielectrics. We have to pay attention to two things in the determination of the roots for the refractive index and impedance values. Firstly, the imaginary part of the refractive index cannot be negative (the signal must not be amplified inside the medium) and the real part of the wave impedance cannot be negative which would otherwise lead to negative resistance. The roots can be determined accordingly by choosing the reasonable solutions while bearing in mind these two restrictions.

Chapter 3

Subwavelength resonators and the road to negative refraction

This chapter intends to address two main issues. First of all, a brief introduction to the commonly utilized subwavelength resonators in the research community is given by starting from the famous split ring resonators and continuing with cut-wire structures. Furthermore, a realistic way of achieving an effective negative refractive index medium is presented. The author's aim is to offer the fundamental ideas even for those who are new to the research area.

3.1 Electromagnetic response of the natural materials

The first topic of a chapter should be relatively easier to grasp. In case of the electromagnetic response of the natural materials, it is just the opposite. We have only an approximate idea of what really is going on at the atomic or molecular level when an electromagnetic wave is interacting with a natural material. Thus, it is easier to handle the man-made materials since we have a better knowledge about their properties. Nevertheless, a natural material might possess induced electric and magnetic dipole moments either as a response to the incoming electromagnetic field or they might already be present in the medium. Their total combination determines the electric and magnetic polarizabilities in Eq. (2.7) and (2.8). These infinitesimal dipoles are defined as

$$p = el\,, \tag{3.1}$$

$$m = \mu_0 i \pi a^2\,, \tag{3.2}$$

where e is charge, l is the separation between the regarding charges, i is the current at the atomic level inside the medium and a is the radius of the loop i is

covering in order to generate a magnetic moment. The descriptive illustration of the induced moments inside the medium is shown in Fig. 3.1.

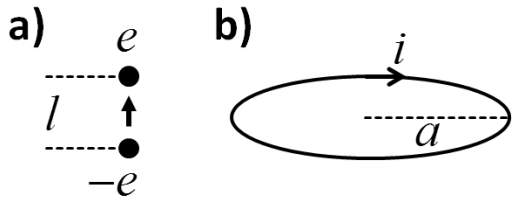

Figure 3.1: Induced (a) electric and (b) magnetic dipoles inside the natural medium.

Hence, the constitutive parameters of the medium can be determined from the relationships given in Eq. (2.5), (2.6), (2.9) and (2.10). The next challenge is to reproduce/mimic this atomic response by constructing periodic structures to attain effective negative permittivity and permeability values.

3.2 Negative permittivity

3.2.1 Negative permittivity in plasma

Plasmas are ionized gases with equal electron and ion densities. The available carriers make plasmas conductive and allow them to respond strongly to the electromagnetic waves. The electrons are much lighter and Newton had postulated his historical equation of motion for them.

$$m\dot{v} = F \tag{3.3}$$

$$m(\frac{dv}{dt} + \frac{v}{\tau}) = eE \tag{3.4}$$

where m is the mass of the electron, τ is a time delay (relaxation time) that would represent the damping factor. Then the velocity of a single electron can be written as

$$v = \frac{eE}{m(j\omega + \frac{1}{\tau})} \tag{3.5}$$

once we assume a harmonic temporal variation. Moreover, if the current density (J) is associated with the velocity of the electron

$$J = Nev = \frac{Ne^2\tau}{m}\frac{E}{1+j\omega\tau}. \tag{3.6}$$

Equations (2.40) and (2.41) remind us the relationship between the applied electric field and the current density.

$$J = \sigma E \Rightarrow \sigma = \frac{\sigma_0}{1+j\omega} \tag{3.7}$$

where $\sigma_0 = Ne^2\tau/m$. Now, we can return back to Maxwell's equations for harmonic fields and make use of this fact in case of the absence of the external current source so that

$$J + j\omega\varepsilon E = j\omega\varepsilon_{eff} E, \tag{3.8}$$

$$\varepsilon_{eff} = \varepsilon - j\frac{\sigma_0}{\omega}\frac{1}{1+j\omega\tau}. \tag{3.9}$$

This equation has two limits, in the low and high frequency limits

$$\varepsilon_{eff,low} = \varepsilon - j\frac{\sigma_0}{\omega}, \tag{3.10}$$

$$\varepsilon_{eff,high} = \varepsilon_0(1-\frac{\omega_p^2}{\omega^2}) \tag{3.11}$$

where ε is assumed to be approaching to ε_0 in the high frequency limit and $\omega_p = \sqrt{Ne^2/\varepsilon_0 m}$ is the plasma frequency. Accordingly, it can be seen that the dielectric constant of an ideal plasma is negative below the plasma frequency, which places them to the 2nd quadrant in Fig. 2.4.

3.2.2 Negative permittivity in wire medium

It can be shown that the wire medium mimics the plasma with a negative dielectric function. If an external spatially invariant electric field parallel to the wires (or a spatially varying electric field impinges onto electrically short wires)

is applied to a periodic wire medium in air [see Fig. 3.2], the induced voltage between the tips (P_1 and P_2) of each wire is equal to

$$V = -\int_{P_1}^{P_2} E \cdot dl = El \tag{3.12}$$

and the current turns out to be (from Ohm's law)

$$I = \frac{V}{Z} = \frac{El}{Z} = Ja^2 \tag{3.13}$$

where a is the unit lattice separation and $Z = R + j\omega L$ is the impedance of the wire.

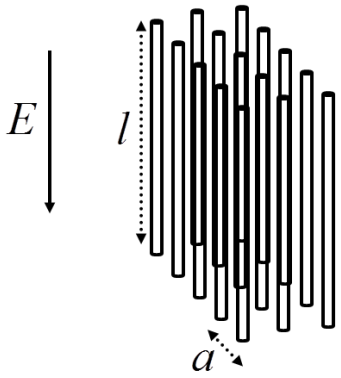

Figure 3.2: The periodic wire medium under the illumination of the external *E*-field.

Equation (3.13) once again relates the current density to the applied electric field as in the case of Eq. (3.7). Then, a similar treatment yields

$$J + j\omega\varepsilon_0 E = j\omega\varepsilon_{eff} E \Rightarrow \varepsilon_{eff} = \varepsilon_0 - j\frac{l/Ra^2}{\omega}\frac{1}{(1+j\omega\tau_w)} \tag{3.14}$$

which resembles Eq. (3.9) when a damping factor associated with the losses of the wires $\tau_w = L/R$ is defined. Then, it is apparent that a negative permittivity can be achieved with such a periodic configuration so that a similar effective dielectric function can be attained. Here, R and L have the following expressions

$$R = \frac{l}{\pi r_w^{\,2}\sigma_0},\ L = \frac{\mu_0 l}{2\pi}\left(\ln\left(\frac{2l}{r_w}\right) - \frac{3}{4}\right) \tag{3.15}$$

where r_w is the wire radius for the thin wires.

3.3 Negative permeability

As the findings of the previous chapter implies, we need dispersive effective medium parameters. Therefore, we require a dispersive permeability function. One way of achieving such a negative permeability is to use resonators. Fabry-Perot type resonators are fairly large (on the order of the operational wavelength). On the other hand, resonators could be built with lumped elements (L and C). However, the lumped elements do not effectively interact with the fields in the medium. Hence, a conductive loop with open ends appears to be the simplest choice for a subwavelength resonator. Such a configuration is depicted in Fig. 3.3 in which the loop is placed in air under the influence of a magnetic flux density.

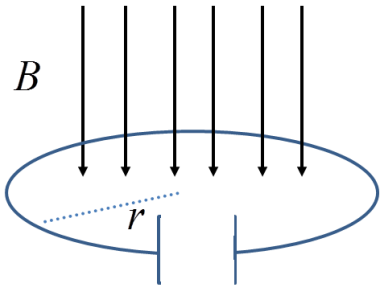

Figure 3.3: The conductive loop crosses the magnetic flux density.

Since the structure is comparably smaller than the operational wavelength, let us assume again a spatially invariant magnetic field. Then, the integral form of Maxwell's equations gives

$$V = \int_S \nabla \times E \cdot ds = \oint_C E \cdot dl = -\frac{\partial}{\partial t} \int_S B \cdot ds \tag{3.16}$$

which is the voltage across the gap in the loop. If we assume harmonic fields, then the induced current on the loop is equal to

$$I = \frac{V}{Z} = \frac{-j\omega\mu_0 \pi r^2 H}{Z} \tag{3.17}$$

where $Z = (j\omega L + 1/j\omega C + R)$ is the total impedance of the loop. Accordingly, the induced magnetic moment is (from Eq. (3.2))

$$m = \mu_0 I \pi r^2 = \frac{-j\omega(\mu_0 \pi r^2)^2 H}{Z}. \tag{3.18}$$

This magnetic moment is sufficient to determine the magnetic susceptibility tensor in Eq. (2.8), which is

$$m = \chi_{mm} H \Rightarrow \chi_{mm} = \frac{-j\omega(\mu_0 \pi r^2)^2}{Z}, \tag{3.19}$$

where $\chi_{mm}^{zz} = \chi_{mm}$ simplification has been done by assuming that the applied field is along *z*-axis. Note that we have safely dropped the tensor notation. Let us say that for N loops the total magnetic moment is $M_m = Nm = -j\omega(\mu_0 \pi r^2)^2 NH/Z$. Then, the effective permeability of the medium turns out to be

$$\mu_{eff} = \frac{B}{H} = \frac{\mu_0 H + M_m}{H} = \mu_0 - j\frac{\omega(\mu_0 \pi r^2)^2 N}{(j\omega L + 1/j\omega C + R)}. \tag{3.20}$$

Akin to the case with the wire medium, the loop medium may result in negative permeability as Eq. (3.20) implies for a certain frequency band.

3.4 Magnetic coupling

In the previous section we have made an assumption that the neighboring loops will not be mutually coupled to each other. However, such loops are obliged to share the incident magnetic field. The coupling may take place in two different scenarios, as shown in Fig. 3.4.

Figure 3.4 depicts the effective medium that comprises several conductive loops. Under these conditions the loops with the same color are aligned such that they share the same axis. Thus, the magnetic fields cannot form a loop for those cases and the conductive loops are positively magnetically coupled. It is just the opposite for those loops with the different color. The

magnetic field changes its sign and a magnetic loop is formed. Hence, those conductive loops are said to be negatively magnetically coupled.

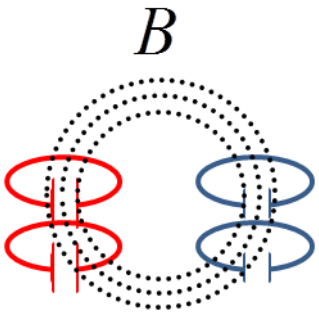

Figure 3.4: Two different magnetic coupling scenarios. The loops with the same colors have positive coupling and those with different colors have negative coupling.

As a result of this coupling scheme, a mutual inductance (*M*) will follow. Then, the voltage at each loop will be slightly different than Eq. (3.17). If we assume that all the elements have the same current, *I*, then

$$I = \frac{V}{Z} = \frac{-j\omega}{Z}(\mu_0 \pi r^2 H + I\sum M_{nn'}) \tag{3.21}$$

gives the induced current at each element as a function of the mutual coupling between *n* and *n'* elements. Thus, this coupling scheme will have either a broadening or a narrowing effect on the band with negative permeability in Eq. (3.20) once we carry out the formalism given in Eqs. (3.18)-(3.20).

3.5 Simultaneous negative permittivity and permeability

Let us return back to the Eqs. (3.14) and (3.20). When we ignore the ohmic losses ($R = 0$), the expressions simplify to

$$\varepsilon_r = \frac{\varepsilon_{eff}}{\varepsilon_0} = 1 - \frac{K}{\omega^2} \tag{3.22}$$

$$\mu_r = \frac{\mu_{eff}}{\mu_0} = 1 + \frac{\omega^2 K_1}{1 - \omega^2 K_2} \tag{3.23}$$

where K, K_1 and K_2 are the combination of the regarding multiplication constants in the previous equations. Then, the question arises if a region ever exists where we can find both of the real parts of the quantities to be negative.

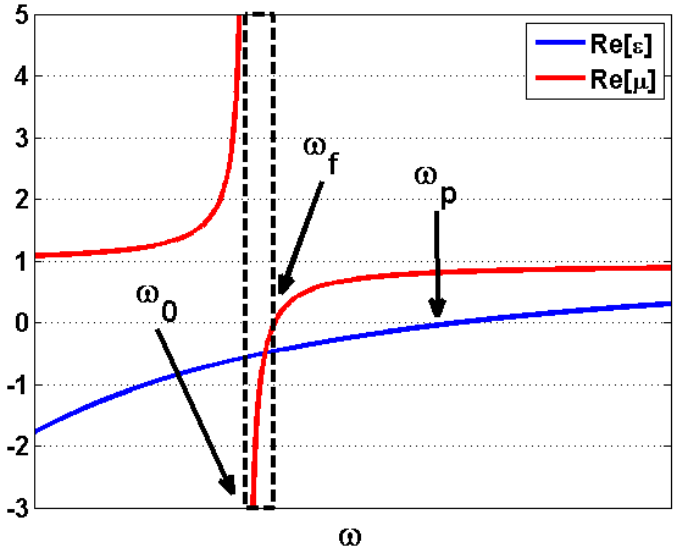

Figure 3.5: The effective permittivity (blue colored line) and permeability (red colored line) vs. frequency.

Simply yes, Fig. 3.5 shows that such frequency bands can be achieved where both of the effective constitutive parameters are negative. This crude analysis presents even at this stage that a LH medium might be present if a metamaterial is engineered from its building blocks, i.e., the wires and conductive loops.

Table 3.1 categorizes the speculated metamaterial structure and its frequency dependent electromagnetic response. ω_0 is the resonance frequency of the conductive loop, it will be called as the *magnetic resonance frequency* from hereafter. It can be perceived as the *LC* resonance of the conductive loop. The effective permeability is positive whereas the permittivity is negative before the magnetic resonance frequency. Hence, according to the definition of the refractive index in Eq. (2.35) the material is lossy and causes attenuations. The

same is also true for the frequency range of $\omega_f < \omega < \omega_p$, as well. Conversely, the propagation is allowed inside the medium in between the frequency ranges $\omega_0 < \omega < \omega_f$ and $\omega_p < \omega$. However, only in the frequency range around the magnetic resonance frequency, both of the constitutive parameters attain negative values.

Table 3.1: Frequency vs. the electromagnetic response.

Frequency	The Electromagnetic Response
$\omega < \omega_0$	Attenuation
$\omega_0 < \omega < \omega_f$	Propagation, LH medium
$\omega_f < \omega < \omega_p$	Attenuation
$\omega_p < \omega$	Propagation, RH medium

Even though such a prospective LH medium that will be constructed as a combination of its fundamental blocks seems to be a very promising idea, the designer should still be cautious. The electromagnetic response of the combined structure does not necessarily have to be the same or unaltered in other words. In contrast, the cases that we are going to be encountering in the following sections will show that the combined electromagnetic response will undergo some changes.

Now, we are left with a recipe to build the metamaterial, the LH medium that we have been investigating, questioning and challenging so far. Such a medium seems to be feasible, mathematically. The dispersive characteristics shown in Fig. 3.5 do not violate the energy conservation rule that was highlighted in the previous chapter. Yet, the exact location of each fundamental block will play a crucial role in the overall electromagnetic response. Although it is much easier to predict this response in comparison to a natural material, the fundamental blocks must be packaged quite dense in order to behave like the atoms and molecules of the natural materials, which makes the fabrication

process rather difficult. These elements should be arranged in close distance to each other in a fashion which will obey the effective medium assumptions.

3.6 A bird's-eye view of split ring resonators

Split Ring Resonators (SRRs) have been around since the mid 80s, but the researchers were not inspired to use them in their quest for a metamaterial. Instead of the simple open-ended loops that we have just analyzed, SRRs contain two concentric loops, which bring both a mutual inductance and a distributed capacitance. The schematic is shown in Fig. 3.6.

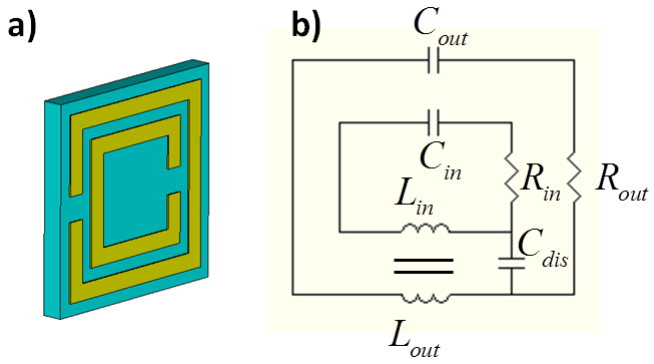

Figure 3.6: (a) Rectangular SRR and (b) the circuit representation of (a).

The distributed capacitance C_{dis} in Fig. 3.6(b) accounts for the capacitance formations between the inner and outer rings, which is usually much higher than the capacitances arising at the gap regions of the inner and outer rings, C_{in} and C_{out}. In many occasions C_{in} and C_{out} have a negligible effect. The inner and outer rings have mutually coupled inductances. Accordingly, there is a very simple method of analyzing SRRs.

(i) The total distributed capacitance in one half plane of the SRR is equal to $C_{half} = \pi r_0 C_{pu}$ for a SRR with a radius of r_0, where C_{pu} the capacitance per unit length. The two half planes' distributed capacitances are in series to each other. Then the total capacitance is $C = C_{half} / 2$.

(ii) The two inductances of the inner and outer rings have similar values such that $L_{in} \approx L_{out} \approx L_{av}$ for such small loops, which is the average inductance.

(iii) Then, the magnetic resonance of the SRR is simply found at $\omega_0 = 2/\sqrt{\pi r_0 C_{pu} L_{av}}$.

The regarding intuitive treatment has been proven to be quite powerful in determining the magnetic resonance of the SRRs in the literature. The simple interpretation has also been verified analytically, as well. Then, the total circuit turns into the one shown in Fig. 3.7.

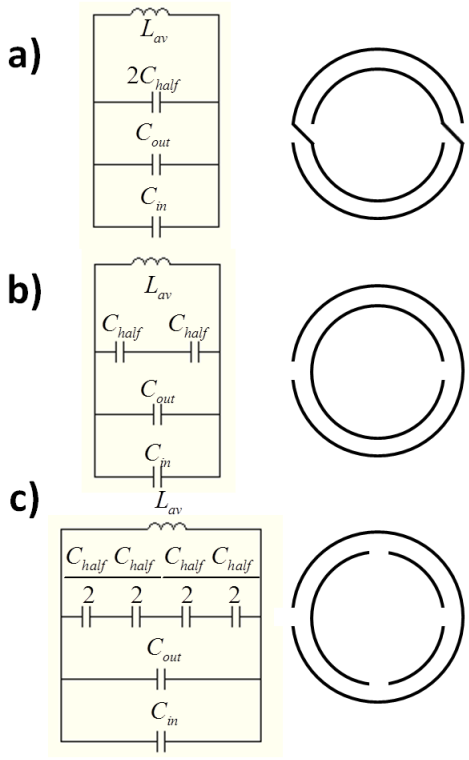

Figure 3.7: Three possible scenarios with SRRs (a) inner ring shorted to the outer ring, (b) the conventional SRR, (c) two extra gaps are inserted into the inner ring.

The conventional SRR circuitry is shown in Fig. 3.7(b). For the other scenarios, the distributed capacitances are sliced into pieces or combined into a single value. The shorted case in Fig. 3.7(a) has just a single distributed

capacitance. We will no longer be able to cut the 2π plane into pieces, whereas the plane is sliced into 4 subplanes for the analysis.

The fundamental idea behind the SRR on top of the single conductive loops that were discussed in the previous chapters is to make use of the inner distributed capacitance and thereby to further lower the resonance frequency, which puts the resonator into the deep subwavelength regime. The regarding transmission curves are depicted in Fig. 3.8. The isolated resonances of the inner and outer loops reside at separate locations in the frequency spectrum while the outer ring has lower resonance frequency, as expected. Both of these resonances are attributed to the *LC* tank in the conductive loops and the resulting magnetic dipole. On the other hand, the resonances do split, the SRR's first resonance shifts to $\omega_0 = 10.32$ GHz, which is a lower frequency than the magnetic resonance of the outer loop solely. This first resonance is the one that we tried to estimate using the intuitive approach in the previous paragraphs. Furthermore, the second resonance ($\omega_1 = 23.24$ GHz) is also caused by the magnetic dipole moment as it can be seen in the field maps (will be discussed in the proceeding sections). Nevertheless, the third dip in the graph ($\omega_3 = 44.48$ GHz) is very likely to be the result of the electrical resonance akin to the electrical dipole antenna, which occurs when the length of the loop is half of the operational wavelength.

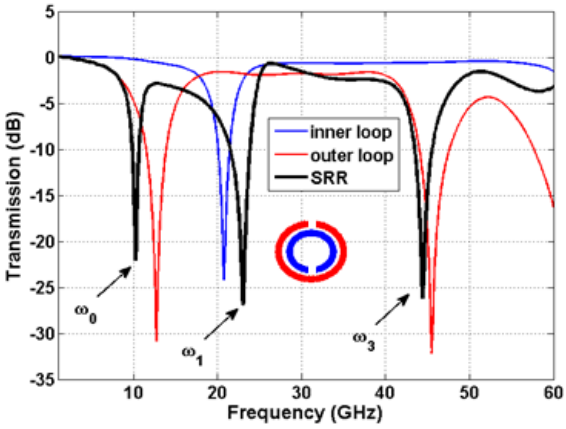

Figure 3.8: Simulated transmission results for the inner loop (blue line), outer loop (red line) and SRR (black line).

Finally, the effect of the shortening of the individual loops has been presented in Fig. 3.9. The shortening of the outer loop effectively kills the resonance. A small dip is still observed at $\omega_2 = 18.82$ GHz, which is close to the magnetic resonance of the inner loop only (see Fig. 3.8). The shortening of the inner loop shifts the magnetic resonance to higher frequencies from $\omega_0 = 10.32$ GHz to $\omega_1 = 12.51$ GHz, which is again close to the individual resonance of the outer loop.

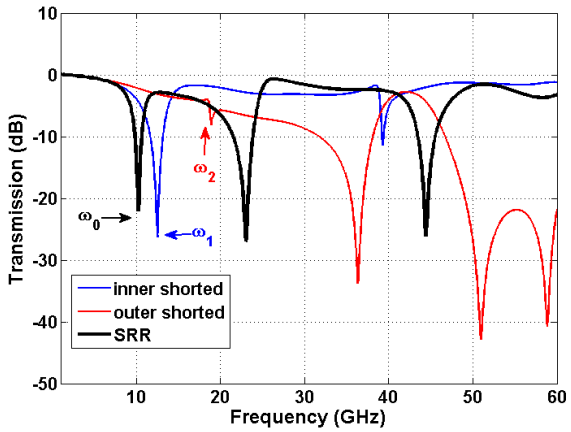

Figure 3.9: Simulated transmission results for the SRR with inner loop shorted (blue line), outer loop shorted (red line) and without any shortening (black line).

Figure 3.10 discusses the possible coupling scenarios to the SRR. The directions of the incident electric and magnetic fields have been given at the right hand side of the regarding figure. The magnetic resonance around 10 GHz is evident in Fig. 3.10(a)-(c). However, it disappears for Fig. 3.10(d), since none of the dipole moments in SRR are induced at that particular frequency. We witness only the electrical resonances in Fig. 3.10(d). We are going to return to this part after a few more words about the polarizability of the SRRs.

The striking information is hidden in Fig. 3.10(c) which shows the bianisotropic nature of the SRRs. Fig. 3.10(c) portrays the case with no magnetic coupling. Therefore, the appearance of the magnetic resonance can be quite plausible. However, a careful examination of the SRR geometry shows that it possesses bianisotropic nature. If we return back to Eqs. (2.7) and (2.8),

we realize that the SRR structure has cross-polarizations susceptibilities in order to yield the magnetic resonance without any direct magnetic coupling. The detailed derivations are out of the scope. Nevertheless, the dipole moments can be written in the following forms in general.

$$m_x = \chi_{xx}^{mm} B_x^{ext} - j\chi_{yx}^{em} E_y^{ext} \tag{3.24}$$

$$p_z = \chi_{zz}^{ee} E_z^{ext} \tag{3.25}$$

$$p_y = \chi_{yy}^{ee} E_y^{ext} + j\chi_{xy}^{me} B_x^{ext} \tag{3.26}$$

These equations are the dipole moments that have been illustrated in Fig. 3.11. Onsager relation dictates that an external electric field can induce an electric dipole moment just like an external magnetic field induces the magnetic dipole. The regarding field distributions are plotted in Fig. 3.12. The incoming electric field in 3.11(a) in *y* direction gives rise to a magnetic dipole moment in *x* direction which results in the magnetic field accumulation inside SRR.

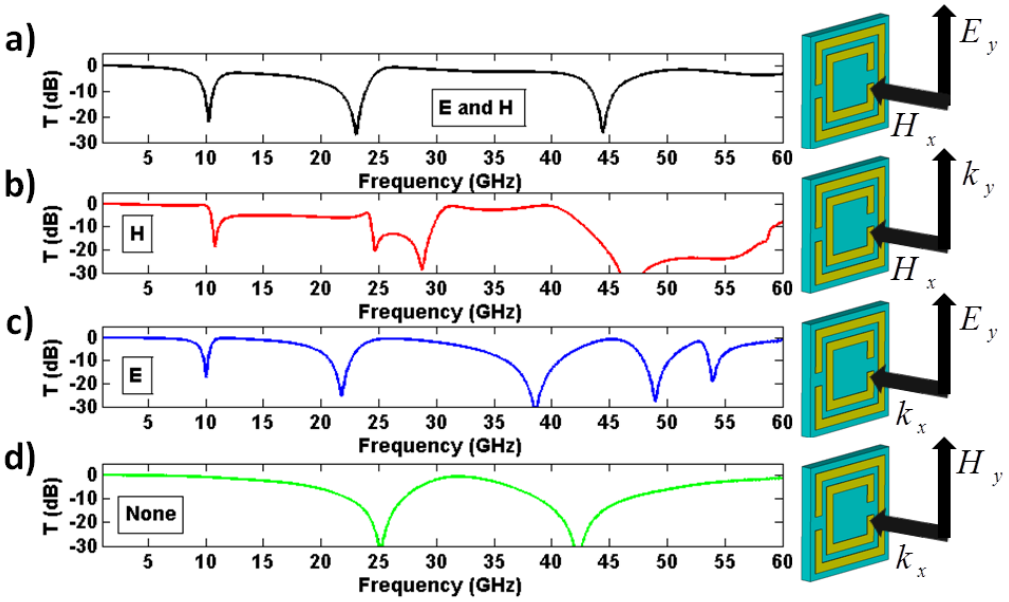

Figure 3.10: Simulated transmission results for (a) E and H coupled, (b) only H coupled, (c) E coupled and (d) the case without any coupling of the electromagnetic waves.

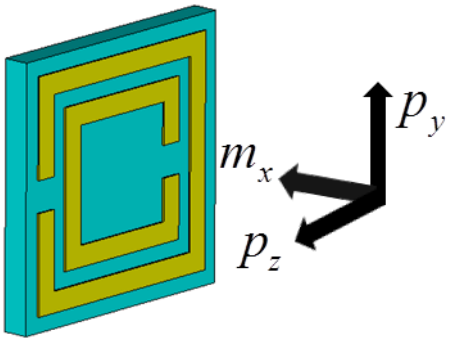

Figure 3.11: The dipole moments that can be induced by external fields exerted on the SRR.

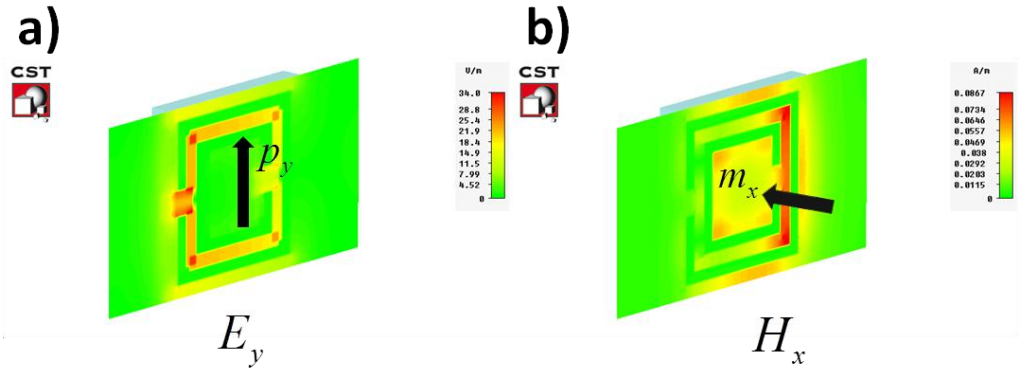

Figure 3.12: (a) Induced electric dipole and (b) induced magnetic dipole as a consequence of E_y.

Actually, the inspection of the field distributions turns out to be very useful in the determination of the physical phenomena. The gradual unequal distribution of the electromagnetic fields in Fig. 3.12 is the reasoning behind the circulating currents and the magnetic resonance. Figure 3.13 undertakes the responsibility of reopening the discussion of the magnetic resonances in Fig. 3.10(a) for the *E* and *H* coupling by utilizing the field maps. Figure 3.13(a)-(f) deals with the *E*-*H* coupled case that is portrayed in Fig. 3.10(a). Around the magnetic resonances at $\omega_0 = 10.32$ GHz and $\omega_1 = 23.24$ GHz, the incident magnetic field is coupled into SRR and a magnetic dipole moment is created as it can be seen in Fig. 3.13(b) and (d). We do not see the same thing happening at $\omega_3 = 44.48$ GHz. While the field distributions are gradually varying for the

magnetic resonances, the fields are rather abruptly distributed at 44.48 GHz. Finally, the case without coupling that corresponds to that of transmission in Fig. 3.10(d) has been studied. These structures are illuminated with an incident plane wave. Thus, periodic boundary conditions are imposed. It can be clearly seen in Fig. 3.13(g) and (h) that the fields are localized between either inter element spacings (along the transverse longitudinal direction) or gaps separating the metallic parts in the unit lattice for both of the cases which are attributed with the electrical resonance in Fig. 3.10(d).

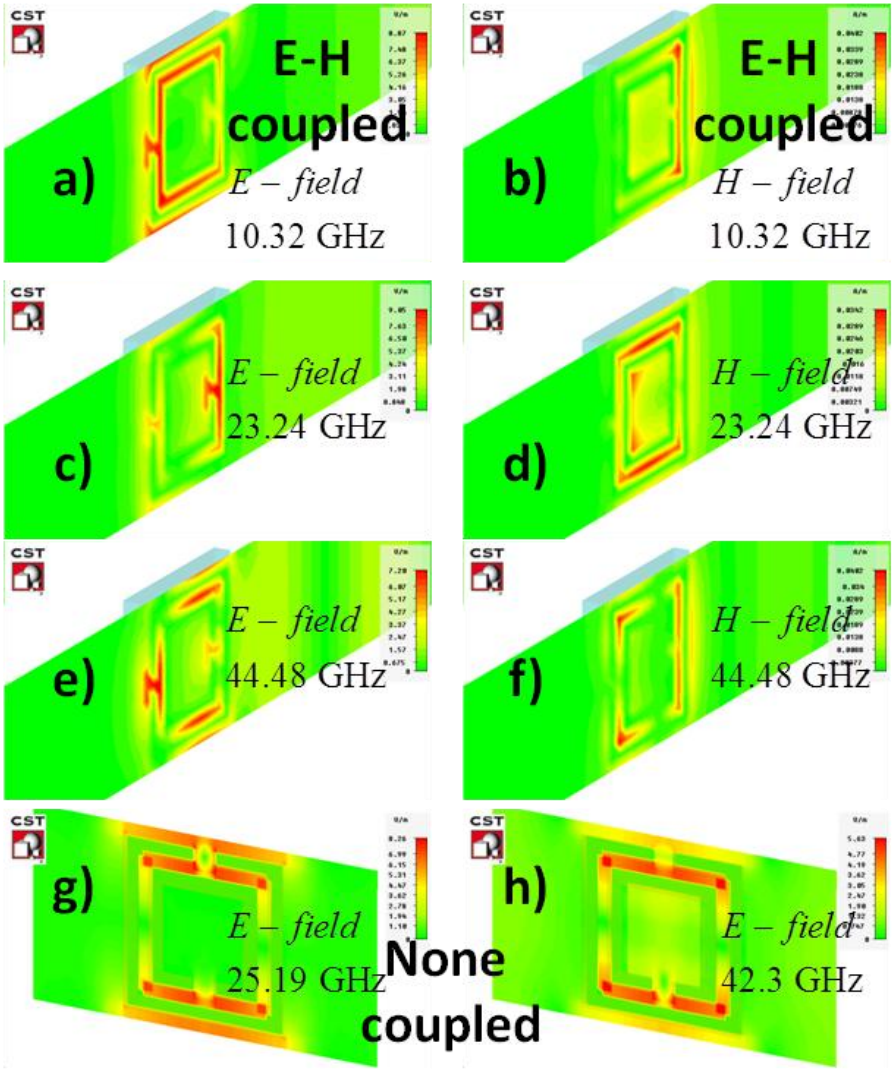

Figure 3.13: Electrical field maps for *E-H* coupled case at (a) 10.32 GHz, (c) 23.24 GHz and (e) 44.48 GHz. Magnetic field maps for *E-H* coupled case at (a) 10.32 GHz, (c) 23.24 GHz and (e) 44.48 GHz. Field maps for the uncoupled case at (g) 25.19 GHz and (h) 42.3 GHz.

3.7 Negative refraction with planar metamaterials: cutwires+wires

Parts of this section was published as "*Planar bilayer metamaterial with left-handed transmission and negative refraction at microwave frequencies"* Atilla Ozgur Cakmak, Kaan Guven and Ekmel Ozbay Physica Status Solidi (b), volume 244, page 1188 (2007) Reproduced (or 'Reproduced in part') with permission from WILEY-VCH Verlag GmbH & Co. KGaA, Weinheim. © WILEY-VCH Verlag GmbH & Co. KGaA, Weinheim.

A planar composite metamaterial consisting of bilayers of metal cutwire pairs and long wire pairs which are separated by a thin dielectric layer is designed and fabricated for microwave frequencies. The simulated and experimentally measured tranmission spectra of the metamaterial and its individual components (cutwire-only and wire-only) indicates that the metamaterial exhibits a transmission band within the common stop bands of its components, and thus acts as a medium with negative index of refraction. The existence of $n < 0$ is further supported by refraction and phase measurement experiments.

A one dimensional metamaterial can be constructed by stacking SRR and wire layers alternatingly. The combined configuration of wires and SRRs is called the composite metamaterial (CMM). There are numerous studies which employ different SRR/wire patterns for metamaterials. Most of these designs adhere to the aforementioned SRR topology. In this case, the electromagnetic wave vector is required to be *in* the plane of metamaterial layers and significant number of layers should be stacked to provide sufficient thickness for the incident field, as shown in Fig. 3.14(a). This requirement turned out to be a major drawback to fabricate metamaterials at infrared and optical frequencies [22-25].

Conversely, a different topology for obtaining magnetic resonance is proposed and demonstrated [26]. The SRR is replaced by metal cutwire strips

separated by a dielectric layer, like a parallel plate capacitor (see Fig. 3.14(b)). The magnetic field *parallel* to the plane of metal strips can induce a resonance which leads to $\mu(\omega) < 0$. This allows the electromagnetic field to propagate *normal* to the metamaterial plane, as opposed to the *parallel* propagation of the former SRR/wire topology. Following this, a number of metamaterial studies are reported [27-29].

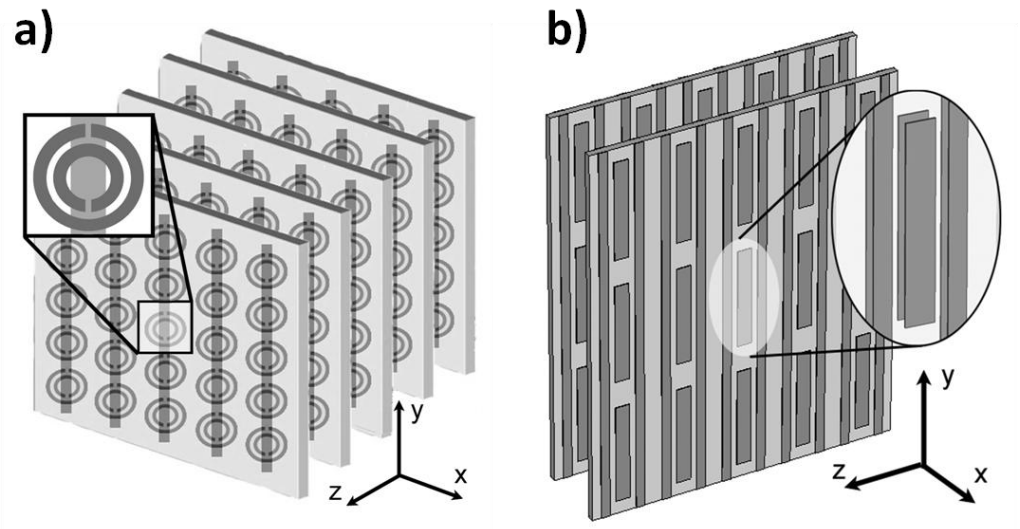

Figure 3.14: CMMs made out (a) SRRs + wires and (b) cutwires + wires. The propagation direction of the incident wave is along *x*-axis.

In this study we have employed this topology to design and fabricate CMMs for microwave frequencies. Transmission and phase spectra of the CMM have been analyzed. A refraction experiment has been carried out to clearly identify our structure as a metamaterial.

The bilayer is fabricated from dielectric layers (thickness d = 0.4 mm, dielectric constant ε_r = 4.2) with a metal coating (t = 30 μm) on both sides. Figure 3.15 shows the schematic view of the CMM unit cell. d is the thickness of the dielectric spacer between the pair elements. The cutwire dimensions are w_{cutw} = 0.8 mm, y_{cutw} = 5.5 mm, and the wire dimensions are w_{wire} = 0.5 mm, y_{wire} = 7.0 mm. The unit cell has dimensions a_x = 2.0 mm, a_y = 7.0 mm, a_z = 3.5 mm. a_x is the stacking periodicity in the propagation direction. With these parameters, the simulated cutwire structure exhibits a magnetic resonance

around, $f_m \approx 14$ GHz. The wire units are designed with a high cut-off frequency in order to ensure the $\varepsilon < 0$ within the $\mu < 0$ stop band of cutwires. The wires are present on either side of the bilayer for symmetry.

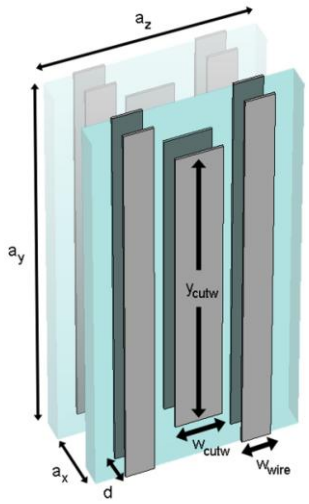

Figure 3.15: Schematic view of the bilayer metamaterial. The cutwires and wires are located on both sides of a thin dielectric layer, *d*. The unit cell contains one paired cutwire and two paired long wire elements. The geometrical parameters and periodicity of the structure are given in the text. The bilayers are stacked in the *x* direction with periodicity a_x.

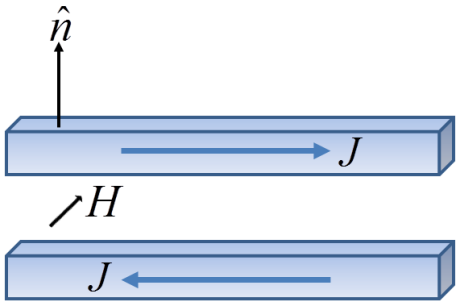

Figure 3.16: The excited mode and induced currents on the cutwires.

Under the illumination of an electric field along the axis of the parallel cutwires, the odd mode with antiparallel currents will be supported. Accordingly the magnetic field will be coupled to the cutwires. Hence, at the boundary of the cutwire-air interface

$$\hat{n} \times (\overline{H_1} - \overline{H_2}) = \hat{n} \times \overline{H_1} = \overline{J}\,, \tag{3.27}$$

so that for the *y* directed surface current, $\overline{H_1}$ is along *z* direction. Then,

$$\overline{H_1} = \hat{y}\frac{I}{w_{cutw}} \tag{3.28}$$

$$L = \frac{\int_S B \cdot ds}{\oint_C B \cdot dl} \sim \frac{\mu_0 \times d \times y_{cutw}}{w_{cutw}}. \tag{3.29}$$

The capacitance between the plates is calculated straightforwardly.

$$C \sim \frac{\varepsilon_0 \times \varepsilon \times w_{cutw} \times y_{cutw}}{d} \tag{3.30}$$

The magnetic resonance is $\omega_0 = 1/\sqrt{LC} \sim 1/y_{cutw}$.

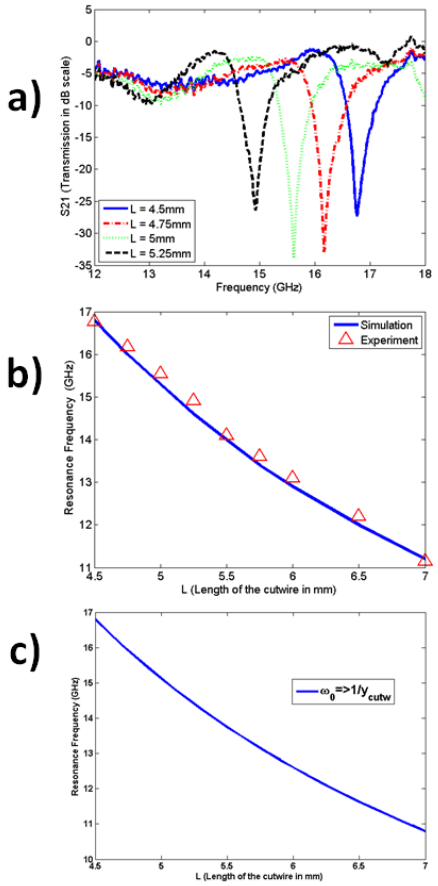

Figure 3.17: (a) Measured transmission results for cutwires with different lengths, (b) simulated and measured resonance frequencies vs. *L* (length of the cutwire, y_{cutw}), (c) the direct adaptation of the simple intuitive result.

Figure 3.17 shows that the static field based calculations of the L and C produce very accurate results in determining the change of the resonance frequency of the cutwires with the cutwire length (y_{cutw}). On the other hand, the resonance frequency should have been immune to the changes in the cutwire width (w_{cutw}). However, Fig. 3.18 explicitly shows that the resonance frequency is also shifting with such changes for some constant y_{cutw} value. Hence, the simple LC tank formulation is not taking into account the fringing fields while w_{cutw} is attaining larger values in the periodic structure. The mutual coupling between the unit lattices (see Sec. 3.4) might have become dominant. Then again, the change is a secondary effect, because the shifts are not as strong as in the case of Fig. 3.17(a).

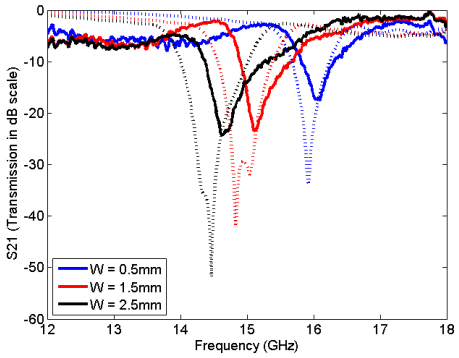

Figure 3.18: Measured (dotted) and simulated (solid) transmission results for cutwires with different widths.

The transmission spectra of the CMM, cutwire-only and wire-only structures were measured in free space, by a HP8510C Network Analyzer and a set of antennas (see Fig. 3.19(a)). We employ a similar analysis conducted for SRR/wire type CMM in order to identify the left-handed transmission band [30]. Figures 3.19(b) and (c) summarize the measurement and simulation results, respectively. The ω_p (plasma frequency) of the wire-only structure is very high, thus, $\varepsilon(\omega) < 0$, as indicated by the stop band spanning the measured frequency range. The cutwire only structure exhibits a clear resonance gap around 14.25 GHz. In order to identify this, we used a complementary structure in which the cutwire pairs are electrically shorted. This removes the capacitive coupling of

the cutwire pair, and the resonance. Thus, we deduce that the gap is due to the magnetic resonance, and implies $\mu(\omega) < 0$.

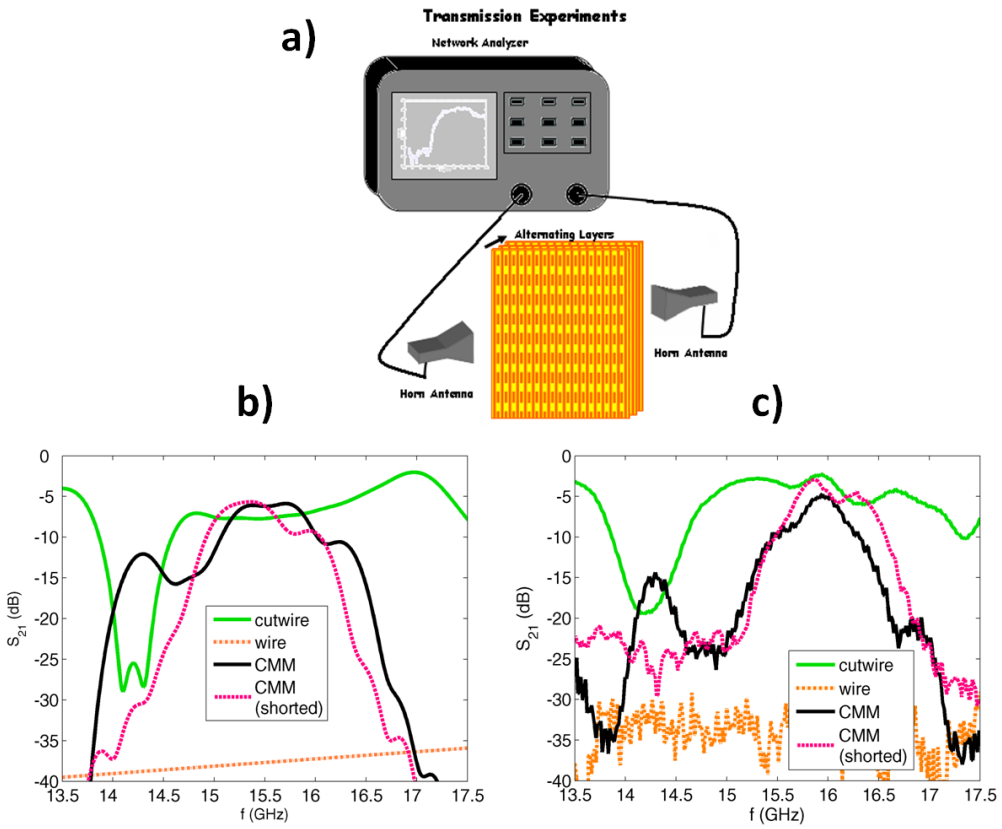

Figure 3.19: (a) Transmission setup, (b) measured and (c) simulated transmission spectra of the CMM and its individual components. The left-handed transmission peak of the CMM around 14.25 GHz appears in the magnetic resonance gap of the cutwires. The transmission band extending from 15.5 to 17 GHz is right handed. Note that the shorted cutwire does not exhibit the magnetic resonance gap, which leads to the absence of the left-handed peak for the shorted CMM.

The CMM exhibits two distinct peaks. The left peak coincides with the magnetic resonance of the cutwires. A complementary CMM which incorporates shorted cutwires does not show the left transmission peak. Therefore, we conclude that the transmission band around 14.25 GHz is left-handed. The second transmission band is right handed, since it is common to both CMM and the complementary CMM. We note that the cutwires couple to the electric field as well, which has a dominating effect on the overall electric response of the CMM. Indeed, if the $\varepsilon(\omega) < 0$ behaviour of the CMM were due to the wires only, the aforementioned right-handed peak should not be present.

The simulations are performed by the commercial software (CST Microwave Studio®). In the simulations, the structure is assumed to extend infinitely along the lateral directions. We anticipate that the finite size of the fabricated structures in the *y* direction may have an effect on the electric response of the CMM. Nevertheless, all the essential features of the experimentally observed spectra were obtained by simulations, with a good agreement in spectral position.

In order to confirm that the CMM acts as a medium with $n_{eff} < 0$, we performed a negative refraction experiment using a bulk CMM structure consisting of 4 layers. The electromagnetic signal is incident at $\Theta = 10^{o}$ to the center of the CMM surface from the left side. The transmitted signal is scanned laterally along the exit surface of the CMM. The scanning experimental setup is represented in Fig. 3.20(a). Accordingly, if the slab has a negative refractive index, it is expected to detect the outgoing signal at the left hand side and vice versa is true for the right handed medium.

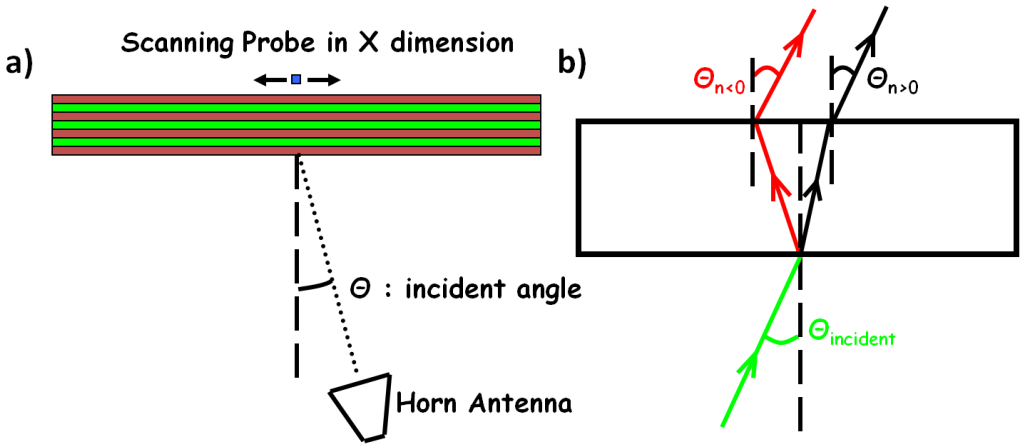

Figure 3.20: (a) Scanning experiment setup and (b) the positive/negative refraction scenarios.

Figure 3.21(a) and (b) shows the lateral and frequency distribution of the transmitted signal with color coded transmission level. Evidently, the beam transmitted within the left-handed band appears on the *left* side of the origin (blue line) in Fig. 3.21(c), indicating that the beam refracted negatively upon entering the CMM. The lateral power profile taken at f = 14.3 GHz (within the

left handed band) confirms the negative lateral shift of the beam. Conversely, the beam is positively refracted inside the right-handed band and falls on the *right* hand side of the origin at the exit side.

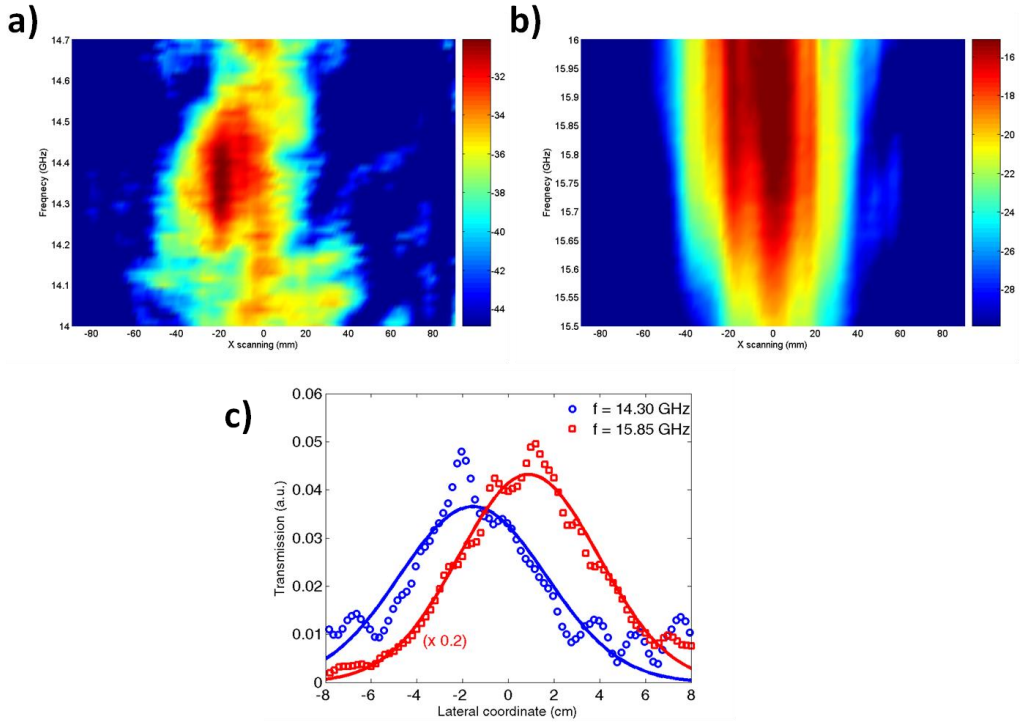

Figure 3.21: Frequency and lateral spatial distribution of the transmitted signal at the CMM surface for 10^0 incidence within (a) the left-handed and (b) right-handed bands. Warm color indicates higher transmission. (c) Lateral power profile taken at f = 14.3 GHz (blue line) and at f = 15.85 GHz. The peak appears at the *negative* side of the origin for f = 14.3 GHz. The incident signal (not shown in the figure) is centred at the origin.

Finally, unlike the usual positive medium behavior the added layers increase the accumulated phase in the left-handed transmission band (see Fig. 3.22(b)). Then, the negative phase velocity can be observed. Assuming a homogenized structure along the propagation direction, the accumulated phase change due to the replacement of the slab of length, L_1 by another slab of L_2 can be written in the following form for $+j\omega t$ convention

$$\Delta\phi = -\Delta\bar{k}\cdot\bar{r} = -2\pi n\Delta L/\lambda\,. \tag{3.31}$$

where $\Delta L = L_2 - L_1$. If $\Delta L > 0$ and $n > 0$ then the phase change must be negative, which can be observed throughout the right-handed band.

Alternatively, for $\Delta L > 0$ and $n < 0$ the phase change is positive owing to the effective negative refractive index.

Figure 3.23 presents the retrieved effective parameters of the single layer CMM structure. The details of the employed retrieval analysis have been covered in Sec. 2.9. The retrieval algorithm has been applied to a slightly different CMM whose substrate layer has now been changed to FR4. This is the main reason of the minor shift of the LH transmission band. Nevertheless, the results are similar to the expectations of Fig. 3.5. The LH band emerges at the location where simultaneously both of the constitutive parameters attain negative values. ω_p resides at 16 GHz and the electrical resonance of the CMM structure is around 17.5 GHz. At the electrical resonance, the field is localized between the two metallic segments of the wires and cutwires, correspondingly. The localized field is shown in Fig. 3.23(d). Hence, the antiparallel currents that are shown in Fig. 3.16 are not preserved. Cutwires are not coupled to the incident wave magnetically by forming an effective inductive loop between the two sides of the substrate.

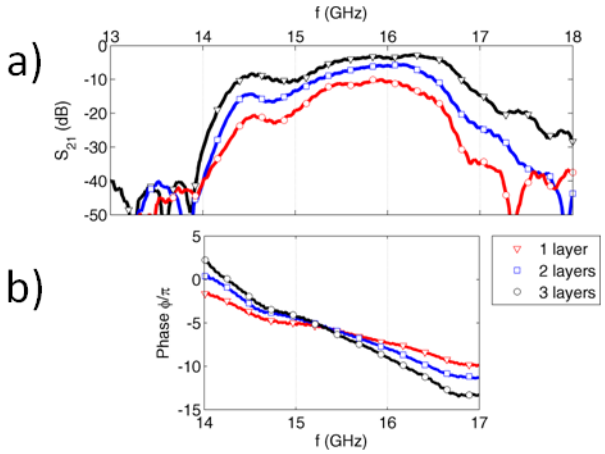

Figure 3.22: a) The transmission and b) phase spectra of the CMM structure for a different number of layers in the propagation direction.

One of the most plausible things that should be questioned is the region where $\mathrm{Re}[n] < 0$ in Fig. 3.23(c), while $\mathrm{Re}[\mu] < 0$ in Fig. 3.23(b). There is an artificial effective negative refractive index associated with the CMM

configuration inside that band. The losses are relatively large $\mathrm{Im}[n] \approx 6$ and therefore the transmission is not allowed for the mentioned frequency region.

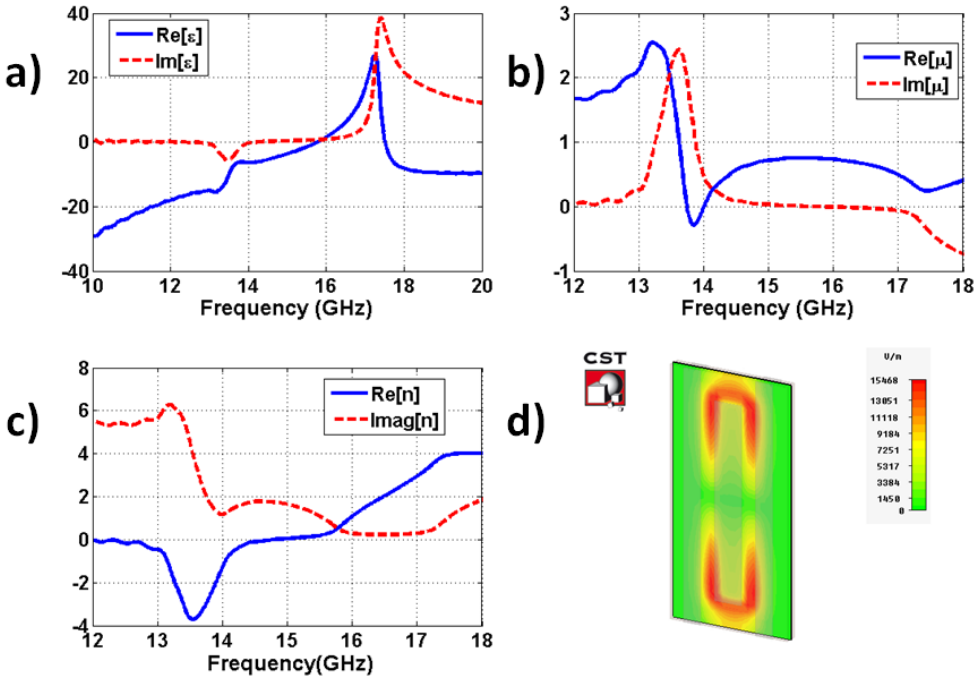

Figure 3.23: Retrieved effective parameters for a) real (blue line), imaginary (dashed red line) parts of the permittivity, b) real (blue line), imaginary (dashed red line) parts of the permeability and c) real (blue line), imaginary (dashed red line) parts of the refractive index. (d) The localized field distribution around the electrical resonance (17.5 GHz).

3.8 A Couple of possible application fields of the metamaterials

The subwavelength imaging has been the main driving force behind the progress of the research field of metamaterials in the recent years. Cloaking, nonlinear phenomena in metamaterials, chirality have been just a small group of the new emerging research focuses in the metamaterial community. Apart from these applications, I have been able to investigate the suitability of the metamaterials for antenna applications during my thesis. The purpose of this part is merely to present couple of possible applications of the covered metamaterials.

Another striking output of the retrieval parameters and phase spectra given in the previous section is the frequency region where $n \approx 0$ and a zero index material is observed, consequently. Thus, such a structure may find applications in the antenna research. As a result, directive antennas can be obtained. Figure 3.24 shows one such example. A monopole's isotropic radiation is converted into a directive output at the exit side of the metamaterial slab which is placed right in front of the CMM. The full-width at half maximum of the outgoing radiation is found to be 8^0. Of course, the losses inside the CMM configuration are detrimental. They have to be taken care of in order to make a fair comparison and come to the conclusion that the metmaterial in the current example increases the antenna gain. Of course, one should also check the power transmission levels before reaching a sudden conviction. The modification of the antenna radiation should not be accompanied by terrible losses.

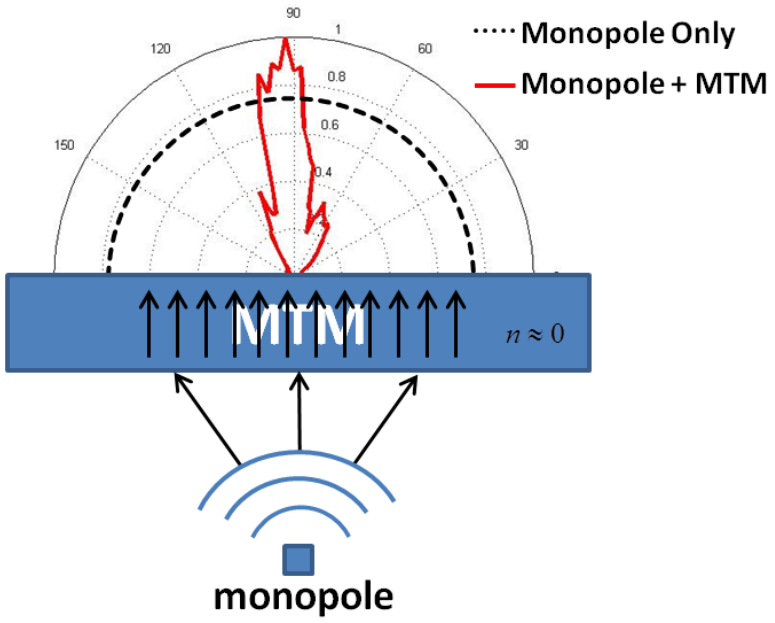

Figure 3.24: The measured modified radiation pattern (red pattern) of the monopole probe that is placed in front of the CMM configuration in Fig. 3.15. The isotropic radiation pattern of the monopole probe is given just as a reference with no physical correspondence.

It has been shown in the research field that the metamaterial incorporated antennas' reactance values were significantly compensated by the SRRs. Hence,

the radiation efficiencies are increased with the addition of the resonance structures. After all, MTMs can be perceived as transducers that convert the wave energy into loop currents and voltages. Another application that may find grounds is the miniaturization of the conventionally available antennas. A regarding example of the metamaterial loading (actually just the SRR without the continous wires) of the loop antenna is shown in Fig. 3.25, for which the input reflection coefficient of the loop antenna is improved. A better matching comes with a 30% miniaturization. The loop antenna's original operational band has shifted to lower frequencies after the metamaterial loading. The inclusion of the plain FR4 layer (magenta color) already pulled down the resonance frequency by increasing the dielectric filling around the loop antenna. The loop antenna's quality factor is similar to that of the series *RLC* network, which is $Q \sim \sqrt{L/C}$. The added SRR layer brings in an inductive slab into the picture. A higher quality factor is achieved at a smaller resonance frequency ($\omega_0 \sim 1/\sqrt{LC}$).

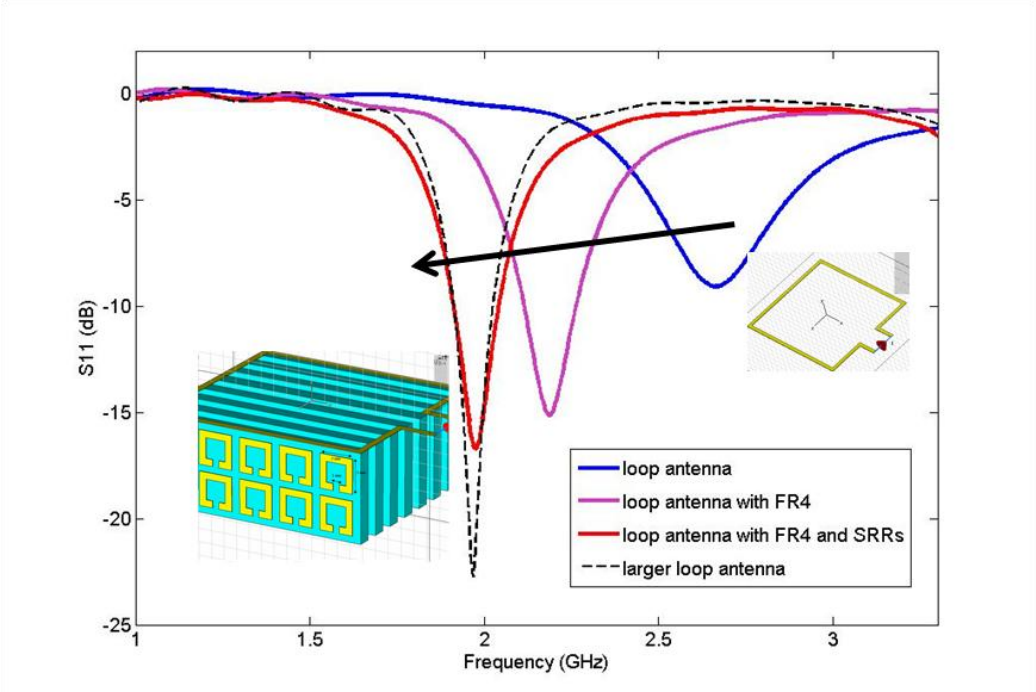

Figure 3.25: Miniaturization of the loop antenna with the SRR loading.

Chapter 4

Subwavelength Apertures

4.1 Single Aperture

In this part we are not going to be restricting our attention to the subwavelength apertures. Instead, the section will start by outlining a general perspective for the transmission through apertures. Then, the discussion concerning the subwavelength apertures will be laid out.

4.1.1 Kirchhoff scalar diffraction from an aperture

For scalar waves of the form $\psi(r,t)=\psi(r)\exp(j\omega t)$ the following equations and $\psi(r)=Ae^{-jkr}/r$

$$(\nabla^2+k^2)\psi(r)=0, \tag{4.1}$$

$$(\nabla^2+k^2)g(r,r')=-\delta(r,r'), \tag{4.2}$$

account for the solutions with (nonhomogenous differential equation) and without (homogenous differential equation) a point source in the regarding volumes. $g(r,r')$ is the free space Green's function. If we rearrange Eq. (4.1) and (4.2) such that

$$(\nabla^2+k^2)\psi(r)g(r,r')-(\nabla^2+k^2)g(r,r')\psi(r)\ldots.$$

$$\ldots=\nabla^2\psi(r)g(r,r')-\nabla^2g(r,r')\psi(r)=\nabla\cdot(\nabla\psi(r)g(r,r')\ldots$$

$$\ldots-\nabla g(r,r')\psi(r))=\delta(r,r')\psi(r) \tag{4.3}$$

Then, Gauss's theorem gives

$$\int_V dr\nabla\cdot[\nabla\psi(r)g(r,r')-\nabla g(r,r')\psi(r)]=\iint_{dV}\overline{ds}\cdot[\nabla\psi(r)g(r,r')\ldots$$

$$\ldots-\nabla g(r,r')\psi(r)]=\int_V dr\delta(r,r')\psi(r)=\psi(r') \tag{4.4}$$

Equation (4.4) shows how a field on a surface (S) determines the wave off the surface ($\psi(r')$) for an observation point r', which is the mathematical representation of Huygen's principle. Figure 4.1 presents a more general picture and explicit way of expressing a field in terms of the fields on the selected surfaces. Here, S_{inf} is the surface at infinity. Then, the field at the observation point is

$$\psi(r') = \iint_{dV(S)} ds\hat{n} \cdot [\cdots] + \iint_{dV(S_{\text{inf}})} ds\hat{n} \cdot [\cdots] \tag{4.5}$$

where the dotted places ($[\ldots]$) should be filled with the expressions that are in similar format to Eq. (4.4) at two surfaces. Hence, it can be shown that the terms for the second integral in Eq. (4.5) cancel each other in the far field and Huygen's principle can be expressed in the most general way like the following

$$\psi(r') = \iint_{dV(S)} ds\hat{n} \cdot [\nabla\psi(r)g(r,r') - \nabla g(r,r')\psi(r)]. \tag{4.6}$$

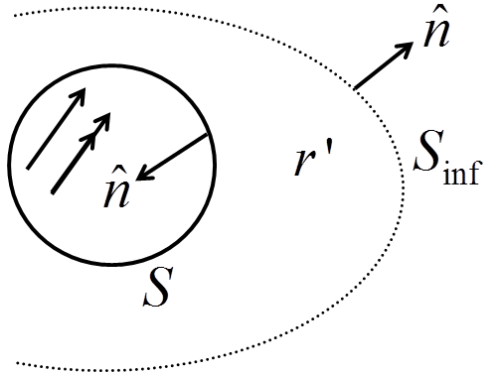

Figure 4.1: Figurative representation of Huygen's principle.

If we adapt the problem for our current study of apertures, we can reconfigure the problem as it has been done in Fig. 4.2. If we rewrite Eq. (4.6),

$$\psi(r') = \int_{S_{\text{inf}}} + \int_{S_1} + \int_{S_3} + \int_{S_2} [\nabla\psi(r)g(r,r') - \nabla g(r,r')\psi(r)] \cdot \hat{n}ds = \ldots$$

$$\ldots \int_{S_2} [\hat{n}\frac{e^{-jk|r-r'|}}{4\pi|r-r'|}\frac{\partial\psi(r)}{\partial n} - \hat{n}\psi(r)\frac{\partial}{\partial n}(\frac{e^{-jk|r-r'|}}{4\pi|r-r'|})] \cdot (-\hat{n})ds\,. \tag{4.7}$$

Equation (4.7) is true under the assumption that $\partial\psi(r)/\partial z = 0$ and $\psi(r) = 0$ for surfaces S_1 and S_3 which are encapsulating the semi-infinite perfect electric conductor (PEC) walls. It was previously mentioned that the terms in the S_{inf} integral cancel each other. Furthermore, S_2 signifies the area of the aperture.

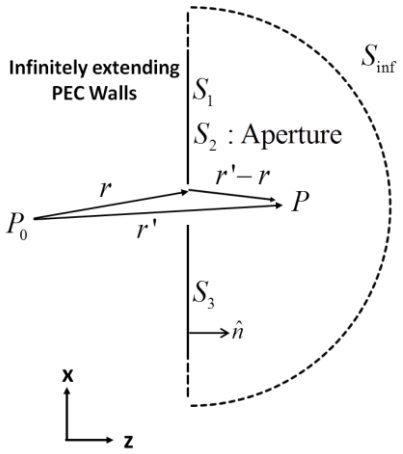

Figure 4.2: Figurative representation of the diffraction problem.

Equation (4.7) can be further simplified by writing

$$\frac{\partial\psi(r)}{\partial n} = \frac{\partial\psi}{\partial r}\frac{\partial r}{\partial n},\quad \frac{\partial g(r,r')}{\partial n} = \frac{\partial g(r,r')}{\partial r''}\frac{\partial r''}{\partial n} \tag{4.8}$$

where $r'' = |r'-r|$. Then,

$$\frac{\partial\psi(r)}{\partial n} = (-jk - \frac{1}{r})A\frac{e^{-jkr}}{r}\cos\theta \tag{4.9}$$

$$\frac{\partial g(r,r')}{\partial n} = (-jk - \frac{1}{r''})\frac{e^{-jkr''}}{r''}\cos\phi \tag{4.10}$$

where θ and ϕ are the angles between the surface normal vector, $\hat{n}$ and r, $\hat{n}$ and $|r\text{-}r'|$, respectively. Then, Eq. (4.7) becomes

$$\psi(r') = -\int_{S_2} A\frac{e^{-jk(r''+r)}}{4\pi r''r}[\cos\theta(-jk - \frac{1}{r}) - \cos\phi(-jk - \frac{1}{r''})]ds\,. \tag{4.11}$$

If we assume that $k = 2\pi/\lambda >> 1/r$,

$$\psi(r') = j\frac{A}{\lambda}\int_{S_2}\frac{e^{-jk(r''+r)}}{r''r}\frac{[\cos\theta-\cos\phi]}{2}ds\,. \tag{4.12}$$

Equation (4.12) can be written in terms of the transmission coefficient ($t(r)$) of the diffraction grating that is under test. An incident wave with a wavefunction ($u_{inc}(r)$) is bound to get diffracted in the general formula

$$\psi(r') = \frac{j}{\lambda}\int_{A} t(r)u_{inc}(r)\frac{e^{-jk(r'')}}{r''}\frac{[\cos\theta-\cos\phi]}{2}ds\,. \tag{4.13}$$

An interesting property of this formulation is its symmetry with respect to the source and observation point. It is therefore also referred to as the reciprocity theorem of Helmholtz.

Now, assume that the observation distance, r'' is quite large and approximately lies on the *z* axis. Then,

$$kr'' = k\sqrt{z^2+(x-x_0)^2+(y-y_0{}^2} = kz(1+\frac{1}{2}(\frac{x-x_0}{z})^2+\frac{1}{2}(\frac{y-y_0}{z})^2+\cdots)\ldots$$

$$\ldots = kz(1+\frac{x^2+y^2}{2z^2}-\frac{xx_0+yy_0}{z^2}+\frac{x_0{}^2+y_0{}^2}{2z^2}+\cdots). \tag{4.14}$$

Furthermore, the solution to $[\cos\theta-\cos\phi]/2=\cos\delta$ from the given relations in Fig. 4.3.

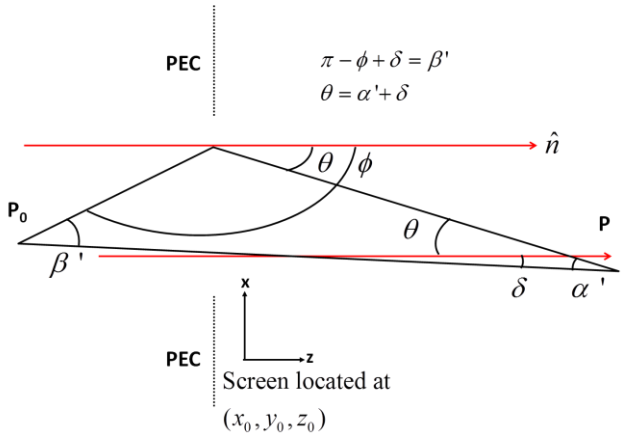

Figure 4.3: Angle relations for the diffraction problem.

Using Eq. (4.14) in Eq. (4.12), the Fresnel approximations are obtained.

$$\psi(r') = j\frac{A}{\lambda}\int_{S_2}\frac{e^{-jkr}}{r}e^{-jkz}\frac{e^{\frac{-jk}{2z}((x-x_0)^2+(y-y_0)^2)}}{z}\cos\delta dx_0 dy_0 \qquad (4.15)$$

This approximation brings Fresnel integrals due to the square terms.

4.1.2 Fresnel Diffraction from a Gaussian aperture

This small example is given because the implications of this example will be useful in understanding the results at the output of the Photonic Crystal based structures. The diffraction in such examples will resemble the Gaussian aperture case. A Gaussian aperture has the form $\exp(-(x_0^2 + y_0^2)/w_0^2)$, where $2w_0$ is the aperture width. Then, considering both Eq. (4.13) and (4.15) together, $t(r) = 1$ around the aperture, $u_{inc}(x_0, y_0) = \exp(-(x_0^2 + y_0^2)/w_0^2)$, $\cos\delta = 1$, the incident waves are aligned to the normal axis of the aperture. We have just interchanged the scenario that the impinging wave is a Gaussian wave and the aperture is the same one that we have just analyzed previously. As a result,

$$\psi(r') = \frac{j}{\lambda}\int_{S_2}\exp(-(x_0^2 + y_0^2)/w_0^2)e^{-jkz}\frac{e^{\frac{-jk}{2z}((x-x_0)^2+(y-y_0)^2)}}{z}dx_0 dy_0 . \qquad (4.16)$$

However, Eq. (4.16) is nothing but the convolution of the Gaussian incident wave with the phase term in the integral. Consequently, Eq. (4.16) becomes

$$\psi(r') = \frac{j}{\lambda z}e^{-jkz}\int[F(\exp(\frac{-(x^2+y^2)}{w_0^2}))F(\exp(\frac{-jk}{2z}(x^2+\ldots$$

$$\ldots y^2)))]\exp(j2\pi v_x x)\exp(j2\pi v_y y)dv_x dv_y \qquad (4.17)$$

where $F(\ldots)$ represents the Fourier transform. Accordingly,

$$F(\exp(\frac{-(x^2+y^2)}{w_0^2}))F(\exp(\frac{-jk}{2z}(x^2+y^2))) = \frac{-j\lambda z w_0^2}{4\pi}\ldots$$

$$\ldots\exp((v_x^2 + v_y^2)(-w_0^2/4 + j\lambda z/4\pi)). \qquad (4.18)$$

In the end, the diffracted field becomes

$$\psi(r') = \frac{j}{\lambda z} e^{-jkz} \frac{-j\lambda z w_0^{\,2}}{2(\pi w_0^{\,2} - j\lambda z)} \exp\left(\frac{-(x^2+y^2)[j\lambda z\pi + w_0^{\,2}\pi^2]}{\pi^2 w_0^{\,4} + \lambda^2 z^2}\right). \quad (4.19)$$

Hence, the intensity of the diffracted beam is arranged as

$$I(r') = |\psi(r')|^2 = \frac{w_0^{\,2}}{w_0^{\,2} + \left(\frac{\lambda z}{\pi w_0}\right)^2} \exp\left(\frac{-2(x^2+y^2)}{w_0^{\,2} + \left(\frac{\lambda z}{\pi w_0}\right)^2}\right) \quad (4.20)$$

Thus, the phenomenon can be observed in Fig. 4.4 where the diffraction problem a Gaussian wave from an aperture is addressed. The Gaussian beam diverges as it propagates along *z*-axis, but it always preserves its shape as a Gaussian, which stems from the fact that the Fourier transform of a Gaussian is another Gaussian wave. The divergence angle, $\theta = \lambda / (\pi w_0)$ is defined.

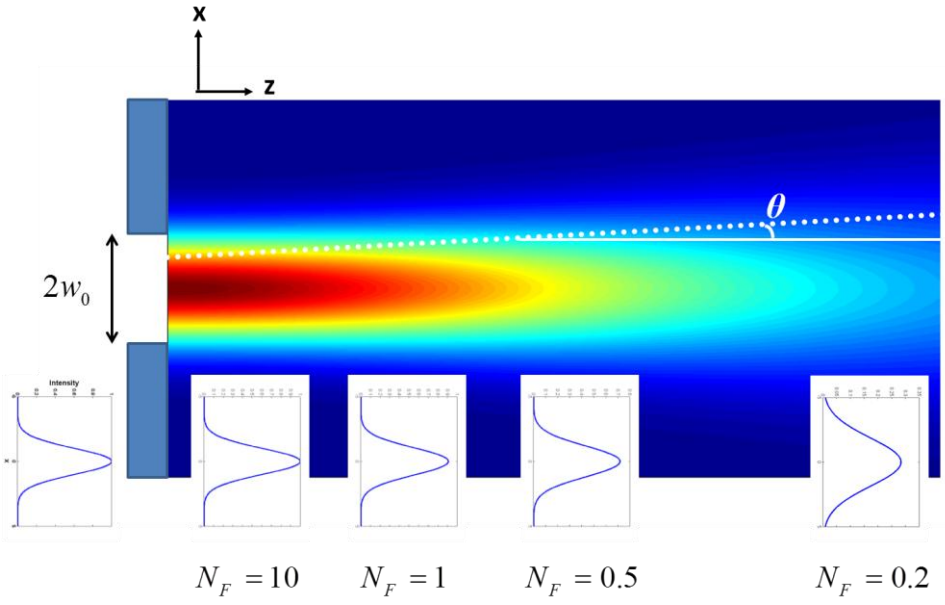

Figure 4.4: Diffraction of a Gaussian beam.

Figure 4.4 also presents a method of identifying the measurement distance as a parameter of the Fresnel Number, N_F. Fresnel number defines the starting point of the Fraunhofer zone and its boundary with the Fresnel zone. Then, $N_F \geq 1$ is the restriction to stay in the Fresnel region where $N_F = A/(\lambda z)$. Here, A is the aperture area ($A = w_0^{\,2}$). While $N_F < 1$ with

increasing distance from the aperture, we enter the Fraunhofer zone in which the phase fronts become planar.

4.1.3 Shortcomings of the scalar Kirchhoff diffraction

In the previous example of the Fresnel diffraction from a Gaussian wave, the aperture size was taken to be 2 times the operational wavelength. Kirchhoff scalar diffraction gives very good results as long as the aperture opening is large in comparison to the operational wavelength. However, Kirchhoff diffraction makes use of the following assumptions around the aperture for the general form in Eq. (4.6).

(i) $\psi(r)$ is zero at the right hand side of the aperture everywhere except for the area allocated by the aperture.

(ii) $\nabla\psi(r) = 0$ at the right hand side of the aperture.

Accordingly, the power is predicted to decay with $1/\lambda^2$ as it can be seen in Eq. (4.11). Nevertheless, as the aperture becomes more and more subwavelength in terms of its electrical size, the side lobes start to bend towards the screen and both (i) and (ii) start to lose their validity.

On the other hand, the problem had been addressed once again in the mid 40s by Bethe who treated the problem by setting out the boundary conditions and accounting for the field discontinuities in the form of magnetic current and charge densities. In the end, Bethe had formulized that for subwavelength apertures

$$P_{total} = \frac{64}{27\pi} k^4 a^6 S_i = \sigma_{eff} S_i \tag{4.21}$$

where P_{total}, S_i are the outgoing power from the subwavelength aperture and the power flux at the input, respectively for an aperture with an area of πa^2. The striking difference is that now the outgoing power scales with $1/\lambda^4$ in Eq. (4.21) and σ_{eff} defines the effective aperture cross section. His calculations always assumed that the metal of the screen had no skin depth such that the

fields would be unable to penetrate into the considered metal. While Kirchhoff's scalar diffraction theory was absorbing the total power that is sent onto the screens, the PEC walls with a tiny hole in the middle is considered by Bethe's procedure.

4.1.4 Can we still enhance the transmission?

The transmission problem presented by Bethe can be heuristically converted into an antenna problem with a scatterer, as indicated in Fig. 4.5.

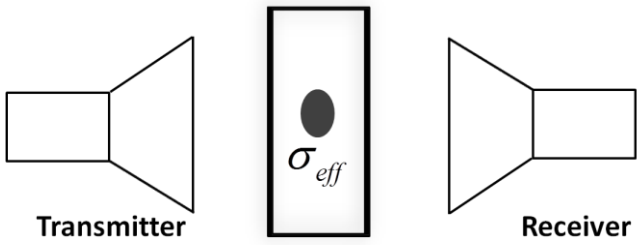

Figure 4.5: The problem of transmission through a subwavelength aperture. The aperture in infinitely extending PEC screen is placed in the middle of the transmitter and receiver antennas.

Then, for infinitely extending PEC walls we can ignore the secondary diffractions from the edges of the PEC at the time being. The antenna problem is now treated as

$$P_R = S_i \times \frac{\sigma_{eff}}{4\pi r_2^2} \times \frac{\lambda^2}{4\pi} \times G_R = \frac{P_T}{4\pi r_1^2} \times G_T \times \frac{\sigma_{eff}}{4\pi r_2^2} \times \frac{\lambda^2}{4\pi} \times G_R \qquad (4.22)$$

which is derived from FRIIS transmission equation for two antennas separated by a distance of r_1 and r_2 from the scatterer. P_T, P_R are the transmitted and received power quantities, respectively. The gain of the antennas are labeled as G_T, G_R. Of course, FRIIS transmission equation is valid for two antennas in their respective Fraunhofer zone. Conversely, all of the transmission enhancement phenomena that we will be discussing in the proceeding chapters are associated with near field zone. The evanescent mode below the cutoff frequency of the aperture, which is coupled to the subwavelength aperture will not be able to survive for long distance as we are going to witness. Nevertheless, Eq. (4.22)

still offers an intuitive description of the transmission problem. Eq. (4.22) gives away clues about how the enhanced transmission can be achieved. (*The intuitive explanations still should be considered with precaution*) The incoming electromagnetic fields either need

(i) a subwavelength field localizer that will couple the incident energy into the subwavelength aperture by modifying the gain of the antennas so that the antennas' directivity would enable a beaming beyond the diffraction limit. (Actually, such "antennas" are present in the literature in nanoscale. The researchers call them "nanoantennas", indistinctively, even though the entailed physics involve a subwavelength structure in most of the cases which can only localize the incoming field rather than a radiating.)

(ii) a better scatterer, which will modify the effective aperture size. A resonator is a good candidate as the mentioned scatterer, which will play the role of a transducer by converting the incoming electromagnetic wave into the induced surface currents and giving rise to highly elevated field values in the vicinity of the aperture.

Hence, we have worked with such configurations that will enable us to detect enhanced transmission values at the output side. The details will be covered in the upcoming chapters. At this stage, it is noteworthy to mention that the inclusion a subwavelength resonator can be intuitively interpreted as an increase in the effective aperture size or as a field localization problem in the vicinity of the aperture.

4.1.5 The induced dipole moments at the aperture

A small aperture can be represented by the electric and magnetic dipoles that are shown in Fig. 4.6. It can be intuitively deduced that an electric field along the normal of the interface causes fringing fields at the output side that resemble the field formation by an infinitesimal dipole, which is shown in Fig.

4.6(b). Likewise the fringing magnetic fields result in induced infinitesimal dipole moment that is parallel to the screen. Consequently, these dipole moments are

$$p = \varepsilon_0 \chi_{ee} \hat{n} E_n \delta(x - x_0)\delta(y - y_0)\delta(z - z_0) \tag{4.23}$$

$$m = -\mu_0 \chi_{mm} \overline{H_t} \delta(x - x_0)\delta(y - y_0)\delta(z - z_0)\,. \tag{4.24}$$

The values for the electric and magnetic polarizations can be found in several sources for different orientations of apertures. For the circular aperture with a radius of r, they are derived as $2r^3/3$ and $4r^3/3$, correspondingly for the electric and magnetic polarizations.

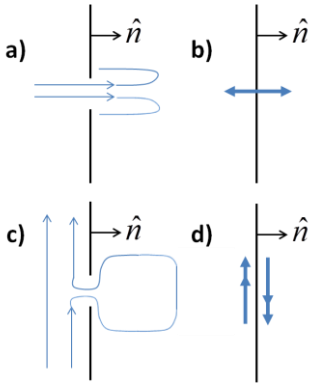

Figure 4.6: a) Incident electric field onto the aperture, b) its electric dipole representation, c) incident magnetic field onto the aperture and (d) its magnetic dipole representation.

These dipole moments play a crucial role in coupling theory in microwave engineering for apertures inside waveguides. They are allowed to radiate and they account for the scattering problem on both sides.

4.2 Aperture Arrays

4.2.1 TE_{10} mode of a regular rectangular waveguide

First we start by formulazing the modes of regular waveguides, which will be extremely helpful in understanding the enhanced transmission in periodic aperture arrays. If we go back to Maxwell's equations (source free) in Eq. (2.1) and (2.2), for the harmonic fields we can write

$$\nabla \times \overline{E} = -j\omega\mu\overline{H} \tag{4.25}$$

$$\nabla \times \overline{H} = j\omega\varepsilon\overline{E}\,. \tag{4.26}$$

Inside the waveguide along the *z*-axis, we have only a $e^{-jk_z z}$ *z* dependence, which turns Eq. (4.25) and (4.26) into

$$\frac{\partial E_z}{\partial y} + jk_z E_y = -j\omega\mu H_x \tag{4.27}$$

$$-\frac{\partial E_z}{\partial x} - jk_z E_x = -j\omega\mu H_y \tag{4.28}$$

$$\frac{\partial E_y}{\partial x} - \frac{\partial E_x}{\partial y} = -j\omega\mu H_z \tag{4.29}$$

$$\frac{\partial H_z}{\partial y} + jk_z H_y = j\omega\varepsilon E_x \tag{4.30}$$

$$-\frac{\partial H_z}{\partial x} - jk_z H_x = j\omega\varepsilon E_y \tag{4.31}$$

$$\frac{\partial H_y}{\partial x} - \frac{\partial H_x}{\partial y} = j\omega\varepsilon E_z \tag{4.32}$$

Then, the transverse elements (E_x and H_x together with E_y and H_y) can be expressed in terms of E_z and H_z. The important to remember is that the wave vector of the propagating beam inside the waveguide is $k^2 = k_z{}^2 + k_c{}^2$, where k_c is the cutoff wave number and $k = \omega\sqrt{\varepsilon\mu}$. After a few manipulations,

$$H_x = \frac{j}{k_c^2}(\omega\varepsilon \frac{\partial E_z}{\partial y} - k_z \frac{\partial H_z}{\partial x}) \tag{4.33}$$

$$H_y = \frac{-j}{k_c^2}(\omega\varepsilon \frac{\partial E_z}{\partial x} + k_z \frac{\partial H_z}{\partial y}) \tag{4.34}$$

$$E_x = \frac{-j}{k_c^2}(k_z \frac{\partial E_z}{\partial x} + \omega\mu \frac{\partial H_z}{\partial y}) \tag{4.35}$$

$$E_y = \frac{j}{k_c^2}(-k_z \frac{\partial E_z}{\partial y} + \omega\mu \frac{\partial H_z}{\partial x}). \tag{4.36}$$

For TM waves $E_z \neq 0$ and $H_z = 0$, likewise for TE waves $E_z = 0$ and $H_z \neq 0$ such that Eq. (4.33)-(4.36) can be further simplified. According to the wave equation the magnetic field should satisfy

$$(\frac{\partial^2}{\partial x^2} + \frac{\partial^2}{\partial y^2} + \frac{\partial^2}{\partial z^2} + k^2)H_z = 0. \tag{4.37}$$

But these modes have the form $H_z = h_z(x, y)\exp(-jk_z z)$, then the wave equation gets its reduced form

$$(\frac{\partial^2}{\partial x^2} + \frac{\partial^2}{\partial y^2} + k_c^2)h_z(x, y) = 0. \tag{4.38}$$

This partial differential equation can be solved for $h_z(x, y) = X(x)Y(y)$ with separated variables while $E_z = 0$,

$$Y\frac{d^2X}{dx^2} + X\frac{d^2Y}{dy^2} + XYk_c^2 = 0 \Rightarrow \frac{d^2X}{dx^2} + k_x^2 X = 0 \tag{4.39}$$

The same could be written for *Y*(*y*) as well. The general solution of the problem is

$$h_z(x, y) = (A\cos k_x x + B\sin k_x x)(C\cos k_y y + D\sin k_y y). \tag{4.40}$$

When we use Eq. (4.35) and (4.36)

$$e_x(x,y) = \frac{-j}{k_c^2}\omega\mu k_y (A\cos k_x x + B\sin k_x x)(-C\sin k_y y + D\cos k_y y) \quad (4.41)$$

$$e_y(x,y) = \frac{-j}{k_c^2}\omega\mu k_x (-A\sin k_x x + B\cos k_x x)(C\cos k_y y + D\sin k_y y) \quad (4.42)$$

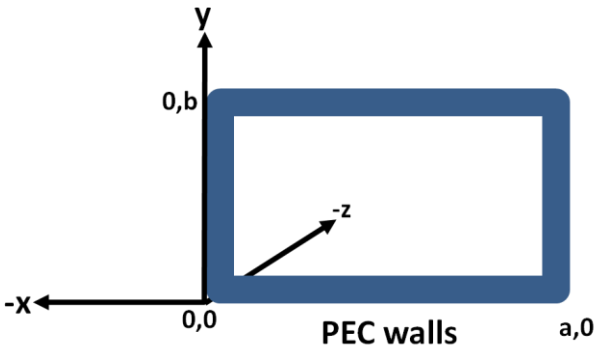

Figure 4.7: Regular rectangular waveguide with dimensions a and b.

The rectangular waveguide is shown in Fig. 4.7. Then, the boundary conditions should be satisfied so that the tangential components of the electric field should be zero.

$$e_x(0,b) = 0 \text{ and } e_x(0,0) = 0 \quad (4.43)$$

$$e_y(a,0) = 0 \text{ and } e_y(0,0) = 0 \quad (4.44)$$

Then, the solutions of Eq. (4.40)-(4.42) become

$$H_z(x,y,z) = A_{m,n}\cos(\frac{m\pi x}{a})\cos(\frac{n\pi y}{b})\exp(-jk_z z) \quad (4.45)$$

$$E_x(x,y,z) = \frac{j\omega\mu n\pi}{k_c^2 b}A_{m,n}\cos(\frac{m\pi x}{a})\sin(\frac{n\pi y}{b})\exp(-jk_z z) \quad (4.46)$$

$$E_y(x,y,z) = \frac{-j\omega\mu m\pi}{k_c^2 a}A_{m,n}\sin(\frac{m\pi x}{a})\cos(\frac{n\pi y}{b})\exp(-jk_z z) \quad (4.47)$$

where $k_x = m\pi/a$, $k_y = n\pi/b$ and m, n are positive integer numbers including zero.

Accordingly, $k_c = \sqrt{(m\pi/a)^2 + (n\pi/b)^2}$ and $k_z{}^2 = k^2 - (m\pi/a)^2 - (n\pi/b)^2$. For a rectangular waveguide with $a > b$, the first propagating mode should satisfy $0 = k^2 - (m\pi/a)^2$ at the cutoff frequency in order to start allowing propagation. This mode is the dominant mode, $m = 1,\ n = 0$ (TE_{10}), and has the lowest cutoff frequency. This mode gives

$$H_z(x,y,z) = A_{1,0}\cos(\frac{\pi x}{a})\exp(-jk_z z) \tag{4.48}$$

$$E_y(x,y,z) = \frac{-j\omega\mu a}{\pi} A_{1,0}\sin(\frac{\pi x}{a})\exp(-jk_z z) \tag{4.49}$$

$$H_x(x,y,z) = \frac{jk_z a}{\pi} A_{1,0}\sin(\frac{\pi x}{a})\exp(-jk_z z) \tag{4.50}$$

Other electric and magnetic field components are zero ($E_x = E_z = H_y = 0$). Then, the power flow down the waveguide for this mode is

$$P_{10} = \frac{1}{2}\mathrm{Re}[\int_0^a\int_0^b (\overline{E}\times\overline{H}^*)\cdot\hat{z}dydx] = \frac{1}{2}\mathrm{Re}[\int_0^a\int_0^b E_y H_x{}^* dydx]\ldots$$

$$\ldots = \frac{1}{2}\mathrm{Re}[\frac{\omega\mu a^2 b\,|A_{1,0}|^2}{\pi^2} k_z{}^* \int_0^a \sin^2(\frac{\pi x}{a})dx] = \frac{\omega\mu a^3\,|A_{1,0}|^2\, b\,\mathrm{Re}[k_z]}{4\pi^2}. \tag{4.51}$$

Alternatively, a similar treatment for the TM modes reveals that there are no TM_{10} or TM_{01} modes.

4.2.2 Plasmons with perfect conductors?

Perfect conductors at low frequencies do have a very small skin depth, which in turn implies that the incident electromagnetic waves cannot penetrate into the conductors. Thus, surface plasmons which can be induced at optical wavelengths and which can travel long distances while being attached to the dielectric-metal interface do not exist. Conversely, these surface plasmons were well established in the literature and their contribution to the transmission enhancement in the case of the subwavelength apertures was known. Yet, it was

extremely surprising to witness that a similar phenomenon appeared at microwave frequencies for the perfect metals, as well.

The following derivations are taken from the first explanations of the regarding phenomenon, which was proposed by Pendry.

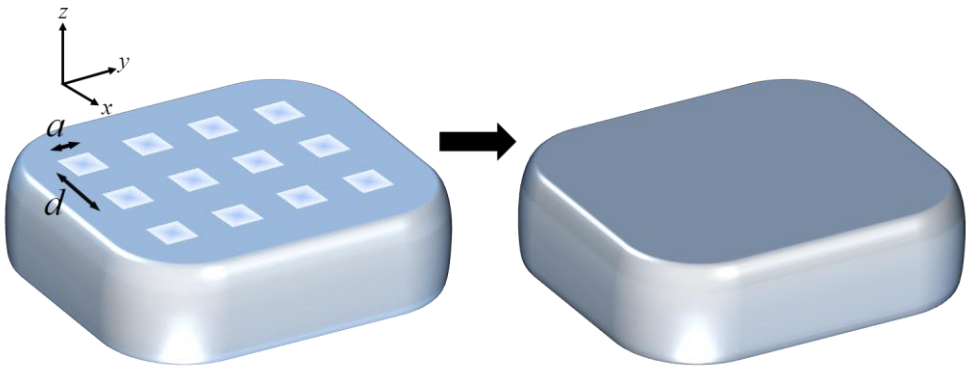

Figure 4.8: The perfect conductor with drilled holes and its homogenized version.

The transmission enhancement occurs when $a < d \ll \lambda$. Then, the cutoff frequency of the holes is well beyond the operational frequency. Let us assume that the fields are zero on the conductor, but are allowed to propagate even before the cutoff frequency. If we barrow the expressions for the propagating waves inside the small holes for TE_{10} mode,

$$k_z = j\sqrt{(\frac{\pi}{a})^2 - k^2} \tag{4.52}$$

where $k^2 = \omega^2 \varepsilon\mu$. The field is given in Eq. (4.49). On the other hand, the incoming electric field sees an anisotropic homogenous medium, as it is depicted in Fig. 4.8. The apertures that are smaller than the operational wavelength cannot be resolved. Thus, for the effective medium $\varepsilon'_x = \varepsilon'_y$, $\mu'_x = \mu'_y$ and the propagating field is expressed as

$$E'_y(x,y,z) = A'_{1,0} \exp(-jk'_x x)\exp(-jk'_z z) \tag{4.53}$$

where $k_z = k'_z$. The average fields at the surface should be the same in both cases in order to match the incident and reflected fields. Then, we equate the

average field at the surface per unit cell for the waveguide and the effective medium

$$(E_y)_{average} = \frac{1}{d^2} \times \frac{-j\omega\mu a}{\pi} A_{1,0} \int_0^a \int_0^a \sin(\frac{\pi x}{a}) dy dx = \frac{-j\omega\mu 2a^3}{d^2\pi^2} A_{1,0} = A'_{1,0} \quad (4.54)$$

Moreover, the power flow along the waveguide (per unit lattice) and the homogenous structure must be equal. Then, by making use of the results presented in Eq. (4.51),

$$\frac{P_{10}}{d^2} = \frac{\omega\mu a^4 \mid A_{1,0} \mid^2 \mathrm{Re}[k_z]}{4\pi^2 d^2} = \frac{1}{2}\mathrm{Re}[-E'_y H'^{*}_x] = \frac{\mathrm{Re}[k'_z] \mid A'_{1,0} \mid^2}{2\omega\mu'_x} \quad (4.55)$$

and after some manipulations,

$$\mu'_x = \mu'_y = \frac{8\mu a^2}{\pi^2 d^2}. \quad (4.56)$$

Furthermore,

$$k_z = k'_z = \omega\sqrt{\varepsilon'_y \mu'_x} = j\sqrt{(\frac{\pi}{a})^2 - \omega^2\varepsilon\mu} \Rightarrow \ldots$$

$$\ldots \varepsilon'_y = \frac{\pi^2 d^2}{8\mu a^2}(1 - (\frac{\pi}{a})^2 \frac{1}{\omega^2\varepsilon\mu}). \quad (4.57)$$

The results of Eq. (4.57) are essentially important in understanding the enhanced transmission in perfect conductors. The effective dielectric function of the corrugated perfect conductor (with drilled holes), however the apertures are small, have bound surface states very similar to the case with metals at optical wavelengths (please refer to Eq. (3.11)). Hence, the plasma frequency of Eq. (4.57) is

$$\omega_p = \frac{\pi}{a\sqrt{\varepsilon\mu}} \quad (4.58)$$

which is also the cutoff frequency of the waveguides. The effective response of the aperture arrays will have surface plasmon polariton (SPP) like behavior and yield enhanced transmission as do the SPPs in optical wavelengths.

4.2.3 Transmission enhancement as a periodic phenomenon

The explanations of the spoof plasmons rescued the theory of the enhanced transmission that was observed in aperture arrays. However, the problem in microwaves had already been addressed in the last century within the context of the diffraction from subwavelength apertures. The periodic arrangement in Fig. 4.9 can be perceived as a waveguide with PEC walls (top and bottom) and PMC walls (on both sides) by making use of the equivalence theory.

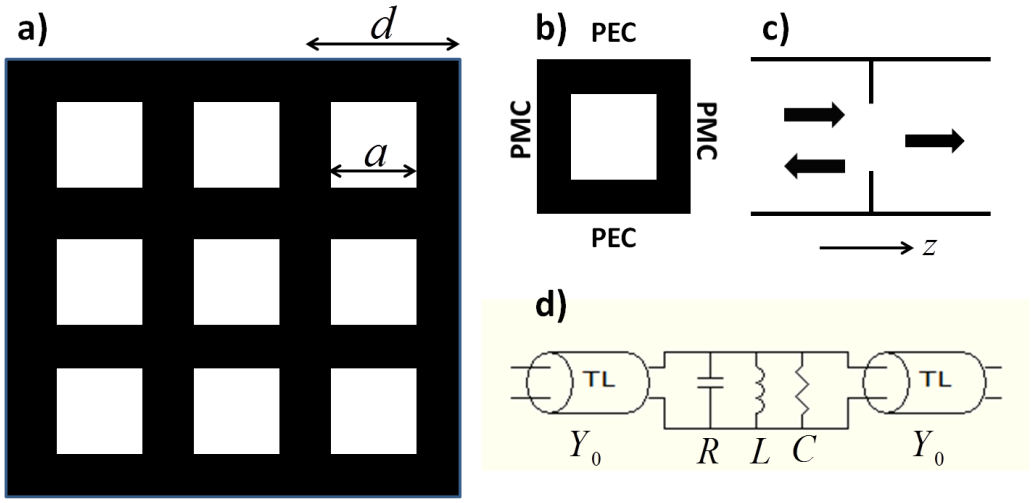

Figure 4.9: (a) The aperture array, (b) the equivalent problem with PEC and PMC walls, (c) lateral view of the scattering problem at the aperture array, (d) the equivalent circuit at the discontinuity for the infinitesimally thin screen.

Then, the modes of such an artificial waveguide will differ from those of the regular waveguide that we covered in the previous sections. If we consider TM modes of the form $E_z = e_z(x,y)\exp(-jk_z z)$, the reduced Helmholtz equation will be similar to Eq. (4.38)

$$(\frac{\partial^2}{\partial x^2} + \frac{\partial^2}{\partial y^2} + k_c{}^2)e_z(x,y) = 0 \tag{4.59}$$

where $e_z(x,y) = (A\cos k_x x + B\sin k_x x)(C\cos k_y y + D\sin k_y y)$. Then, from Eq. (4.33)-(4.36) we have

$$h_x(x,y) = \frac{j}{k_c^{\,2}}\omega\varepsilon k_y(A\cos k_x x + B\sin k_x x)(-C\sin k_y y + D\cos k_y y) \quad (4.60)$$

$$h_y(x,y) = \frac{-j}{k_c^{\,2}}\omega\varepsilon k_x(-A\sin k_x x + B\cos k_x x)(C\cos k_y y + D\sin k_y y) \quad (4.61)$$

$$e_x(x,y) = \frac{-j}{k_c^{\,2}}k_z k_x(-A\sin k_x x + B\cos k_x x)(C\cos k_y y + D\sin k_y y) \quad (4.62)$$

$$e_y(x,y) = \frac{-j}{k_c^{\,2}}k_z k_y(A\cos k_x x + B\sin k_x x)(-C\sin k_y y + D\cos k_y y) \quad (4.63)$$

This time the boundary conditions require that

$$e_x(0,b) = 0 \text{ and } e_x(0,0) = 0 \quad (4.64)$$

$$h_y(a,0) = 0 \text{ and } h_y(0,0) = 0 \quad (4.65)$$

Hence, it turns out that $B = C = 0$, $k_x = m\pi / d_x$ and $k_y = n\pi / d_y$. Then, the field components become

$$E_z(x,y) = A_{m,n}\cos(\frac{m\pi x}{d_x})\sin(\frac{n\pi y}{d_y})\exp(-j\omega k_z z) \quad (4.66)$$

$$E_x(x,y) = \frac{j}{k_c^{\,2}}k_z m\frac{\pi}{d_x}A_{m,n}\sin(\frac{m\pi x}{d_x})\sin(\frac{n\pi y}{d_y})\exp(-j\omega k_z z) \quad (4.67)$$

$$E_y(x,y) = \frac{-j}{k_c^{\,2}}k_z n\frac{\pi}{d_y}A_{m,n}\cos(\frac{m\pi x}{d_x})\cos(\frac{n\pi y}{d_y})\exp(-j\omega k_z z) \quad (4.68)$$

$$H_x(x,y) = \frac{j}{k_c^{\,2}}\omega\varepsilon n\frac{\pi}{d_y}A_{m,n}\cos(\frac{m\pi x}{d_x})\cos(\frac{n\pi y}{d_y})\exp(-j\omega k_z z) \quad (4.69)$$

$$H_y(x,y) = \frac{j}{k_c^{\,2}}\omega\varepsilon m\frac{\pi}{d_x}A_{m,n}\sin(\frac{m\pi x}{d_x})\sin(\frac{n\pi y}{d_y})\exp(-j\omega k_z z) \quad (4.70)$$

The same routine can be done for TE modes where $E_z = 0$,

$$H_z(x,y) = A_{m,n}\sin(\frac{m\pi x}{d_x})\cos(\frac{n\pi y}{d_y})\exp(-j\omega k_z z) \quad (4.71)$$

$$H_x(x,y) = \frac{-j}{k_c^{\,2}} k_z m \frac{\pi}{d_x} A_{m,n} \cos(\frac{m\pi x}{d_x}) \cos(\frac{n\pi y}{d_y}) \exp(-j\omega k_z z) \qquad (4.72)$$

$$H_y(x,y) = \frac{j}{k_c^{\,2}} k_z n \frac{\pi}{d_y} A_{m,n} \sin(\frac{m\pi x}{d_x}) \sin(\frac{n\pi y}{d_y}) \exp(-j\omega k_z z) \qquad (4.73)$$

$$E_x(x,y) = \frac{j}{k_c^{\,2}} \omega\mu n \frac{\pi}{d_y} A_{m,n} \sin(\frac{m\pi x}{d_x}) \sin(\frac{n\pi y}{d_y}) \exp(-j\omega k_z z) \qquad (4.74)$$

$$E_y(x,y) = \frac{j}{k_c^{\,2}} \omega\mu m \frac{\pi}{d_x} A_{m,n} \cos(\frac{m\pi x}{d_x}) \cos(\frac{n\pi y}{d_y}) \exp(-j\omega k_z z) \qquad (4.75)$$

Moreover, different from the regular rectangular waveguide, the symmetry of the current problem of the artificial waveguide does only support symmetric modes. Consequently, the first modes that need to be considered are TE_{20} and TM_{02}. These modes are going to be the main contributors of the transmission problem from this subwavelength aperture array.

The scattering problem of Fig. 4.9(c) can be written for E_y in the following way

$$E_y(x,y) = T + \sum_{m=1}^{M} A_{m0}^{TE} f_{m0}(x,y) + \sum_{n=1}^{N} A_{0n}^{TM} f_{0n}(x,y) \ldots$$

$$\ldots + \sum_{m,n=1}^{N,M} (A_{mn}^{TE} + A_{mn}^{TM}) f_{mn}(x,y) \qquad (4.76)$$

The first term is the transmission coefficient through the subwavelength aperture while rest of the terms comes from the modes of the artificial waveguide, which also contribute to the extraordinary transmission. It can be seen in Eq. (4.68) and (4.75) that $f_{mn}(x,y) = \cos(m\pi x / d_x)\cos(n\pi x / d_y)$. The fourth term represents the contributions from the higher order terms. For the subwavelength apertures before the cutoffwavelength, the main contribution comes from the second and third terms. The intuitive explanation is based on the inspection of the mode profiles which are depicted in Fig. 4.10.

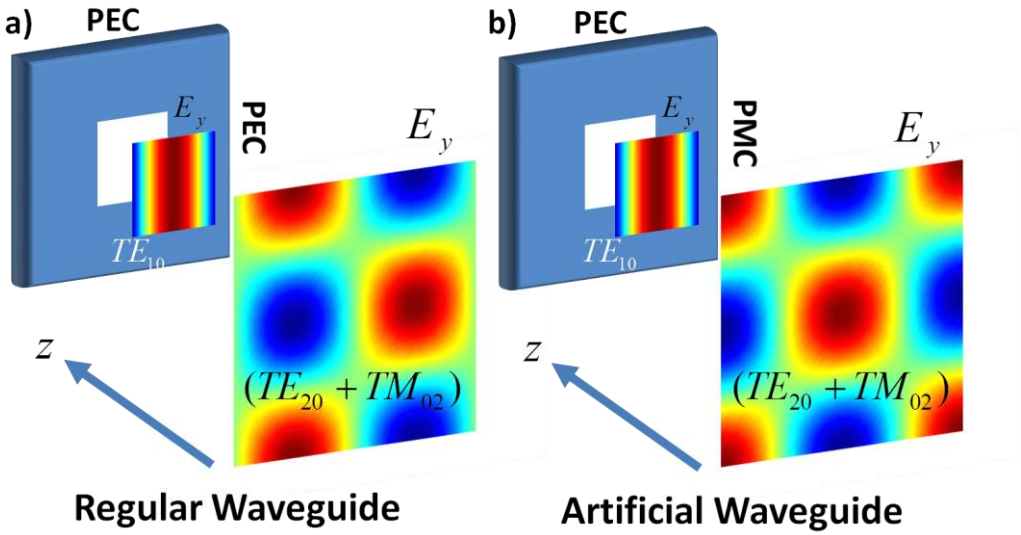

Figure 4.10: Electric field (E_y) for (a)the regular waveguide and (b) the artificial waveguide.

The dominant mode of the inner waveguide (the aperture) is TE_{10} mode. As it was calculated for this specific mode, the mode profile is given around the aperture (the small mode profile picture in Fig. 4.10). The cutoff for this mode is found as $\lambda_{c,a} = 2a$ (a is the size of the square aperture). On the other hand, the cutoff wavelength of the surrounding waveguide is $\lambda_{c,w} = d$ (d is the unit lattice size of the square array). In Fig. 4.10(a) the incident waveguide modes (only TE_{20}, there is no TM_{02} in the regular waveguide) does not interact with the TE_{10} mode of the inner waveguide. The center of the regarding mode is the zero field region. Conversely, the artificial waveguide's modes (TE_{20} and TM_{02}) have non-zero field magnitudes at the center and thereby contribute to the enhanced transmission.

The modal impedances of the regarding modes of the artificial waveguide are

$$Z_{TE} = \frac{E_x}{H_y} = \frac{\frac{j}{k_c^2}\omega\mu n\frac{\pi}{d}A_{m,n}\sin(\frac{m\pi x}{d})\sin(\frac{n\pi y}{d})\exp(-j\omega k_z z)}{\frac{j}{k_c^2}k_z n\frac{\pi}{d}A_{m,n}\sin(\frac{m\pi x}{d})\sin(\frac{n\pi y}{d})\exp(-j\omega k_z z)}\cdots$$

$$\ldots = \frac{\omega\mu}{k_z} = \frac{\omega Z_0\sqrt{\varepsilon\mu}}{\sqrt{k^2 - (\frac{2\pi}{d})^2}} = \frac{kZ_0}{k\sqrt{1-(\frac{\lambda}{d})^2}} = \frac{Z_0}{\sqrt{1-(\frac{\lambda}{\lambda_{c,w}})^2}} \tag{4.77}$$

$$Z_{TM} = \frac{E_x}{H_y} = \frac{k_z}{\omega\varepsilon} = \frac{Z_0\sqrt{k^2 - (\frac{2\pi}{d})^2}}{\omega\sqrt{\varepsilon\mu}} = Z_0\sqrt{1-(\frac{\lambda}{\lambda_{c,w}})^2}\,. \tag{4.78}$$

Equations (4.77) and (4.78) tell that the modes of an infinitely long waveguide have the impedances that are in the form of inductive and capacitive expressions for $\lambda > \lambda_{c,w} = d$ (below the cutoff frequency). Accordingly, the discontinuity presents an *LC* tank formation that is similar to the one shown in Fig. 4.9(d), while the TLs represent the regions filled with air. Precisely, TM_{02} is inductive as TE_{20} is capacitive for the forward propagating wave. However, the enhanced transmission stems from the backward propagating waves. Then, we have to return back to Eq. (4.33)-(4.36). For the backward propagating waves at frequencies that are lower than the cutoff frequency, TM_{02} is capacitive while TE_{20} is inductive with the following formulae

$$Z_{TE_{20}} = \frac{jZ_0}{\sqrt{(\frac{\lambda}{\lambda_{c,w}})^2 - 1}} \tag{4.79}$$

$$Z_{TM_{02}} = -jZ_0\sqrt{(\frac{\lambda}{\lambda_{c,w}})^2 - 1}\,. \tag{4.80}$$

Then the total admittance at the discontinuity is $Y_{total} = Y_{TE_{20}} + Y_{TM_{02}}$. Hence, at a certain frequency the susceptance becomes zero, for which the extraordinary transmission occurs. The extraordinary transmission is right before the Rayleigh Wood anamoly (f_{RW}). At this particular frequency, $f = f_{RW} = f_{c,w}$ the capacitive impedance in Eq. (4.80) is nulled such that the total impedance is shorted,thereby the transmission becomes zero. This frequency is also depicted in Fig. 4.11 in which the transmission values for

several cases are shown. The stacking periodicity between the layers is $a_z = 2$ mm. Then, at low frequencies the aperture array behaves like an inductive element and $Y_{TE_{20}}$ is dominant. As the frequency gets higher $Y_{TM_{02}}$ becomes more dominant.

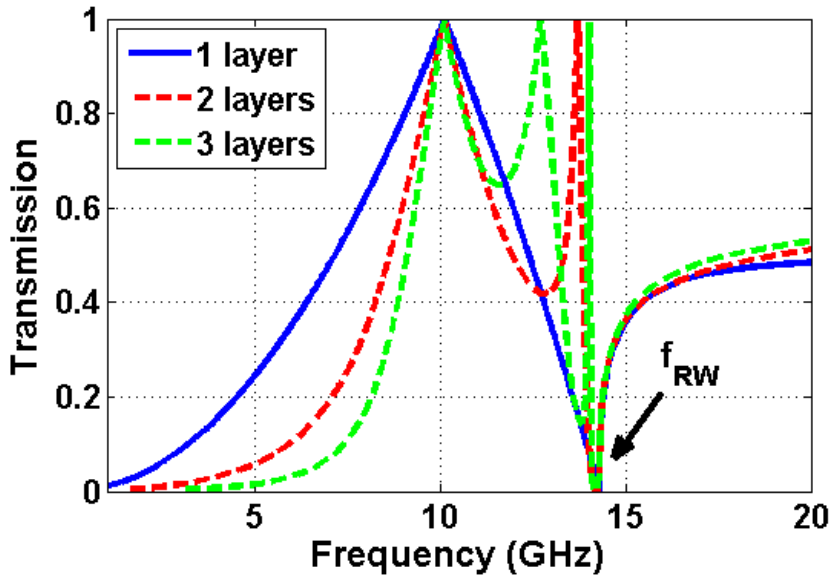

Figure 4.11: Transmission spectra for three cases (1 layer-blue line, 2 layers-dashed red line, 3 layers-dashed green line).

The transmission coefficient is calculated from $T = 1 - |\Gamma|$ in Fig. 4.11, where the seen input impedance in the case of the stacked layers are found by using Eq. (2.36).

Of course, these are over-simplified expressions for infinitesimally thin screens. The analyses here present the basics of the enhanced transmission in aperture arrays. The detailed derivations for the thicker realistic screens are available in the literature.

Chapter 5

Transmission Enhancement Through Subwavelength Apertures

5.1 Transmission enhancement with a split-ring resonator

Reprinted with permission from "*Enhanced transmission through a subwavelength aperture using metamaterials"* Atilla Ozgur Cakmak, Koray Aydin, Evrim Colak, Zhaofeng Li, F. Bilotti, L. Vegni and Ekmel Ozbay, Applied Physics Letters, volume 95, number 5, 052103 (2009). Copyright 2009, American Institute of Physics.

The interest in transmission through subwavelength apertures has recently rapidly increased [31,32]. The topic was addressed during the 1940s, where Bethe put forward his theoretical analysis suggesting relatively poor transmission figures at the output side of a subwavelength aperture [33]. The problem remained a major challenge until the pioneering work of Ebbesen *et al.* [34]. From that moment on, the main focus has been shifted to elucidate the enhancement mechanism for subwavelength apertures [35]. Researchers have set out to identify the role of the surface plasmons and to offer physical explanations for the transmission enhancement phenomenon [36,37]. Methods have been sought to effectively guide the incoming electromagnetic (EM) wave into the subwavelength aperture that will in return result in enhanced transmission. A slightly different approach was adapted in a paper by Alu *et al*., in which a matematerial cover over the aperture was theoretically shown to produce enhanced, directional transmission by minimizing the diffraction losses [38]. On the other hand, split ring resonators (SRRs) had already gained a well-established background in the metamaterial community [39]. Innovative models

were developed for SRRs that were placed inside a small circular metallic aperture [40]. Subsequently, Aydin *et al.* proposed in a rather recent work an alternative method for transmission enhancement by putting a SRR in front of a subwavelength aperture [41].

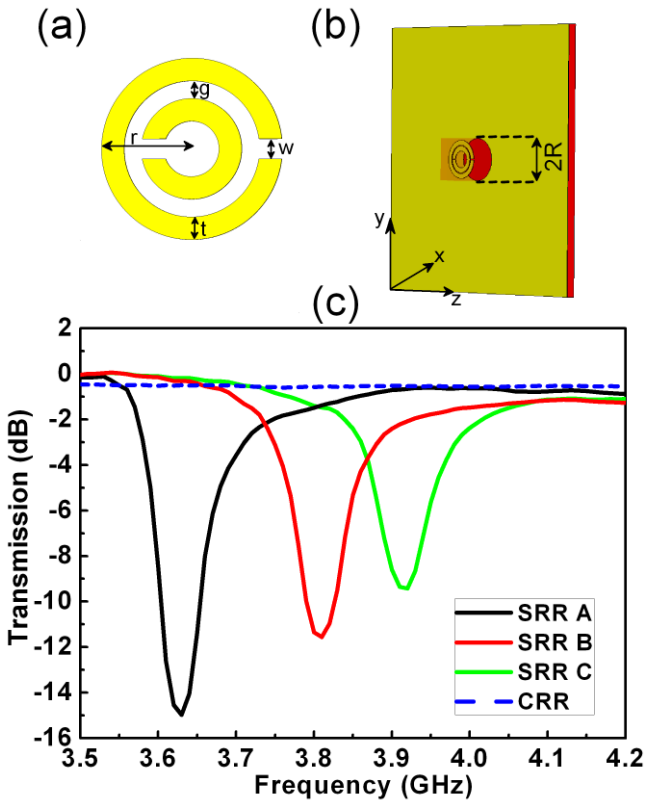

Figure 5.1: (a) The SRR configuration and the labeled SRR design dimensions: split width (*w*), the distance between the inner and outer rings (*g*=0.2 mm), the metal width (*t*=0.9 mm) and the outer radius (*r*=3.6 mm). (b) The experimental setup: SRR is attached to the aperture with a diameter of *2R*. SRR is shifted by an amount of *R* (in the –*z* direction) with respect to the aperture. (c) Measured transmission results for Sample SRR A (solid black line), B (solid red line), C (solid green line), and the CRR (dashed blue line).

We present here a more detailed analysis of the enhanced transmission process by focusing on a magnetically coupled SRR that was made to cooperate with a subwavelength aperture. The resonator nature of the SRR was exploited to concentrate the fields in the vicinity of a subwavelength aperture to facilitate considerable improvement in the transmission factors at microwave frequencies. Besides, the dependence of the resonance frequency of the SRRs on the enhanced transmission was studied by employing three different SRRs in the

simulations and experiments. Induced surface currents were calculated in order to discuss the enhancement mechanism. The transmission improvement figures were obtained as a function of various aperture radii.

Three distinct SRR designs with the labeled dimensions, which are shown in Fig. 5.1(a), were used. SRRs are deposited on a dielectric printed circuit board (PCB) with a thickness of 1.6 mm and a dielectric constant of ε=3.85. The deposited copper thickness is 30 μm. Samples A, B, and C have split widths of w_A=0.2 mm, w_B=0.4 mm, and w_C=0.6 mm. A closed ring resonator (CRR) was obtained by shortening the split of sample A. Each one of the CRR and SRRs possesses a supporting PCB of 8x8 mm^2. An aperture with a radius of R=4 mm was prepared by etching the copper on a single side copper coated separate PCB (Fig. 5.1(b)). The metal side of the resonators was affixed to the metal side of the PCB. There was a separation distance of approximately 0.1 mm between the two metal faces. Conventional waveguide antennas were connected to the Agilent N5230A network analyzer to collect the transmission results. The transmission characteristics of the SRR samples are depicted in Fig. 5.1(c). The incident beam had an electric field component along the y-axis (see Fig. 5.1(b) for directions). The magnetic resonance of the single SRRs was observed when the SRR plane was perpendicular to the propagation of the incident beam. The magnetic resonance frequencies of samples A, B, and C were found at 3.63 GHz, 3.81 GHz, and 3.92 GHz, respectively.

Then, the transmission spectrum was acquired for the aperture (black line in Fig. 5.2(a)). Since the aperture is too small in comparison to the wavelength of operation, we witnessed low transmission figures [33]. However, a peak in the transmission spectrum around 3.7 GHz was spotted once sample A was placed in the near field of the aperture (solid green line in Fig. 5.2(a)). The experiment was repeated by replacing sample A with the CRR. CST Microwave Studio was used in order to realize the same configurations in the simulation environment. The results are illustrated in Fig. 5.2(b), which show the good agreement between the simulation and experimental outcomes. Figure 5.2 points

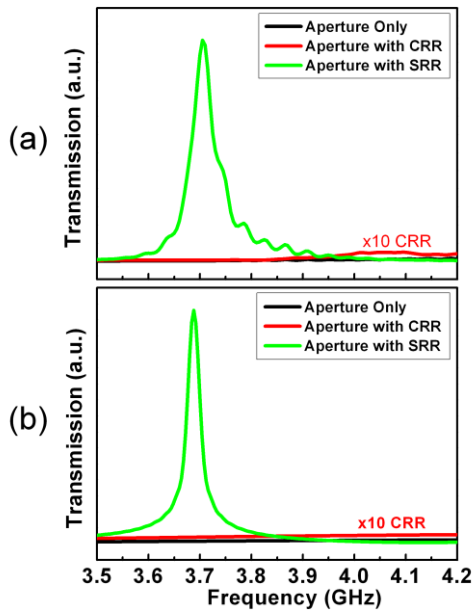

Figure 5.2: (a) Experimental and (b) simulation results of the transmission spectra. Aperture Only (solid black line), Aperture with CRR (solid red line), and Aperture with Sample SRR A (solid green line).

out that the increase in the transmission figures was caused by effectively coupling the electric field component of the incoming field to the SRR structure. Sample A, which already had a magnetic resonance around 3.63 GHz, triggered an enhanced transmission at 3.7 GHz. The absence of a magnetic resonance for the CRR configuration prevented an extraordinary transmission within the same frequency band. Figure 5.3 exhibits the experimental and simulation based enhancement factors in linear scale when the same procedures were followed for samples B and C. The transmission peaks occurred at 3.7 GHz (sample A), 3.89 GHz (sample B), and 4.01 GHz (sample C), which coincide well with the magnetic resonances of the SRRs. Moreover, the measurements with the SRR attached aperture yielded remarkable transmission improvement factors as high as 530, 288, and 232 for samples A, B, and C, respectively. Originally, the losses were not added to the calculations. The losses dropped the numerically computed enhancement factor to 540 from 856 for sample A (see Fig. 5.3(b)) while broadening the enhancement peak when the metals are modeled with copper and the dielectrics with a loss tangent of δ=0.01. The precise location of the SRR with respect to the aperture severely influences the transmission

enhancement frequency. The enhancement turned out to be located at 3.59 GHz and 3.75 GHz when sample A is misaligned by 0.3 mm and -0.1 mm respectively from the origin of the aperture along the z axis (solid gray and light gray lines in Fig. 5.3(b)).

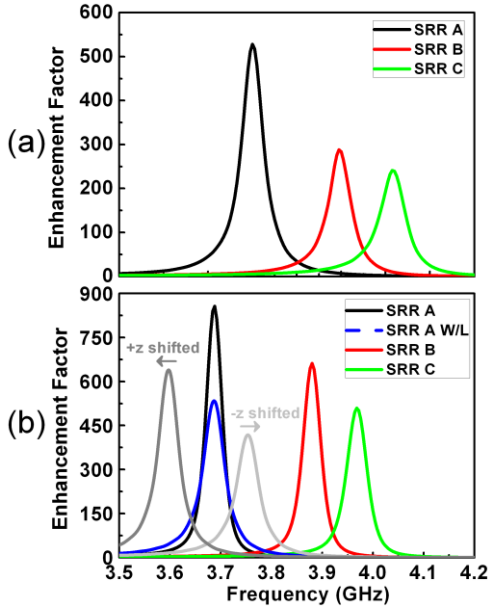

Figure 5. 3: (a) Experimental and (b) numerical analysis of the enhancement figures for three different samples. Sample SRR A (solid black line), B (solid red line), and C (solid green line). Sample SRR A with the losses (solid blue line). Sample SRR A is shifted -0.1 mm (solid light gray line) and 0.4 mm (solid gray line) in the z direction with respect to origin of the aperture. The losses are also taken into account during the shifting procedure.

The effect of the aperture radius on the enhancement factors was considered in Fig. 5.4. As the aperture radius ranged from 2.4 mm to 7 mm, the simulation results showed that the transmission enhancement frequencies were also altered although the same SRR (sample A) was employed throughout the entire analyses (see Fig. 5.4 inset). The electromagnetic response of the combined system, the aperture together with the SRR, had to be taken into account. The Subwavelength Transmission Enhancement (S. T. E.) Factor is defined as the multiplication of the transmission enhancement factors with the (R/λ) values for different aperture radii (λ is the operational wavelength). The S. T. E. Factor helps us to make a fair comparison to determine the optimal aperture geometry for the current investigation. Figure 5.4 reveals that the

optimum aperture radius for this scheme is approximately 4.8 mm, which corresponds to $(1/18)^{th}$ of the operational wavelength.

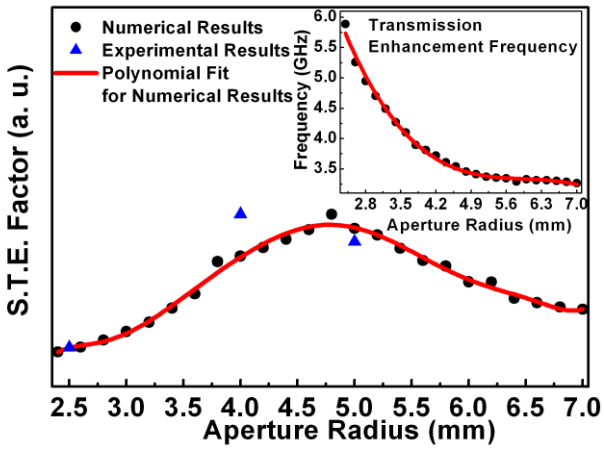

Figure 5.4: Subwavelength Transmission Enhancement (S. T. E.) Factor for various aperture radii, in the range 2.4 mm – 7 mm. Numerical Results (black dots), experimental results (blue triangles), and a polynomial fit curve for the numerical results (solid red curve) Inset: Calculated transmission enhancement frequencies corresponding to different aperture sizes.

Inspection of the induced surface currents provides physical insight. Figure 5.5 shows the induced surface currents. The magnified images are especially taken around the aperture. According to Figure 5.5(a), the surface currents on the metal block primarily remained parallel to the metal surface and attained the highest values at the discontinuities in the absence of the SRR. The weak contribution to the radiation came from the diffractions at the edges. The presence of the CRR did not cause any dramatic changes in Fig. 5.5(b). On the contrary, the surface currents turned out to be quantitatively amplified and focused around the aperture as soon as the CRR was substituted with the SRR at the enhancement frequency (see the color bars in Fig. 5.5). SRR, near the slit on the metal surface, concentrated the induced currents owing to its resonance behavior, acted like an antenna and prepared the ground for a transmission enhancement through the opening. The metal block created image currents that nullified the induced surface currents on the SRR. Then, we can identify an effective antenna area that essentially involves the uncompensated induced surface currents on the SRR within the region overlapped by the aperture. The

effective antenna area determines the enhancement frequency and the enhancement factors. This is the main reason why the sample SRR resonance frequencies did not perfectly coincide with the respective enhancement frequencies. We can further manipulate the effective antenna area by modifying the aperture radius. Smaller aperture radius values bring the enhancement to higher frequencies (see Fig. 5.4 inset). Misalignments generate a similar outcome. The effective area is reduced by allowing the metal plate to cover a smaller portion of the SRR that in turn lessens the enhancement factors and increases the enhancement frequencies (see Fig. 5.3(b)).

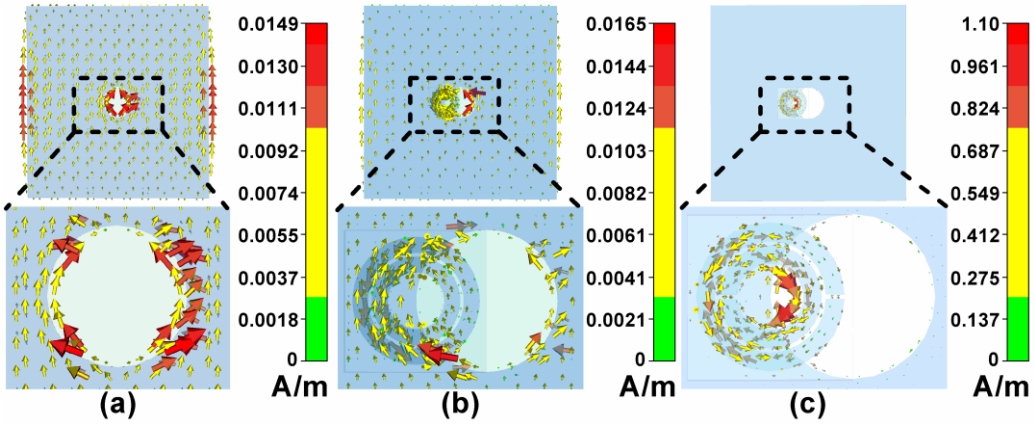

Figure 5.5: (a) The induced surface currents on the aperture, (b) aperture with CRR, and (c) aperture with Sample SRR A. The region around the aperture is magnified for each case for clarification.

In conclusion, we studied the extraordinary transmission by utilizing a magnetically coupled SRR in the near field of a subwavelength aperture. The measurements and simulations demonstrated that a transmission enhancement figure of 530 could be achieved. This is a noteworthy accomplishment for an aperture with a radius of $(1/20)^{th}$ of the wavelength of operation when compared with previous experiments [34]. Furthermore, we verified that the observed transmission enhancement effect is indeed due to the resonance behavior of the subwavelength resonant element by carrying out systematic experiments and numerical calculations.

5.2 Transmission enhancement with connected split-ring resonators

This paper was published in Optics Express and is made available as an electronic reprint with the permission of OSA. The paper can be found at the following URL on the OSA website: http://dx.doi.org/10.1364/OE.18.003952. Systematic or multiple reproduction or distribution to multiple locations via electronic or other means is prohibited and is subject to penalties under law.

Only a small portion of an incident beam is allowed to pass through a tiny hole in an opaque screen. This phenomenon was electromagnetically explained in the last century by Bethe [33]. He showed that the transmission efficiency of such a hole would be proportional to $(r/\lambda)^4$. Here, r represented the radius of the hole and λ corresponded to the operational wavelength of the electromagnetic signal. His theories were based on an idealized two dimensional diffraction model of an infinitesimally thin screen. In accordance with Bethe's predictions, electromagnetic wave transmission through subwavelength holes remained a challenging topic until the first proposals of Ebbesen *et al*. [34]. Extraordinary transmission phenomenon through an array of subwavelength holes milled in an opaque metal screen was first demonstrated with the aid of the surface plasmons. Several orders of magnitude more transmission than Bethe's calculations was observed owing to the resonant interactions of the incident photons with the surface plasmon polaritons of the metal surface. This study has gained an increasing attention and has encouraged the researchers to seek brand new transmission enhancement results through subwavelength apertures. Extraordinary transmission phenomenon through subwavelength hole arrays have been theoretically examined [35,37,42-46] and experimentally investigated [32,36,47-51]. It has been realized that the dimensions and periodicity of the holes in an array have a huge influence on the transmission spectrum. Surface plasmons compensate for the poor transmission figures through each hole. Every hole acts like a point source and the phenomenon can

be described as a reconstruction of the incident beam at the exit side by means of a classical interference mechanism. On the other hand, a single aperture could be thought of as the simplest optical component. Therefore, the single aperture case was also considered in a similar treatment. Wave propagation through these single slits was analyzed [52-55]. Corrugations were added around the aperture in order to provide the necessary momentum and energy matching conditions. As a result, the transmission efficiency of the single aperture was significantly increased [56,57]. The incoming wave was coupled to these periodic grooves that were located around the aperture and a narrow beam at the output side could be generated [58-62]. Moreover, such a simple device illustrates broad technological implications. The ability to concentrate the photons at a tiny aperture opens up technological possibilities and application fields. These application fields demand optical signals beyond the diffraction limit. Super-resolution is intended to be achieved by the use of subwavelength holes [63]. The aperture configurations were adapted to extract more light out of the system [64,65]. Surface plasmon assisted lithography techniques that exploit the transmission enhancement methods were employed to attain smaller feature sizes [66,67]. Further application fields include biophysics, chemical sensing, and molecular fluorescence [68-70]. Subwavelength apertures have been utilized in many ways and have proven to be promising candidates for scientific innovations.

Surface plasmons are not thought to exist in the microwave region. Nevertheless, subwavelength holes create spoof plasmons at microwave frequencies, and these spoof plasmons play the same role as their counterparts do in the optical domain [71,72]. Plasmon-like waves govern the main physics, even though the metals are perfect conductors at these wavelengths. Additionally, metamaterials with their subwavelength features already have a well-established background in the microwave regime [39]. Hence, Alu *et al*. suggested covering the aperture with a metamaterial slab that would lead to improved transmission figures by minimizing the diffraction losses [38]. Independently, Marques *et al*. developed theories that discussed the analytical

models of split ring resonators (SRRs) that were incorporated with an aperture [40]. Recently, Aydin *et al*. experimentally showed a 740-fold transmission enhancement by guiding the incoming wave into the subwavelength aperture with the help of the metamaterials [41]. A SRR was used in order to effectively couple the electromagnetic waves to the output side. Aydin *et al*. worked with an aperture whose radius was 20 times smaller than the operational wavelength. Subsequently, Cakmak *et al*. discussed the physical origins of such an enhancement by considering a SRR that was excited by the electric field component of the incident beam at the SRR's resonance frequency [73]. Various other types of metamaterials were also combined with subwavelength apertures in later studies that yielded extraordinary transmission [74,75]. However, in the present study we present an approach that offers astonishingly higher transmission results while working with a super tiny aperture. We report these drastically improved transmission figures through a deep subwavelength aperture with an electrical effective area that is significantly smaller than the operational wavelength. Instead of employing electrically large covers or corrugations around the aperture [56-70,38] to facilitate the input signal coupling, our approach makes use of the magnetic resonance of the connected SRRs (CSRRs) that are integrated with an electrically miniaturized hole at microwave frequencies. In the following sections of the present study, we aim to address both the theoretical and experimental analysis of the transmission enhancement mechanism that is maintained by the aid of two types of CSRR configurations. We conclude by discussing the novelties that the CSRRs exhibit compared to the earlier studies that were also realized with the adjustment of single negative metamaterials around the subwavelength apertures.

The respective design parameters of the CSRRs (Sample A&B) are depicted in Fig. 5.6(a). We have demonstrated the extraordinary transmission by using these samples. These distinct SRR samples are deposited on a dielectric printed circuit board (PCB). The PCBs are used in the experiments as a substrate layer with a thickness of 1.6mm. The deposited copper thickness is 30μm. The split width, *g*, is the same for the inner and outer rings in all configurations and

is equal to 0.5mm. The same is true for the copper width, *w*, and its value is again 0.5mm for each case. The separation distance between the SRRs, *l*, is identical for both samples and is 5.5mm.

We simulated the transmission characteristics of these configurations in order to determine the magnetic resonance frequencies. These simulations were carried out in CST Microwave Studio. The same structures were realized in the simulation environment and the transmission results were collected as it is illustrated in Fig. 5.6(b). Periodic boundary conditions were adopted in the simulations. The structures were illuminated with an incident wave whose magnetic field component was perpendicular to the SRR plane, while the electric field component was along the SRRs' splits.

The respective magnetic resonance frequencies of the configurations are shown in Table 5.1. The resonance frequencies shift to relatively higher values for the combined systems. SRRs can be modeled with inductors and capacitors [40]. The two resonators having the same characteristics are merged. In the end, the resonance frequency is slightly altered due to the non-ideal contributions coming from the uncompensated inductors and capacitors of the overall system. Moreover, the resonance strength of the combined system is considerably reduced. It is reasonable to expect a drop in the resonance strength of the CSRRs since the split gaps are shorted as we join two SRRs together. We force the SRRs to work in phase with each other. The CSRRs may not be an intelligent choice as single negative metamaterials at these frequencies, but they are going to serve as a key element for our purposes during the transmission enhancement phenomenon. The details are discussed in the subsequent sections.

Table 5.1. List of the magnetic resonance frequencies

Configuration	f_{res}
Sample A	3.61 GHz
SRRA	3.53 GHz
Sample B	4.34 GHz
SRRB	4.26 GHz

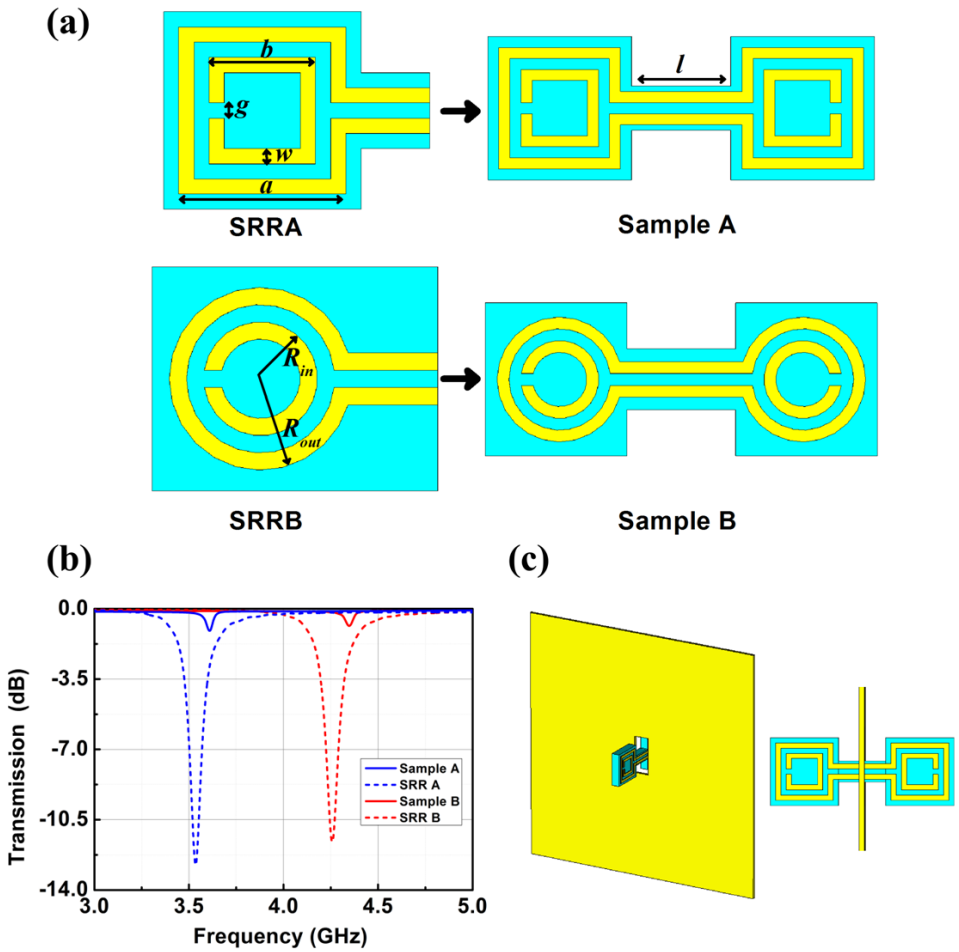

Figure 5.6: (a) CSRR configurations and the labeled dimensions (a=5.5mm, b=3.5mm, g=w=0.5mm, l=5.5mm, R_{in}=1.75mm, R_{out}=3mm), (b) Simulated transmission spectra for Sample A (solid blue line), SRR A (dashed blue line), Sample B (solid red line), SRR B (dashed red line), and (c) Sample A incorporated with the deep subwavelength aperture. The front and side views are given together.

Fig. 5.6(c) illustrates how we incorporate the samples with the aperture. We drilled an opening on a large metal plate of 1m×1m. The dimensions of the metal plate were intentionally picked to be large in order to minimize the diffraction effects at the edges. The thickness of the metal plate is 0.5mm. The opening on our metal screen constituted the subwavelength aperture. The area of the subwavelength aperture is $3\times7.5\text{mm}^2$ (width × height). The CSRRs are inserted inside the aperture. We tried to manually align the samples to the midpoint of the aperture while leaving equal portions on both half planes. Transmission measurements were performed with conventional horn antennas

operating around the frequency band of our interest. The antennas were located 8cm away from each other and the metal plate was positioned in between these antennas. The antennas were connected to the HP8510C Network Analyzer. The polarizations of the antennas were properly chosen to excite the magnetic resonance of the CSRR structure.

The transmission characteristics of the electrically large copper plate with the specified aperture were investigated. The numerical analyses are performed by modeling the horn antennas in CST Microwave Studio. The plate is inserted in between the antennas. The antennas are numerically characterized with their S parameters and radiation patterns. The modeled antennas have been validated to work in our frequency range with proper gain values and low losses. Then, the frequency response of the transmission through the aperture is collected both experimentally and numerically. S_{21}, which is defined as the ratio between the transmitted and the incident microwave signals in electrical engineering, is used as a measure of transmission in our examinations. Open boundary conditions were employed throughout the simulations in all directions. We tried to model the experimental setup in the simulation domain by staying loyal to the dimensions as much as possible. The simulated horn antennas were excited with waveguide ports. A dielectric constant ε=4 with a loss tangent of δ=0.014 was chosen to represent the dielectric media in our experiments. The copper had an electrical conductance of $\sigma_{cu}=5.8\times10^7$ S/m.

The simulation results are plotted in Fig. 5.7 (solid blue line). The transmission results are smaller than the actual signal to noise ratio of our Network Analyzer at certain frequencies. Such values would not be detectable in the experiments. Besides, simulations always offer better isolation and poor transmission figures. The diffractions at the edges of the metal plate are avoided in the simulations by placing perfect absorbers at the boundaries. Then, the transmission tends to increase as the frequency values get higher. However, the experiment results are not straightforward to process (solid black line). Sudden peaks and drops are caused by the higher order diffractions and reflections. The

large plate is a perfect conductor at these frequencies and it deteriorates the measurement results by giving rise to the undesired scattered fields. It is rather difficult to simultaneously cancel those influences experimentally. Nonetheless, the transmission results of the aperture are going to be our references while acquiring the transmission enhancement results. We might end up with spurious enhancement results (likely to be caused by the valleys) if we are not extra careful. In order to circumvent that possibility, we smoothed the measurement results to a reasonable level. The smoothed plot is also presented in Fig. 5.7 (dashed red line).

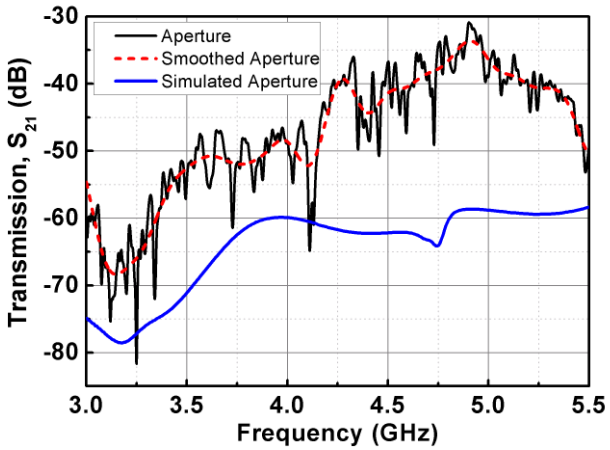

Figure 5.7: Measured transmission results (solid black line), smoothed measurement results (dashed red line), simulated transmission results (solid blue line).

We suspect that the transmission contributions of the diffraction mechanisms play an important role especially after 4 GHz. Diffractions are attributed to be the main difference in the absolute transmission values between the simulations and experiments. However, a further theoretical analysis is needed to clearly demonstrate their significance. The diffractions at the edges of the metal plate are taken into account while calculating the transmission coefficients in Fig. 5.8(a). The diffractions gave rise to almost 25 dB transmission improvement at higher frequencies and sudden drops start to appear in the transmission spectrum. Fig. 5.8(b) illustrates the diffraction effects at the edges at 4.5 GHz. The transmitter antenna is placed 0.5mm away from the

metal plate on the left hand side. The receiver antenna is aligned with the aperture and the transmitter antenna. It lies on the right hand side of Fig. 5.8(b). In this case, the diffracted fields act like a point source and an interference pattern is formed for different frequencies. This interference pattern explains the sudden peaks and drops in Fig. 5.7. The transmission through the subwavelength aperture is relatively weak in comparison to these diffraction effects. Still, in spite of the contributions coming from the diffractions, transmission results are lower than the experimental values. It is noteworthy fact that the fields can reach the edges even though the transmitter antenna is placed only 0.5mm apart from the subwavelength aperture. This can be best understood when we examine the mode profile at the exit of the waveguide portion of the horn antenna (see Fig. 5.8(c)). The fields rapidly extend in $\pm y$ directions. Then the separation distance between the transmitter antenna and the metal plate becomes the key parameter. The fields are plotted once again when we position the transmitter antenna 5mm away from the aperture (see Fig. 5.8(d)). The fields are depicted on the same scale. The diffraction clearly manifests itself and stronger interference patterns are observed at the receiver side. Subsequently, the discrepancies between the numerically attainable and experimentally collected single aperture transmission results are clarified. The transmission results for the single aperture turn out to be very sensitive to the variations in the separation distance between the plate and the transmitting horn antenna. We attempted to keep that distance as small as possible. However, it produces significant difficulties due to the mechanical limitations (e.g. the finite radius of curvature of the large and thin metal plate and the difficulty of the perfect manual alignment of the horn antenna with respect to the aperture).

The measured transmitted intensity results are portrayed in Fig. 5.9(a) and Fig. 5.9(d) in linear scale. The peaks are the evidence of the transmission enhancement in the presence of the samples. Single aperture transmission results were multiplied with 10 to be able to visualize both results on the same graph. Likewise, Fig. 5.9(b) and Fig. 5.9(e) depict the simulation results. The

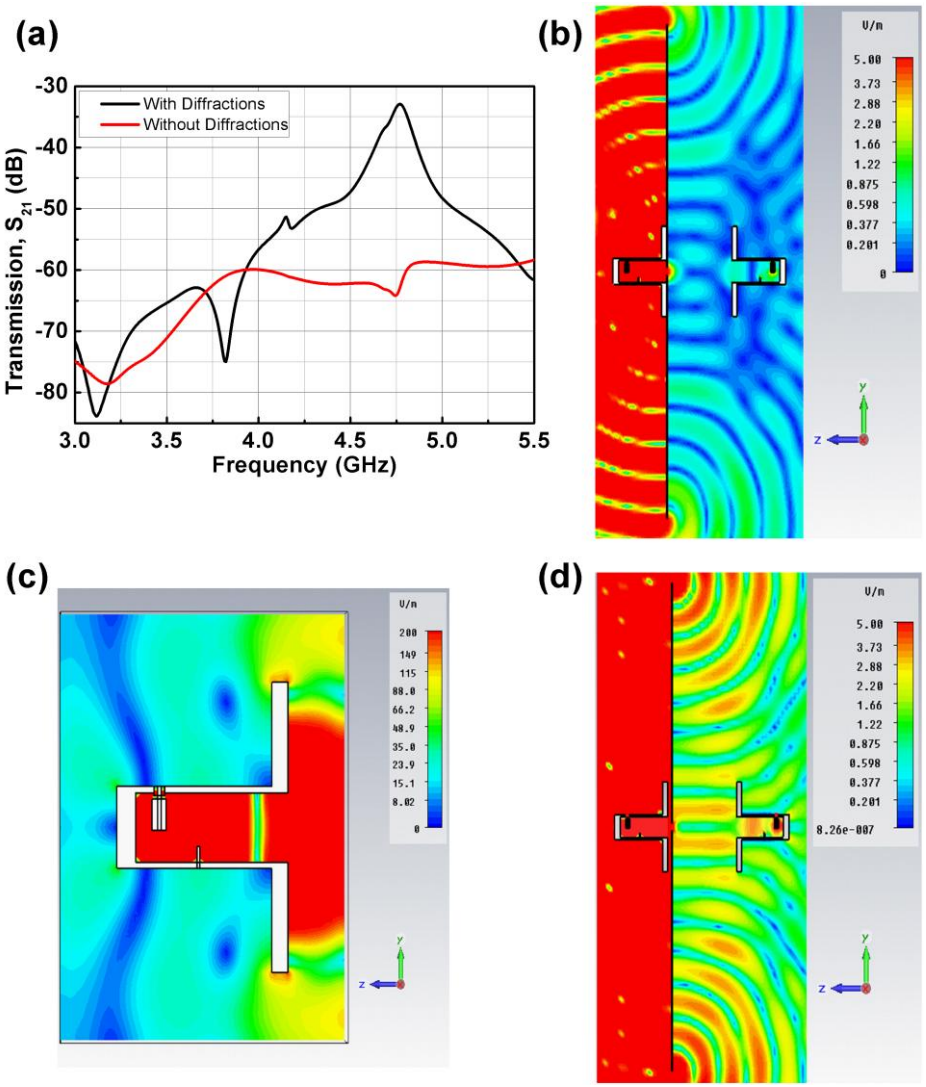

Figure 5.8: (a) Simulated transmission results in the presence of diffractions (solid black line), and without diffractions (solid red line) when the transmitter antenna is 0.5mm away from the plate. (b) Simulated field maps on *y*-*z* plane when the transmitter antenna is 0.5mm away from the metal screen within a frequency range of 3.3-5 GHz. (c) Simulated field maps on *y*-*z* plane for the modeled antennas within a frequency range of 3.5-5 GHz. (d) Simulated field maps on *y*-*z* plane when the transmitter antenna is 5mm away from the metal screen within a frequency range of 3.3-5 GHz.

simulation results agree well with the experimental results. The enhancement peaks are spotted at similar frequencies. Finally, the measured enhancement figures are plotted in Fig. 5.9(c) and (f). The enhancement results are calculated by dividing the transmission values obtained from the apertures with the samples to the only aperture case for every frequency that in turn gives an estimate of the power gain of the overall system. The transmission enhancement

took place at the respective frequencies that are listed in Table 5.2. At these frequencies, the subwavelength aperture is λ/31×λ/12 (width × height) for Sample A, and λ/25×λ/10 (width × height) for Sample B. We experimentally observed a more than 70,000 times power transmission enhancement for Sample A, whereas a higher than 5,300-fold power transmission improvement was achieved with Sample B. These values are much higher than the earlier reported results [41,73]. Sample A generated an order of magnitude higher enhanced transmission figure. The main reason for this is that Sample A is designed to operate at lower frequencies, where the single aperture transmission is considerably lower (see Fig. 5.7).

Table 5.2. Transmission Enhancement

Configuration	**f_{enh}**	**Subwavelength Aperture in terms of λ_{enh}** (width × height)	**Power Transmission Enhancement Figure**
Sample A	3.23 GHz	λ/31×λ/12	70,860
Sample B	4.03 GHz	λ/25×λ/10	5,350

Figure 5.10 demonstrates the transmission enhancement phenomenon by making use of the field maps. The field maps are plotted on the same scale in order to exhibit the power coupling efficiency from the input side to the output side in the presence of the CSRRs. The simulated electric fields have no significant component that penetrated to the output side through the subwavelength hole for the single aperture case. Counter intuitively, the field magnitudes are drastically enhanced when we situate Sample A, another substance into the electrically small aperture. The next section of the present study is devoted to the detailed physical discussions of this surprising phenomenon. Nevertheless, we can immediately state that CSRRs improve the transmission enhancement by thoroughly guiding the incident waves to the output side. Furthermore, the guided beams are focused to a certain point at the output side, which facilitates subwavelength focusing at the same time (see Fig. 5.10(b)).

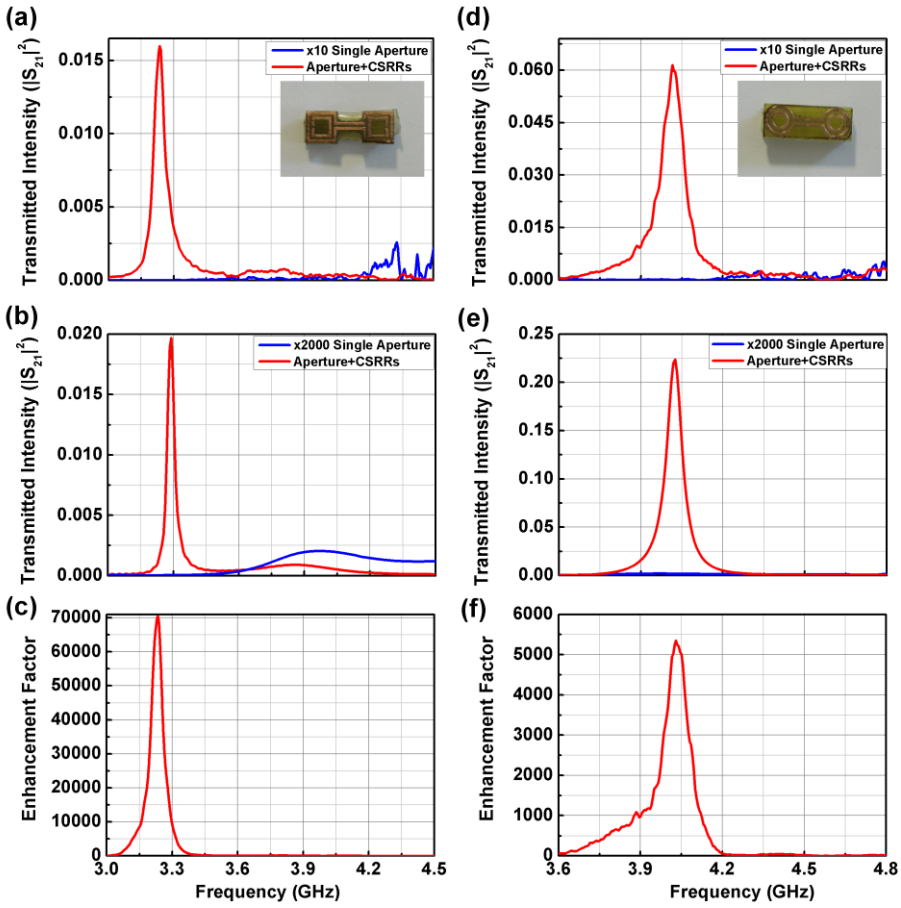

Figure 5.9: (a) Measured, (b) simulated transmitted intensity results for Sample A (solid red lines) and the aperture (solid blue lines). (c) Experimentally validated enhancement factor for Sample A. (d) Measured, (e) simulated transmitted intensity results for Sample B (solid red lines) and the aperture (solid blue lines). (f) Experimentally validated enhancement factor for Sample B.

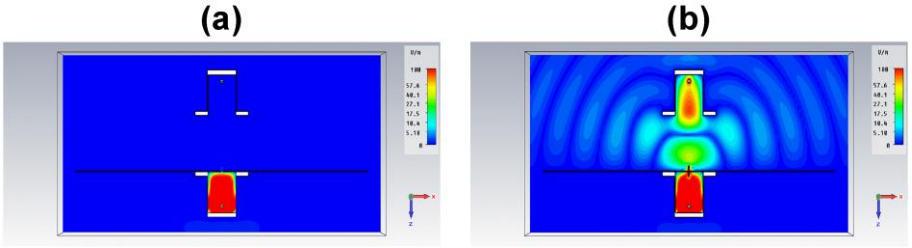

Figure 5.10: Simulated field maps on *x*-*z* plane for (a) the single aperture case, (b) Sample A incorporated subwavelength aperture case at the numerically calculated enhancement frequency (3.3 GHz). The transmitter antenna is in the lower half plane and it is located 0.5mm away from the metal plate.

It should also be noted that even higher enhancement factors are achievable numerically. Numerical analyses point out to a power transmission improvement of 800,000 and 225,000 for Sample A and Sample B respectively

owing to the lower single aperture transmission figures. Consequently, several orders of higher transmission enhancement figures are theoretically available.

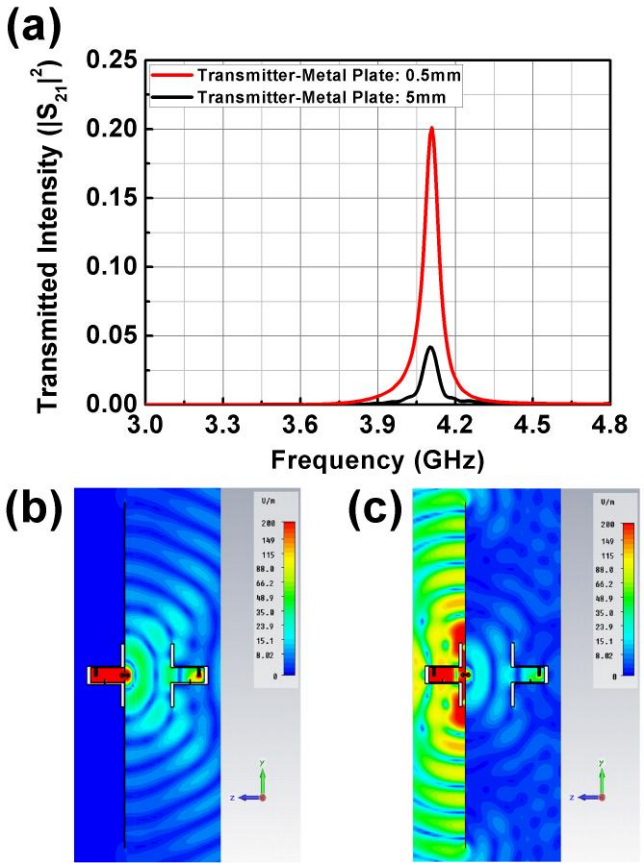

Figure 5.11:.(a) Simulated transmitted intensity figures for different transmitter antenna metal plate separations with Sample B (Metal plate-transmitter distance: 0.5mm solid red line, metal plate-transmitter distance: 5mm solid black line). Simulated field maps on *y-z* plane in the presence of Sample B when transmitter antenna to the metal plate separation is (b) 0.5mm and (c) 5mm.

The minor discrepancies in between the calculated and measured enhancement frequencies are associated with the small variations in the manufacturing processes, the crude modeling and insufficient meshing of the materials in the simulation domain as well as the possible slight misalignments in the experiments. Yet, the main differences in the absolute transmission values are again attributed to the diffraction effects as it is pointed out in Fig. 5.11. A significant portion of the incident beam is not properly coupled to the aperture but lost to the diffractions and scatterings instead. Hence, the absolute transmission value of the CSRR loaded aperture is also very sensitive to the

separation distance especially after 4 GHz, where the diffractions within the system are more pronounced. The mechanical limitations compel us to work with very precise positioners for the repeatability of the absolute transmission values that remain above 4 GHz throughout the experiments.

In the previous section, the horn antennas were modeled in order to investigate the transmission enhancement performances of the proposed samples realistically. A rather large real life electromagnetic problem was realized in the computational domain. Thus, we had the opportunity to compare the absolute transmission and transmission enhancement values within the operational frequency range of the horn antennas (3-5.5 GHz). Nonetheless, we need a broadband excitation source that can allow us to explore the deep subwavelength regime that covers frequencies even lower than 3 GHz. Therefore, we excite our structures with a plane wave in this section, which is dedicated to the understanding of the transmission enhancement phenomenon. The plane wave excitation enabled us to make a fair quantitative comparison between the enhancement figures appearing at distinct frequencies since the results are independent of the frequency response of the transmitting and receiving antennas. The electric field values are recorded by utilizing probes that were located 12.5cm away from the aperture. The boundary termination conditions were selected in such a way that the diffractions from the plate edges are totally obstructed.

Figure 5.12 shows the transmitted electric field values in dBV/m scale. Samples yielded a transmitted electric field improvement at around the expected frequencies. We worked with two different apertures. Aperture1 is $3\times7.5\text{mm}^2$ and Aperture2 is $1\times2.5\text{mm}^2$. On the other hand, Bethe's well-known transmission prediction for an annular hole on a two dimensional infinitely extending screen [33] is plotted in the same graph (dashed orange lines). It is apparent that Bethe's prediction provides a reliable insight. Bethe's predictions are adapted and fitted for the two apertures. The ratio of the fitting constants, r_1/r_2 is $(100)^{1/3} \approx 4.64$.

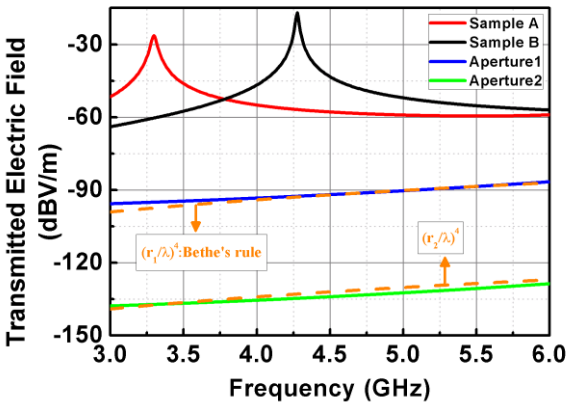

Figure 5.12: Plane wave transmission results in dB scale collected with E-field probes for Sample A (solid red line), Sample B (solid black line), Aperture1 (solid blue line) and Aperture2 (solid green line). Bethe's transmission efficiency predictions for Aperture1 and Aperture2 (dashed orange lines).

The main reason for the transmission enhancement is the magnetic response of the SRRs. The incident fields are trapped inside the magnetic loop of the SRRs. The incoming waves are properly coupled to the aperture and guided to the output side. The transmission enhancement frequencies (see Table 5.2) are close to the calculated magnetic resonance frequencies of the samples (see Table 5.1), even though a periodic arrangement was simulated while identifying the transmission spectrum of the CSRRs. We tested the role of magnetic resonance in a canonical way by shorting the loops. We expect the transmission enhancement to disappear when we short the loops. Figure 5.13 shows the simulated transmission and field enhancement results after we shorted the rings. Shorting the outer rings destroyed the magnetic resonance at around 4.2 GHz (solid blue line) and prevented the transmission enhancement for Sample B. Conversely, only the enhancement frequency is modified when the inner rings are shorted (solid black line). The magnetic response of the SRRs is not totally lost by solely shorting the inner rings. The outer rings still dominate the magnetic response within this frequency range. Hence, we can clearly state that the magnetic resonance is the responsible element for the transmission enhancement.

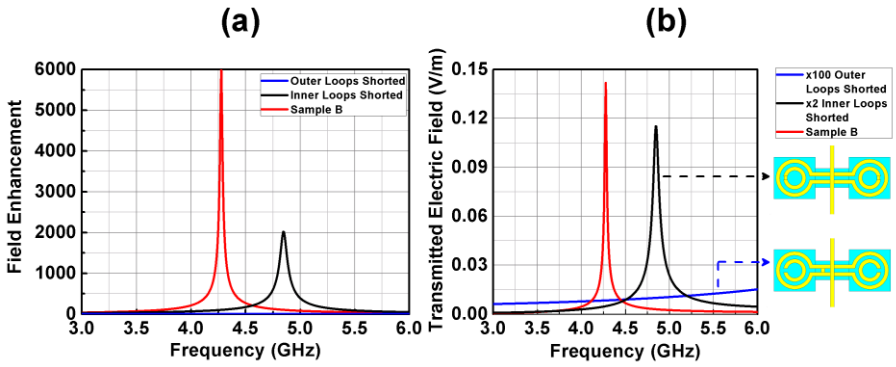

Figure 5.13: (a) Simulated field enhancement results with respect to the single aperture for Sample B incorporated aperture (solid red line), Sample B with inner rings shorted (solid black line), and Sample B with outer rings shorted (solid blue line). (b) Simulated transmitted electric fields at the exit side for Sample B (solid red line), Sample B with inner rings shorted (solid black line), and Sample B with outer rings shorted (solid blue line).

Ref. 73 discusses the frequency blue shifts of the enhancement frequency with respect to the original magnetic resonance frequency. According to ref. 73, we have to treat the resonator together with the aperture as a combined system. Although the resonator establishes the grounds for a transmission enhancement, the two frequencies, namely the transmission enhancement frequency and the magnetic resonance frequencies of the samples do not match exactly. They are rather slightly separated. The slight mismatch between the magnetic resonance frequency values of the CSRRs (see Table 5.1) and the transmission enhancement frequencies of the respective CSRRs (see Table 5.2) are attributed to this effect. As the aperture shrinks, the enhancement frequency tends to move to higher frequencies.

The resonator sizes were always comparable to the subwavelength aperture size in previous studies [41,73-75]. Since the electromagnetic fields were highly localized around the aperture, the transmission enhancement frequencies were not highly robust against the changes in the geometrical parameters of the aperture. However, in the present study, we have a higher degree of freedom while designing the resonator structure. We do not have a strict restriction on the size of the resonator. Fig. 5.14(b) shows the simulated transmission spectra for Aperture1 and Aperture2. The outer loop ring of the SRR has a width of 12.5mm, whereas the width of the inner rings is 10.5mm.

Under these conditions, the selected resonator is significantly larger than the aperture. Nevertheless, the CSRRs still allow the incoming waves to interact with the aperture. Fig. 5.14(b) demonstrates that the same amount of transmission is attained numerically regardless of the aperture size. Additionally, the amount of the transmitted fields through the aperture at these deep subwavelength frequencies is comparable to the previously obtained results for Sample B (see Fig. 5.13(b)). Consequently, tremendous field enhancement figures have been observed for an ultra-tiny aperture (in terms of its electrical size) in Fig. 5.14(a). This opens up the possibility for even more ambitious transmission enhancement results to be at least theoretically envisaged at these deep subwavelength frequencies. Furthermore, the transmission enhancement frequency has not changed, owing to the aperture independent nature of the proposed transmission enhancement mechanism.

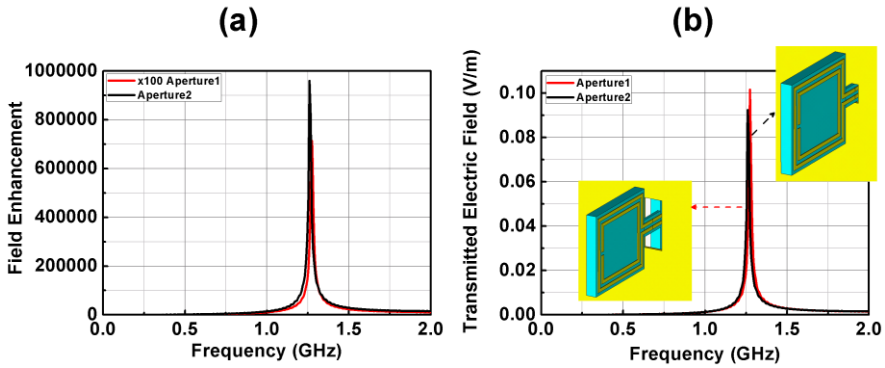

Figure 5.14: (a) Simulated field enhancement results with respect to the single aperture for the CSRR with given dimensions. The same CSRR is incorporated with Aperture1 (solid red line), which is 3×7.5mm^2 and with Aperture2 (solid black line), which is 1×2.5mm^2. (b) Simulated transmitted electric fields at the exit side for Aperture1 (solid red line) and Aperture2 (solid black line).

The aperture independent transmission mechanism suggests clues for the role of the connecting bars. In the earlier studies [41,73-75], resonators were attached to one side of the metal plate. This case was investigated numerically, and the transmission characteristics are plotted in Fig. 5.15 (solid blue line). We omitted the SRR at the exit side of the aperture. Single SRR produced a relatively moderate transmission in accordance with the earlier reported results. Additionally, the transmission results without the connecting bars were checked

in order to distinguish their role in the enhancement phenomenon. SRRs without the connecting bar provide better coupling compared to the single SRR case. However, Sample A still yields superior transmission, in turn resulting in amazingly higher enhancement figures. Moreover, the presence of the connecting bars once again manifests itself when we examine the shifts in the enhancement frequencies. Connecting bars brought aperture independency to the system, while keeping the enhancement resonance frequency close to the resonance frequency of the SRRs.

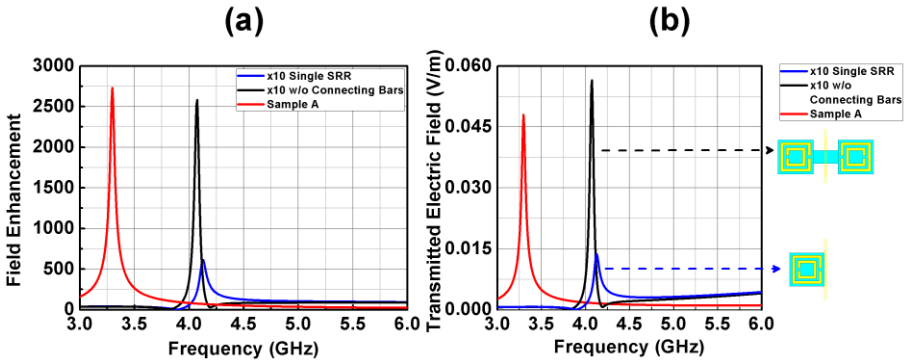

Figure 5.15: (a) Simulated field enhancement results with respect to the single aperture for Sample A incorporated aperture (solid red line), Sample A without connecting bars (solid black line), and single SRR (solid blue line). (b) Simulated transmitted electric fields at the exit side for Sample A incorporated aperture (solid red line), Sample A without connecting bars (solid black line), and single SRR affixed to the input side of the aperture (solid blue line).

Several of these topics were addressed in Fig. 5.16. The magnetic response of the SRRs causes excess amounts of looping induced surface currents (see Fig. 5.16(a)). Only at the resonance frequency, the SRRs start working in phase by sharing equal portions of the induced surface currents. The incoming fields are trapped around the aperture due to this magnetic resonance, as shown in Fig. 5.16(b). Originally, the fields are concentrated and enhanced in the vicinity of the split width of the SRR that is located at the input side, as previously discussed in ref. 41. Once the fields are localized with the assistance of the SRR, the connected bars couple the waves by safely guiding them through the aperture. The second SRR at the output side is strongly excited (Fig. 5.16(d)) compared to the case without the connecting bars (Fig. 5.16(c)). Single SRR might be a better resonator. It might store stronger electrical fields, yet it lacks

the ability to properly excite the second SRR. In our scheme, SRRs are not isolated any longer. The fields remain inside the loops. Individual SRRs stop working separately and the overall system acts like an antenna linking the input to the output. Trapped fields and induced surface currents are shared equally between the two resonators. Eventually, it provides an improved coupling mechanism between the input and output planes.

In summary, we presented an alternative approach that offers higher transmission enhancement results than the previously studied methods. We numerically simulated the transmission characteristics of a subwavelength aperture incorporated with the CSRRs. The transmission peaks that appeared in the simulation results suggested transmission enhancement. We also verified the transmission enhancement phenomenon experimentally. Our experiments indicated a transmission improvement factor above 70,000 through a subwavelength aperture that had a width of $\lambda/31$ and a height of $\lambda/12$ in terms of the operational wavelength. We discussed the diffraction mechanisms, mechanical difficulties and the key parameters of our experimental setup in order to achieve high transmission improvement results. We have shown that even higher transmission enhancement figures are numerically available. We attempted to emphasize the role of the connecting bars during this process. We numerically showed that the connecting bars linked the otherwise isolated SRRs to each other and guided the incoming wave through the subwavelength hole. The highly localized fields around the aperture, owing to the magnetic resonance of the SRRs, efficiently coupled the input wave to the exit side. This approach brings in the opportunity of attaining excessive transmission enhancement factors by minimizing the dependence on the aperture geometry.

Electromagnetic transmission through a subwavelength hole used to be a challenging problem that belonged to the area of physics. However, researchers have tackled these difficulties by employing different kinds of coupling structures around the aperture in recent years. These innovations immediately found technological applications. The devices that relied on the extraordinary

transmission effects were adopted in nanophotonics, biophysics, chemical sensing, nanolithography, and more. Yet, we analyzed the case with a single resonator that was located in the vicinity of a hole instead of the electrically large designs that have been made technologically available. We obtained very large transmission enhancement factors by making use of the CSRRs. A single resonator is easier to tune and control. We believe a device that is based on the CSRRs can be engineered in the optical domain. Such a device would enhance our resolution and signal strength, which might enable us to see how deep the rabbit hole goes.

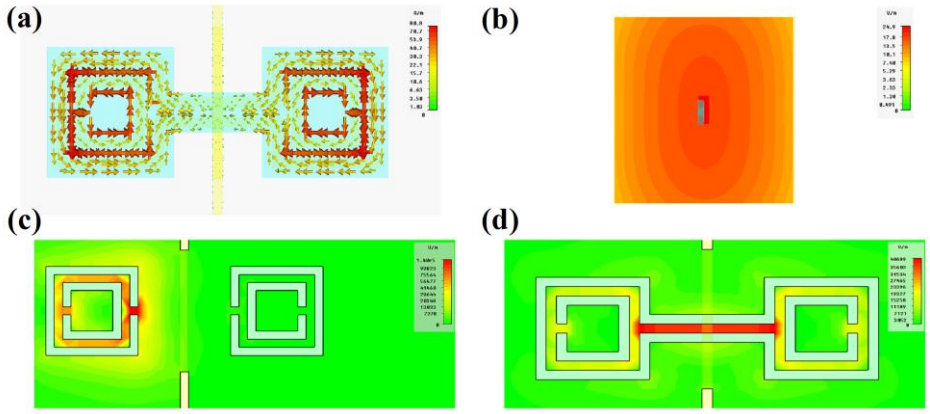

Figure 5.16: Animations based on numerical results at the enhancement frequency. (a) Induced surface currents on the CSRRs. (b) Field localization around the aperture (aperture is in the middle of the plane) with the help of the CSRRs. (c) Electric field localization around the aperture without the connecting bars. (d) Electric field localization around the aperture with the connecting bars.

5.3 Near-field light localization using subwavelength apertures incorporated with resonators

This section appeared in Optics Communications, Damla Ates, Atilla Ozgur Cakmak and Ekmel Ozbay, "Near-field light localization using subwavelength aperturesincorporated with metamaterials," Optics Communications, volume 16, number 7, pages 3390-3396, 2012. An order to reproduce parts of this paper in the current thesis has been placed at the time of

the dissertation. Please check the copyright forms at the end. You may refer to the published article for the media files.

The transmission characteristics of light through apertures have been the subject of the studies for a long time. The earlier explanations based on the Kirchhoff scalar diffraction theory gave good results as long as the opening attained comparably larger values with respect to the operational wavelength, λ. In 1940s, H. Bethe addressed the shortcomings of the Kirchhoff scalar diffraction theory and developed a new approach that attempted to elucidate the electromagnetic wave transmission for the subwavelength apertures [33]. According to Bethe, the transmission efficiency scaled as $(r/\lambda)^4$ for an infinitesimally thin metallic screen with perfectly conducting walls extending to infinity, where r stands for the radius of the subwavelength aperture. Both of the theories concentrated on the opaque screens which were constituted from the ideal material parameters and excluded the contributions of the evanescent surface waves on the transmission characteristics. It was only after the pioneering works at the turn of the century which pointed out the possibility of an extraordinary transmission through subwavelength aperture arrays, the attention of the scientific community has once again been directed towards the perforated metallic slits [34]. This era also marked the beginning of the scientific debates over the leading mechanisms of the extraordinary transmission. Initially, the extraordinary transmission was associated with the surface-plasmon phenomenon at the dielectric-metal interface at optical wavelengths. Thereafter, several results targeting the extraordinary transmission started to be reported at microwave frequencies as well as in optical wavelengths [35,42,43,76,77]. The observed surface waves at microwave frequencies are ascribed to the designer surface plasmons that exist due to the modification of the surface impedance by making use of the pure geometrical parameters [71]. Moreover, the researchers have investigated the effect of periodicity and size of the hole arrays. Scientists designed corrugations around the apertures and surfaces to establish an improved coupling [56,78]. The accumulated theoretical and experimental experience enabled the extraordinary

transmission to be attributed to the coupling of the leaky surface waves at both ends of the aperture through the evanescent waveguide modes of the subwavelength opening. The corrugated surfaces increased the transmission and provided better coupling conditions. Alternatively, Alu *et al*. suggested covering the aperture with a metamaterial slab in order to achieve superior coupling efficiencies [38]. On the other hand, Bilotti *et al*. proposed exploiting the resonance characteristics of the metamaterials, which in turn yielded the amplification of the electromagnetic fields around the aperture [75]. Since the metamaterials provide the field localization opportunity in the vicinity of the resonance frequency, they can be considered as a strong candidate for a prospective corrugation design that boosts the transmission efficiency. Accordingly, Aydin *et al*. experimentally showed a 740-fold transmission enhancement by inserting a split ring resonator inside the aperture [41]. Then, in one of our previous studies we discussed the physical origins of the enhancement in terms of the induced surface currents [73]. Recently, we have demonstrated a 70,000-fold enhancement experimentally and analyzed the parameters of the designed structure [79].

Independently, the localization theory has been developed in 1960s and light localization obtained in a wide range of areas from lasers to photonic crystals and gratings has gained a significant interest from the scientific community in the recent years [80,81]. One of the most striking ways to localize fields is using metamaterials. Nanowire metamaterial designs and asymmetrical split ring resonators were employed to localize the electric fields [82-84]. Cavities that resemble the counterparts in photonic crystal literature are utilized to confine the electromagnetic waves [85,86]. Conversely, there have been attempts to localize the fields outside the metamaterial specimen. This subject has been first attended by Pendry *et al*. under the topic of super lenses [87]. N. Fang and X. Zhang considered the imaging properties of the metamaterial super lenses and observed that the evanescent waves are strengthened at the exit side [88]. Furthermore, scientists such as Grbic *et al*. treated the negative index lens as a transmission line to realize the subdiffraction imaging [89]. Aydın *et al*. has

achieved a strong localization by focusing the evanescent waves with the aid of negative index materials [90].

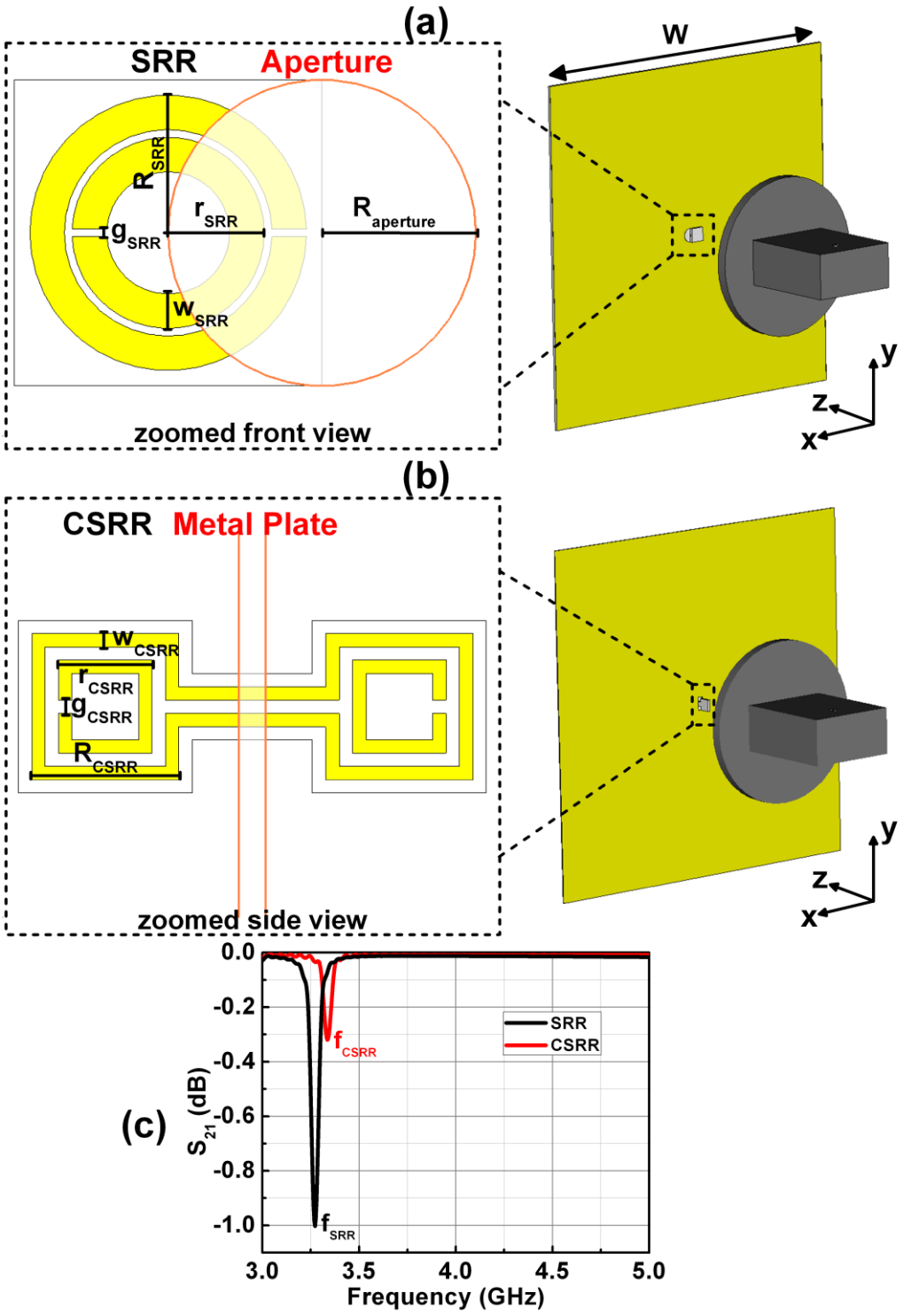

Figure 5.17: (a) The SRR and the aperture, (b) the CSRR and the aperture, (c) simulated transmission results (S_{21}) for the SRR (black line) and the CSRR (red line).

For the purposes of this study we will be mainly concentrated on the field localization at the output side of a subwavelength hole and a subwavelength slit incorporated with two distinct metamaterial designs. The localized beam already results in extraordinary transmission. Firstly, the transmission mechanism offered by using two different metamaterial configurations will be discussed. Secondly, the confinement capabilities of the proposed structures will be investigated and compared.

A single resonator embedded close to a subwavelength aperture is the key element in elevating the electromagnetic fields and will comprise the fundamental building block for the subwavelength field localization. The first configuration is illustrated in Fig. 5.17(a). The zoomed perspectives are also shown for convenience. The split ring resonator (SRR) is carefully aligned at the midpoint of the aperture such that the gaps of the SRR, g_{SRR} are parallel to *y*-axis. The propagation direction is *z*-axis and the aperture is illuminated with a waveguide in the experiments. This particular waveguide is modeled in CST Microwave Studio and shown in gray color. The aperture has a radius $R_{aperture}$=4 mm and resides on a square plate with a width W=200 mm. The SRR gaps are g_{SRR}=0.2 mm, while the inner and outer radius of the structure are r_{SRR}=2.7 mm and R_{SRR}=3.6 mm. The metal width is w_{SRR}=0.9 mm.

Subsequently, we have designed split ring resonators that have connecting bars and the configuration is depicted in Fig. 5.17(b). These connected SRRs are labeled as CSRR. The samples are fabricated in a similar way to the previous design. They are deposited on a dielectric printed circuit board (PCB) with a 1.6 mm thickness. The connected bar length is l_{CSRR}=5.5 mm. The remaining parameters for the individual SRRs are g_{CSRR}=w_{CSRR}=0.5 mm, and r_{CSRR}=3.5 mm, R_{CSRR}=5.5 mm. The area of the rectangular aperture is 3x7.5 mm^2. The CSRR is inserted midway into the aperture. The thicknesses of the deposited copper are the same in both configurations and it is equal to 30 μm.

The resonance frequencies of the regarding resonators are shown in Fig. 5.17(c). The launched beam has an electric field component parallel to *y*-axis. Then, the gap of the SRR captures the incoming electric field which induces circulating currents and creates accumulated charges at the resonance condition. A similar action will take place for CSRR which will only result in smaller resonance strength in contrast to the single SRR. The effect of shortening the SRRs destroys the charge accumulation at the resonance frequency. As it can be seen from Fig. 5.17(c), the shorted SRRs in CSRR do not totally lose their resonance owing to the fact that shortening is performed over a longer path. Nevertheless, a significant portion of the charges will leak away through the connection bars. One might also wonder the overall shallow depths of the transmission results. The attained S_{21} results are one order of magnitude higher (in *dB* scale) than the usually inspected values for conventional SRRs around the resonance frequency. Given that a single resonator will be positioned around the aperture in the proceeding sections, the transmission characteristics have been investigated for a single SRR in order to avoid the contributions coming from the coupling mechanisms in a SRR array. Therefore, the SRR and CSRR are illuminated with a beam of finite width that can circumvent the resonators and reach the detector. Periodic boundary conditions are not allowed in the simulations. Consequently, the resonators could capture a limited amount of the propagating waves. Yet, we obtain the individual resonance frequencies of our configurations as f_{SRR}=3.27 GHz and f_{CSRR}=3.33 GHz.

Once the resonator is placed in the vicinity of the subwavelength aperture simulated and measured transmission characteristics are plotted in Fig. 5.18(a) and (b) for the SRR configuration, respectively. The transmission enhancement frequency turned out to be 3.6 GHz in the simulation results, whereas a peak is spotted at 3.56 GHz in the experiments. There is a good agreement between the experimental and simulation based results in terms of the general transmission characteristics. This subwavelength aperture has a cutoff frequency for the lowest allowed modes at almost 22 GHz. Then, the aperture can be visualized as a *LC* tank with a dominant inductive character which forces

the opening to act as a high pass filter [91]. According to Bethe, we would anticipate a dramatically weak transmission at the output of the subwavelength aperture in the absence of the resonator. Instead of the electrically large cover suggested by Alu *et al.* in ref. 38, we make use of the resonance mechanism of a single negative material as pointed out in ref. 75. It was indicated in ref. 75 that only the effective permeability would be the determining constitutive parameter and a transmission enhancement could also be sustained at another frequency where the reduced permeability μ=-1 is feasible. However, the detected transmission enhancement is solely due to the induced resonance of the SRR for our configuration which offers approximately a 27 *dB* improvement in the transmission figures on top of the subwavelength aperture. A parallel magnetic dipole and a perpendicular electric dipole (with respect to the screen) are the responsible dipole moments for the transmission through the subwavelength opening. In our current configuration, the strong dipole moments are along *y*-axis for the electric and *z*-axis for the magnetic counterpart. Thus, we do not have a chance to elevate drastically the amplitudes of the original dipole moments of the subwavelength aperture around the resonance frequency. Nonetheless, the induced dipoles in the SRR cancel out the equivalent dipole of the subwavelength aperture in the neighborhood of the transmission enhancement frequency owing to the bianisotropy of the SRR, as indicated in ref. 40. Thus, we encounter a dip in the transmission graph inside the band starting from 4 GHz up to 4.5 GHz. Finally, the shorted SRR loses its magnetic resonance and causes an augmentation in the loss figures, which further verifies the resonance based explanations.

In the meantime, the transmission characteristics have been laid out for the CSRRs in Fig. 5.18(c) and (d). The cutoff wavelength of the slit is at even higher frequencies (42.8 GHz). As a result, smaller amount of transmission is detected for the subwavelength aperture case. The experiments are carried out with horn antennas connected to HP 8510C Network Analyzer. Absorbers have been placed in order to minimize the diffractions at the edges of the metallic screen, which can easily outbalance the main signal. Such effects trigger the

ripples in the measured results in Fig. 5.18(d). Similar scenarios had been investigated in ref. 79. In contrast to the real life problem, we can numerically tackle this particular difficulty with perfectly absorbing boundaries. The resonance mechanism presents a transmission enhancement higher than 50 *dB* at the enhancement frequency of 3.28 GHz. Now, the transmission mechanism depends on the connected bars and we do not detect a transmission dip just after the enhancement frequency. The transmission figures stay improved over 20 *dB* with the addition of the CSRR on top of the single slit transmission. Lastly, the CSRR had been shorted from the midpoint of the connecting bars. In the end, this shortening of the connecting bars proved to have a comparable influence on the transmission spectra by destroying the magnetic resonance of the individual SRRs.

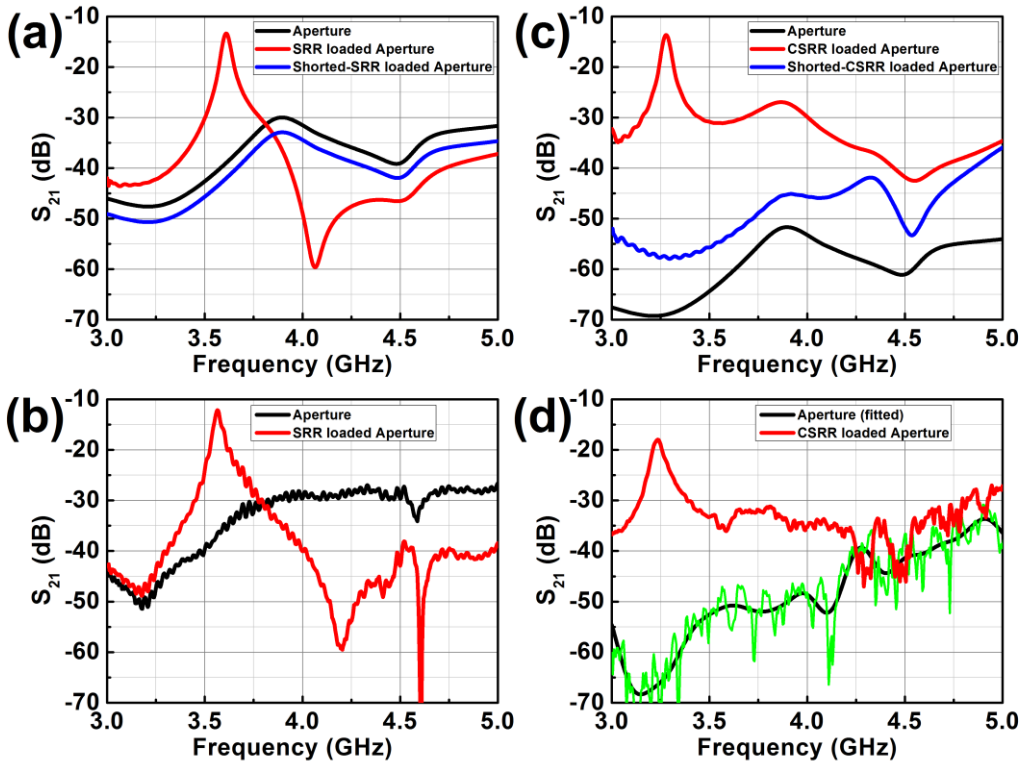

Figure 5.18: Transmission spectra of the (a) simulated results for the single aperture (black line), the SRR loaded aperture (red line), the shorted SRR loaded aperture (blue line), (b) measurement results for the single aperture (black line), the SRR loaded aperture (red line), (c) simulation results for the single aperture (black line), the CSRR loaded aperture (red line), the shorted CSRR loaded aperture (blue line), (d) measurement results for the single aperture (green line) [the measurement result is fitted to a curve (black line) because of the sudden ripples], the CSRR loaded aperture (red line).

Figure 5.19 is presented in order to shed light to the underlying physical mechanisms of the transmission enhancement phenomenon. The induced surface currents in the vicinity of the aperture are illustrated at the resonance frequency in Fig. 5.19(a). Then, the addition of the SRR strengthens an electric dipole along the *y*-axis. However, this induced dipole and thereby the induced surface currents are nullified at a certain degree by the image current formation on the metallic screen, as shown in Fig. 5.19(a). Consequently, the shaded area will be the main contributor of the induced currents whose function will be to transmit the impinging field to the exit side. In other words, the shaded area will play the role of an effective aperture for an ordinary antenna. In a very general manner the effective aperture of an antenna is defined as $A_{eff} = P_{out} / P_{inc} = G\lambda^2 / 4\pi$, where P_{out} is the delivered power by the antenna, P_{inc} is the incident power in terms of watts per unit area and G is the antenna power gain. The effective aperture is proportional to the operational wavelength. The SRR together with the aperture constitute a new transmission system. This is the main reason behind the mismatch between the given resonance frequency of the isolated SRR (see Fig. 5.17(c)) and the transmission enhancement frequency of the total system. Such a shift has also been reported in ref. 75. Unlike the cases in the earlier studies [41,73,75] the SRR's resonance is not magnetically excited and the SRR is directly facing the metal screen. These factors found the ground for a more pronounced shift to be observed between the self-resonance frequency and the transmission enhancement frequency. Then, an alteration of the exact location of the SRR directly determines the enhancement frequency. We have not observed a strong difference between the experimental and numerical values but a small misalignment would be likely to produce quite different transmission characteristics. Ref. 73 considered the misalignments only in one dimension and showed that a shift of δx_1=-0.1 mm and δx_2=+0.3 mm would move the transmission enhancement frequency to the higher and lower frequencies from its original location respectively, as predicted from the qualitative effective aperture discussions. The transmission enhancement values attained lower figures for those cases, since the maximum electric dipole can be induced when

the SRR is carefully positioned at the midpoint of the aperture assuming that the aperture is perfectly aligned with the incoming illumination. The other way of modifying the effective aperture size of the system is to tune the radius of the opening. It was also depicted in ref. 73 that the transmission enhancement frequencies spanned a band from 3.3 GHz to 6 GHz for the corresponding aperture radii ranging from 2.8 mm up to 7 mm.

Figure 5.19(b) shows the calculated electric fields around the aperture at the designated resonance frequency. The CSRR can be regarded as a loop antenna connecting the two sides of the aperture. The connecting bars conduct the induced currents over a broad range of frequency. The induced currents continue to be shared outside the enhancement band. We are comparably much less limited by the resonance bandwidth of the structure. An electric dipole parallel to the screen is again induced. This time different from the SRR case, a magnetic dipole parallel to the screen is also excited and the interactions with the screen are comparably reduced. In turn, the transmission enhancement frequency shifted relatively less from the isolated resonator configuration in contrast to the SRR case. We do not have a strong dependency to the geometrical sizes of the aperture. The incoming fields are captured by the loop antenna and the fields are safely guided to the output plane. The shaded region localizes the fields during the transmission of the electromagnetic fields. Eventually, the connecting bars play the role of a subwavelength waveguide. The width of this particular waveguide turns out to be as small as $\lambda/180$ at the transmission enhancement frequency. The fields are confined to this deep subwavelength waveguide for a propagation length of $\lambda/18$. As it is previously discussed in ref. 79, the inner loops of the individual SRRs do not play a major part in the transmission enhancement. The magnetic dipole is permanently obstructed when the outer loops are shorted and the waveguiding effect of the highly confined electric fields is thereby demolished. At these regarding peaks not only we obtain a high transmission but we also have a chance to localize the evanescent wave at the exit side of the aperture. In the next section, the discussions will be devoted to the examination of these scenarios.

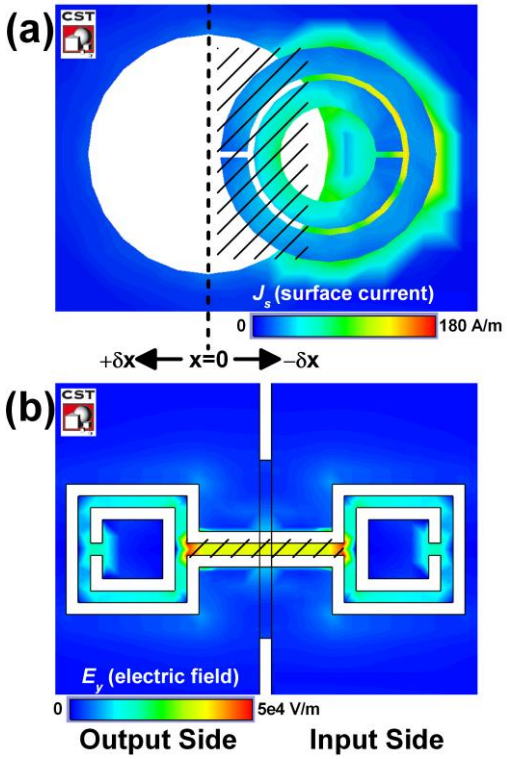

Figure 5.19: (a) Induced surface currents on the SRR at *f*=3.6 GHz. The shaded region encompasses the effective aperture of the overall SRR subwavelength aperture system. (b) The electric fields (E_y) in the vicinity of the subwavelength aperture at *f*=3.28 GHz. The shaded region emphasizes the strong spatial confinement of the electric fields inside the aperture.

In this part, we analyzed the characteristics of the near field localization around the resonance frequencies. The fields at the output side have been numerically collected and presented in Fig. 5.20 and 5.21 simultaneously. Figure 5.20 entails the SRR loaded subwavelength hole while Figure 5.21 involves the CSRR incorporated subwavelength slit. Figure 5.20(a) and 5.21(a) exhibit the field distribution on the *x*-*z* plane, whereas Figure 5.20(b) and 5.21(b) portrays the field distribution on the *y*-*z* plane at their respective resonance frequencies in *dB* scale. All of the field distributions are normalized with respect to the maximum attained value in the concerning scenarios. The cutoff frequencies of the subwavelength hole and slit were calculated to be well below the operational frequency range. The transmitted fields in Fig. 5.20 and 5.21 are originally the evanescent modes of the subwavelength openings. Therefore, the fields decay dramatically in the direction of propagation.

Consequently, intensified fields are localized in the near field zone of the aperture. Yet, the overall configurations propose to restrict the transmitted evanescent modes only on the *x*-*z* plane. For instance, the loop antenna nature of the CSRR compels the fields to radiate isotropically on the *y*-*z* plane, while the radiation is not allowed along the induced magnetic dipole direction (*x*-axis), which is clearly observed in Fig. 5.21(a) [92]. Accordingly, the field profiles are plotted in Fig. 5.20(c) and 5.21(c) in order to explore the localization capabilities of the total systems. The minimum realizable Full Width at Half Maximum (*FWHM*) values of the overall systems are revealed as $\lambda/23$ and $\lambda/29$ for the SRR and CSRR incorporated approaches, respectively. The excitation source with *FWHM* values around $\lambda/3$ is down converted by taking advantage of the subwavelength resonators placed in the reactive near field zone of the illumination. Then, the precise beam spot-size conversion values are calculated to be 7.12 and 9.11 for the systems with SRR and CSRR, correspondingly. It might not sound interesting to come across such a focusing effect at the output side of the subwavelength apertures. Nevertheless, the proposed designs have not only amplified the evanescent mode, but also narrowed down the outgoing fields exceeding the capabilities of the subwavelength openings, as shown in Fig. 5.20(c) and 5.21(c). We numerically integrated the intensity profiles on *x*-*y* plane along the direction of propagation (*z*-axis). Figure 5.20(d) and 5.21(d) explicitly demonstrates that the power values drop rapidly in the direction of propagation. Approximately 10% of the initial power is conserved in the case of SRR loaded apertures whilst around 20% is preserved for the configuration with the CSRR. On the other hand, when the *FWHM* values are inspected, $\lambda/5$ *FWHM* is still feasible at a distance of 0.15λ away from the aperture loaded with the SRR. The same FWHM values can be observed in the CSRR at a location 0.1λ away from the metallic screen. The SRR configuration extracts more intensity from the subwavelength structure by focusing down the amplified evanescent fields, which can even get higher values than the source itself, as it can be seen in the field profiles of Fig. 5.20(c). Conversely, the CSRR structure

promises an improved spot size conversion ratio when the FWHM values are taken into consideration.

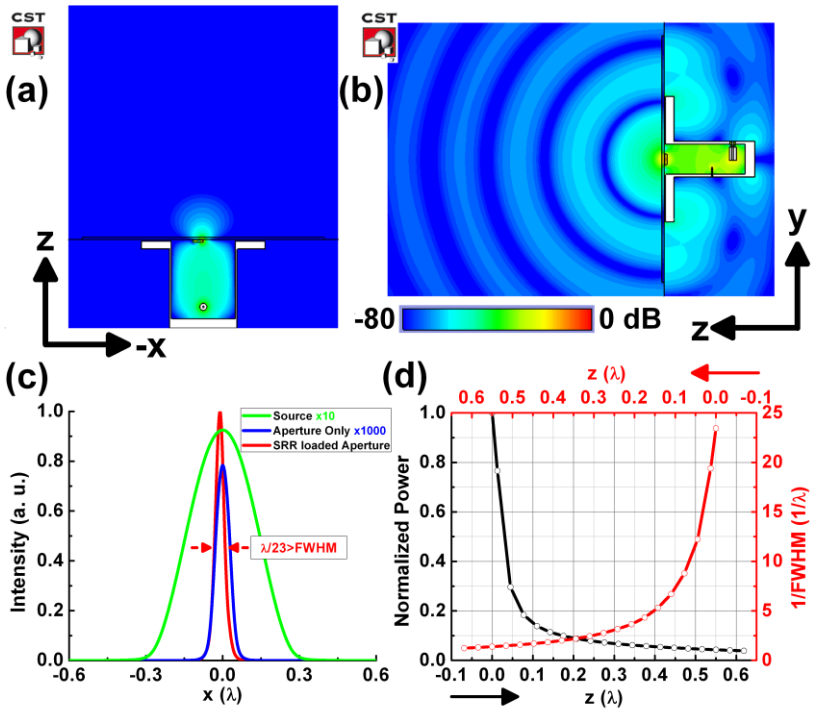

Figure 5. 20: Field distributions on (a) *x*-*z* plane (Media 3), (b) *y*-*z* plane (Media 4) in *dB* scale at *f*=3.6 GHz for the SRR loaded aperture. (c) Intensity profiles along *x*-axis for the single aperture (blue line), the SRR loaded aperture (red line) and the source in free space (light green). (d) Normalized power (black line) and 1/*FWHM* values (red line) along the propogation direction (*z*-axis).

Transmission enhancement through subwavelength apertures is still a challenging topic in experimental physics. In this study, we have demonstrated alternative methods for improving the transmission figures of the otherwise opaque screens. The resonance nature of the SRR and CSRR is exploited in order to boost the transmission efficiency of the evanescent modes by factors of 27 dB and 50 dB, respectively. The physical origins of the extraordinary transmission are discussed in details. It is emphasized that the SRR loaded holes must be regarded as a combined system which has a certain effective aperture size. Through this effective aperture the leaky modes are transmitted to the outer plane. On the other hand, the CSRR loosens the dependency on the geometrical parameters of the aperture while behaving like a loop antenna. The captured

fields are guided via the connecting bars to the exit side. Furthermore, we investigated the field distributions of the outer plane. The overall system offers spot conversion ratios as high as 7.12 and 9.11 for the SRR and CSRR designs, respectively. *FWHM* values down to $\lambda/29$ are demonstrated numerically in the near field of the excitation source by attaching the CSRR to the subwavelength slit.

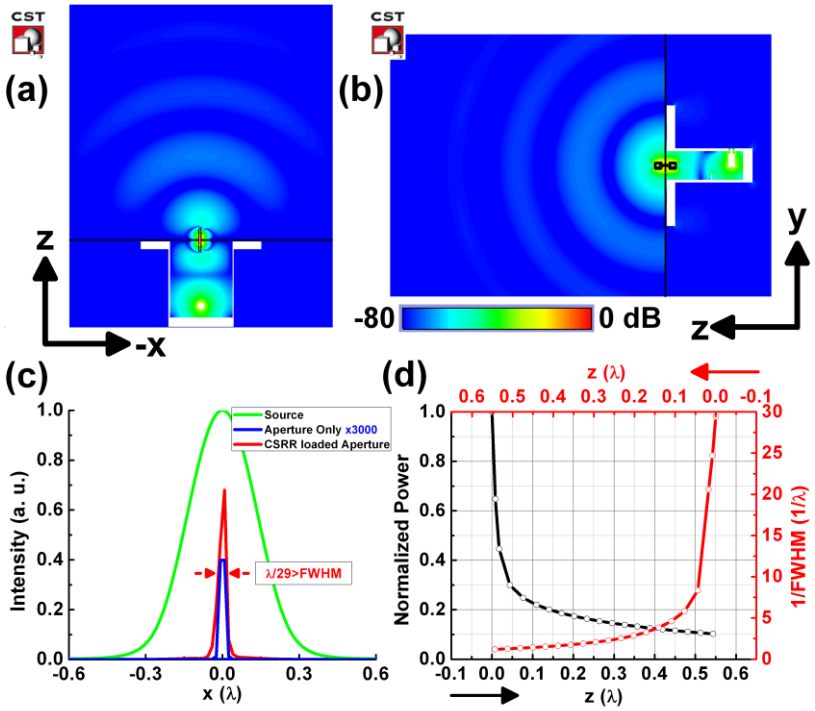

Figure 5.21: Field distributions on (a) *x*-*z* plane (Media 5), (b) *y*-*z* plane (Media 6) in *dB* scale at *f*=3.28 GHz for the CSRR loaded aperture. (c) Intensity profiles along *x*-axis for the single aperture (blue line), the CSRR loaded aperture (red line) and the source in free space (light green). (d) Normalized power (black line) and 1/*FWHM* values (red line) along the propogation direction (*z*-axis).

The proposed designs are simulated and measured at microwave frequencies while bearing in mind the prospective design adaptable for optical wavelengths. An analogy which will be suitable for the optical regime would prove to find essential application fields ranging from sensors, biophotonics, SNOM and subwavelength imaging. The horn antennas have to be replaced with the optical light sources such as lasers. The designer will encounter the additional losses coming from the material properties of the metals at optical

wavelengths and will have to overcome the difficulties of the nanofabrication. Nevertheless, a careful design is expected to bring numerous novelties on top of the conventional systems for those who are interested in the near-field optics.

5.4 Deep subwavelength transmission enhancement with multi-split-ring resonators

Multi split ring resonators (MSRRs) have several concatenated circles. Thus, the magnetic resonance of the single SRR is shifted drastically to the subwavelength regime. The MSRR has been shown in Fig. 5.22(a). The resulting structure possesses multi resonances unlike the simple single SRR case. The first two resonances are depicted in the top subplot of Fig. 5.22(c). Consequently, such a resonator is expected to give an enhanced transmission at even longer wavelengths. The simulation results are portrayed in the middle portion of Fig. 5.22(c). The single aperture transmission (blue line) has been shown alongside with its MSRR integrated case (red line). In agreement with our earlier claims in the previous sections, the transmission is enhanced at the resonance bands. Once the magnetic dipole and/or electric dipole moments are excited, the fields are largely intensified around the vicinity of the aperture. As a result, tremendous transmission enhancement factors can be reached.

The measurement results have been given in Fig. 5.23 for 3 different scenarios in which the MSRR is excited in different ways. The electrically coupled MSRR produces the highest transmission enhancement factor in Fig. 5.23(b). One important remark has to be made about the experimental results in Fig. 5.23. The enhancement results are much lower than the simulated values in Fig. 5.22(c). Then, one wonders about the possible reasons of the reduced transmission enhancement factors. The effect of the periodicity has been suggested as an explanation.

A possible cause of the mismatch between the simulated and measured transmission results is suggested to be stemming from the boundary conditions in the simulations. The aperture in Fig. 5.22(b) has been illuminated with a

plane wave in the simulations, which require the structure to be periodic in the transverse directions. Yet, in the experiments a single aperture was employed. Somehow, the transmission enhancement could be associated with the interference from the aperture array.

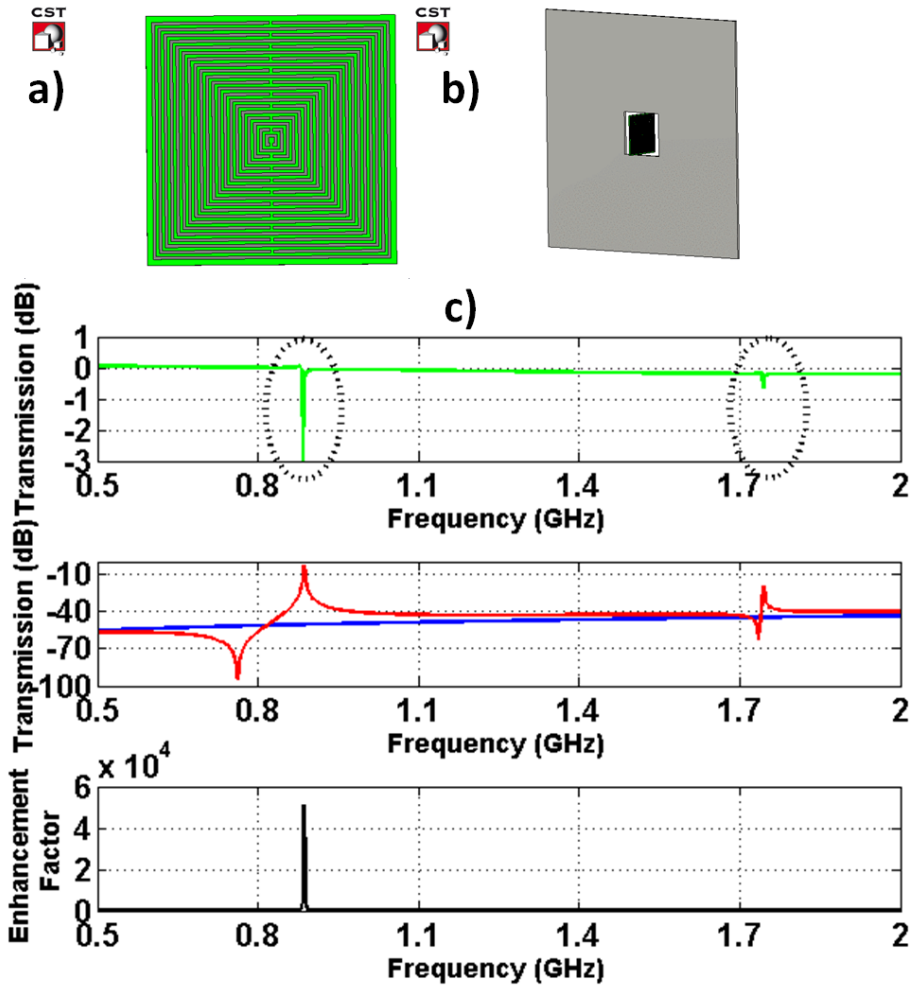

Figure 5.22: (a) MSRR configuration, (b) MSRR incorporated with the aperture. (c) Top subplot: Simulated transmission results for the MSRR, Middle subplot: Simulated transmission results for the single aperture (blue line) and the MSRR incorporated version (red line), Bottom subplot: The resulting transmission enhancement factor.

The SRR was inserted inside a subwavelength aperture and elevated transmission levels were observed in the end in Fig. 5.24. The aperture was surrounded by a waveguide which is made out of a perfect conductor. Thus,

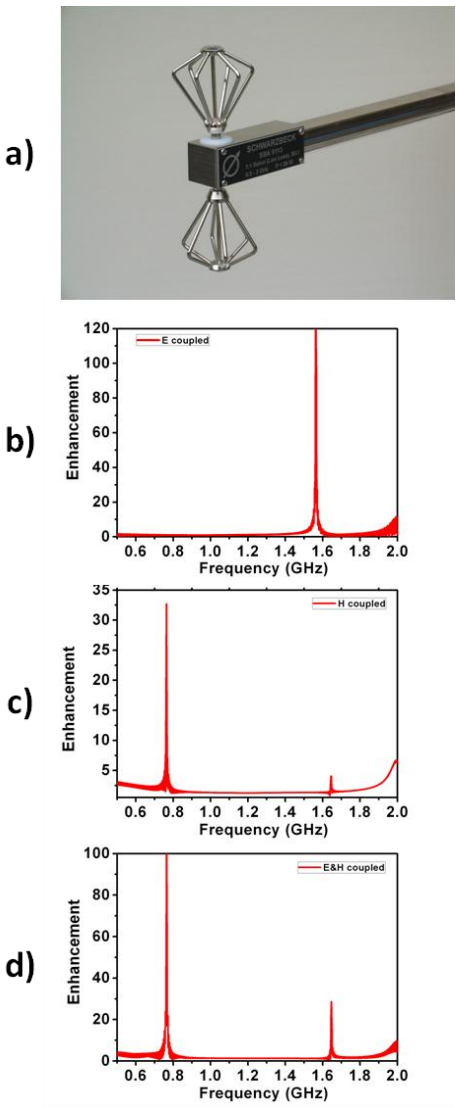

Figure 5.23: (a) The biconical antenna that we have employed in the experiments. Measured transmission enhancement results for (b) E-coupled, (c) H-coupled and (d) E&H-coupled cases. The coupling scenarios correspond to the excitation of the magnetic and electric dipoles of the MSRR, e.g. H-coupled (E-coupled) stands for the case in which only the magnetic (electric) dipole of the MSRR is excited.

image currents are formed on the walls of the conductor, which turned the transmission enhancement phenomenon into an improved transmission from quasi-periodic apertures. Furthermore, an array of subwavelength apertures incorporated with MSRRs had been shown to yield complete transmission. These studies strengthen the theory that is associated with the periodicity and underlines the effect of the interference and diffraction mechanisms in such arrays within the context of the transmission enhancement.

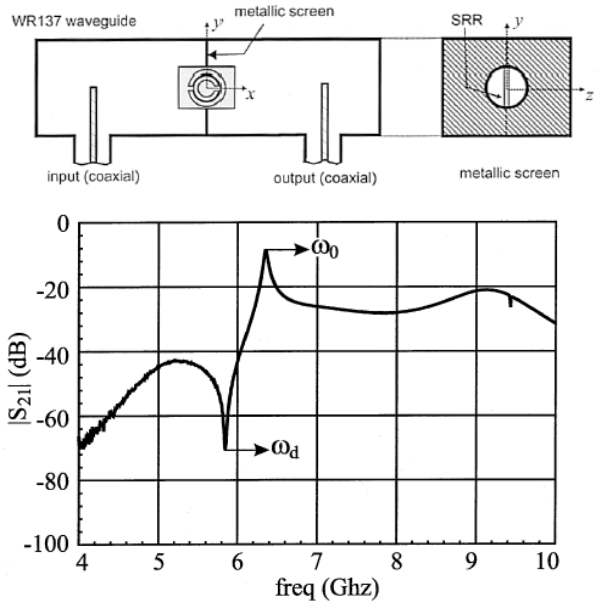

Figure 5.24: The SRR incorporated with a subwavelength hole inside a waveguide. The measured transmission results with the incorporation of the SRR. [40] Copyright © 2003, IEEE

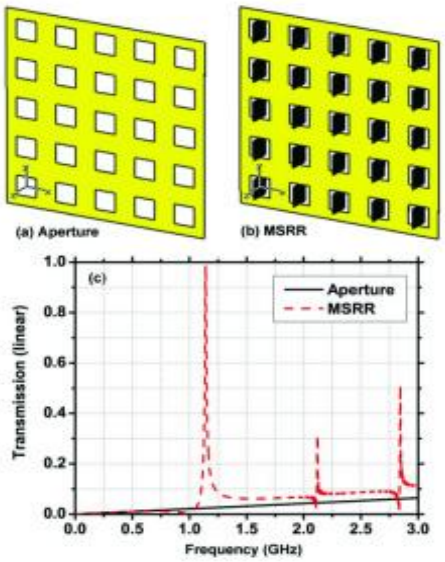

Figure 5.25: The periodic subwavelength arrays are incorporated with MSRRs. The overall configuration results in unity transmission. [74] This paper was published in **Optics Express** and is made available as an electronic reprint with the permission of OSA. The paper can be found at the following URL on the OSA website: **http://www.opticsinfobase.org/oe/abstract.cfm?uri=oe-17-8-5933** Systematic or multiple reproduction or distribution to multiple locations via electronic or other means is prohibited and is subject to penalties under law.

Nevertheless, a careful examination of the cases in the previous sections reveals that the transmission enhancement could also be observed for a single subwavlength aperture incorporated with a resonator. The problem did not necessarily have to involve periodic boundary conditions. The puzzling reduced transmission enhancement factors in the current MSRR study are attributed to the low directivity of the utilized antenna in the measurements. Horn antennas were not readily available at these long wavelengths and a biconical antenna that is exhibited in Fig. 5.23(a) is used instead. Subsequently, the biconical antenna does not offer the directivity figures of the horn antennas. The impinging fields illuminate the edges of the finite perfect conductor screen and secondary diffractions from these edges manifest themselves. As we have discussed in the previous section, these diffractions give rise to significantly enhanced transmission figures even for the single aperture and the transmission enhancement factors become much more reduced. We had discussed the importance of the coupling of the incoming electric fields to the resonator with a horn antenna in sec. 5.2. The problem happens to be even more difficult at these long wavelengths with the biconical antenna for the MSRR incorporated aperture problem. In summary, the problems that are investigated in the previous studies in Fig. 5.24 and 5.25 do not immediately match the current problem at hand in Fig. 5.22. The single MSRR problem can be fully treated as a single aperture problem with an attached resonator, just like the previous cases that are studied so far.

5.5 Transmission enhancement with aperture arrays and simultaneously opening left and right handed transmission channels in fishnet metamaterials

This section has been submitted as a paper to J. Nanophotonics and is expected to appear. Atilla Ozgur Cakmak, Evrim Colak and Ekmel Ozbay

Simultaneously opening transmission channels with left- and right-handed behavior for the stacked subwavelength apertures in fishnet metamaterials with hybrid unit lattices, Journal of Nanophotonics. 2012 (to appear). The movie files are expected to be available once the paper appears in the journal.

The problem of electromagnetic wave transmission through subwavelength apertures had been addressed in 1940s by H. Bethe [33]. Bethe had shown that the transmission efficiency scaled as $(r/\lambda)^4$ for a subwavelength opening with a radius of r in a perfectly conducting thin screen at the operational wavelength, λ. Accordingly, the poor transmission figures of the subwavelength apertures presented a challenge for the researchers in the last century. After the pioneering work of Ebbessen *et al*. [34] at the turn of the century, the scientific community has started to seek alternative methods to tackle this fundamental problem in physics with the aid of the periodically perforated plates. Several papers have aimed to understand the underlying physics of the Extraordinary Transmission (EOT) through subwavelength aperture arrays and slits [35,42,43,76,77]. It was initially thought that the surface plasmons were the main responsible contributors for the EOT at optical wavelengths. In the optical regime, the dielectric and metallic interfaces allowed the propagation of the surface plasmons by exploiting the dispersive characteristics of the metals. The demonstration of the similar phenomenon at microwave frequencies with perfect conductors was explained by making use of the designer surface plasmons [71]. On the other hand, separate research groups have emphasized the analytical models of the propagating modes through such subwavelength openings [93-95]. Hence, the EOT is associated with the coupling of the leaky surface waves at both sides of the metallic screen via the evanescent modes of the subwavelength apertures.

Independently, the quest for obtaining negative refraction has resulted in the realization of the artificial materials called metamaterials that are carefully engineered to yield negative refractive index. Fishnet-like periodic metallic configurations have been favored as a prospective metamaterial building block

by the researchers due to its planar manufacturability, reduced transmission losses and polarization insensitivity. Furthermore, the fishnet metamaterials overcame the magnetic saturation problems which were heavily suffered by alternative methodologies and this enabled the fishnet based configurations to operate at higher frequencies [96-97]. In ref. 98 and 99, it was pointed out that two seemingly distinct phenomena (EOT and negative refraction) manifest themselves in the same type of fishnet designs. Once the connection between EOT and negative refraction has been formed, the validity of the effective constitutive parameters extracted from the fishnet metamaterials has been discussed in ref. 100. It was shown in ref. 101 that the analyses based on the effective parameters are prone to failure for incident angles that are even slightly higher than the normal incidence. Consequently, the homogenized artificial material built out of the stacked fishnet metamaterials are treated in many cases as one dimensional metamaterials with transmission line models similar to the ones proposed in ref. 102.

Likewise, the electromagnetic wave propagation through stacked fishnet structures is investigated in the present study. Unlike the previous studies [103,104], a hybrid unit lattice along the propagation direction is considered in our structures. Consequently, the unit lattice is divided into sections filled with alternating dielectric media that are sandwiched by fishnet patterned metallic layers. Although it was not intended to study the electromagnetic wave propagation within the framework of the subwavelength apertures, hybridized unit lattices were also exploited in the recent studies and the *LC* resonator nature of the various similar fishnet configurations were utilized in order to define a metamaterial building block [105-109]. Another hybrid unit lattice fishnet structure was theoretically studied at optical wavelengths and the excited surface plasmons from one side were demonstrated to be coupled to the output surface with the aid of the virtual current loops on the metallic structures [110], where the relation between the transverse *H*-field and the induced current loop is similar to the cases studied in [105-109]. In our present work, we show for the first time the clear distinction between the hybridized unit lattice configurations

and the homogenous unit lattice designs under certain conditions. We examine the ratios of the volumes occupied by the dielectric materials in the unit lattice with a parametrical study and identify the coupling effects between each metallic fishnet pair. We report and emphasize that the hybridization of the unit lattice is not a minor modification on top of the counterparts with homogenous unit lattices. The Left-Handed (LH) transmission channel can be managed by the hybridization process. It is also shown that a cavity mode with Right-Handed (RH) characteristics is attainable with the same type of stacked fishnet layers. As a result, we show that LH and RH transmission channels can be opened after certain manipulations at frequency bands in which the former case (homogenous unit lattice) did not allow transmission. The designs are scaled up to operate at near-infrared region. The contribution of the plasmonic effects to the transmission is discussed in order to determine the governing phenomenon that is responsible for the subwavelength wave propagation. The simulations and transfer matrix method based discussions are backed up by experimental validations.

Firstly, we begin by introducing a homogenous unit lattice design shown in Fig. 5.26(a), which is similar to the topologies considered in ref. 103 and 104. The relevant dimensions are given in the figure caption. This is the first configuration that we are going to be investigating. The metallic plate is perforated with aperture arrays in the *x*-*y* plane. The metallic layers are separated by air spacings. The distance between each metal layer is fixed to the same value. Thus, such designs fall under the category of homogenous unit lattice configurations. The propagation direction is along *z*-axis. Then, the cutoff frequency of the individual square shaped holes is $f_c = c/2w \approx 21.42$ GHz. This is the lowest propagating mode, TE_{10} of the square aperture. However, we are confronted with transmission values reaching up to unity in Fig. 5.26(c), which spans a frequency region from 10 GHz up to 20 GHz. We carried out our simulations in CST Microwave Studio, which employs Finite Integration Technique (FIT). The dispersion graph is also plotted in Fig. 5.26(b) in order to distinguish the characteristics of the propagating modes, as in the case of ref.

111. Each mode is represented with a different color and the frequency band is partitioned into 4 regions. The 1st band approximately resides between 13 GHz and 14 GHz and has a negative slope, $\partial\omega/\partial k < 0$, which dictates that the transmission band has LH characteristics while ω is the angular frequency. In other words, the phase and group (the direction of the Poynting vector) velocities travel in opposite directions, as it is commonly encountered for metamaterials. The dispersion graph has been calculated for the infinitely extending periodic structure along the propagation direction. Then, the transmission results for the 5 layer case are expected to match the outputs of the dispersion graph.

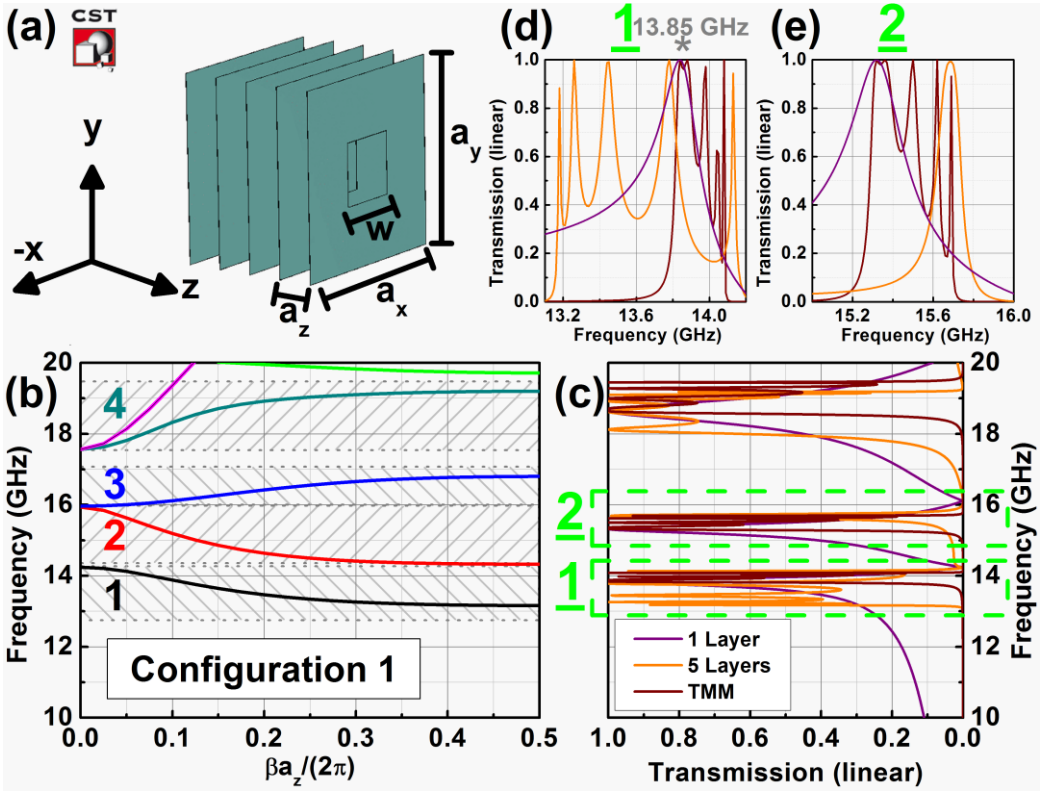

Figure 5.26: (a) Stacked metallic layers with subwavelength apertures. w=7 mm, a_{x1}=a_{y1}=21 mm, a_z=4 mm. (b) Dispersion diagram of the given configuration, (c) the transmission results for the single layer (purple line) and 5 layer structures (orange line). TMM results are also plotted in (c). (d) Zoomed version of the transmission window 1 in (c). (e) Zoomed version of the transmission window 2 in (c). The frequency domain is separated into distinct intervals as shown in the dispersion graph and these frequency bands are labeled numbers with the corresponding color of the propagating modes.

Two operational frequency windows from Fig. 5.26(c) have been zoomed for convenience and replotted in Fig. 5.26(d) and (e). The 1^{st} (2^{nd}) transmission window in Fig 1(d) (Fig. 5.26(e)) attends to the 1^{st} (2^{nd}) transmission band that is depicted in the dispersion graph in Fig. 5.26(b). The same color coding of the curves in Fig. 5.26(c) have been preserved for its zoomed versions in Fig. 5.26(d) and (e). The discrepancy between the transmission results of the single (purple line) and five layer (orange line) configurations is caused by the stacking of the alternating layers as far as the 1^{st} band is concerned in Fig. 5.26(d). The oscillatory behavior within the 1^{st} transmission band is a classical feature of the widening of the transmission band as soon as the additional layers are inserted. Five peaks have emerged inside the 1^{st} transmission band of the 5 layer structure due to the periodical arrangement [see Fig. 5.26(d)]. The effective parameters of the single layer structure have been retrieved and incorporated into the Transfer Matrix Method (TMM) formalism in order to identify the effects coming from the stacking of the metallic layers. Even though the TMM results fall short in the elucidation of the whole transmission spectrum, the general attributes can be immediately spotted. The TMM results (wine colored line) are illustrated in Fig. 5.26(c) as well. The ringing inside the 1^{st} transmission band can be more clearly noticed in the zoomed version of the 1^{st} frequency window [see Fig. 5.26(d)]. We again have five peaks. We specifically define the appearance of two main effects for the stacked layers. These effects are the stacking and coupling effects which come into the picture for structures with multiple layers TMM formalism offers a simple method to distinguish the effects coming from the layer stacking and the mutual coupling between the alternating layers. TMM makes use of the single unit lattice transmission parameters while calculating for the stacked case. Then, the results that are reproducible with the aid of the TMM formalism are recognized as the outcome of the periodic reflections along the propagation direction. These results that are comparable to the (transmission) simulation results for multiple layers exhibit the so called the stacking effect. On the other hand, the results that are not duplicated with the TMM formalism are ascribed to

the coupling effects between the stacked layers, i.e., coupling is effective between the layers and a simple stacking effect cannot explain the observed phenomena in the considered case. TMM results have been recurrently compared with single layer and 5 layer transmission results based on the FIT. Consequently, based on the TMM formalism we can conclude that the narrow EOT band for the single layer (purple line) in Fig. 5.26(d) is broadened and the oscillations in the transmission band come into play owing to the stacking of the alternating layers [compare single layer (purple line) and TMM results (wine colored line) in Fig. 5.26(d)]. Moreover, the flattening of the zero transmission regions with the additional layers is also associated with the stacking effect. Yet, further broadening of the EOT band is a result of the mutual coupling between the stacked resonators [compare 5 layer (orange line) and TMM results (wine colored line) again in Fig. 5.26(d)].

The sudden drop in the transmission levels between the 1st and 2nd transmission bands in Fig. 5.26(c) is ascribed to the Rayleigh Wood (RW) anomaly. The tangential components of the magnetic and electric fields are set to zero at the walls of the boundaries, which lie on the *y*-*z* and *x*-*z* planes, respectively. As a result, the unit lattice is in a way placed inside a larger waveguide that encapsulates the fishnet configuration and imposes periodicity on the *x*-*y* plane. The RW frequency of this relatively larger artificial waveguide is found as $f_{RW1} = c/a_{x1} \approx 14.29$ GHz, which coincides with the null in the transmission in Fig. 5.26(c). The EOT that is observed in ref. 103 and 104 have also been reported just below f_{RW}.

The remaining transmission bands extending beyond f_{RW} have been out of the main focus in ref. 103 and 104. Nevertheless, these bands have been portrayed in Fig. 5.26 in our present study in order to capture the main features of the rest of the transmission bands. The 2nd band possesses a negative slope as well. Although the detailed examination of these bands (2nd, 3rd and 4th transmission bands in Fig. 5.26(b) and (c)) are beyond the scope of this work, it is interesting to note that the ringings have not appeared in the FIT based

simulation results (orange line) for the 5 layer case in the 2nd band in Fig. 5.26(e), while the TMM formalism (wine colored line) predicted the recurrence of such peaks within the 2nd frequency window. Further simulations have been performed with 11 stacked layers (results are not shown here). The 2nd transmission band starts to disappear for thicker arrangements in the FIT based simulation results. The 3rd band is not efficiently coupled to the periodic arrangement and does not contribute effectively to the simulated transmission results, whilst multimode operation is apparent in the 4th band judging from the dispersion results in Fig. 5.26(b). Overall, only the first two bands have LH characteristics and the boundaries of the transmission bands agree well with the edges of the bands depicted in the dispersion results [see Fig. 5.26(b) and (c)].

The recipe for achieving EOT with LH transmission characteristics in subwavelength apertures is given in ref. 103 and 104 with the following relationship between the geometrical parameters, $r < \lambda_c < a < \lambda$, where r is the radius and λ_c is the cutoff wavelength of the subwavelength aperture. The lattice constant in the transverse direction is represented with a. The first configuration whose dimensions are given in the figure caption of Fig. 5.26 obeys these geometrical restrictions and an EOT band appears around 13.84 GHz. Conversely, the fishnet metallic layers with the same aperture size and air spacing along the propagation direction do not produce an EOT band as soon as the lattice constants in the transverse direction (a_{x2} and a_{y2}) are reduced to 14 mm, for which the recipe given above is not satisfied any longer. The regarding dispersion and transmission results are shown in Fig. 5.27 for the second configuration. The structure exhibits a RH transmission band between 18 GHz and 20 GHz. Actually, this dense configuration acts as a well-known dichroic filter. Several other features presented in the transmission results in Fig. 5.26 are now lost except for the effect that arises from the stacking of multiple layers. The transmission band undergoes a sharpening with respect to the single layer transmission results with the additional layers and similar oscillatory peaks can be noticed throughout the pass band [compare single (purple line) and 5 layer (orange line) transmission results in Fig. 5.27(b)]. It can be argued that the

TMM results (wine colored line) can closely pursue the simulation results up to 19 GHz, which is a signature of the reduced mutual coupling between the layers for this configuration. The discrepancies between the TMM results and the FIT based 5 layer transmission results are labeled after 19 GHz in Fig. 5.27(b). This frequency band marks the region where the retrieved effective parameters of the second configuration can no longer be used to consider the current transmission problem as that of a uniform material.

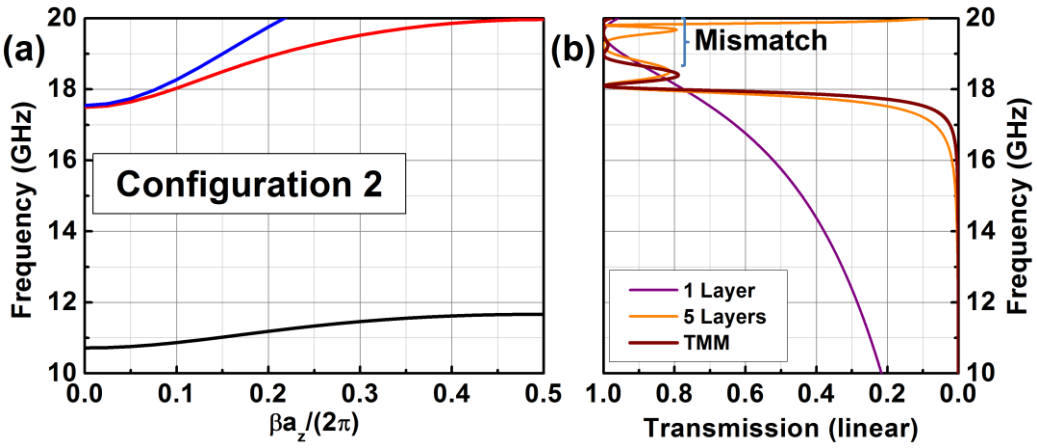

Figure 5.27: (a) Dispersion diagram for the configuration with w=7 mm, a_{x2}=a_{y2}=14 mm, a_z=4 mm. (b) The transmission results for the single layer (purple line), 5 layer structures (orange line) and the TMM results (wine colored line) based on the retrieved parameters for the single layer. The mismatch between the TMM and FIT based results at higher frequencies is labeled.

It is stated in ref. 95 that the EOT is a consequence of the interactions between the TEM modes of the artificial waveguide and the lowest order mode (TE_{10}) of the subwavelength aperture as long as $\beta \cdot a_{x,y} > \pi$ for square lattices, where β is the propagation constant of the impinging wave at normal incidence. Under such conditions, the fishnet composition brings higher diffraction orders as in the case of a diffraction grating and TE_{10} is perturbed. Even though this condition is satisfied for both configurations, the RW anomaly is shifted to $f_{RW2} = c/a_{x2} \approx 21.42$ GHz with the adjustment of the lattice constant in the transverse plane in the second configuration. Therefore, a cross coupling between the modes of the artificial waveguide and that of the subwavelength aperture turns out to be impossible around 14 GHz for the second configuration.

The symmetry of the problem allows only even-numbered modes. The lowest modes of the artificial waveguide are TE_{20} and TM_{02}. These modes are the main contributors of the transmission in the vicinity of the f_{RW} and their modal admittances for a thin metallic plate can be analytically expressed as $Y_{TE} = -Y_0\sqrt{1-(f_{RW}/f)^2}$ and $Y_{TM} = -Y_0\Big/\sqrt{1-(f_{RW}/f)^2}$, where Y_0 is the admittance of the electromagnetic wave in free space. It can be readily seen that when $f < f_{RW}$ Y_{TE} and Y_{TM} become inductive and capacitive, respectively. Hence, every plate can be considered as a shunt *LC* tank circuitry with a singularity at $f=f_{RW}$ and a total impedance $(Y_{TE}+Y_{TM})^{-1}$. At low frequencies the modal admittance of TE_{20} becomes dominant and the subwavelength aperture happens to be inductive. As we sweep the frequencies to higher values, the susceptance of the regarding modes' modal admittances cancel each other to generate the EOT. For frequency values higher than the EOT band TM_{02} governs the transmission phenomenon and the incoming electric field is totally reflected due to the singularity at f_{RW}. This creates a null in the transmission, which we have considered within the framework of the RW anomaly. The electric field components of the TM_{02} mode has the following form

$$\begin{aligned} E_x &\propto \sin(m\pi x/a_x)\sin(n\pi y/a_y) \\ E_y &\propto \cos(m\pi x/a_x)\cos(n\pi y/a_y) \\ E_z &\propto \cos(m\pi x/a_x)\sin(n\pi y/a_y), \end{aligned} \tag{5.1}$$

where the mode numbers are represented with *m* and *n*. The steady state field components are compared in Fig. 5.28 for both cases that are considered in Fig. 5.26 and 5.27. On the left hand side, we have the field components of the dense configuration (second configuration) ($a_{x2}=a_{y2}=14$ mm) at 18.15 GHz, whereas Fig. 5.28(d)-(f) depicts the conditions for the original case (first configuration) in Fig. 5.26 ($a_{x1}=a_{y1}=21$ mm) at 13.85 GHz. These frequency values are selected, because they reside inside the transmission bands of the considered configurations. As Eq. (5.1) implies, we do not have either *x* component of the electric field or *y* component of the magnetic field around the EOT band.

Furthermore, E_z does not possess a variation along x-axis but has an odd symmetry around x-axis in accordance with Eq. (5.1), as it is shown in the small inset picture in Fig. 5.28(e), where the fields are plotted on y-z plane. The red thick arrows in Fig. 5.28(a) and (d) indicate the direction of the phase velocity inside the structures while the launched field is propagating in $+z$ direction. The negative phase advance in Fig. 5.28(d) can be monitored in the linked movie file (Video 2) and can be compared with the case depicted in Fig. 5.28(a) (Video 1), for which the ordinary RH propagation is taking place. The most significant difference in the field distributions can be visualized in the z and x components of the electric and magnetic fields, respectively. The fields are in the propagation regime of the dichroic filter's pass band and travel with less harmony in Fig. 5.28(b) in comparison to the case given in Fig. 5.28(e). The fields are intensified at the edges of the stacked apertures owing to the diffractions at these discontinuities on the surface of the perfect conductor screens in Fig. 5.28(b) and naturally the fields are not scattered uniformly which results in comparably abrupt field distributions between the plates along the propagation direction. On the other hand, the phase information of the electric field is preserved in Fig. 5.28(e) and the fields are rather uniformly distributed between the plates, which enables one to define transmission line parameters along the propagation direction. The same situation is also true for the magnetic fields in Fig. 5.28(f). In contrast to the case in Fig. 5.28(c), the magnetic fields are uniformly shared. Thus, the air spacing between the metallic plates plays the role of the series distributed capacitors while the subwavelength holes are predominantly inductive in the vicinity of the EOT band, as it is discussed. Then, as a combination of the shunt inductors and series distributed capacitors the LH transmission line models are applicable to understand the wave propagation in Fig. 5.28(d)-(f) [98]. The differences of the calculated transmission spectra and the field maps in between the configurations 1 and 2 demonstrate the application of the geometrical recipe given above. The first configuration satisfies the recipe and exhibits uniform fields accompanied with

the EOT, whereas the geometric parameters of the second configuration does not obey the recipe.

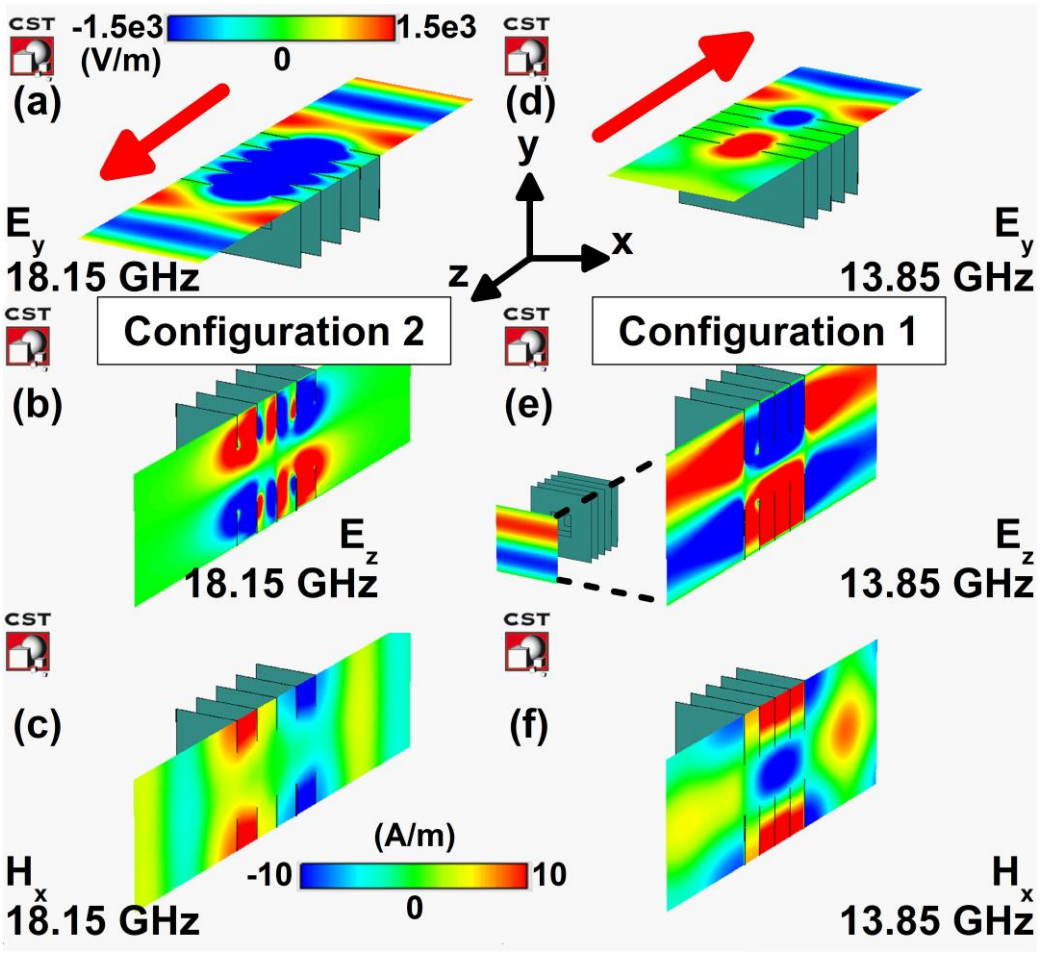

Figure 5.28: The steady state field distributions at 18.15 GHz for the dense configuration (a_{x2}=a_{y2}=14 mm) are given on the left hand side, whereas the field distributions at 13.85 GHz are shown on right hand side for the first configuration (a_{x1}=a_{y1}=21 mm). CST Microwave Studio offers the field maps in the form of $|E_{y,z}|\times e^{-j\phi}$ and $|H_x|\times e^{-j\phi}$ for electric and magnetic fields, respectively. The given plots are the captured scenes at an instantaneous phase, ϕ. E_y on the x-z cut plane in (a) and (d) (Video 1 and 2), E_z on the y-z cut plane in (b) and (e) and H_x on the y-z cut plane in (c) and (f). The arrows in (a) and (b) indicate the directions of the phase velocities. (Video 1, MPEG, 825 KB; Video 2, MPEG, 826 KB)

It is possible to create a cavity mode for the dense configuration (a_{x2}=a_{y2}=14 mm) following the formalism in ref. 112. Once a single layer is taken away from the middle of the 5 layer system, a Fabry-Perot (FP) based cavity is formed. The field distribution and the new transmission spectrum are

shown in Fig. 5.29(a) and (b), respectively. The defect peak appears at 15.4 GHz with a *Q* factor of 128 [inspect the peak value of blue line in Fig. 5.29(b)]. This frequency band originally did not allow transmission, as it was depicted in Fig. 5.27(b). The symmetric field distributions and the intensified fields inside the cavity are evident in Fig. 5.29(a), which are the signatures of the FP based cavity modes. Moreover, the reflectivity of the 2 layer structures can be estimated to be $r \times e^{-j\psi}$ for every frequency. As soon as these 2 layer structures are assumed to be the mirrors of the FP cavity, the following condition has to be satisfied to sustain the constructive interference mechanism inside the cavity structure

$$\Phi = \beta \cdot L + \psi = m \cdot \pi, \tag{5.2}$$

where L is the cavity length, it is equal to a_z in our case and m is an integer. The extracted reflectivity values for 2 layer mirrors have been used in order to find out the frequency at which Eq. (5.2) is satisfied. The results are plotted in green color in Fig. 5.29(b). The integer solution of the m parameter (m=0) coincides with the defect transmission peak that is illustrated on the same graph, which removes the doubts about the origins of the opened RH transmission channel. Additionally, the TMM formalism is exploited in order to determine the defect peak in the transmission spectrum (red line). The same retrieved parameters that are used to reproduce the transmission spectrum in Fig. 5.27(b) have been utilized. Subsequently, the defect peak is detected at 15.54 GHz, which points to a 0.14 GHz shift with respect to the simulation results for the 5 layer case. Figure 5.29(b) once again shows that the TMM formalism can be adapted till 19 GHz in correlation with the outputs of Fig. 5.27(b). TMM results suggest an enhanced *Q* factor for the cavity mode. The broadening in the defect transmission peak is associated with the mutual coupling between the alternating metallic layers.

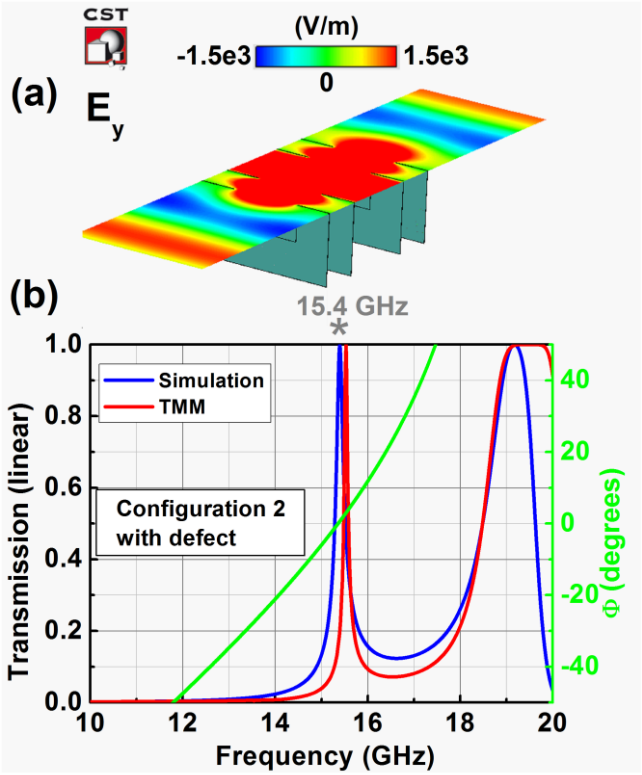

Figure 5.29: (a) The steady state electric field distribution at 15.4 GHz, (b) transmission results for 5 layer structure (blue line) and TMM results (red line) together with the phase value (Φ) calculated from Eq. (5.2) for every frequency value (green line).

In this section, we will discuss how to achieve a LH transmission channel from the dense fishnet configuration (second configuration) and we will emphasize the differences in the underlying physics with regard to the EOT accompanied by the evanescent TEM modes of the artificial waveguide which was considered in the previous sections. We can break the homogeneity of the unit lattice spacing along the propagation direction by inserting a second dielectric (other than air) at the back of the fishnet layers. Teflon is selected as the substrate due to its low losses in the microwave regime. The permittivity of Teflon substrate is ε=2.16 and it has a loss tangent of tan(δ)=0.005 and a thickness of t=1 mm. The transmission spectrum of the dielectric loaded second configuration is shown in Fig. 5.30(b) for 5 layers. As it can also be inspected from the regarding dispersion curves in Fig. 5.30(a), the pass band of the dichroic filter is shifted towards lower frequencies with the addition of the dielectric medium [compare Fig. 5.30(b) and Fig. 5.27(b)]. This is nothing but a

red shift which occurs by the addition of the higher permittivity into the unit lattice. The bandwidth of the pass band is intact and it is again around 2 GHz. The impedance matching at the fishnet surface has been altered and the transmission values have decreased to 90% rather than the unity transmission as in the case of the former situation without the dielectric loading.

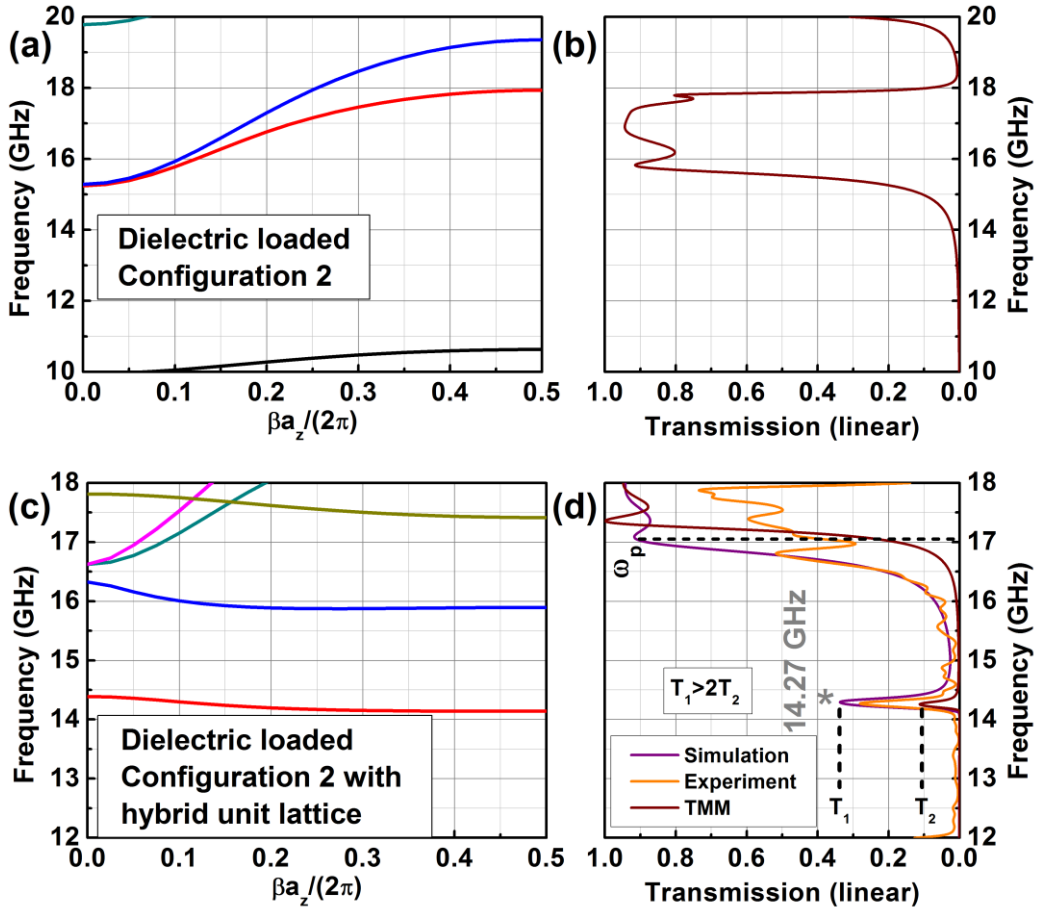

Figure 5.30: (a) Dispersion diagram for the dense configuration with dielectric loading and (b) the calculated transmission spectrum for the same sample. (c) Dispersion diagram when a second metallic grid is stacked at the back of the dielectric medium and (d) the calculated (purple line), measured (orange line) and TMM formalism based (wine colored line) transmission results.

The LH transmission band is opened as soon as we stack a second fishnet metallic layer at the back side of the dielectric medium, as it can be seen in Fig. 5.30(d). Thus, the LH transmission band is observed around 14.27 GHz, again for 5 layers. The negative slope of the corresponding band (red colored band) in Fig. 5.30(c) reveals that the transmission peak observed at this

particular frequency is a LH transmission channel. The RH pass band of the dichroic filter is reshifted back to higher frequencies. Actually, the starting edge of the RH pass band can be regarded as the plasma frequency (ω_p) of the metallic grid [71]. The effective permittivity of this metallic grid is below zero and thereby does not allow transmission before the plasma frequency. The addition of the second metallic grid at the back of the dielectric increased the density of metals in the unit volume and resulted in the increase of the plasma frequency of the system in Fig. 5.30(d) in comparison to Fig. 5.30(b). The experiments have also been carried out for the same configuration with conventional 12.4-18 GHz horn antennas that are connected to HP 8720B network analyzer. The experimental results (orange line) are in good agreement with the numerical expectations (purple line). TMM results based on the single layer configuration predict a relatively lower transmission at the LH band and a higher plasma frequency value. This point will be revisited in the following sections.

The field maps and surface currents at 14.27 GHz (left hand side) and 18.15 GHz (right hand side) are presented in Fig. 5.31 for the hybrid configuration. These are two frequencies selected from the relevant LH and RH transmission bands, respectively. The attached movie files (Video 3 and 4) once again depict the reverse and forward phase propagation inside the stacked units in Fig. 5.31(a) and (e), correspondingly. The field components at 18.15 GHz bear resemblance to the field distributions that are already considered for the previous cases in Fig. 5.28(a)-(c). Nevertheless, the surface currents and field components for the LH transmission band have striking differences. The antiparallel surface currents on each side of the metallic fishnet patterns are shown in Fig. 5.31(b) from a side view on the *y*-*z* plane. These circulating currents enable us to define a virtual current loop. On the other hand, the surface currents turn out to be parallel to each other for the RH transmission band in Fig. 5.31(f). The existence of such a virtual current loop amplifies the circulated magnetic fields (H_x) inside the dielectric medium, as shown in Fig. 5.31(c). The electric field component (E_z) in Fig. 5.31(d) is also mainly confined to the

dielectric medium, whereas the propagating field components are primarily localized in the air spacings rather than the substrate for the RH transmission band. Consequently, the hybridized unit lattice boils down to a series of stacked coupled resonators within the LH transmission band.

Then, we can define quasi-static inductance and capacitance formulae for these resonators. The formalism is presented in ref. 109. The capacitance value can be easily expressed by taking into account the parallel plate capacitance formation between the faces of the metallic patterns $C \propto \varepsilon a_x a_y / t$. The detailed calculation of the total inductance is also given in ref. 109. A careful examination of the surface currents in Fig. 5.31(b) shows that there are two inductors parallel to each other. These inductors that are modeled for the walls of the aperture carry the surface currents in two different directions, as designated by the arrows in Fig. 5.31(b) and the surface currents meet at the square shaped nodes. Then, the total inductance becomes $(L_1 \,||\, L_2)^{-1}$, where $L_1 \propto (a_{y2} - w)t / a_{x2}$ and $L_2 \propto wt / (a_{x2} - w)$. Finally, the overall resonance frequency can be found as:

$$f_R = \frac{1}{2\pi\sqrt{LC}} \propto \sqrt{\frac{1}{\varepsilon} \times \left(\frac{1}{a_{y2}(a_{y2} - w)} + \frac{(a_{x2} - w)}{a_{x2} a_{y2} w}\right)}\,. \qquad (5.3)$$

The reported resonance frequencies are 21 GHz and 13 GHz in ref. 105 and 109 for the fishnet designs with the relevant dimensions, respectively. By making use of the proportionality in Eq. (5.3), our envisaged resonance frequency turns out to be 14.22 GHz, which is a very close value to the mentioned peak location of the LH band.

These quasi-static definitions for the modeled inductance and capacitance of the subwavelength aperture can only hold for the resonator type structures. The proportionality does not hold for the first configuration (w=7 mm, a_{x1}=a_{y1}=21 mm) even if its unit lattice is hybridized along the propagation direction, as we will be discussing in the proceeding parts. Another drawback of the simple resonator formulation in Eq. (5.3) is the insensitivity of the resonance

frequency to the thickness of the inserted dielectric slab. We cannot indefinitely increase the substrate thickness. The ratio of the volumes occupied in the unit lattice for the two dielectric layers plays a key role in the coupling mechanisms for the transmission through the stacked layers. In summary, Eq. (5.3) offers a first order approximation of the resonance frequency. Yet, the restrictions on the surface currents and field maps have to be considered carefully before blindly adapting the resonance formalism. Accordingly, we are obliged to take into account the higher order evanescent modes and their dynamic modal expressions (as a function of frequency) while analyzing the EOT band in the homogenous lattice configuration.

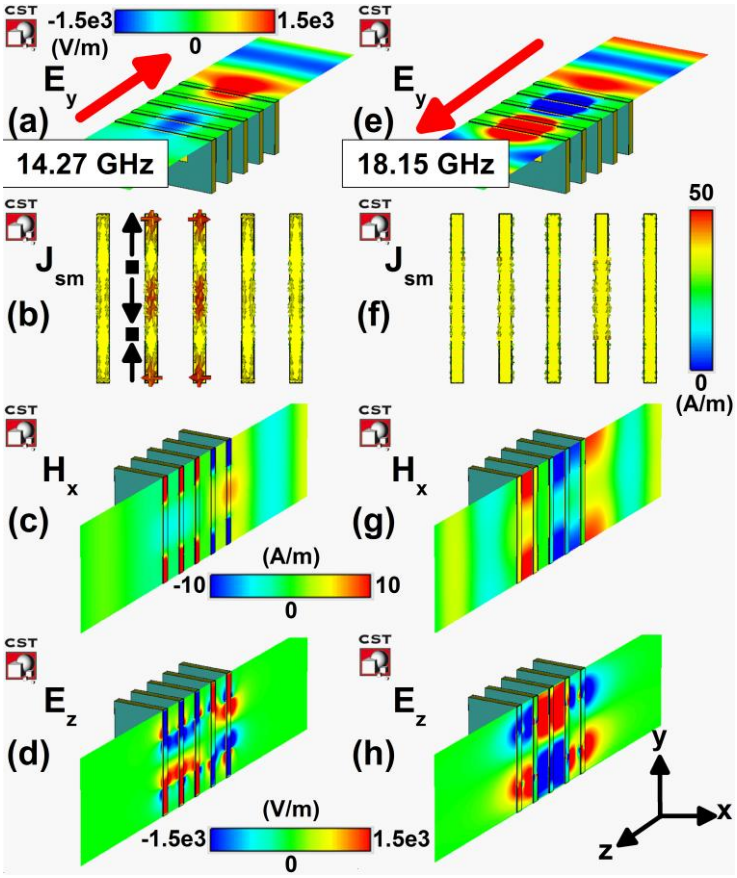

Figure 5.31: The steady state field and surface current distributions for the dense configuration. The electric field component (E_y) is plotted at (a) 14.27 GHz (Video 3) and (e) 18.15 GHz (Video 4). The arrows in (a) and (b) indicate the directions of the phase velocities. The surface currents calculated at (b) 14.27 GHz and (f) 18.15 GHz. The directions of the surface currents in (b) is highlighted with additional arrows for the designated side. The magnetic field component (H_x) is plotted at (c) 14.27 GHz and (g) 18.15 GHz. The electric field component (E_z) is plotted at (c) 14.27 GHz and (g) 18.15 GHz. (Video 3, MPEG, 829 KB; Video 4, MPEG, 835 KB)

So far, two transmission bands with LH characteristics have appeared in the dispersion graphs of Fig. 5.26(b) and Fig. 5.30(c). In this part, we will be focusing on the aspects that govern the LH transmission for the considered configurations with different lattice constants on the transversal plane. First of all, it can be noticed that the stacking effect did not yield ringing inside the LH transmission band for the hybrid configuration in Fig. 5.30(d). The reason is the confinement of the propagating fields inside the dielectric substrate. The dense configuration is a series of stacked resonators and the transmission phenomenon is dominated by the coupling between these resonator structures. Hence, the peak value of the LH transmission band computed by the FIT (T_1) is elevated by more than 2 times in comparison to the TMM results (T_2) owing to this particular coupling mechanism, as it is shown again in Fig. 5.30(d). On the other hand, the transmission figures already reach unity or close to perfect transmission with the TMM formalism, as it can be seen in the 1st zoomed window in Fig. 5.26(d). Thus, the coupling effect has not altered the transmission magnitudes for the first configuration.

Figure 5.32(a) depicts the scenario when the first configuration's unit lattice is hybridized along the propagation direction by following the same steps applied to the dense case which is studied in Fig. 5.30. In fact, ref. 113-115 dealt with the situations when the subwavelength aperture is loaded with a dielectric medium. The dielectric loading was realized in order to match the impedance at the surfaces of the fishnet samples. The dielectric slab suppressed the RW anomaly and dramatically changed the transmission spectrum by reducing the maximum attainable transmission value in rectangular lattices (rectangular lattice is achieved in the transversal plane by selecting $a_x \neq a_y$) depending on the thickness and permittivity of the substrate. On the contrary, in our case the transmission spectrum is not fundamentally modified with the addition of the dielectric substrate, except for the slight shifts [compare blue and green lines in Fig. 5.30(a)].

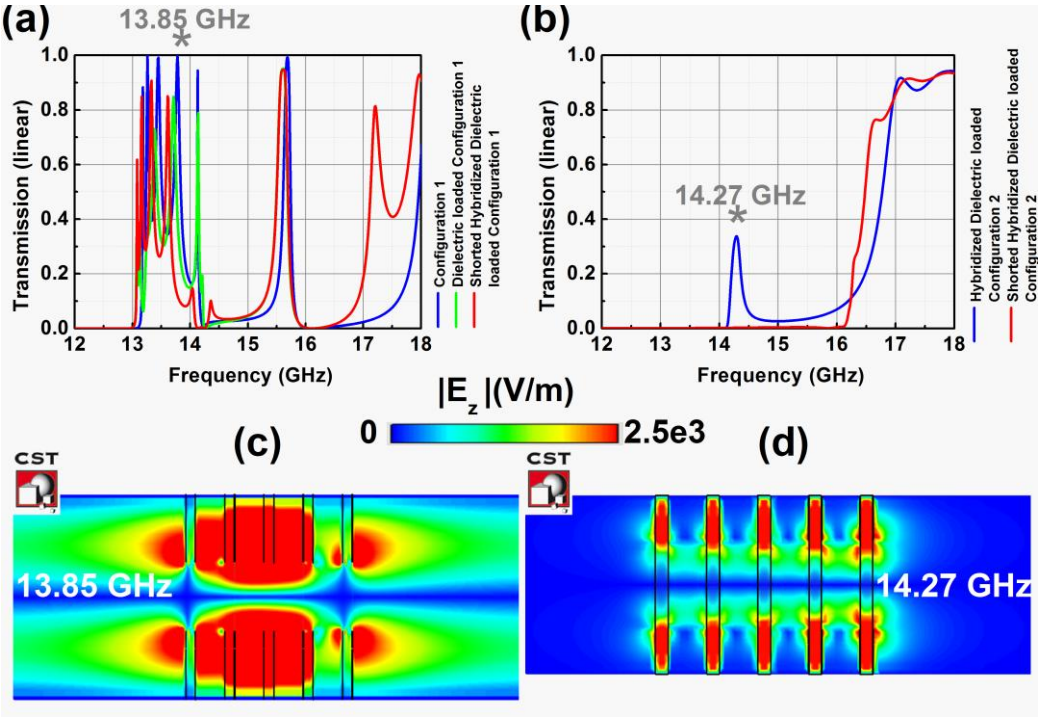

Figure 5.32: Transmission spectrum for (a) the first configuration (blue line), the dielectric substrate loaded first configuration (green line) and the shorted hybridized original configuration (red line). Transmission spectrum for the (b) dense configuration (blue line) and its shorted version (red line). The field maps for the average electric field component (E_z) for (c) the original case at 13.85 GHz and (d) the dense configuration at 14.27 GHz. The average field values extracted from CST Microwave Studio are different from the previously given steady state field maps. Unlike the previous cases which were plotted at a random phase value, the fields undergo an averaging within the time period of the incoming wave.

We used a finite array in our experiments and carried out the measurements in the near field zone. Hence, we were still able to witness the LH transmission band for the dense configuration regardless of the distance between the transmitter and receiver antennas. In contrast, the performance of the measurements were severely degraded for finite arrays and the researchers were compelled to work in the Fraunhofer zone since the evanescent modes interacting with the subwavelength aperture array had long propagation lengths for the first configuration [115]. The resonator nature of the dense configuration removed the necessity of long measurement distances in the experiments for our structure.

The most critical distinction appears when we short both of the hybrid fishnet configurations, i.e., the hybrid forms of the configurations 1 and 2. The metal patterns on both surfaces are shorted with small metallic inclusions at the corners of the layers. The dielectric medium between the metallic layers is still present. Then, the virtual current loop is also broken with the shortening of the fishnet structures on both surfaces of the metallic layers. The LH transmission band automatically disappears, as it is shown in Fig. 5.32(b) [compare red and blue colored lines], whereas the shortening has little effect on the transmission spectrum for the first configuration which is depicted in Fig. 5.26(a), being hybridized. The LH EOT band persistently stays in Fig. 5.32(a) (red line) for the first configuration, since the EOT phenomenon is governed by the modal expressions of the higher diffraction orders. The average electric field components (E_z) are illustrated in Fig. 5.32(c) and (d) at 13.85 GHz and 14.27 GHz, respectively. The specific location of these frequencies are indicated in Fig. 5.32(a) and (b). It should be once again stressed that E_z is rather uniformly shared between the metallic plates, which results in a transmission line with distributed capacitances for the first configuration. Alternatively, E_z is localized to the substrate regions because of the resonance nature of the stacked formations in the dense case in Fig. 5.32(d).

The interaction between the electric fields of the localized resonators is evident in Fig. 5.32(d). The field maps for three different lattice spacing values have also been illustrated in Fig. 5.33 for the hybrid dielectric loaded second configuration. The corresponding transmission spectra and dispersion plots in Fig. 5.34 have to be evaluated along with the field maps. As it was pointed out earlier, the coupling between the stacked resonators cause an increase in the transmission figures of the LH band. This is clearly seen in Fig. 5.34(b) when we compare the transmission levels for a_z=2 mm (red line) and a_z=6 mm (blue line). The former situation transmits slightly more than 3 times at the LH band ($T_3 > 3T_4$). Approximately, the same amount of ratios between the peak levels of the considered two cases can be spotted in Fig. 5.34(a) as a result of the TMM

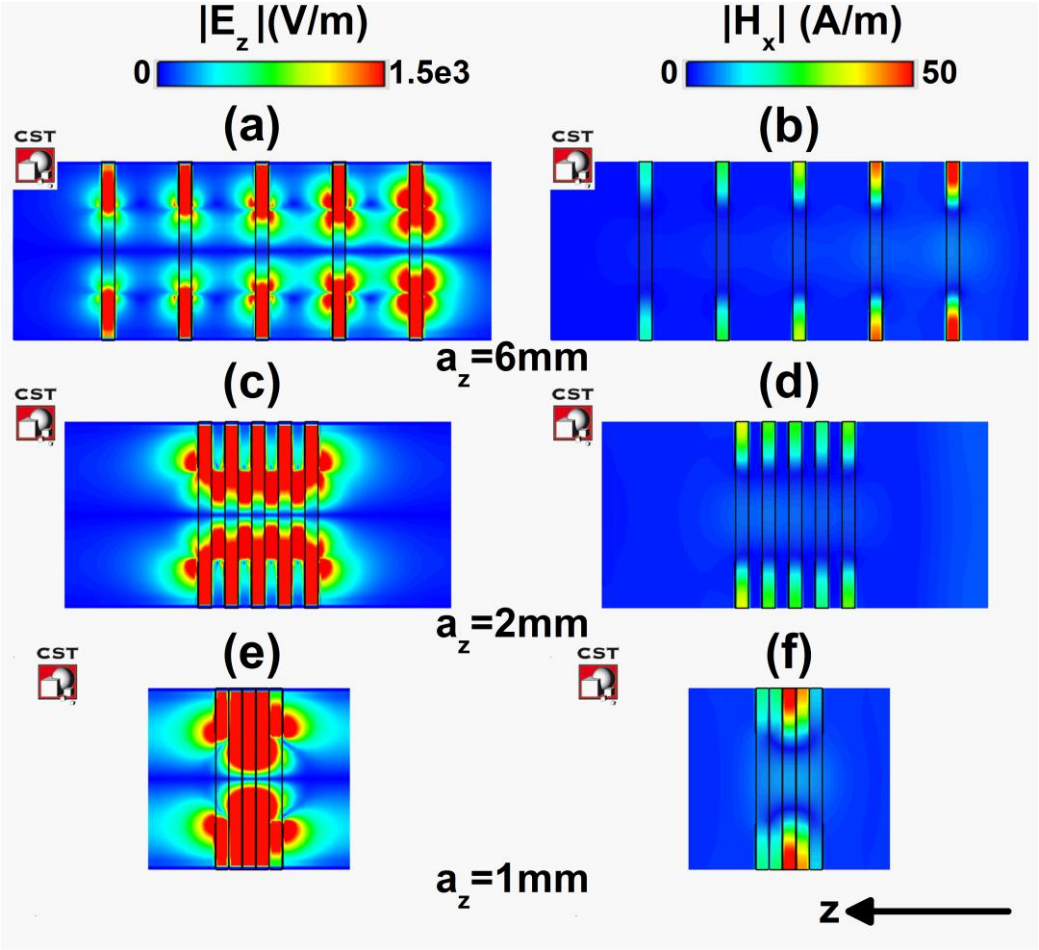

Figure 5. 33: The field maps for the average electric field component (E_z) and the magnetic field component (H_x) are given on the left hand side and right hand side of the figures, respectively. (a) E_z and (b) H_x at 14.27 GHz for a_z=6 mm. (c) E_z and (d) H_x at 14.38 GHz for a_z=2 mm. (e) E_z and (f) H_x at 13.68 GHz for a_z=1 mm.

formalism ($T_5 > 3T_6$). However, there is also another 2 times difference between the TMM and 5 layer simulations, which is a direct outcome of the coupling effect ($T_3 > 2T_5$, $T_4 > 2T_6$). Under these conditions, the retrieved effective parameters for the single layer may not be suitable for the representation of the stacked case and a convergence in the effective parameters cannot be met rapidly even at normal incidence, as ref. 116 also suggests. The LH transmission peak resides at 14.21 GHz, 14.27 GHz and 14.38 GHz for a_z=6 mm, a_z=4 mm and a_z=2 mm cases, respectively. TMM results are very close to these values. The LH transmission peak experiences a blue shift due to the compact stacking of the alternating layers. The LH peak is located at 14.19 GHz for the single

layer transmission results (not shown here). The relatively isolated case, a_z=6 mm, produces the closest results to the single layer transmission. The blue shift in the LH peak can be ascribed to the decrease in the average magnetic flux in each layer when the interspacing distance gets smaller. Figure 5.33 portrays the magnetic field values inside the resonator structures for different a_z. The magnetic fields are equally shared between the resonators when a_z=2 mm in Fig. 5.33(d) whereas the intensified magnetic fields are encapsulated by the first layers in Fig. 5.33(b). Hence, the average magnetic field value is higher for a_z=6 mm and thereby the inductance of the resonator system is large in comparison to a_z=2 mm. The larger inductances yield LH transmission bands at lower frequencies. The bandwidth of the LH transmission band is also increased for decreasing inter separation distance, as it can be noticed both in Fig. 5.34(a) and (b). In other words, the LH band gets broader when we decrease the fraction of the volume occupied by air spacings. TMM results also confirm this broadening effect. Accordingly, we can conclude that the broadening is a consequence of the smaller inter-separation distance between the alternating layers, i.e., the stacking effect and it is not a direct consequence of the coupling between the fishnet resonators.

The plasma frequency is lowered down with larger separation distances between unit lattices in Fig. 5.34(b). This is consistent with our earlier claims concerning the change in the metal density per unit volume. Nevertheless, the retrieved effective parameters are liable to errors while describing the transmission spectrum for the RH band, as it can be noticed when the RH transmission bands in Fig. 5.34(a) and (b) are compared. Therefore, the TMM results can be mainly utilized to understand the transmission effects around the LH band. Lastly, the configuration with air[2] is also simulated and the results are plotted (purple line) in Fig. 5.34(b). The unit lattice is still partitioned into two sections and this configuration can still be considered to possess a hybrid form.

[2]Teflon substrate between the facing fishnet patterns is replaced with air as the dielectric loading.

However, the LH transmission peak cannot be spotted. The dielectric medium that lies inside the resonator plays a key role in tuning the resonance frequency, as Eq. (5.3) implies. For air, the LH transmission band cannot be adjusted to lower frequencies and only the RH band is witnessed in the transmission spectrum.

As the last scenario, the case without the air spacing is investigated. Then the unit lattice separation becomes[3] a_z=1 mm. For such an arrangement, the unit lattice is again homogenous. The transmission results (green line) are given in Fig. 5.34(b). The formerly pronounced LH band is degenerated. Now, the plasma frequency is shifted down and the RH transmission band is merged with the LH transmission band. The propagation of the electromagnetic beam is more complicated, because a multimode behavior accompanies this configuration unlike the rest of the considered hybrid cases. The dispersion graph in Fig. 5.34(c) predicts both LH and RH propagation at the same frequency, since the regarding bands are merged. TMM results can predict the degeneration of the modes for a_z=1 mm case up to some extent [notice the double humps inside the LH transmission band and the elevated transmission figures between the LH and RH bands]. The degeneration which occurs as a_z decreases can also be deduced from the illustrated electric field maps in Fig. 5.33(a), (c) and (e). The coupling mechanism between the resonators is the most efficient when a_z=2 mm. The intensified fields are distributed symmetrically for each layer. The fields are less interacting in Fig. 5.33(a) for a_z=6 mm and the intensified field amplitudes drop along the propagation direction due to the accompanying losses with each stacked layer. Then again, the multimode operation produces an asymmetrical field map for a_z=1 mm case in Fig. 5.33(e) owing to the interference of the modes with LH and RH characteristics. After all, the re-homogenized configuration (a_z=1 mm case) does not accurately yield a well-established LH transmission band.

[3]Actually, $a_z = t + 2t_{metal}$ and t=1 mm, t_{metal}=20 μm. a_z is rounded to 1 mm.

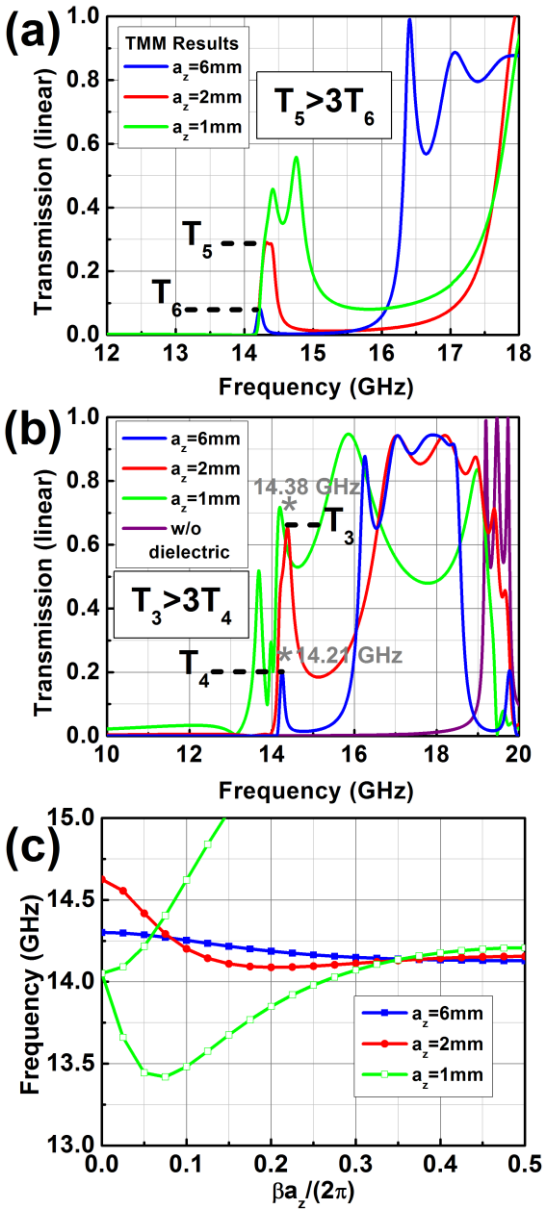

Figure 5.34: (a) Transmission spectrum based on TMM results for a_z=6 mm (blue line), a_z=2 mm (red line) and a_z=1 mm (green line). (b) Calculated transmission spectrum for a_z=6 mm (blue line), a_z=2 mm (red line), a_z=1 mm (green line) and the case without dielectric loading (purple line). (c) Dispersion diagram for a_z=6 mm (blue line), a_z=2 mm (red line) and a_z=1 mm (green line).

Both of these bands can be functionalized at the same time when the hybrid unit lattice is adapted and a defect is formed by removing one layer in the middle. The transmission results for this case are portrayed in Fig. 5.35. The experimental validation of the relevant transmission channels are also plotted on the same graph (blue line). It is verified that there is a good connection between

the experimental and numerical results. The slight shift in the frequency domain is attributed to both the differences in the material properties that are provided by the supplier in contrast to the modeled structure in the simulations (e.g., the permittivity of Teflon substrate, spatial shifts between the metallic patterns on both faces) and difficulties in the manual alignment of the stacked layers. The mentioned spatial shift of the metallic patterns on both faces of the same layer also causes unavoidable misalignment in the experiments. The effect of the oblique incidence that mimics our misalignment problem in our experiments had severely caused non-idealities in ref. 117. The oblique incidence had triggered shifts in the frequency spectrum owing to the anisotropic nature of the stacked fishnet layers. Previous studies with hybrid unit lattice configurations had also shown that even a small tilting of the incident wave could destroy the LH transmission band while pulling down the transmission values [106]. Regardless of these secondary factors, two transmission channels with LH and RH propagation characteristics have been observed for the same sample configuration at previously impenetrable frequency values.

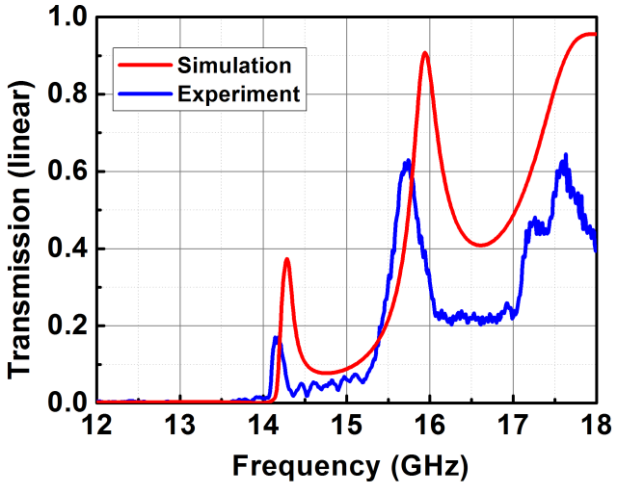

Figure 5.35: The demonstration of the simultaneous opening of the LH and RH transmission channels on the transmission spectrum. Numerical results are plotted in red color and measurement results are depicted in blue color.

The considered structures can be designed at optical wavelengths owing to the scalability of Maxwell's equations. Likewise, Fig. 5.36 studies the arrangements at the optical regime. Two main configurations that have been

investigated throughout the present study are modeled in Fig. 5.36(a) and (b). The metal thickness, t_m=40 nm for both structures. The subwavelength aperture arrays have a square opening whose side w=500 nm, again for both cases in Fig. 5.36(a) and (b). Such apertures can be patterned with the aid of the electron beam or focused ion beam lithography techniques on the metal layers. However, the metallic patterns can no longer remain suspended in air. The volume that is occupied by the air spacing in the microwave configurations is replaced with the glass substrate (ε_1=2.25) with a thickness, t_1=170 nm.

The configuration in Fig. 5.36(a) is the homogenous unit lattice design whose transmission was governed by the higher order diffractions. The lattice constants on the transversal plane, $a_{x3}=a_{y3}$=1500 nm. The regarding transmission spectrum is given in Fig. 5.36(c). First, the simulations are carried out with Aluminum (blue line) and Silver (red line) metallic layers. Then, the effect of the glass substrate is studied. Drude models have been adapted for the metals, where ω_{pAl}=2.4x10^{16} rad/sn, ω_{pAg}=1.325x10^{16} rad/sn, ν_{cAl}=175 THz, ν_{cAg}=130 THz and $\varepsilon_{\infty Al}=\varepsilon_{\infty Ag}$=1. The classical features of the transmission spectrum dominated by diffractions are evident in Fig. 5.36(c). The corresponding RW anomaly should be located at $\lambda_{RW}=a_{x3}=a_{y3}$=1500 nm for the case where perfect metal layers are involved. The effect of the plasmons causes a slight red shift in the RW anomaly. Since Al has a higher plasma frequency, this red shift is less pronounced in comparison to the case with Ag [compare blue and red colored lines around 1.5 μm]. In accordance with the earlier claims and designs in the microwave domain, the EOT emerges just after the RW anomaly (i.e., at a longer wavelength) and transmission values exceeding 70% can be detected. As in the case of the studied microwave examples, the glass substrate underneath the metallic pattern caused another red shift in the EOT (green line). This shift in the EOT wavelength is calculated to be as high as 0.18 μm [compare the peak transmission levels of blue and green colored lines].

Conversely, the transmission spectrum is given for the hybrid unit lattice configuration in Fig. 5.36(d). A secondary dielectric medium is sandwiched

between two metallic patterns, as in the case of the microwave designs. The thickness of the second dielectric medium is chosen to be t_2=150 nm. The sandwiched dielectric layer must have a higher dielectric permittivity than the glass substrate. Accordingly, SiC and Al_2O_3 with ε_{SiC}=6.708, ε_{Al2O3}=3.132 at near-infrared wavelengths have been utilized. The stacked layers are shown in Fig. 5.36(b). The first metallic pattern (Al or Ag) is deposited on top of the glass substrate, whereas the second metallic pattern at the topmost is developed on top of the secondary dielectric medium (SiC or Al_2O_3) with a relatively high index.

The LH transmission peaks appear at wavelengths designated by the color-coded arrows in Fig. 5.36(d). Then again, the LH transmission peak could also be achieved theoretically with the employment of a Perfect Electric Conductor (PEC) at these wavelengths, too [see purple colored line in Fig. 5.36(d)]. We do not have a PEC at optical wavelengths and the metals have dispersive characteristics, but the presence of the LH peak with a purely theoretical PEC material at near-infrared frequencies shows that the observed peak is not invoked by the special features of the Surface Plasmon Polaritons (SPP). Instead, the observed LH peak with the PEC material is the manifestation of the same physics that is investigated in details at microwave frequencies. Correspondingly, we can use the proportionality offered by Eq. (5.3) in order to determine the specific location of the LH peak on the wavelength axis,

$$\lambda_{PEC} = \frac{c}{f_{GHz}} \times \frac{\sqrt{\frac{1}{\varepsilon_{teflon}} \times \left(\frac{1}{a_{y2}(a_{y2}-w)} + \frac{(a_{x2}-w_{GHz})}{a_{x2}a_{y2}w_{GHz}}\right)}}{\sqrt{\frac{1}{\varepsilon_{SiC}} \times \left(\frac{1}{a_{y4}(a_{y4}-w)} + \frac{(a_{x4}-w)}{a_{x4}a_{y4}w}\right)}}, \qquad (5.4)$$

where c is the speed of light and the relevant dimensions of the hybrid configuration (second configuration) are used. Once we carry out the algebra and insert the values f_{GHz}=14.27 GHz, ε_{teflon}=2.16, a_{x2}=a_{y2}=14 mm and w_{GHz}=7 mm, the envisaged LH peak turns out to be at λ_{PEC}=2.646 μm when SiC layer is sandwiched between the metallic patterns. On the other hand, the LH transmission peak is located at 2.658 μm in Fig. 5.36(d) with the PEC [see the

purple arrow], which is a very close value to the estimated one by using the simple *LC* resonator.

Then again, the real metals have to be taken into account at optical wavelengths. The excited SPP once again causes a red shift with respect to the PEC case. The detected LH peaks are located at 2.845 μm and 3.037 μm for Al and Ag, respectively. The LH bands are followed by the RH bands in Fig. 5.36(d) regardless of the material selections. The PEC case yields the highest transmission figures within the LH transmission band. Particularly, the transmission peak value is increased more than 3 times with the PEC configuration in contrast to the real metal applications. From this point of view, the plasmonic effects have a degrading effect on the performance characteristics. In summary, the entailed plasmonic effects in the resonator structure cause a red shift in the LH transmission peak, decrease the detected peak values of the LH bands, broadens the LH bands and tend to destroy the valley between the LH and RH bands by tending to merge the initially separated LH and RH bands. Aluminum turns out to be a better candidate than the silver option as a metal deposition layer if we compare the LH transmission bands in Fig. 5.36(d). The LH band is more isolated from the RH band when Al is selected due to the higher plasma frequency of Al. Then, a multimode operation with the concurrent LH and RH phase advance which was observed at the microwave frequencies with the collapse of the RH band into the LH band [see a_z=1 mm case in Fig. 5.34(b)] is less likely to happen even with the employment of different dielectric media. Nevertheless, the difficulties of the microfabrication related to Al manufacturing have to be resolved with alternative methods.

Following the formalism in ref. 110, the location of the LH transmission bands can be roughly estimated. The conservation of the momentum at the metallic interface dictates that

$$k_{SPP} = k_0 \sin(\phi) + \frac{2\pi}{a_{x4}} m + \frac{2\pi}{a_{y4}} n, \tag{5.5}$$

where k_{SPP} is the wave vector of the SPP (in scalar format), k_0 is the wave vector of the incident light, ϕ is the incident angle, m and n are the integer values. For the incoming light at normal incident (ϕ =0), the mode with the largest wavelength (m=1 and n=0 or m=0 and n=1) is located at $\lambda_{SPP}=a_{x4}=a_{y4}$. This value is equal to the formerly introduced f_{RW} for this design. On the other hand, at large wavelengths (as in our case) the following formula can be used to find the relation between λ_{SPP} and λ_0

$$\lambda_0 = \lambda_{SPP}\sqrt{\varepsilon_2 \times \frac{t_2 + 2\coth(\omega_p t_m / c)/(\omega_p / c)}{t_2}}\,. \qquad (5.6)$$

The sandwiched dielectric medium is SiC and the peak values of transmission are calculated to occur at 2.798 μm and 2.976 μm for Al and Ag, respectively. These are good estimates of the simulated LH transmission band peak locations. The peak is calculated at 1.912 μm by using Eq. (5.6) when Al_2O_3 is used as the secondary dielectric layer instead of SiC. The corresponding peak value is found at 1.958 μm (green arrow) in the simulated transmission spectrum in Fig. 5.36(d). The peak values of the simulation results with SiC (2.845 μm) and Al_2O_3 (1.958 μm) secondary dielectric layers do scale with $\sqrt{\varepsilon_{SiC}/\varepsilon_{Al_2O_3}}$ in accordance with both Eq. (5.3) and (6) for the designs employing Al metallic layers. The LH band is not as separated from the RH band as in the case of the SiC choice for the Al_2O_3 case in Fig. 5.36(d). Yet, the LH band provides higher transmission at smaller wavelengths for the Al_2O_3 case.

Finally, the electric field maps (E_z) for the 5 layer hybrid configuration at specific wavelengths that are chosen from the RH and LH bands are depicted in Fig. 5.36(e) and (f), respectively. The negative phase advance can be monitored in the linked movie file (Video 5) while the incident light is approaching to the periodic arrangement from the right hand side. It can be immediately noticed that the fields are localized in the higher permittivity layers due to the resonator nature of the stacked layers in Fig. 5.36(f), whereas the fields do not have a specific preference at the RH band in Fig. 5.36(e). This is a very similar

situation that we had encountered in the previous sections for the LH transmission band at microwave frequencies (e.g., Fig. 5.31(d) and Fig. 5.32(d)).

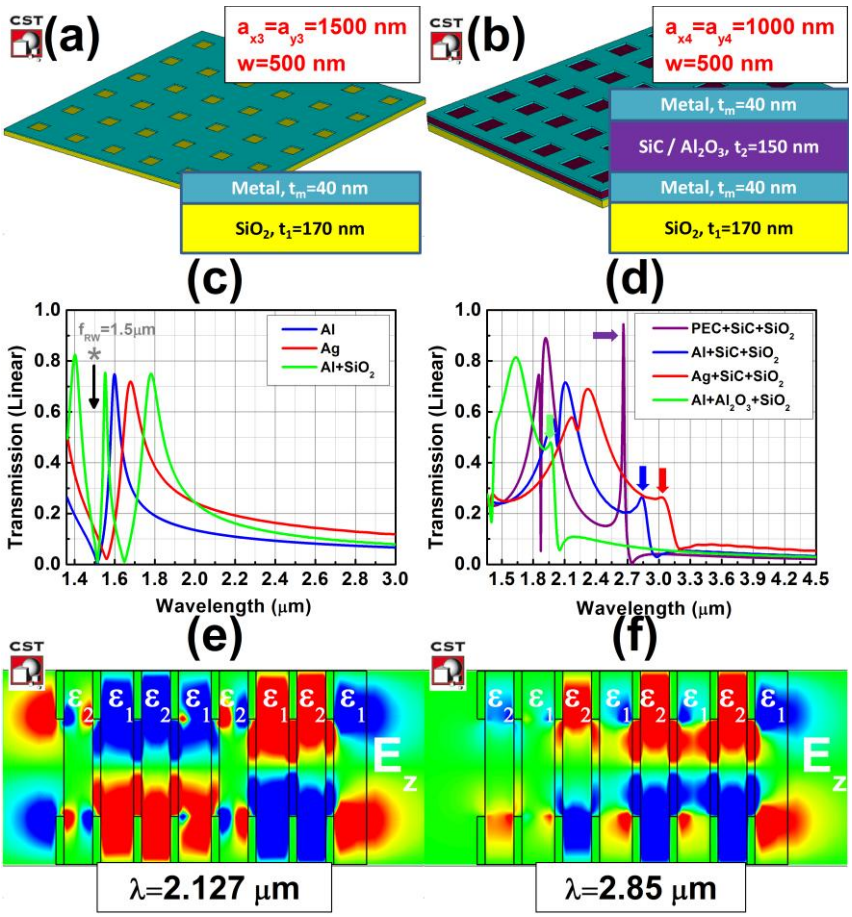

Figure 5.36: The considered configurations at optical wavelengths. (a) The first configuration and (b) the hybrid configuration. The regarding deposited layers are shown in the figure insets with their relevant thicknesses. (c) The transmission spectrum for the first configuration with Al (blue line), Ag (red line). Aluminum pattern is developed on top of the glass substrate (green line). (d) The transmission spectrum for the second configuration with different metallic and sandwiched dielectric layers, PEC+SiC (purple line), Al+SiC (blue line), Ag+SiC (red line), Al+Al_2O_3 (green line). The color-coded arrows indicate the peak points of the LH transmission bands, which are located at λ_{PEC}=2.658 μm, λ_{Al+SiC}=2.845 μm, λ_{Ag+SiC}=3.037 μm, $\lambda_{Al+Al2O3}$=1.958 μm. The steady state field distributions (E_z) for the 5 layer hybrid structure at (e) 2.127 μm and (f) 2.85 μm (Video 5). The incoming field is launched from the right hand side. (Video 5, MPEG, 828 KB)

As a summary, we have started our analyses with two similar configurations with subwavelength apertures. One of the configurations had a relatively dense periodic arrangement in comparison to the other. We have first simulated the transmission spectrum for these designs with homogenous unit

lattices. The variations of the so called first configuration were already inspected in the literature under the framework of the EOT through subwavelength apertures. The physical origins of the emerging EOT band have been discussed by borrowing the established theoretical background from the literature and it is shown that the EOT band is achieved with the aid of the higher diffraction orders of the artificial waveguide surrounding the unit lattice. Conversely, the dense configuration did not yield a LH transmission band in its original form.

First, a RH transmission band that is based on the FP cavity formation is examined for the dense configuration. Later on, a LH transmission band is also realized by hybridizing the spatial distribution of the unit lattice along the propagation direction. The underlying physics of this type of wave propagation is studied with the help of the field maps and dispersion diagrams. It has been shown that the electromagnetic wave propagation inside the LH transmission band for the dense configuration is governed by the stacked resonators that are coupled to each other. Thus, the origins of the LH band are different in each case (for the first and second configurations). We conclude that the EOT does not heavily rely on the spatial arrangement of the unit lattice (for a fixed value of the unit lattice) as long as the contribution of the higher diffraction orders is guaranteed for the first configuration, whereas the fractions of the volume occupied by different dielectric media play a key factor for the hybridized unit lattice orientations of the dense configuration. The losses are mainly due to the included dielectric loading. Yet, the discussed coupling and stacking effects might be advantageous or disadvantageous depending on the application field. A designer has to carefully take into consideration the aforementioned effects before building a device with the hybrid configurations. As a final point, the issue of the scalability of these configurations to the optical wavelengths has been addressed. The LH transmission band has been demonstrated in the near-infrared region. In general, the plasmonic effects have been shown to degrade the performance of the stacked resonators. Nevertheless, the LH band based on the resonator nature of the hybrid unit lattice is still achievable at optical wavelengths once the fabrication difficulties are overcome. Different dielectric

and metallic layers have been simulated and their influence on the performance characteristics has been discussed.

The hybrid unit lattices can be exploited as the building blocks to construct a LH prism, a demultiplexer or a lens that could potentially be used at optical frequencies. Some of the promising devices that offer and introduce interesting new features have already been scaled up to optical wavelengths by the metamaterial research community once the researchers fully explained the underlying physical mechanisms and shed light on the possible performance related deteriorating factors, as we have attempted to do throughout the present study.

5.6 Negative refraction and wedge experiments with periodically arranged subwavelength aperture arrays

This section is going to be submitted as a paper to Journal of Applied Physics.

The hybrid lattice fishnet configuration that is studied in the previous section can be utilized in different application fields. A wavelength demultiplexer is one of such exemplary application fields. In this part of the thesis, the hybrid aperture array will be functionalized in order to construct a wedge shaped arrangement. The wedge arrangement is shown to negatively refract the incoming waves. The dispersive characteristic of the prism which is built out of these fishnet unit lattices enables the application of the proposed design in communication circuits.

First of all, the hybrid fishnet configuration has been subject to the retrieval analysis which offered the retrieved parameters for the single layer of periodic apertures in Fig. 5.37. The numerical and experimental transmission results have been utilized in the retrieval analyses. The results of Fig. 5.37 demonstrate the agreement between the two. The plasmon resonance of the

overall structure is well separated from the magnetic resonance in comparison to the cutwire retrieval results in Sec. 3. Hence, the fishnet arrangement offers a better impedance match and an isolation of the LH and RH transmission bands with regards to the cutwire based designs. Consequently, the negative refraction is expected to occur around 14 GHz, when $\mathrm{Re}[\varepsilon] < 0$ and $\mathrm{Re}[\mu] < 0$ simultaneously.

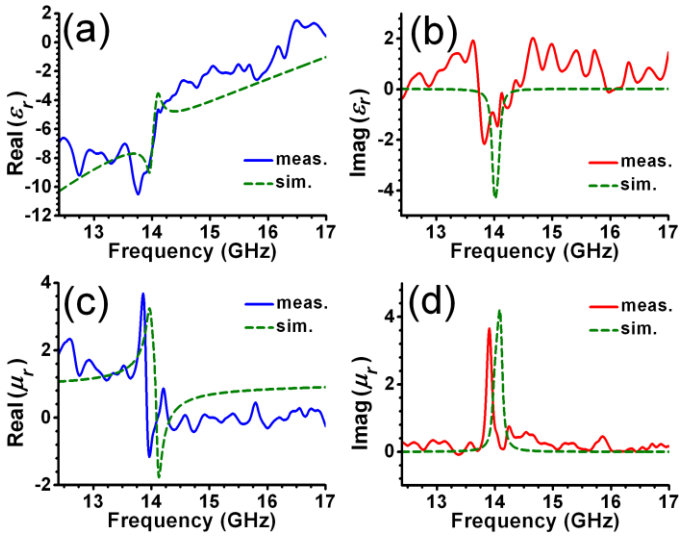

Figure 5.37: Retrieved results for a single fishnet layer (a) real part of the effective permittivity (simulations – green dashed line and measurements – blue line), (b) imaginary part of the effective permittivity (simulations – green dashed line and measurements – red line), (c) real part of the effective permeability (simulations – green dashed line and measurements – blue line)and (d) imaginary part of the effective permeability (simulations – green dashed line and measurements – red line).

The dispersion graphs have been given in Fig. 5.38 for different values of the lattice spacing along the propagation direction. The negative and positive slopes of the dispersion graphs are spotted in the regarding LH and RH bands. Then, the LH band, as it was already discussed in the previous sections, possesses negative phase velocity. The stacked fishnet configuration presents a 1-D metamaterial along the direction of propagation. The retrieved results are used to extract the propagation constant of the 1-D TL in the same manner that was shown in the previous theoretical chapters. Explicitly, one can write $k = \omega\sqrt{\mu\varepsilon}$. Then, the extracted value for k is plotted together with the

dispersion graph in Fig. 5.38(c). The agreement between two methods confirms that the retrieved constitutive parameters can be safely used to describe the electromagnetic response of the 1-D fishnet system along the propagation direction.

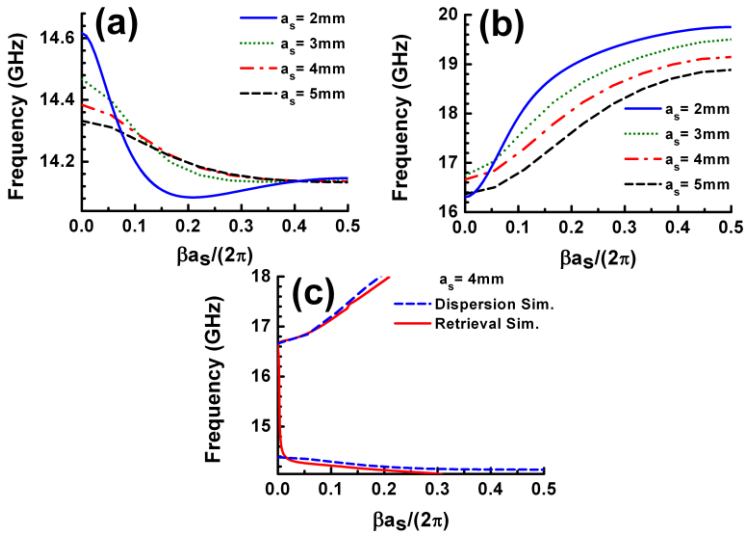

Figure 5.38: Dispersion graphs around (a) LH, (b) RH band for different lattice spacing values along the propagation direction. (c) The retrieved values (red line) are used to extract the wavevector value. The dispersion results are plotted together (dashed blue line).

Later on, these layers of fishnet metamaterials have been stacked to form a wedge shaped arrangement, as shown in Fig. 5.39(a). The wedge has been formed by 19 unit lattices in the transverse plane and lateral direction. The incident beam comes from a horn antenna with a certain angle. The validity of the homogenization of such a wedge arrangement has been checked in the experiments and simulations by making use of a scanning at the output side [see Fig. 5.39(b)].

The experimental results in Fig. 5.40 shows the negatively refracted waves around the LH transmission band for different a_s values. In contrast, the fields are positively refracted inside the RH transmission band in Fig. 5.41. The origin of the negative and positive refractions has been sought in order to clear away the doubts. The negative and positive refractions have been shown to be a result of the zero order transmission rather than a higher order diffraction. The

contribution of the higher order diffractions have been found out to be impossible within the frequency region of interest. The yellow zone in which the diffraction orders are expected to be detected at the observation angles is free of the contribution from the higher orders in Fig. 5.42.

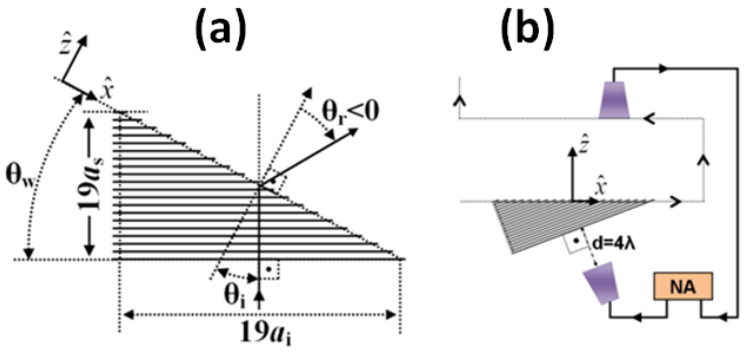

Figure 5.39: (a) The wedge arrangement with 19 periods both in lateral and transverse direction. (b) The scanning experiments.

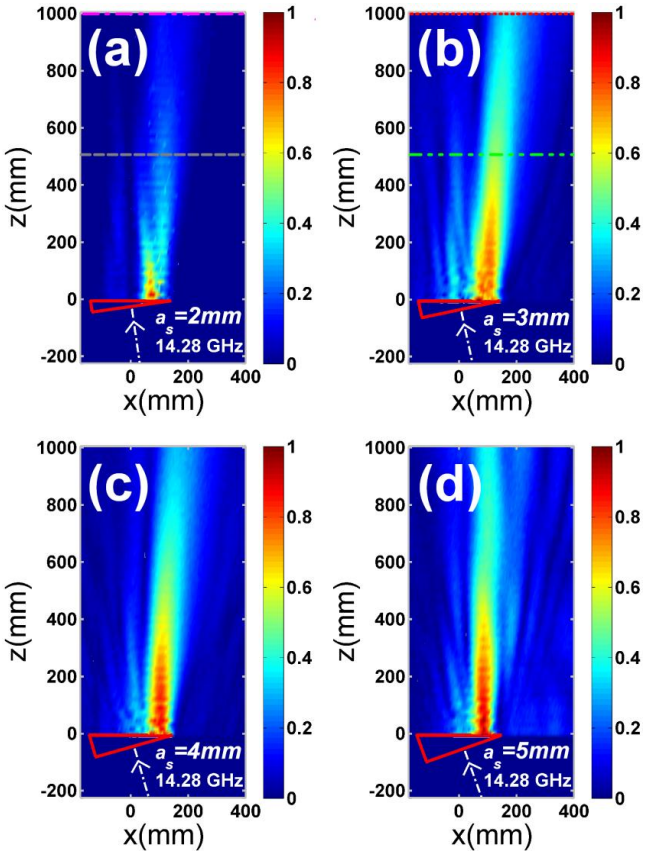

Figure 5.40: The experimental results of the scanning experiments at 14.28 GHz for (a) a_s=2 mm, (b) a_s=3 mm, (c) a_s=4 mm and (d) a_s=5 mm.

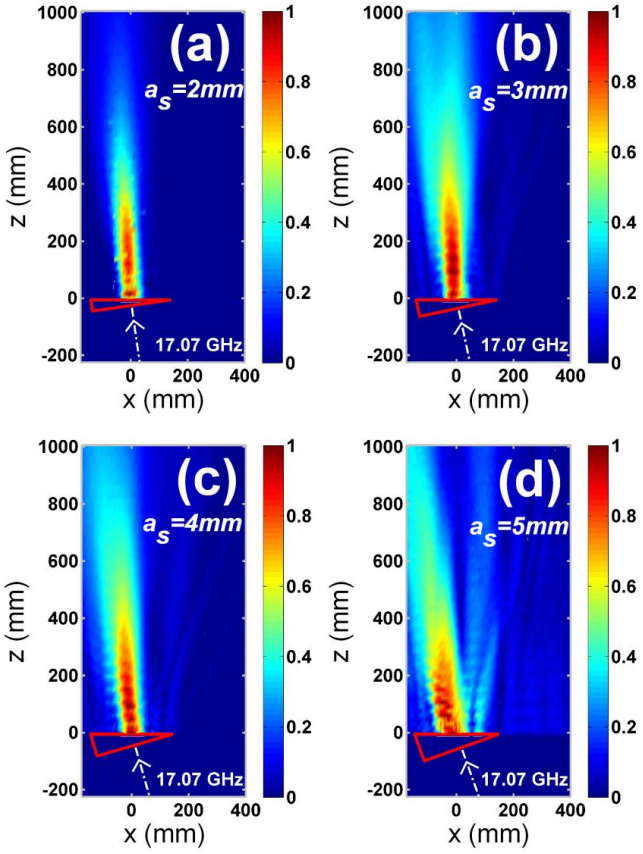

Figure 5.41: The experimental results of the scanning experiments at 17.07 GHz for (a) a_s=2 mm, (b) a_s=3 mm, (c) a_s=4 mm and (d) a_s=5 mm.

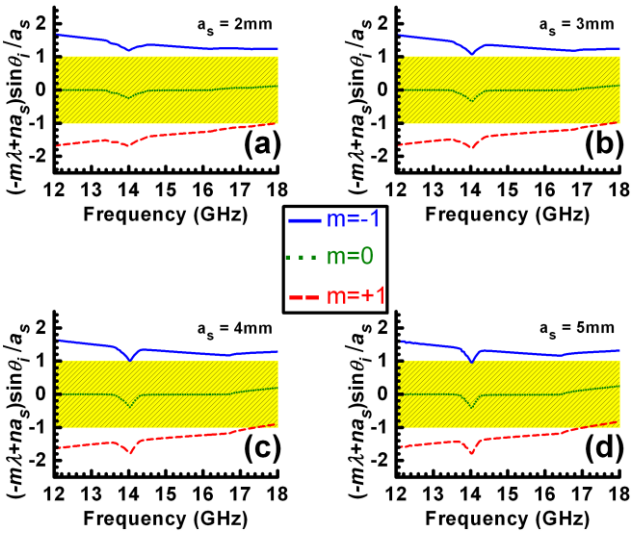

Figure 5.42: Checking for the contribution from the higher order diffraction terms. The yellow zone shows the solution to the real valued problem of the observation angles. The blue and red lines show the contribution from the higher order (+1 and -1) diffractions. The green line is the zero order transmission solution. The routine has been done for (a) a_s=2 mm, (b) a_s=3 mm, (c) a_s=4 mm and (d) a_s=5 mm.

The regarding parametrical analyses for a_s has been made in order to understand the performance characteristics of such a prism made out of the metamaterials. The following important points have been verified.

(i) The losses are evident in the wedge shaped configuration (especially around the LH transmission band) such that the outgoing beam exits the wedge at a location close to the tip of the wedge in Fig. 5.40. Yet, this is in agreement with the loss values (the imaginary parts of the retrieved parameters) in Fig. 5.37.

(ii) Then, the question arises. The higher order diffractions are not the cause of the negative refraction, but it was discussed in the literature [118,119] that the asymmetric effective aperture formation at the exit surface of the wedge configuration could be the origin of the negative refraction. However, in our case we witness that the wave can propagate more inside the wedge with smaller a_s values. The coupling between the stacked layers is more efficient with smaller a_s [see the relevant discussions in the previous section]. This is the main reason of the losses. The negative slope in the dispersion graphs assure that we are really observing the negative refraction phenomenon rather than a loss oriented transmission peculiarity.

(iii) The Snell's law is still applicable in our current example up to some extent. A direct homogenization cannot be done to the wedge configuration. First of all, it should be noted that the investigated structure is a composition of the 1-D TLs with different thicknesses at normal incidence. Each column of the wedge configuration bears a relatively different propagation constant. These propagation constants of the cascaded 1-D TLs vary the most when a_s is small. Hence, the overall structure does not work properly for a_s=2 mm case in Fig. 5.40(a). The elevated coupling effect between the lattices along the propagation direction for a_s=2 mm drastically alters the propagation constant for different thicknesses.

(iv) Once the precautions in item (iii) have been taken, the validity of the homogenization process for the wedge structure is examined in Fig. 5.43. The

retrieved parameters for 8-3 layers (a_s=2-5 mm) coincide well with the extracted refractive index value from Snell's law.

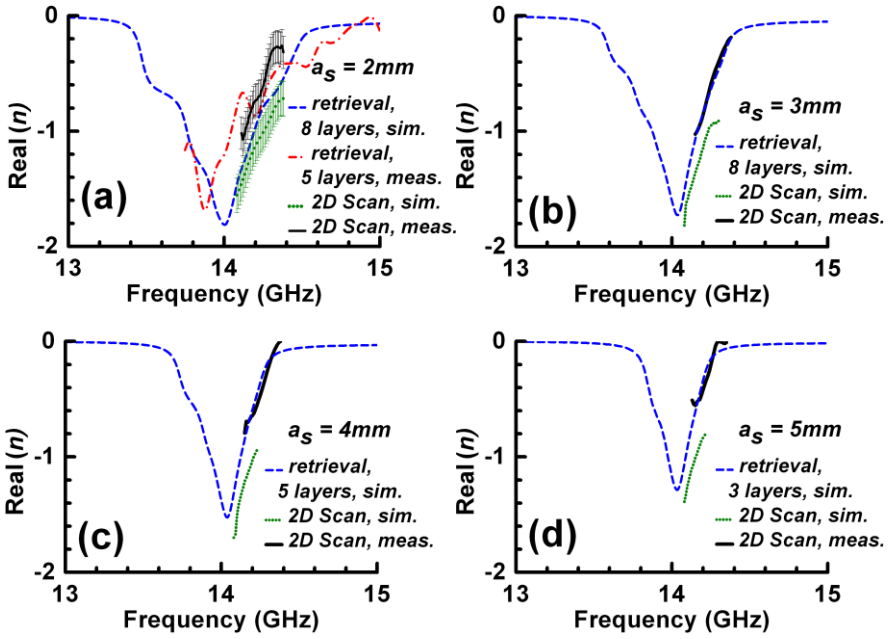

Figure 5.43: Retrieved real part of the refractive index (dashed blue line), extracted refractive index from 2-D simulation (dotted green line), measurements (solid black line) for (a) a_s=2 mm, (b) a_s=3 mm, (c) a_s=4 mm and (d) a_s=5 mm. The retrieved real part of the refractive index from a 5 layer measurement has also been given in (a). The retrieval parameters for 8 layers, 8 layers, 5 layers and 3 layers have been given for a_s=2 mm, a_s=3 mm, a_s=4 mm and a_s=5 mm, respectively. Because the main portion of the exiting beam has been considered. The beam exits from higher columns when a_s is small.

Chapter 6

Fundamentals of Photonic Crystals

This chapter aims to investigate the fundamentals of Photonic Crystals (PCs). PCs can be considered to be any periodic configuration that presents a band gap along a certain direction of propagation. First of all, the wave equations that govern the electromagnetic wave propagation will be presented for PCs. The Plane Wave Expansion Method (PWEM) will be introduced in order to discuss the band gaps in PCs. The chapter will be concluded with possible applications of PCs.

6.1 Wave equation and the eigen value problem in PCs

The wave equations in PCs have to be adapted from Maxwell's equations. Once we return back to Eq. (2.1)-(2.4), for a source free region ($J = M = 0$ and $\rho_e = \rho_m = 0$)

$$\nabla \times \overline{E}(r,t) = -\frac{\partial \overline{B}(r,t)}{\partial t} \tag{6.1}$$

$$\nabla \times \overline{H}(r,t) = \frac{\partial \overline{D}(r,t)}{\partial t} \tag{6.2}$$

$$\nabla \cdot \overline{B}(r,t) = 0 \tag{6.3}$$

$$\nabla \cdot \overline{D}(r,t) = 0\,. \tag{6.4}$$

In PCs the spatial variance of the permeability is not significant and it is equal to the free space permeability ($\mu(r) = \mu_0$). Then, another manipulation of Eq. (6.1)-(6.4) makes

$$\nabla \times \nabla \times \overline{E}(r,t) = -\mu_0 \frac{\partial(\nabla \times \overline{H}(r,t))}{\partial t} = -\mu_0 \varepsilon_0 \frac{\partial^2(\varepsilon(r)\overline{E}(r,t))}{\partial t^2} \tag{6.5}$$

For harmonic waves of the convention $\exp(j\omega t)$, Eq. (6.5) becomes

$$\frac{1}{\varepsilon(r)}\nabla\times\nabla\times\overline{E}(r)=-\mu_0\varepsilon_0(j\omega)^2\overline{E}(r)=(\frac{\omega}{c})^2\overline{E}(r). \tag{6.6}$$

Equation (6.6) is the master equation in PC literature, which defines the eigen value problem. $\zeta=1/\varepsilon(r)\nabla\times\nabla\times$ is the operator, $\overline{E}(r)$ is the eigen function and the frequency values $(\omega/c)^2$ are the eigen values; $\zeta\overline{E}(r)=(\omega/c)^2\overline{E}(r)$.

The vector identity and Eq. (6.4) dictate

$$\nabla\times\nabla\times\overline{E}(r)=(\nabla(\nabla\cdot\overline{E}(r))-(\nabla^2\overline{E}(r))=-(\nabla^2\overline{E}(r)). \tag{6.7}$$

The periodicity of the dielectric function in Eq. (6.5) forces the fields to be characterized by Bloch waves. Then, after having dropped the vector notation

$$E(r)=u_k(r)e^{-jkr} \tag{6.8}$$

where $u_k(r)=u_k(r+a)$ and a is the lattice constant, $E(r)=E(r+a)$. The Bloch states are plane waves multiplied by a periodic envelope function. Then,

$$-(\nabla^2E(r))=-e^{-jkr}[\nabla^2+(-jk)^2]u_k(r) \tag{6.9}$$

$$-\frac{1}{\varepsilon(r)}[\nabla^2+(-jk)^2]u_k(r)=(\frac{\omega}{c})^2u_k(r) \tag{6.10}$$

is the wave equation.

6.2 The scalability of the wave equation

The scalability of Maxwell's equations allow us to work at different wavelengths and make predictions about different wavelength regimes as long as the material at hand has non-dispersive characteristics. PCs are the most suitable candidates for such a treatment. PCs are made out of pure dielectrics in several considered cases in this thesis (metallic PCs and other rare scenarios, however more realistic they can be, are omitted in this thesis work). The material properties permit us to carry out our analyses and experiments at

microwave regime, while the similar phenomenon is expected to appear at optical wavelengths.

Let us assume that $r' = r / s$, s is the scaling coefficient. Then,

$$-\frac{1}{\varepsilon(r')}[s^2\nabla'^2 + (-jsk')^2]u_k(r') = (\frac{\omega}{c})^2 u_k(r') \tag{6.11}$$

$$-\frac{1}{\varepsilon(r')}[\nabla'^2 + (-jk')^2]u_k(r') = (\frac{\omega'}{c})^2 u_k(r') = (\frac{\omega}{cs})^2 u_k(r') \tag{6.12}$$

The wave equations that are valid at one frequency are also appropriate at another frequency band while the dimensions are scaled proportionally.

6.3 The group velocity

The group velocity is once again the quantity that is associated with the electromagnetic wave's energy flow.

$$v_g \triangleq \nabla_k \omega = \frac{\partial \omega}{\partial k} \tag{6.13}$$

The following relationship should hold

$$\langle u_k, \nabla_k[\zeta u_k]\rangle = \left\langle u_k, \nabla_k[(\frac{\omega}{c})^2 u_k]\right\rangle \tag{6.14}$$

$$\langle u_k, [\nabla_k \zeta]u_k + \cancel{\zeta[\nabla_k u_k]}\rangle = \left\langle u_k, \frac{2\omega}{c^2}u_k \nabla_k \omega + \cancel{(\frac{\omega}{c})^2 \nabla_k u_k}\right\rangle \tag{6.15}$$

$$\frac{c^2}{2\omega}\frac{\langle u_k, [\nabla_k \zeta]u_k\rangle}{\langle u_k, u_k\rangle} = \nabla_k \omega \tag{6.16}$$

On the other hand,

$$u_k(r) = E(r)e^{jkr} \tag{6.17}$$

$$\zeta = \frac{1}{\varepsilon(r)}\nabla\times\nabla\times = \frac{1}{\varepsilon(r)}(-jk+\nabla)\times(-jk+\nabla)\times\ldots$$

$$\ldots = \frac{1}{\varepsilon(r)}(-jk+\nabla)^2 \times \tag{6.18}$$

$$\nabla_k \zeta = \nabla_k \frac{1}{\varepsilon(r)}(-jk+\nabla)^2 \times = \frac{-2j}{\varepsilon(r)}(-jk+\nabla)\times \tag{6.19}$$

$$\frac{c^2}{2\omega}\frac{\left\langle E(r)e^{jkr}, \frac{-2j}{\varepsilon(r)}(-jk+\nabla)\times E(r)e^{jkr}\right\rangle}{\left\langle E(r)e^{jkr}, E(r)e^{jkr}\right\rangle} = \nabla_k \omega \tag{6.20}$$

Since $\nabla \times E(r) = -j\omega\mu_0 H(r)$ and $\nabla \times E(r)e^{jkr} = e^{jkr}\nabla \times E(r) + \nabla e^{jkr} \times E(r)$

$$\nabla_k \omega = \frac{\langle E(r), H(r)\rangle}{\varepsilon_0 \varepsilon(r)\langle E(r), E(r)\rangle} = \frac{\frac{1}{2}\mathrm{Re}[\int d^3 r E(r)\times H^*(r)]}{\frac{1}{2}\varepsilon_0\varepsilon(r)\int d^3 r \,|E(r)|^2} \tag{6.21}$$

The final result is quite significant. The numerator is the Poynting vector, whereas the denominator is the total electromagnetic energy density (since $\varepsilon_0\varepsilon(r)\int d^3 r\,|E(r)|^2 = 1/2\times[\varepsilon_0\varepsilon(r)\int d^3 r\,|E(r)|^2 + \mu_0\int d^3 r\,|H(r)|^2]$ and the total energy density is shared between the electric and magnetic fields equally). Hence, by definition the velocity of energy propagation ($\nabla_k \omega$) is the ratio of the averaged (in time and over the unit cell) energy flux to the averaged energy density.

6.4 The emergence of the band gap and the PWEM

The periodic arrangement of the dielectric function results in the forbidden transmission bands in different propagation directions. Figure 6.1 shows the modulation of the dielectric function in 1-D, 2-D and 3-D. The considered PCs in this thesis work have mainly been of 2-D type.

As the simplest example, 1-D PC has been considered in Fig. 6.1(a) with $\varepsilon_1 = 13$, $\varepsilon_2 = 1$. These distinct dielectrics occupy half of the lattice spacing.

(both are $a/2$). The transmission results are presented in Fig. 6.2(b). The results are obtained with TMM formalism that is already discussed in Sec. 2.9.

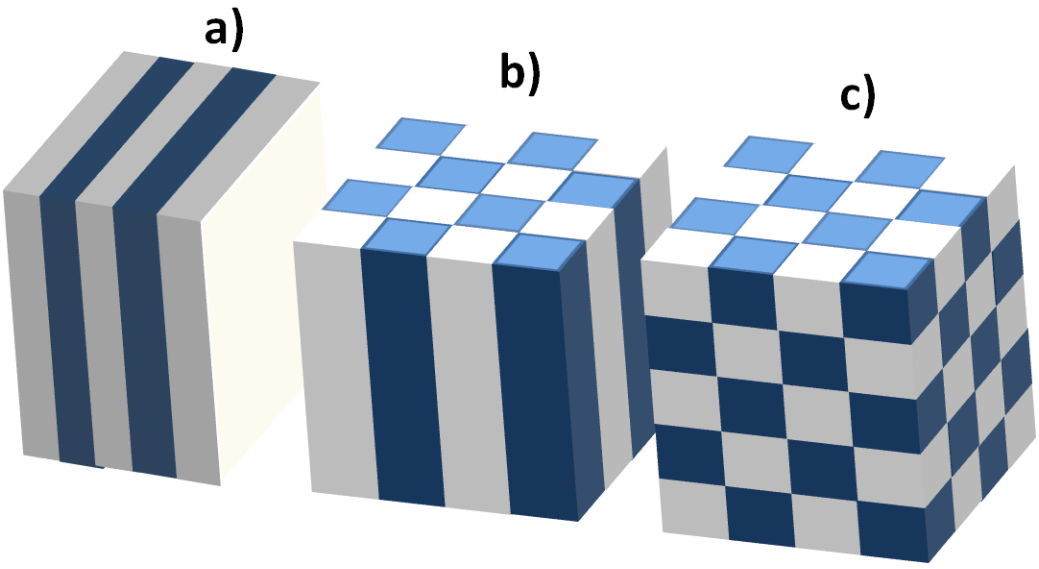

Figure 6.1: Periodic arrangements. (a)1-D periodicity, (b) 2-D periodicity and (c) 3-D periodicity.

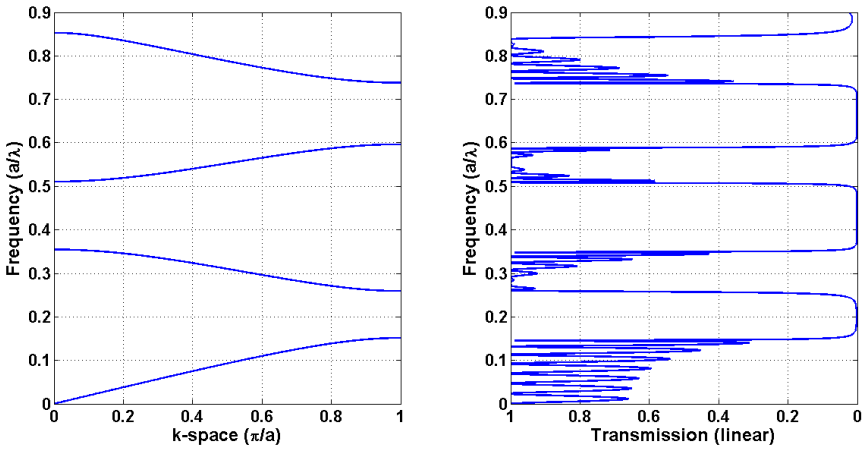

Figure 6.2: (a) The dispersion graph (obtained with PWEM) and (b) the corresponding transmission spectrum (obtained with TMM) for the 1-D PC with $\varepsilon_1 = 13$, $\varepsilon_2 = 1$ and each dielectric occupies the same amount of volume in the unit lattice in Fig. 6.1(a).

In this part, we are going to be giving the basics of the PWEM. This method will be utilized in order to figure out the band diagrams. The band diagrams (dispersion graph) has already been plotted in Fig. 6.2(a) for the

considered 1-D case. The bands for the 1-D PC coincides approximately with the transmission results depicted in Fig. 6.2(b). The first forbidden gap appears roughly in between 0.149 a/λ - 0.259 a/λ and 0.15 a/λ - 0.26 a/λ for TMM based and PWEM results, respectively. The scalability of Maxwell's equations allow us to work with dimensionless units (a/λ), as it is illustrated in Fig. 6.2.

If we return back to the master eigen value equation in Eq. (6.6), we see that we will need the dielectric function in terms of an expansion.

$$\frac{1}{\varepsilon(r)} = \sum_{G} \kappa(G) \exp(jG \cdot r) \tag{6.22}$$

where G is the reciprocal lattice vector and $\exp(jG \cdot a) = 1$ (a is again the lattice spacing). The propagating electric field is also expanded in terms of the plane waves with assigned Fourier coefficients.

$$E(r) = \sum_{G} E(G) \exp(j(k+G) \cdot r) \tag{6.23}$$

Then, the master equation dictates for the harmonic fields dictate

$$-\sum_{G'} \kappa(G-G') \exp(j(G-G') \cdot r)\{(k+G') \times (k+G') \times E(G')\} \ldots .$$

$$\ldots \exp(j(k+G') \cdot r) = (\frac{\omega}{c})^2 E(G) \exp(j(k+G) \cdot r) \tag{6.24}$$

Equation (6.24) is attained by following the phase matching condition. This general solution can be reduced significantly for the 1-D problem, where $G = 2\pi m/a$ and m is an integer value.

$$\frac{1}{\varepsilon(x)} = \sum_{m} \kappa_m \exp(j \frac{2\pi x}{a} m) \tag{6.25}$$

$$E(r) = \sum_{m} E_m \exp(j(k + \frac{2\pi}{a} m)x) \tag{6.26}$$

$$-\sum_{m''} \sum_{m'} \kappa_{m'} \exp(j \frac{2\pi x}{a} m')[\nabla^2 E_{m''} \exp(j(k + \frac{2\pi}{a} m'')x)] \ldots$$

$$\ldots = (\frac{\omega}{c})^2 \sum_m E_m \exp(\, j(k + \frac{2\pi}{a} m)x) \tag{6.27}$$

Then, the eigenvalue problem can be expressed with the following matrix, i.e. the m^{th} element on the right hand side has to be written with a finite number of contributions from the neighboring plane waves.

$$\begin{bmatrix} \kappa_0(k+\frac{2\pi}{a}(-m))^2 & \kappa_{-1}(k+\frac{2\pi}{a}(-m+1))^2 & \kappa_{-2}(k+\frac{2\pi}{a}(-m+2))^2 \\ \kappa_1(k+\frac{2\pi}{a}(-m))^2 & \kappa_0(k+\frac{2\pi}{a}(-m+1))^2 & \kappa_{-1}(k+\frac{2\pi}{a}(-m+2))^2 \cdots \\ \kappa_2(k+\frac{2\pi}{a}(-m))^2 & \kappa_1(k+\frac{2\pi}{a}(-m+1))^2 & \kappa_0(k+\frac{2\pi}{a}(-m+2))^2 \\ \vdots & & \end{bmatrix} \times \ldots$$

$$\ldots \begin{bmatrix} E_{-m} \\ E_{-m+1} \\ E_{-m+2} \\ \vdots \end{bmatrix} = (\frac{\omega}{c})^2 \begin{bmatrix} E_{-m} \\ E_{-m+1} \\ E_{-m+2} \\ \vdots \end{bmatrix}. \tag{6.28}$$

The results of this calculation constitute the $\omega - k$ diagrams and they are exhibited in Fig. 6.2(a). The band formations in PCs can be utilized in order to construct efficient optical components which can tailor the course of the electromagnetic waves. In the following sections, couple of examples are going to be laid down.

6.5 Surface waves in PCs and beam steering with PCs

This paper was published in Optics Express and is made available as an electronic reprint with the permission of OSA. The paper can be found at the following URL on the OSA website: http://dx.doi.org/10.1364/OE.17.009879. Systematic or multiple reproduction or distribution to multiple locations via electronic or other means is prohibited and is subject to penalties under law.

The arrangement in Fig. 6.3 is used to excite the surface waves in PCs. A monopole probe is used to provide an isotropic radiation. A receiver horn antenna is employed to detect the radiation pattern at a distance that is 1m away from the PC surface. The dispersion graph is shown in Fig. 6.4. The dashed double dotted red line is the air line in Fig. 6.4. The slope of this line is given as $\omega/k_0 = c$. The conduction and valance bands are the edges of the photonic band diagram for the 2-D PC which is placed under the monopole in Fig. 6.3. This 2-D PC is made out of long dielectric rods (Alumina rods that are electrically long). The dispersion graph is also computed with a 2-D PWEM.

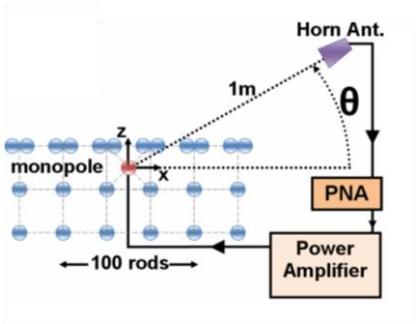

Figure 6.3: The excitation of the surface wave with dimers.

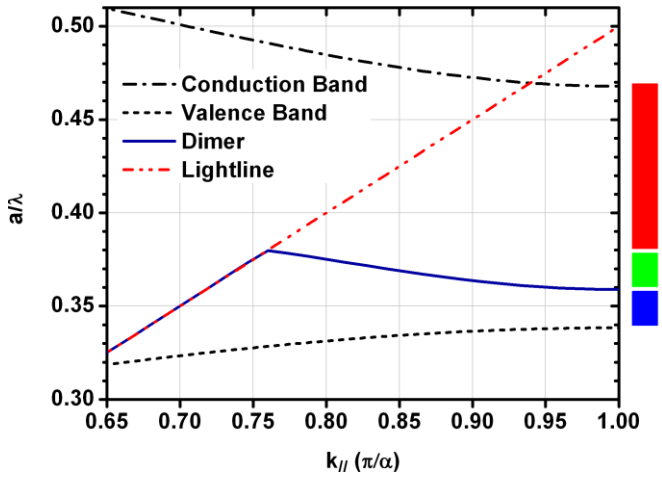

Figure 6.4: The dispersion graph for the surface waves.

A surface wave that is attached to the dimers is spotted as soon as the dimers are located at the PC surface. This band (shown with blue line in Fig. 6.4) lies inside the forbidden band of the regular PC. Therefore, it is totally

uncoupled to the regular PC. A field at the PC surface can be written approximately in the form of

$$E \propto E_y(r)\exp(-jk_{\|}r_{\|})\exp(-jk_z z). \tag{6.29}$$

The boundary conditions at the dimer-air interface implies that the tangential component of the propagation constant ($k_{\|}$) is conserved. Consequently, for the band that is below the light line in Fig. 6.4 the coupling to the radiative modes is quite weak due to the losses stemming from the relation

$$k_0^2 = k_{\|}^2 + k_z^2 \Rightarrow k_z = j\sqrt{k_{\|}^2 - k_0^2} \tag{6.30}$$

since below the light line $k_0 < k_{\|}$. Accordingly, the waves are confined to the surface layer inside this band. Figure 6.5 explicitly demonstrates this phenomenon. The radiation is detected at the edge locations ($\theta = 0$ and $\theta = 180$). The surface layer of the PC with the dimers can be considered as an antenna array and an endfire radiation is monitored (orange colored radiation in Fig. 6.5). Conversely, the regular PC just reflects back the monopole and an isotropic-like radiation is illustrated in Fig. 6.5 (purple and grey colored radiation profiles in Fig. 6.5).

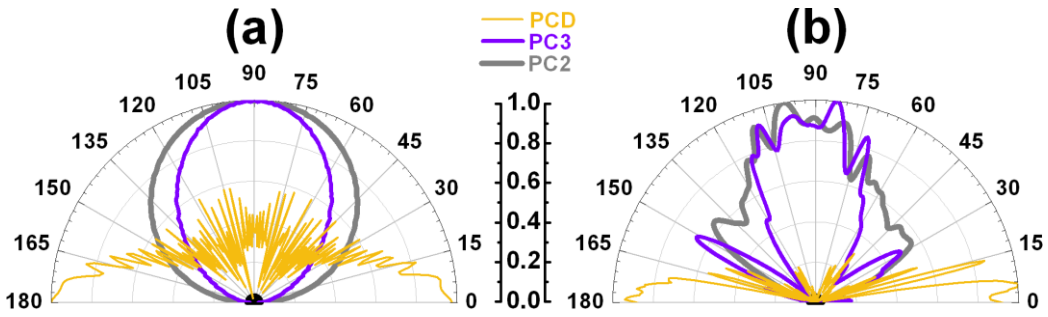

Figure 6.5: Radiation patterns for (a) simulation and (b) experimental results inside the surface wave band (under the light line).

On the other hand, the dimer mode extends up above the light line. These modes can couple to the air owing to the fact that the real part of $k_{\|}$ gets small values and $k_{\|}$ itself is now complex. If we define

$$k_{\|} = \alpha + j\beta \tag{6.31}$$

$$(\alpha + j\beta)^2 + k_z^2 = k_0^2 \Rightarrow |\,\mathrm{Re}[k_z]\,| > |\,\beta\,| > |\,\alpha\,| \ . \tag{6.32}$$

The comparison of the quantities in Eq. (6.32) reveals that the radiation is directed towards broadside. While the frequency is increasing the complex $k_{\|}$ attains smaller values as it can be deduced by inspecting Fig. 6.4. Then, the beam is expected to be steered towards the normal direction, as shown in Fig. 6.6.

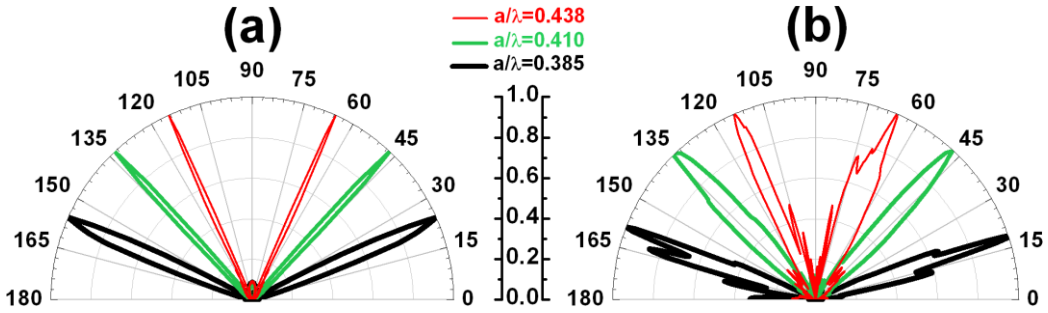

Figure 6.6: Radiation patterns for (a) simulation and (b) experimental results inside the radiating wave band (above the light line).

The complex nature of $k_{\|}$ can be observed in Fig. 6.7. The surface wave is shown in Fig. 6.7(a), which corresponds to the radiation patterns in Fig. 6.5. Conversely, the leaky wave is depicted in Fig. 6.7(b). The surface wave is coupled to the air in Fig. 6.7(b) and cannot propagate for long distances in contrast to the case in Fig. 6.7(a), where the surface wave reaches the end of the dimer layer on both sides. This justifies the relationship given in Eq. (6.32).

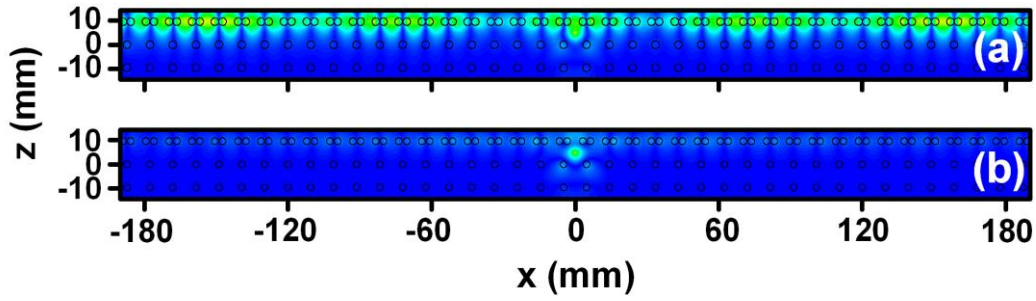

Figure 6.7: The electromagnetic wave propagation along the dimer layer for (a) the surface waves (below the light line) and (b) the radiating waves (above the light line).

Finally, the negative phase advance for these surface waves is inspected. The results are depicted in Fig. 6.8. The dispersion plots in Fig. 6.4 illustrates that $\partial\omega/\partial k < 0$. This is a manifestation of the negative phase advance and a signature of the backward wave propagation, as it was already discussed in the metamaterial related chapters.

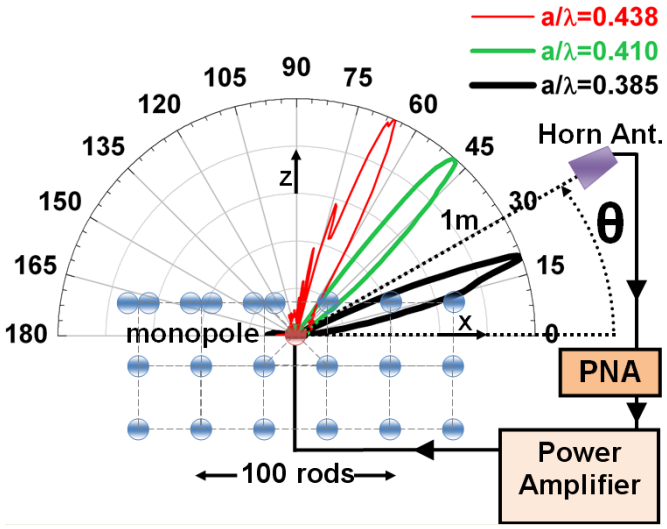

Figure 6.8: The demonstration of the backward wave propagation in surface waves.

The tangential *k*-vector at the surface is preserved and it is in the opposite direction with respect to the Poynting vector, which is a direct implication of the negative phase advance. The tangential *k*-vector is along +*x*-axis. Hence, the radiation is detected in the first quadrant ($0 \le \theta \le 90$).

6.6 Iso-frequency Contours (IFCs) and spatial filtering with PCs

Reprinted with permission from E. Colak, A. O. Cakmak, A. E. Serebryannikov and E. Ozbay, "Spatial filtering using dielectric photonic crystals at beam-type excitation," J. Appl. Phys., Vol: 108, No: 11, pp. 113106 (8 pages), 2010. Copyright 2010, American Institute of Physics.

PCs are very useful in guiding the incident electromagnetic wave to the desired locations.One such example is presented in Fig. 6.9. A very simple

regular PC structure (without any defects) has been utilized to serve as a spatial filter. The main motivation of the spatial filter is to filter out the impinging waves at certain incidence angles in the communication channel.

IFCs come very handy in analyzing the behavior of PCs at different incident angles. The treatment resembles the case with the Einwald circles in previous chapters. The incident wave impinges at the surface with a certain angle (10^o, 30^o or 50^o in this example). The wave vector in air is drawn with respect to the air band circles just as we have already done in the earlier cases. However, in contrast to the cases with the boundary problem entailing two isotropic materials, the PC has non-isotropic features. The IFCs are depicted in Fig. 6.10.

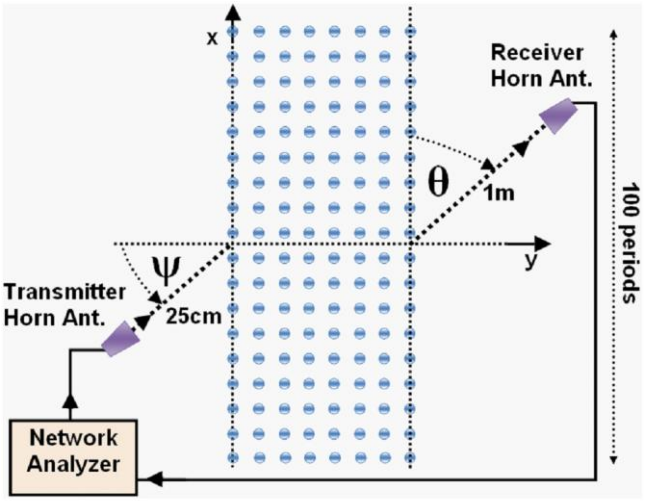

Figure 6.9: Spatial filtering with a 2-D PC design.

IFCs are nothing but the contours of the photonic bands. The IFCs are centered around Γ point of the Brillouin zone of the square lattice for the 2nd Band, while IFCs are located around M point for the 3rd Band. The number of the related bands are shown in the regarding figure. Then, an incident wave at 10^o and 50^o can be coupled to the Floquet Bloch modes of the PC by making use of the phase matching at the interface. Conversely, the incident wave at 30^o cannot couple to the PC owing to the mismatch of the tangential component of the wave vector at the interface.

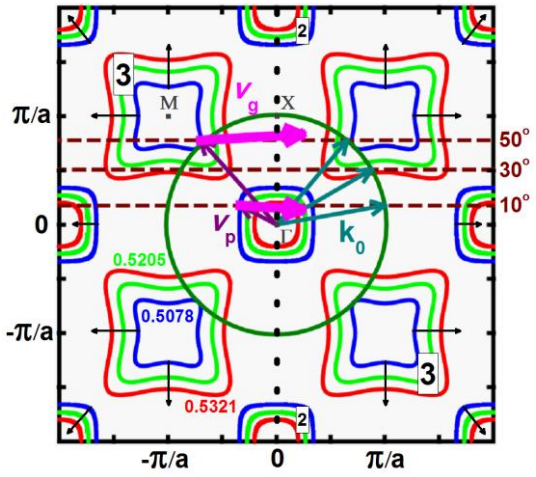

Figure 6.10: IFCs of the PC in Fig. 6.9 at three different frequencies (0.5078 a/λ – blue colored, 0.5205 a/λ – green colored and 0.5321 a/λ – red colored). The green circle depicts the air band at 0.5078 a/λ. Construction lines are drawn at this particular frequency for three incident angles (10°, 30° and 50°) in order to check for the phase match at the PC-air interface. The PC-air interface is represented with the dotted black line at the middle of the figure. The black arrows show the direction of the possible group velocities. k_0: incident wave, v_p: coupled FB wave, v_g: the group velocity of the coupled FB wave inside the PC.

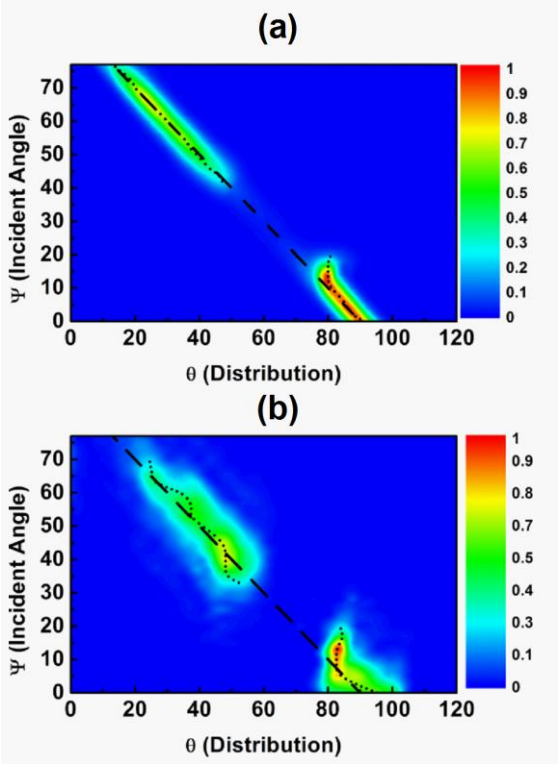

Figure 6.11: Incident angle vs observation angle domains for (a) simulated and (b) measured results at 0.5078 a/λ.

Thus, the predictions of the IFCs are shown to hold for the 2-D transmission results in Fig. 6.11 both in the simulations and experiments. The transmission values are plotted in incident angle vs observation angle domain. A certain incident angle domain is filtered. A similar filtering action is also achieved at the observation angle domain, as well.

The group velocity of the coupled Floquet Bloch wave is found from the nomal to the IFC in Fig. 6.10. The direction of the group velocity of the coupled Floquet Bloch modes turns out to be almost normal to the surface interface. The IFCs in the 2nd Band (around Γ point) are shrinking down as the frequency is attaining higher values. In contrast, the IFCs are expanding out in the 3rd Band (around M point). Such a behavior highlights the left handed and right handed characteristics for the 2nd and 3rd Band Floquet Bloch modes, respectively. In fact, the multiplication of the $v_g \cdot v_p < 0$ is satisfied for both bands. Hence, both of the bands, regardless of their inherent characteristics ($\nabla_k \omega$), support left handed electromagnetic wave propagation.

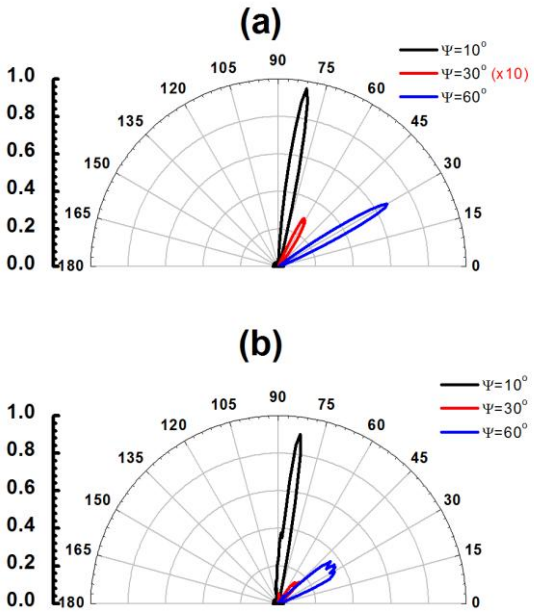

Figure 6.12: Radiation patterns at 0.5078 *a*/λ for different incident angles. (a) Simulated and (b) measured results.

Finally, Fig. 6.12 explicitly shows that the transmission is blocked for the incident angle of 30^{o}. Figure 6.12 illustrates the transmission results for the observation angles.

Chapter 7
Photonic Crystal Grading and Grating

7.1 The propagation of electromagnetic waves inside graded-index photonic crystals

This section has been submitted in the form of a journal paper to Optics Express. Atilla Ozgur Cakmak, Hamza Kurt, Evrim Colak, and Ekmel Ozbay, "The electromagnetic wave propagation in graded-index photonic crystals out of the metamaterial regime," submitted to Optics Express.

It has been widely accepted that the multi-dimensional high-index contrast periodic materials known as photonic crystals (PCs) may contribute to harvest photons in different ways due to the unique properties that arise because of the periodic nature. Accordingly, the PC literature has gotten further familiarized with the graded-index (GRIN) media owing to the increased interest in the last years. The theory of the electromagnetic wave propagation in GRIN media had previously been well established [120] and it constituted a basis where the researchers could borrow inspirational ideas for the examination of the non-uniform periodic compositions [121,122]. The GRIN PC is attained either by the direct index modulation [123,124] or more frequently by the gradual adjustment of the filling factor of a uniform PC [125-134]. The self-collimation, strong-focusing, super-bending, efficient-coupling, mirage of light and negative-index lens are among the phenomena that were implemented by utilizing specially designed GRIN PCs. GRIN PCs have been shown to enhance the control of the light.

GRIN based topologies have been previously investigated in depth in order to tailor the path of the propagating electromagnetic waves. However,

most of the attention has been paid to the operational regimes at rather long wavelengths. The long wavelength regime is also called the metamaterial regime in which the periodic structures can be described in terms of the effective parameters. Conversely, we are going to discuss the propagation of the electromagnetic waves inside the GRIN PC at shorter wavelengths in this paper. A GRIN PC topology that has non-isotropic features with rather rapidly changing grading parameters is going to be addressed. An alternative methodology to examine such seemingly arbitrary structures will be presented with the aid of the Plane Wave Expansion Method (PWEM), Finite Difference Time Domain (FDTD) results and the Fourier analysis of the propagating waves inside the GRIN PC.

In the succeeding parts, distinct topologies that have been suggested in the literature are going to be revisited first. These alternative topologies will found a basis for us to compare the performance characteristics of the presently studied GRIN PC. We will conclude by discussing the working mechanisms of the GRIN PC based lensing at short wavelength regime for the current design.

First of all, we are going to be considering metamaterials (MTMs) for focusing purposes. Subwavelength focusing has been accepted as a pioneering accomplishment for possible future applications, especially in the near-field science. The appearance of the negative-index materials (NIM) has escalated the endeavors towards the construction of improved lenses. MTMs and PCs have been the fundamental building blocks of such lensing activities. The main physic entails the negative refraction and evanescent wave amplification. Figure 7.1 illustrates an exemplary NIM lens that consists of a dispersive homogenized medium in order to mimic the characteristics of a MTM. The constitutive parameters of the medium, and thereby the permittivity and permeability of the MTM are assumed to be of the Drude and Lorentz form, respectively. A similar model had earlier been studied at a different frequency in ref. 135 and the Drude/Lorentz description of a double negative MTM is a common approach. The simulations have been carried out in CST Microwave Studio which is based

on Finite Integration Technique. Meanwhile, the scalability of the Maxwell's equations allows us to make analogies between the microwave and optical frequency ranges. The absolute values of the electric field distribution maps have been plotted at 17.7 GHz under the illumination of a modeled horn antenna. The launched beam possesses wave fronts with spherical features. The phase advancement is along the propagation direction in free space (at P_1 and P_3), whereas the left handed behavior dictates a negative phase velocity with respect to the group velocity inside the MTM (at P_2). The conservation of the momentum at the air-MTM boundary compels the wave fronts to collapse and the focusing is attained. The beam quickly starts to diverge once it leaves the MTM.

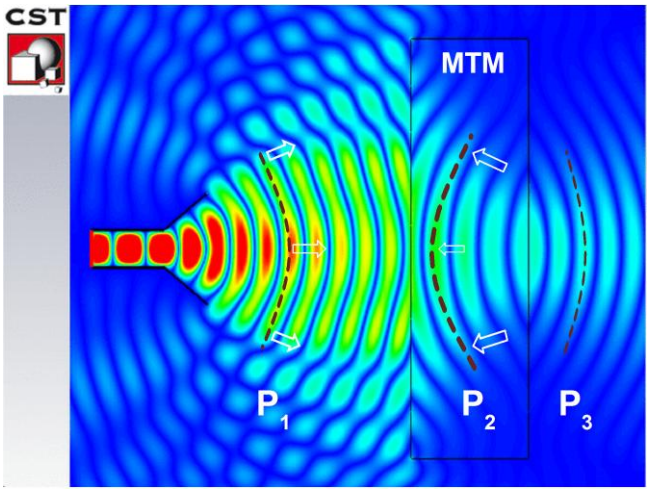

Figure 7. 1: The absolute values of the electric field distributions for a MTM based lens at $f = 17.7$ GHz. P_1, P_2 and P_3 signify three different positions along the direction of propagation. The dashed wine-colored curves exhibit the wave fronts roughly at P_1, P_2 and P_3. The excitation source is modeled with a horn antenna on the left hand side of the figure. The white arrows indicate the direction of the wave-vectors on the same wave front. The effective permittivity function is $\varepsilon_{eff}(\omega) = \varepsilon_\infty - \omega_p / [\omega(\omega - i\nu_c)]$ and the effective permeability function is $\mu_{eff}(\omega) = \mu_\infty + (\mu_s - \mu_\infty)\omega_0^2 / (\omega_0^2 + i\omega\delta - \omega^2)$, $\varepsilon_\infty = 1.62$, $\omega_p = 2\pi \times 31$ GHz, $\nu_c = 30.69$ MHz, $\mu_\infty = 1.12$, $\mu_s = 1.26$, $\omega_0 = 2\pi \times 17$ GHz, $\delta = 500$ MHz.

The conventional MTM configuration suffers from possible losses which stem from the imaginary parts of the constitutional parameters. The impedance mismatches at the air-MTM interface causes standing waves between the source and the structure. Besides, the planar NIM lenses (like the one in Fig. 7.1) do not

have a definite focal length. The MTM lens could focus the incident beams launched from a source that is 4λ away in Fig. 7.1, but an object at infinity would not be resolved by the planar MTM lens. Instead, planoconcave NIM lenses are built with PCs [136] and MTMs [137], which can accept wave fronts with larger radius of curvatures. Consequently, a planar GRIN formalism presents itself as a favorable choice in view of the fact that it may avoid the cost and manufacturing complexities that a planoconcave lens brings. Hence, an increasing number of publications have rapidly adapted the GRIN concept for the MTM lenses as well [138-142]. Essentially, the main disadvantage of the MTM based lens is the frequency dependency of the negative refraction mechanism since the double negative behavior can be sustained for a limited operational band. Liu *et al*. had suggested working with non-resonant metamaterials in ref. 143, which radically increased the frequency bandwidth. The broadband MTM based designs have been utilized by relying on the small variations of the design parameters of the unit lattice along the propagation direction, which results in a gradient change of the refractive index to control the light's trajectory.

In contrast, the GRIN PC already works over a relatively broader frequency region. Given that the lensing effect is based on the phase retardation mechanism owing to the direct lattice spacing modulation, an intuitive examination even at this stage suggests that the GRIN PCs are less sensitive to the frequency variations. Yet, this point is going to be elaborately covered in the succeeding parts.

GRIN PCs have been exploited in the long wavelength regime, for which the effective medium theory holds. Actually, the earliest designs that utilized the effective medium theory within the context of the 1-D GRIN PCs go back to the year 2005. The proposed designs were envisioned to be used in imaging, guiding, mode matching and coupling [144,145]. The GRIN PC has been shown to simultaneously possess the multi-functionality as beam deflectors and beam aperture modifiers [146]. Consequently, waveguide bends [147] and a

cylindrical optical black hole with an omnidirectional absorbance [148] have been made available in the following years. Even a free-space carpet cloak has been proposed by making use of the GRIN PCs in metamaterial regime [149]. However, an extensive study of the possible GRIN PC lenses in metamaterial regime has been carried out in ref. 150 and similar lens design techniques have rapidly been addressed in the literature [151-153].

Accordingly, we have adapted a GRIN PC lens design that is based on the homogenization procedure. The implementation of the homogenization procedure is derived from Maxwell-Garnett theory. The results are presented in Fig. 7.2. GRIN PC comprises alumina rods ($\varepsilon_{rod} = n_{rod}^2 = 9.61$) with varying radii. The dispersion graph in Fig. 7.2(a) indicates the phase difference ($\Delta\phi$) within the 1st band along the propagation distance ($\Delta\phi \propto \Delta k$). The phase difference is expected to be accumulated between two sets of rods with different radii (r_1 and r_2). The radius of the rods change in the transverse direction (x-axis). Then, the refractive index at any point along x-axis is calculated with the formula that is given in the inset of Fig. 7.2(a). Thus, a quadratic refractive index variation can be sustained for $n(x)$, where $f(x) = \pi r^2 / a^2$ is the filling factor for each unit cell and a is the constant lattice spacing in the transverse direction. As a result of the quadratic variation, a focusing effect is observed at the end of the structure. The simulated electromagnetic field is portrayed in Fig. 7.2(b) for a frequency value inside the 1st band. Once the index variation along the transverse direction is defined as $n^2(x) = n_0^2(1-\alpha^2 x^2)^2$, the focusing occurs at a thickness $t = \pi/(2\alpha)$. Then, the kernel function of the linear system is determined as

$$K(x_0, x) = \frac{-ik_0 n_0}{4t} \exp(-2\pi i \frac{x_0 k_0 n_0}{4t} x), \qquad (7.1)$$

where k_0 is the free space wave vector. Eq. (7.1) is derived from the ray transfer matrix parameters for the conventional GRIN structures [120]. Eq. (7.1) implies that the output field [$\psi(x)$] becomes the Fourier transform of the impinging field

[$FT(\psi(x_0))$]. The aperture function [$\Pi(x_0)$] comes into play because of the finite width of the lens. The field at the output side is calculated by convolving these two contributions.

$$\psi(x) = FT(\psi(x_0)) * FT(\Pi(x_0)). \tag{7.2}$$

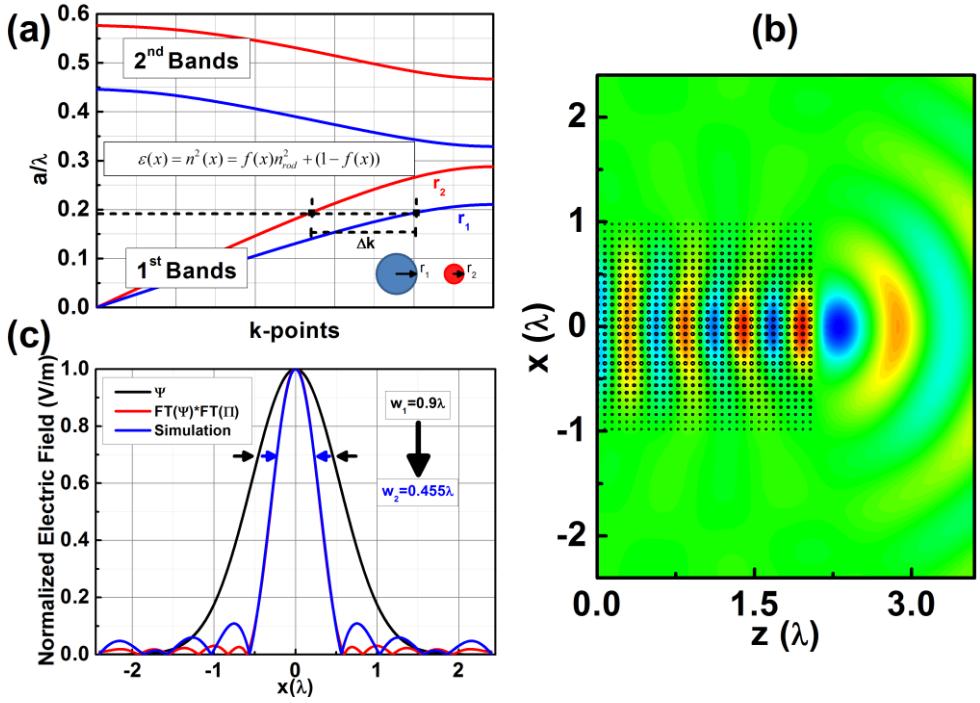

Figure 7.2: (a) Dispersion graph for two radius values: $r_2 = 0.3a$ (blue line) and $r_1 = 0.173a$ (red line). (b) The simulated electric field map at $f = 0.07a/\lambda$. (c) The field distributions along *x*-axis for the incident (black line), theoretically predicted (red line) and simulated field (blue line). The theoretically inferred curve is calculated by using Eq. (7.2), whereas the simulated field distribution is extracted from (b) at the exit side of the GRIN PC.

Figure 7.2(c) shows the field distribution of the incident Gaussian excitation source (black line). The output field is found out by using Eq. (7.2) and it is plotted (red line) together with the simulated field (blue line) at the exit side of the GRIN PC in Fig. 7.2(c). The theoretical predictions of Eq. (7.2) coincide with the simulation results such that they are indistinguishable for the low spatial frequencies, which is in accordance with the findings of ref. 153. The ripples at higher spatial frequencies are caused by the *sinc* function in Eq.

(7.2). The mismatch between the theoretical and simulation results in Fig. 7.2(c) at higher spatial frequencies is ascribed to the limitations of the paraxial approximation and effective medium approach. The Bragg Diffractions start to manifest themselves inside the GRIN PC while the operational frequency is increased. The focusing effect can still be observed at the exit side owing to the inherent phase retardation mechanism. Yet, a GRIN PC that is free of chromatic aberration can only work for a limited bandwidth.

The biggest drawback of the effective medium theory based GRIN PC topologies is the large size of the overall structure. Hence, the GRIN PC in Fig. 7.2(b) consists of 32 stacked layers ($t = 32a$) along *z*-axis, since we are working at long wavelengths. The resolution of the GRIN PC lens is determined by its finite width. Likewise, the width of the GRIN PC lens has to be large enough both to properly process the incoming beam and to increase the numerical aperture (NA) of the lens at these long wavelengths. However, the width of the lens (*w*) cannot be indefinitely increased. There is a minimum ratio between the thickness and width of the lens, $(t/w)_{\min} = \pi n_0 / (4\sqrt{n_0^2 - n_{\min}^2})$, which needs to be satisfied. The rods with the smallest filling ratios at the edges of the lens determine n_{min}. Thus, a larger width of the lens leads to a longer thickness. This problem cannot be tackled by boldly increasing n_0, which will boost the reflections from the lens because of the impedance mismatch at the input side. Furthermore, the condition, $n_0 \le \lambda_0 / (4a)$, must be fulfilled in order to be able to safely work with the effective medium theory assumptions [152]. These critical points had also been emphasized in refs. 152 and 153. Additionally, the spot conversion ratio is also quite low at long wavelengths. It is calculated to be the ratio of the Full Width at Half Maximum (FWHM) of the input and output field distributions and is equal to $w_1 / w_2 \approx 1.98$ for the specific case in Fig. 7.2(c).

There have been recent studies in the field that aimed to figure out the trajectory of the propagating electromagnetic waves inside the GRIN structures. Several of these studies relied on the relatively small anisotropy of the GRIN

media [133,134]. The circular shape of the Iso-frequency Contours (IFCs), which is again a consequence of working at rather long wavelengths and lower bands, made the analysis practical. Moreover, a gradual change of the grading parameter along the direction of propagation in the GRIN PC has enabled to envisage the light's path [128]. Yet, such semi-analytical predictions are only valid for a slow modification between the neighboring lattices.

In other scenarios, the GRIN was shown to exhibit focusing properties even at shorter wavelengths ($a/\lambda > 0.2$) [127]. It has also been illustrated in ref. 127 that the incident Gaussian beams can still be subject to lensing in GRIN PCs under certain conditions regardless of the precise shape of the IFCs at the operational wavelength. Furthermore, a gradual change between the neighboring lattices along the transverse direction had not been sought. However, the details of the lensing activity have not been laid out. The propagating wave is considered to be similar to an ideal Gaussian beam and it was discussed that the propagating beam experiences either converging or diverging oscillatory behavior depending on the instantaneous size of the waist of the beam. References 6 and 7 have adapted a fitting algorithm in order to engineer the phase front of the propagating waves inside the GRIN PCs. Then, the particular spatial grading factor was extracted by carrying out a reverse engineering on the fitted phase fronts. Consequently, GRIN PC lenses have been built at short wavelengths (at higher bands). Nevertheless, the special case of the small anisotropy for the higher photonic bands has played the major part in the relevant studies. The problem of the light propagation inside the GRIN PCs at short wavelengths was only addressed in refs. 154 and 155 for a more general case by making use of the Hamiltonian Optics. Thus, the slow change of the structure parameters at short wavelengths has been utilized and the local dispersion relationships have been used to figure out the trajectory of the propagating waves. Hence, wavelength demultiplexers have been demonstrated.

On the other hand, an investigation that is devoted to the working mechanisms of the GRIN PC lenses at shorter wavelengths (out of the

metamaterial regime) with non-adiabatic spatial distributions and non-isotropic features has yet to be studied. Interestingly, a plain homogenous dielectric slab is shown to focus the light in ref. 156 as good as the studied short GRIN PC. It is suggested in ref. 156 that such a focusing is a result of the multimode interferences at the exit side of the GRIN PC rather than the grading of the spatial parameters for short GRIN PCs. In the subsequent section, we are going to consider a GRIN PC with rapidly changing spatial modulation in the transverse direction. The considered GRIN PC does not possess special features in its IFCs. That is, the structure is not isotropic. Moreover, even a small anisotropy, which would render the effective medium theories to be valid, is not evident. The main attention is going to be focused on the small wavelength regime.

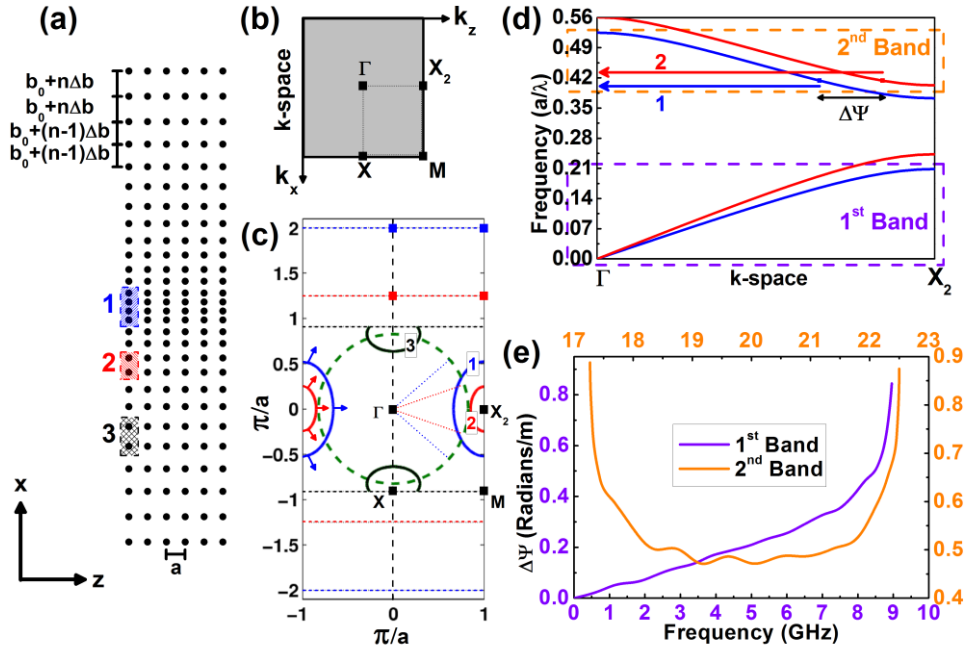

Figure 7.3**: (a) The GRIN PC configuration and the labeled segments representing three different fractions of the GRIN medium. Color coding for the segments; 1 – blue, 2 – red and 3 – black. (b) The Brillouin zone of the labeled segments, (c) and the regarding IFCs at 0.413** ***a/λ*** **(** $f = 17.7$ **GHz). The arrows determine the gradient vectors on the respective IFCs. Thick dashed-black line parallel to the** k_x **is the air-GRIN PC interface. Dashed-green circle is the air band. Dotted-lines originating from the Γ point show the maximum angle of incidence for an incoming wave to be coupled to the Floquet-Bloch waves. The boundaries of the different segments are color coded and shown with the dotted lines parallel to the** k_z**. (d) The 1st and 2nd photonic bands of the corresponding segments along** ΓX_2 **direction. (e) The phase difference between the regarding fragments in (d) in the 1st (purple) and 2nd (orange) bands.**

The GRIN PC that is going to be investigated is once again depicted in Fig. 7.3(a). The GRIN PC is symmetric around *x*-axis and there exist a total number of 28 alumina rods in one column. Accordingly, *n* gets an integer value of 6. The periodicity along the *z*-axis for the GRIN PC is $a = 7\,\text{mm}$. The lateral shifting parameter is $\Delta b = 0.15a$, whereas the offset parameter is $b_0 = 0.5a$. The radii of the rods are $r = 1.585\,\text{mm}$. Only the TM polarization is considered throughout the study. Then, the electric field component is always parallel to the axis of the dielectric rods.

The lattice modulation is maintained with the aid of the gradual modification of the filling factor in the transverse direction for a hexagonal lattice in ref. 125 in which the overall GRIN PC is considered as a combination of several segments in the modulation direction. Likewise, the distinct segments of the GRIN PC are labeled in Fig. 7.3(a). These segments share the same lattice periodicity in the lateral direction. Then, the Brillouin zone (BZ) of the segments happens to get expanded in certain directions unlike the square lattice case [see Fig. 7.3(b)]. The shape of the irreducible BZ is a rectangle with the corner points Γ, X, M and X_2. The strong non-isotropic features are spotted in the IFCs in Fig. 7.3(c). Inevitably, the characteristics of the wave propagation differ along *x* and *z*-axes. The GRIN PC is also decomposed into its building blocks in refs. 128 and 129. Super-bending and mirage effects are interpreted in relation to the IFCs of the building blocks. Accordingly, blue, red and black colors are chosen to represent the IFCs and the corresponding boundaries of the irreducible BZ for the segments 1, 2 and 3, respectively. Figure 7.3(c) illustrates that the IFCs are localized around X_2 point for segments 1 and 2, whereas the IFCs are centered around X point for segment 3. The dashed-green circle represents the air band at 0.413 a/λ ($f = 17.7\,\text{GHz}$). The thick dashed-black line parallel to the k_x domain depicts the GRIN PC interface. The arrows on the IFCs pointing outwards show the possible directions of the coupled Floquet-Bloch waves. In other words, these arrows indicate the directions of the group velocities for the coupled Floquet-Bloch waves, which are perpendicular to the

IFCs from the definition $\overrightarrow{v_g} = \nabla_{\vec{k}}\omega(\vec{k})$. The thin dotted-colored lines connecting the Γ point and the air band form the cones in which the coupling of the incident beam to the Floquet-Bloch waves takes place. They have the same color coding of the corresponding segments. In a way, they offer an estimate for the NA of the distinct segments. If each of these segments were a part of a uniform lattice in the transverse direction, the NA of the segments would be $NA_1 = \sin(40^o) \approx 0.64$ and $NA_2 = \sin(15^o) \approx 0.26$ for segment 1 and 2, respectively. Furthermore, segment 3 (outer segment) would not be supporting the wave propagation along the k_z direction.

The dispersion results are plotted in Fig. 7.3(d) for the examined GRIN PC. Our frequency of operation, 0.413 a/λ, resides in the 2nd band. The negative slope of the 2nd band suggests left-handed characteristics which can also be observed from the IFC curves. The color coded arrows represent the direction of the group velocities which are pointed towards the Γ point. The magnitude of the distance from the Γ point to the crossing points in Figure 7.3(d) is inversely proportional to the phase velocity of the waves that are supported in these distinct segments. There is an evident mismatch in the phase velocities which in turn generates a familiar phase retardation of a classical GRIN structure in optics. The accumulated phase difference per meter between these two fractions has been plotted in Fig. 7.3(e). It is apparent from Fig. 7.3(e) that working with the 2nd band offers a broad operational bandwidth for much shorter GRIN PC structures in comparison to the 1st band.

Even though the inspection of the PWEM results in Fig. 7.3 gives a preliminary insight, we have to make a list of the distinctions between the studied problems in the literature and our case in order to come up with a more comprehensive description of the physical phenomenon. In refs. 128 and 129 the longitudinal shift of the adjacent blocks in the propagation direction was less than 1%, which enabled the authors to deduce the layer by layer propagation of the beam from the local dispersion curves. In our present work, the modulation per lattice is noticeably higher. However, the modulation is in the transverse

direction as in the case of refs. 125, 133 and 134. Then, the most influential factor turns out to be the degree of isotropy of the IFCs. Regardless of the specifications of the application field and the aimed wavelength range, the anisotropy was considerably less pronounced and the studied dispersions in refs. 125, 133 and 134 were approximated to be isotropic, which permitted an effective refractive index to be defined for all cases. On the contrary, we have an arrangement of a non-isotropic nature in our work at the desired frequency of operation. The Bragg reflections are more likely to be the leading scattering mechanism in the 2nd photonic band in comparison to the 1st photonic band for our case. Consequently, an effective index description cannot hold for our structure.

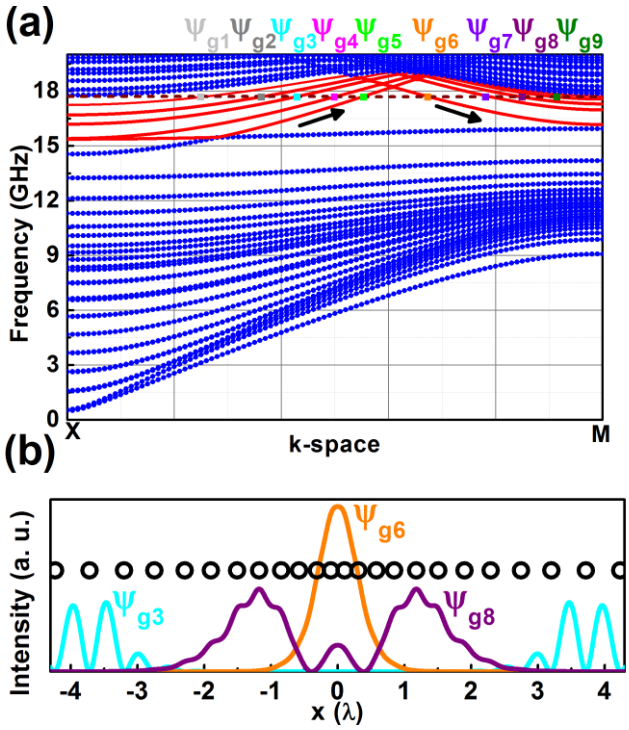

Figure 7.4: (a) Dispersion results for the GRIN PC. The intersected bands are plotted in red. The blue bands are the continuous bands. The sign of the slopes of the intersected bands are designated in with the arrows. (b) The mode profiles for GRIN PC. The intensity values are plotted at $f = 17.7$ **GHz.**

The theory of negative refraction in PCs is explained in details in refs. 157 and 158. Furthermore, ref. 159 discusses the Fourier analyses of the Bloch modes, which bridges the theory of the wave propagation in homogenous media

and the strongly modulated PCs. According to ref. 159, the higher-order BZ must also be taken into consideration so as to clearly identify the left-handed characteristics of a band. Thus, the left handedness suggested by Fig. 7.3(d) is just a consequence of the band folding in the 2^{nd} band. Based on the unfolded version of the bands, we can conclude that the phase velocity of the wave travelling in segment 1 is the slowest and the phase fronts will become concave due to the mismatch of the phase velocities in different segments. After all, it is practical to bear in mind that the PWEM results of Fig. 7.3 can equip us with an initial perception.

Fragmentation of the GRIN PC does not yield a complete picture for our problem, then a more accurate but a computationally lengthier method is practiced. A column of the GRIN PC is assigned to be the super lattice in the PWEM calculations and the results are presented in Fig. 7.4. The results of Fig. 7.4 have to be taken into account concurrently with the outcomes of Fig. 7.5 in which the corresponding mode profiles of the Floquet-Bloch waves are plotted.

The bands for the GRIN PC are shown in Fig. 7.4(a). XM direction is along the *z*-axis. At our frequency of operation the bands of interest are plotted in red. Consequently, there are 9 crossing points which are associated with distinct modes, individually. However, a more careful analysis reveals that there is an artificial inflection point between the 5^{th} and 6^{th} intersection points. Figotin *et al.* had mentioned the likelihood of occurrences of such inflection points under the context of the frozen modes in ref. 160. In spite of this, the occurrence of the inflection point does not necessarily impose the appearance of a stationary point. The inflection point in our case is again a consequence of the band folding. The supported modes Ψ_{g5} and Ψ_{g6} do not reside in the same band. The first 5 bands with the positive slope overlap with the remaining 4 bands with the negative slope. In fact, the exact locations of the first 5 crossing points are very sensitive to the infinitesimal changes in the dimensions of the super lattice. The corresponding mode profiles of the positive slope bands happen to be attached to the most outer shells, which possesses a limited physical meaning. One of

those modes, Ψ_{g3} is plotted as an example in Fig. 7.4(b). Then, we can infer that the first 5 crossing points produce superfluous results, since the outer segments did not support propagating modes in the *z* direction, as indicated by the IFCs in Fig. 7.3(c). Therefore, we focus our attention to the remaining modes. A couple of these modes can be seen in Fig. 7.4(b). They are restricted to the inner segments. The corresponding bands have again attained negative slopes due to the band folding. The dispersion results in Fig. 7.3(d) had also been subject to the band folding and yielded fairly similar consequences. In the band folded case, the mode Ψ_{g6} which is propagating in segment 1, as it is labeled in Fig. 7.4(b), intersects the horizontal line of operational frequency at an earlier *k* value than Ψ_{g8} which rather favors segment 2. Then, Ψ_{g6} has the slowest phase velocity because of the band folding.

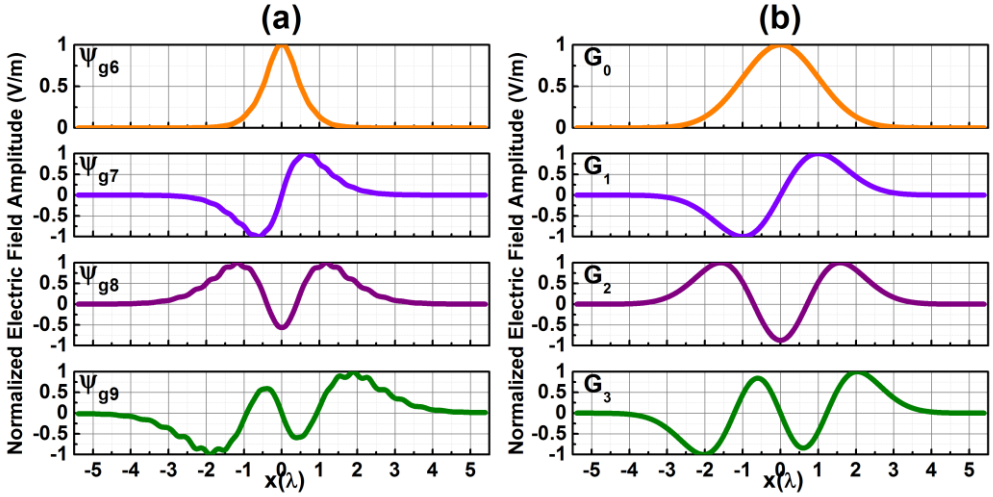

Figure 7.5: The mode profiles for (a) the GRIN PC and (b) the higher order Hermite-Gaussian beams at $f = 17.7$ GHz.

All of the propagating modes are plotted in Fig. 7.5(a). A careful inspection uncovers that these modes bear a strong resemblance to the Hermite-Gaussian beam modes [161-163]. The Hermite polynomial of order m is defined as:

$$H_m(u) = (-1)^m e^{u^2} \frac{d^m e^{-u^2}}{du^m}. \qquad (7.3)$$

Hermite-Gaussian beams are the self-modes of the quadratic GRIN media in classical optics, whose refractive index variation is assumed to be of the form $n(x) \approx n_0(1-\alpha^2 x^2/2)$. Hence, the Hermite-Gaussian beams form an orthogonal and complete basis set for the problem of electromagnetic wave propagation in the quadratic GRIN medium. Hermite-Gaussian beam modes are in the form:

$$G_m(x) = H_m(\sqrt{\alpha k_0}\, x)\exp(-\frac{\alpha k_0 x^2}{2}). \tag{7.4}$$

If we picture the field distribution as quasi-plane waves travelling in the GRIN medium in accordance with the Wentzel-Kromers-Brillouin approach to the Helmholtz equation, the fields inside the quadratic GRIN can be expressed in terms of the Hermite-Gaussian beams with different weights:

$$E_y(x,z) = \sum_m A_m G_m(x) \times \exp(-j\beta_m z), \tag{7.5}$$

where β_m stands for the propagation constant of the mth order, which is inversely proportional to the phase velocity of the regarding mode and expressed as:

$$\beta_m = k_0[1-\frac{2\alpha}{k_0}(1+m)]^{1/2} \tag{7.6}$$

The analogous Hermite-Gaussian beam mode profiles are shown in Fig. 7.5(b). Our case can be considered as a modified version of the classical quadratic GRIN media. The most significant outcome of this comparison is associated with the phase velocity. The phase velocity of the higher order modes are increasing for the classical Hermite-Gaussian beam modes, which is in agreement with our earlier claims concerning the dispersion results. The phase retardation takes place in GRIN medium by reshaping the phase fronts such that the phase velocities of the higher order modes in the outer layers will attain higher values, which in turn causes focusing. The PWEM results for the GRIN PC are in harmony with the analytical expressions for the simple quadratic GRIN medium. As a result, the wave propagation in the GRIN PC can be expressed as a summation of these modified Hermite-Gaussian modes with

different weights at this particular frequency. It can be noticed from the dispersion results of Fig. 7.4(a) that the GRIN PC sustains several of these phase components at frequencies roughly starting from 17.5 GHz. Thus, it is reasonable to expect that the focusing will appear over a large bandwidth. This remarkable feature has been one of the main motivations behind the GRIN studies, as it was briefly mentioned earlier.

The depicted self-modes of the GRIN PC in Fig. 7.5(a) can be categorized depending on their characteristic spatial distribution in the transverse direction. Accordingly, Ψ_{g6} and Ψ_{g8} are the even modes, whereas Ψ_{g7} and Ψ_{g9} are the remaining odd modes. The next step has been to identify the role of these modes for the electromagnetic wave propagation inside the GRIN PC. A GRIN PC of $100a$ has been arranged and the propagation of the electromagnetic waves has been monitored in Fig. 7.6(a) and (c) with an FDTD based simulation for the excitation sources with even and odd parity, respectively. Such a long GRIN PC has been functionalized in order to reduce the contribution of the reflections from both ends. In a way, the electromagnetic wave is guided inside this semi-infinite structure in both cases that are illustrated in Fig. 7.6(a) and (c). The Fourier analysis of the steady-state fields is expected to offer rough estimates about the propagation constants of the supported Floquet-Bloch inside the GRIN PC.

The results of the Fourier analysis are given in Fig. 7.6(b) and (d) for the regarding even and odd excitation sources, respectively. Actually, the Fourier analysis had also been used in an earlier study that involved the refraction phenomena at the PC-air boundary [164]. In contrast to the case in Fig. 7.4(a), the results of the Fourier analysis do not only include the information about the first Brillouin zone (1BZ). Beyond the 1BZ, the Fourier analysis encompasses the outer segments in *k*-space, e.g. the second Brillouin zone (2BZ) as well. It presents the contribution of the plane wave components and becomes handy especially in band folding situations, like ours. The following fundamental relationship applies for the periodic structures:

$$k_z = k_z^{'} + qG, \tag{7.7}$$

where k_z is the propagation constant along z direction for the plane waves inside the GRIN PC, $k_z^{'}$ is the actual wave vector inside the primitive cell with respect to the origin of the k space, G is the reciprocal lattice vector and q is an integer indicating the relevant BZ number [$q = 0,1,2\ldots$ and $q = 0 \rightarrow 1\text{BZ}$]. Only the positive k_z values are plotted in Fig. 7.6(b) and (d). The corner of the 1BZ lies at $G/(2\pi) = 1/(2a) \approx 71.42\,\text{m}^{-1}$. The relationship in Eq. (7.7) brings a walk-off effect. The periodic nature of the plane wave components can be observed in both Fig. 7.6(b) and (d). The higher harmonics of the plane wave components repeat themselves for each G in the upper BZs. Of course, the weight of the higher harmonics are decreasing while the most dominant plane wave contribution originates from the 2BZ, which is in agreement with ref. 164.

The 1BZ and 2BZ are given with zoomed versions in the figure insets. As it can be spotted in the regarding figure insets of Fig. 7.6(b) and (d), the plane wave contributions in 1BZ are approximately the scaled image of those in the 2BZ. Furthermore, there are only 2 dominant plane wave components in each BZ, which are labeled as Ψ_{g6}, Ψ_{g8} in Fig. 7.6(b) and Ψ_{g7}, Ψ_{g9} in Fig. 7.6(d). Under the illumination of an even (odd) type source, only the even (odd) modes are excited. Besides, each mode is associated with a different wave vector. The phase velocity of mode Ψ_{g6} is the smallest, because it has the smallest (highest) plane wave component in the 1BZ (2BZ). We can safely claim it while bearing in mind that 2BZ is the mirror image of 1BZ as long as the unfolded k-space is concerned. Then, the implications of Eq. (7.6) are analogously confirmed for the Floquet-Bloch modes of the GRIN PC. The phase retardation mechanism takes place due to the difference between the phase velocities of the relevant modes. A comparison reveals that Ψ_{g6} and Ψ_{g9} have the slowest and fastest phase velocities, respectively. Actually, it turns out that the propagating modes are not just defined by single plane wave components in contrast to the simplified case in Eqs. (7.5) and (7.6). Instead, several other plane wave components are also contributing to the results in Fig. 7.6(b) and (d) whilst a principal wave vector

can still be visually associated with a propagating mode. Such a broadening in the *k*-space is both caused by Bragg diffractions, the reflections at the PC-air interfaces and the limited resolution of the Fourier analysis.

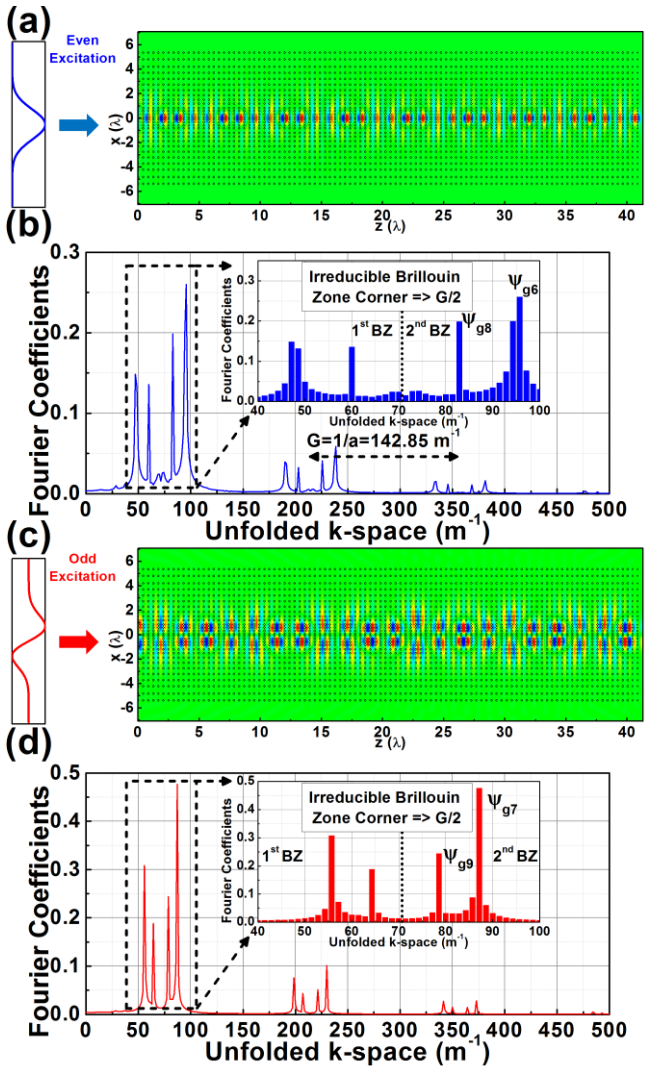

Figure 7.6: (a) The field distribution for an even type excitation at $f = 17.7$ GHz. (b) The results of the Fourier analysis of the field distributions in (a). The figure inset shows the zoomed version of the results that reside inside the 1BZ and 2BZ. (c) The field distribution for an odd type excitation at $f = 17.7$ GHz. (d) The results of the Fourier analysis of the field distributions in (c).

Figure 7.7 illustrates the case when a series combination of even and odd sources, which are previously used in Fig. 7.6, is utilized as the excitation source. The oscillatory behavior of the electromagnetic wave propagation that is a characteristic of the GRIN PCs is still evident in the field distributions in Fig.

7.7(a). The results of the Fourier analysis in Fig. 7.7(b) show that all of the four Floquet-Bloch modes are excited now, simultaneously. The plane wave components belonging to the 2BZ are again the dominant ones. The respective plane wave contributions associated with each mode have not changed their specific locations in *k*-space [compare the results in Fig. 7.6(b), (d) and 7.7(b)]. The unnormalized intensity profiles in Fig. 7.4(b) had demonstrated that the weight of Ψ_{g6}, A_{g6} [see Eq. (7.5)] is bigger than the weight of Ψ_{g8}, A_{g8} in the overall composition of the propagating electromagnetic wave. Thus, the Fourier analysis results in Fig 7.6(b) and 7.7(b) also verify the same relationship between these two quantities. The region that is outlined with orange colored dash lines in Fig. 7.7(a) has undergone a similar Fourier transform independent from the rest of the computational domain. The results are shown in Fig. 7.7(c). Accordingly, we can immediately conclude that the lower Floquet-Bloch modes (Ψ_{g6} and Ψ_{g7}) are attached to the inner segments of the GRIN PC, e.g., Ψ_{g6} has not been detected inside this particular region. This is in agreement again with the findings depicted in Fig. 7.4(b) and 7.5(a). The lowest modified Hermite-Gaussian mode, Ψ_{g6}, is bounded by the central region of the GRIN PC, whereas Ψ_{g9} extends towards the outer fractions of the GRIN PC.

Lastly, the focusing capabilities of the GRIN PC have been investigated. Figure 7.8 exhibits the scenario when a six layer GRIN PC is illuminated with an aperture antenna. The striking difference from the MTM lens in Fig. 7.1 is the reduction of the losses. The MTM lens in Fig. 7.1 had to be designed carefully in order to decrease the reflections stemming from the air-MTM boundary. Furthermore, the inherent losses in MTM lenses could be difficult to tackle in specific cases. Yet, the performance of the studied GRIN PC has not been critically troubled by these issues. An incident wave with rather plane wave like wave fronts has been focused at the exit side of the GRIN PC. In a way, the GRIN PC has fulfilled its main task of phase front transformation.

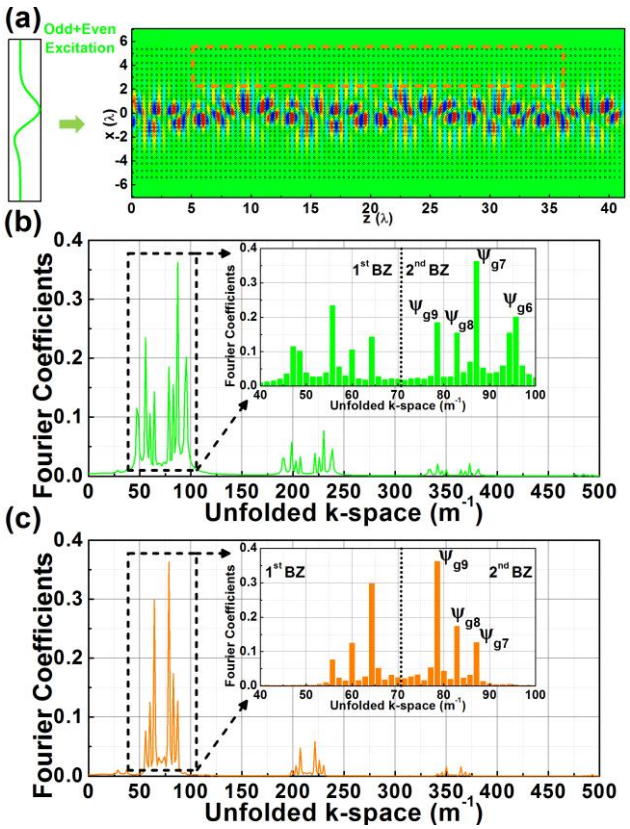

Figure 7.7: (a) The field distribution for a source with a linear combination of the even and odd type excitations that are used in Figure 7.6 at $f = 17.7$ GHz. (b) The results of the Fourier analysis of the field distributions in (a). The figure inset again shows the zoomed version of the results that reside inside the 1BZ and 2BZ. (c) The results of the Fourier analysis of the field distributions that remain inside the orange colored dashed boundary in (a).

The focusing has been achieved at short wavelengths (0.413 a/λ). The field distribution at the output of the GRIN PC (red line) can be seen in Fig. 7.8(b) together with the incident field (blue line). Unlike the case with the GRIN PC lenses in metamaterial regime, a comparably larger spot size conversion ratio ($w_1 / w_2 \approx 9.07$) can be attained. It can be deduced from Fig. 7.8(c) that similar high spot conversion ratios can be obtained even with a three layered GRIN PCs. The GRIN PC has to be truncated at a certain location for an optimum solution. Figure 7.8(c) shows that the waves start to defocus after seven layers. This is a consequence of the classical oscillatory forces exerting on the width of the propagating wave in GRIN structures. The widening and narrowing effects on the width of the propagating wave are also evident in Fig.

7.6. An exact value of the pitch length for the studied GRIN PC cannot be proposed. Yet, the half pitch length of the GRIN PC configuration can be approximated to be around 5*a*. The spot size conversion ratio can be rather insensitive to the layer number as far as the results for the five to seven layered GRIN PC are concerned.

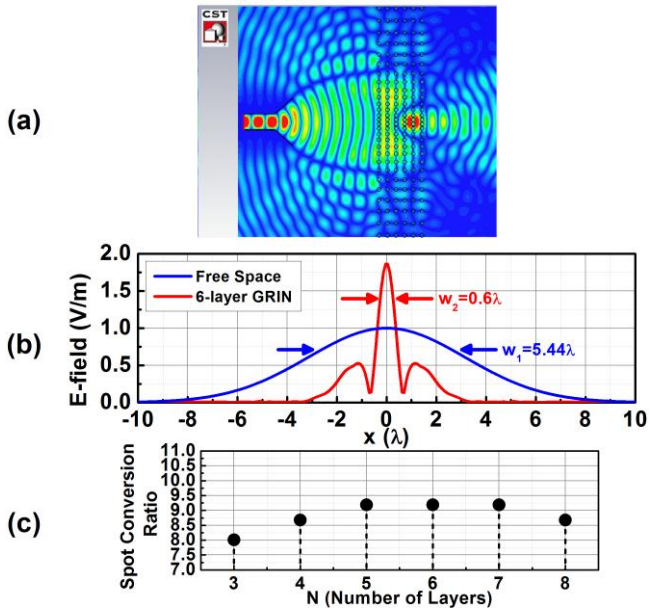

Figure 7.8: (a) The absolute values of the electric field distributions for the GRIN PC lens at $f = 17.7$ GHz. (b) The incident (blue line) and the output (red line) field distributions. (c) The spot conversion ratios vs. number of layers (*N*).

Moreover, such a focusing action has required only 6 layers, in contrast to the case in Fig. 7.2, which involved 32 layers. The comparison of the electrical lengths of the devices reveals that the structure in Fig. 7.2 and the six layered GRIN PC are similar in size. In fact, the structure in Fig. 7.2 is slightly shorter in terms of the electrical length. Yet, the nanofabrication of the GRIN PC that is based on the effective medium theory would be harder, if both structures were to be scaled up to work at the same operational wavelengths. It can be sorted out by revisiting the condition, $a \le \lambda_0 / (4n_0)$ at optical frequencies for the GRIN PCs in metamaterial regime. Apparently, the periodicity must be smaller than 45 nm at visible wavelengths for the effective medium GRIN PC. On the other hand, the smallest periodicity at the central

region of the GRIN PC in Fig. 7.3(a) is still slightly larger than 100 nm. Of course, it is assumed that these two distinct structures are still manufactured out of alumina rods.

The incident wave excites several Floquet-Bloch modes at this wavelength, which we also called the modified Hermite-Gaussian modes and their special interference mechanism at a current distance of 5*a* yielded the lensing effect. Thus, the outer fractions of the GRIN PC have also carried some portion of the incoming power. We think that this is the main reason of the accompanying side lobes at the exit side of the GRIN PC. Hence, these side lobes do not allow the wave at the exit interface to be diverged quickly. On the other hand, the lensing mechanism did not dictate the incoming power to be dispersed to the outer segments of the GRIN PC in Fig. 7.2. Consequently, the GRIN PC in Fig. 7.2 did not possess such elevated side lobes and in turn the outgoing wave diverged quicker.

In the end, a GRIN PC is investigated at short wavelength regime for lensing purposes. It is shown that a short GRIN PC with 6 layers can still be enough to properly focus the light at this operational regime. We have put forward an analogy in between the phase retardation mechanisms of the quadratic graded-index materials and the examined GRIN PC by investigating the dispersion results. It is identified that the supported Floquet-Bloch modes are the modified versions of the Hermite-Gaussian modes of the quadratic graded-index material. The lensing is due to the phase retardation mechanism which is typical for the GRIN structures. Accordingly, it is illustrated that lensing is a consequence of the multimode interference of the modified Hermite-Gaussian waves inside the GRIN PC around the approximated half pitch length. The propagating wave inside the GRIN PC is also decomposed into plane wave components through a Fourier analysis. Thus, the Fourier analysis results confirmed the number of the coupled Hermite-Gaussian waves. Furthermore, the same results give clues about the parity of the coupled modes and their relative phase velocities.

The studied GRIN PC is shown to be more compact than the corresponding designs in the metamaterial regime in terms of the physical length. Besides, much higher spot size conversion ratios are offered by the studied GRIN PC that operates out of the metamaterial regime. It is also discussed that working at higher bands relieves the nanofabrication difficulties at optical wavelengths. The studied GRIN PC is a candidate for not only enhancing the input coupling to the photonic crystal waveguides but also proves itself to be an output coupler, as well. The phase front transformation mechanism of the studied GRIN PC will be investigated within the context of beaming at the exit side of the photonic crystal waveguides as a future task in another study.

7.2 Graded-index photonic crystals as efficient input and output couplers

The presented results here will be submitted to Journal of Applied Physics.

Photonic crystal waveguides (PCWs) are arranged by forming line defects inside PCs. The detailed theoretical and experimental investigations on PCWs have demonstrated that such defects have the fundamental capability of strongly confining electromagnetic waves and thereby considerably reducing the losses of the propagating modes over the sharp bends with the aid of the Bragg reflection mechanism [165,166]. As a consequence, these key features have allowed PCWs to present superior performance characteristics over their dielectric counterparts in photonics, which have come to be fully appreciated by the research community. Subsequently, the problem of efficient coupling of the electromagnetic waves into the PCWs manifested itself due to the mismatch between the modes of the external light-wave circuits and the PCWs.

The poor coupling figures were attributed to the insertion losses triggered by the inadequate product of the overlap integrals of the regarding modes. Researchers have attempted to tackle this challenge through the

utilization of the genuine adiabatic mode conversion techniques. Numerous tapered PCW designs that facilitate the adiabatic mode conversion were put forward [167-171]. Conversely, J-couplers were suggested to address the same issue [172]. Even though these approaches showed promise for a significant improvement in the coupling efficiencies, they simultaneously led to serious drawbacks. Either bulky external configurations were needed as in the case of the J-couplers or they required complicated manufacturing steps for the tapered sections of the PCWs in which the adiabatic-shaping process of the incident mode demanded several layers to be sacrificed.

Independently, Lezec *et al.* had reported the successful employment of the surface corrugations around a subwavelength aperture, which made use of the surface plasmons in a transmission enhancement problem [62]. In a similar fashion, the surface waves were excited by exploiting the grating-like corrugations at the input interface of the PCW, which in turn assisted the funneling of the incident electromagnetic wave into the line-defect site [173-175]. Furthermore, the same strategy has been adopted at the exit side of the PCWs in order to attend to the out-coupling problems of the PCWs. Winn *et al.* had already theoretically pointed out that PCWs did not ideally support surface modes unless a supplementary intelligent modification was applied to the surface layers [176]. Leaky modes at the exit surface were created by altering the termination layers. Various modifications were proposed to achieve a directional beaming at the output side [177-179]. Such a spatially-confined, non-divergent beam turns out to be essential in the communication systems. These additional periodic corrugations can be considered as an array of Huygens emitters whose constructive interference results in highly collimated emission about the axis of the PCW. Likewise, strong resonators in the form of point defects were intentionally located around the exit of the PCW with the aim of taking advantage of the interference mechanism that again gave rise to the directional beams [180,181]. Concurrently, Frei *et al.* concentrated on the topology optimization of a PCW exit to maximize the directional emission [182]. Yet, all of these schemes were very much dependent on the termination

layers, hence alternative studies based on the self-collimated PCs were sought [183-185]. Self-collimated PCs eased the restrictions of the alignment difficulties in the optical circuits. Moreover, they played a role in the reduction of the reflections at the PCW exit, which were caused by the impedance mismatches.

Thus, we report improved not only the input but also the output-coupling efficiencies of a PCW incorporated with two GRIN PCs in the current study. The present study is originally intended to address several topics. Firstly, it aims to revisit the GRIN PCs as input couplers and reveal different aspects of the problem by attempting to present a more detailed perspective for the GRIN PCs under the light of the accumulated discussions in the scientific community. The second major objective is to show that the GRIN PCs are suitable also for producing beaming of light emanating from the exit side of the PCWs. It is illustrated that the combination of these two features can be accomplished by inserting the GRIN PC structures both to the front and back sides of the PCW. Hence, the present work sets forth a new concept to lessen the spatial broadening of the light that exits from the narrow apertures. The present study is organized by initially describing the electromagnetic wave propagation inside the GRIN PC while relying on the plane-wave expansion method (PWEM). Then, the finite integration technique (FIT) and finite difference time domain (FDTD) simulation results are laid out in order to particularize the focusing capabilities of the examined GRIN PCs. Subsequently, the out-coupling abilities of the GRIN PC are examined both numerically and experimentally. The physical mechanisms behind the directional emission properties of the GRIN PC structure are highlighted. Finally, the outcomes of the microwave experiments are provided to make fair comparisons with the theoretical predictions. The study is concluded with the discussions concerning the emergence of the directional beaming in distinct frequency bands.

The dispersion diagram for the studied PCW and the GRIN PC configurations are shown in Fig. 7.9(a) and (b), respectively. The operational

frequency (17.7 GHz) is very close to the air band of the PCW. However, a single mode of operation is still valid in the PCW example, whereas the bands have 9 crossing points that correspond to 9 different modes in the GRIN PC. After some inspection, it can be concluded that the first 5 modes (Ψ_{g1}-Ψ_{g5}) are superfluous solutions appearing due to the band folding in supercell PWEM results. Rest of the 9 modes (Ψ_{g6}-Ψ_{g9}) are real solutions with well defined spatial distributions inside the superlattice, which are shown in Fig. 7.10(b) and (d).

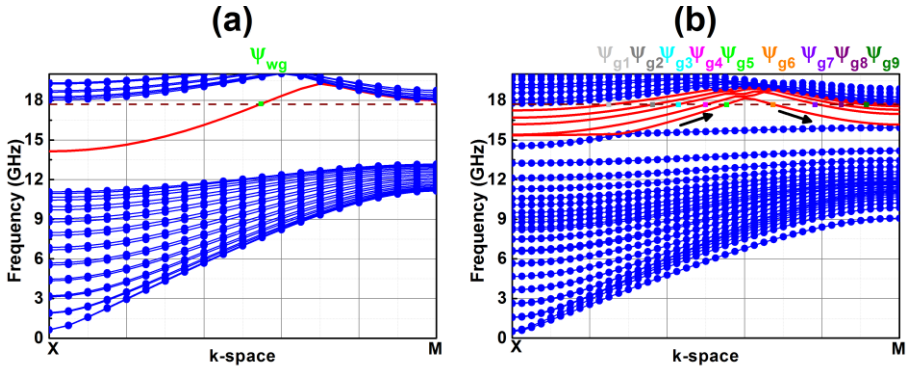

Figure 7.9: Dispersion results for (a) the PCW and (b) the GRIN PC. The intersected bands are plotted in red. The blue bands are the continuous bands. The sign of the slopes of the intersected bands are designated in (b) with the arrows.

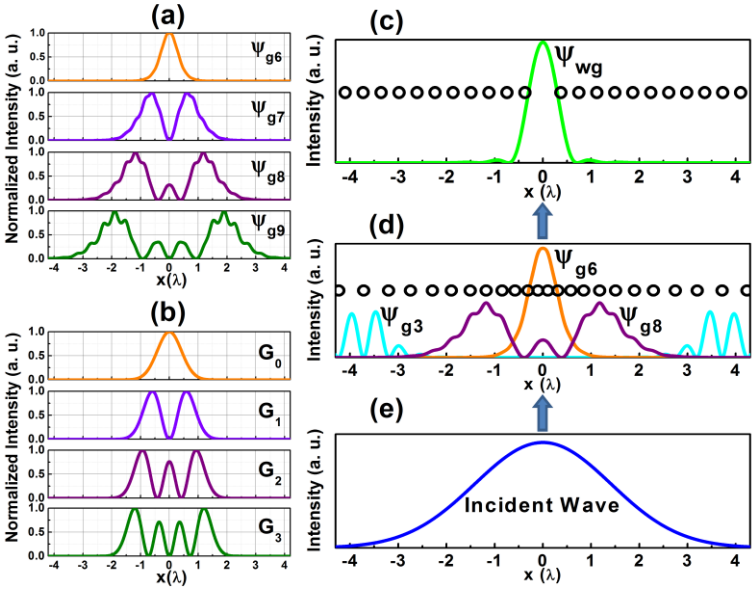

Figure 7.10: The mode profiles for (a) the GRIN PC, (b) the higher order Hermite-Gaussian beams at *f*=17.7 GHz. The mode profiles are plotted as they propagate inside the (c) PCW and (d) GRIN PC. The incident Gaussian beam is plotted as a reference point in (e).

The given role to the first GRIN PC is to focus a spatially wide incident beam into the narrow entrance of the PCW. This is feasible since there exist a noteworthy correlation between the fundamental mode of the GRIN PC, Ψ_{g6}, and the supported mode of the PCW, Ψ_{wg}, as it is suggested by Fig. 7.10(d). The Gaussian beam in Fig. 7.10(e) is plotted in order to represent the incident wave coming from the external light-wave circuits. The aforementioned mismatch between the mode of the PCW and the incident beam is more apparent when we compare the mode profiles of Figs. 7.10(c) and (e). On the other hand, the incident Gaussian beam in Fig. 7.10(e) excites modified Hermite-Gaussian modes such that a significant portion of the incident power is transmitted in the inner segments and the elevated overlap integral of the modes Ψ_{g6} and Ψ_{wg} yields promoted coupling figures with the utilization of the GRIN PC as an input coupler.

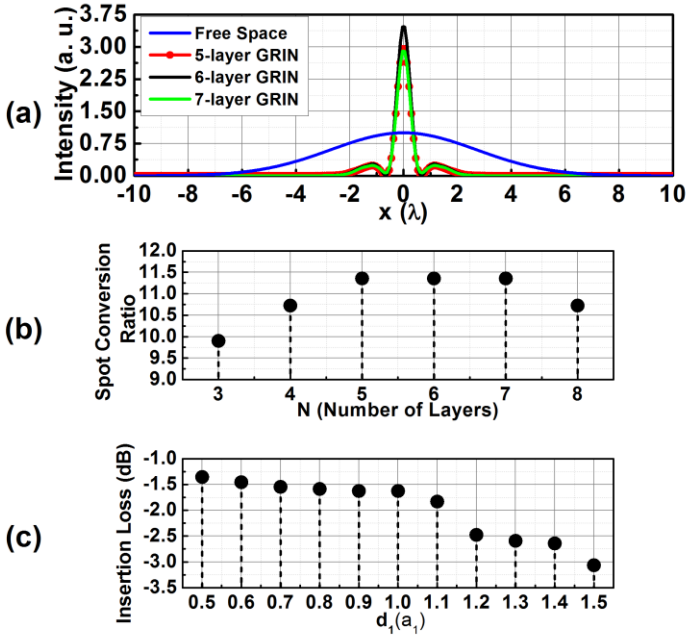

Figure 7.11: (a) The focusing capability of the GRIN PC at *f*=17.7 GHz. The intensity profile of a Gaussian beam in free space is shown with the blue color. The intensities at the exit side of the 5-layer GRIN PC (red line with markers), 6-layer GRIN PC (black line) and 7-layer GRIN PC (green line), respectively. The electric fields are calculated at a distance of $3a_1$ away from the PCW. (b) The calculated spot size conversion ratios for several values of *N*. (c) The calculated *IL* values a function of d_1. The *IL* values are calculated at a distance of 1.0λ away from the PCW.

Yet, the PWEM results were obtained assuming infinite periodic extension in the *z* direction till now. Thus, a single column of GRIN PC has been enough to deduce the physical mechanisms. However, in Ref. 186 it was discussed that the beam propagates in an oscillatory fashion for the infinitely extending problem. In other words, a spatially broad input pulse can be guided by consecutive focusing and defocusing actions inside the GRIN PC. This behavior is attributed to the oscillatory nature of the GRIN medium. The governing ABCD matrix equations have a periodicity of $2\pi/\alpha$, which is also known as the pitch length and α is the gradient coefficient as stated before. Then, the problem of termination becomes important. The GRIN PC must be truncated at a finite thickness. This thickness of the GRIN PC must be properly decided so that focusing must be observed at the output side with the employment of minimum number of GRIN PC layers. The FDTD results in Figs. 7.11(a) and (b) depict the focusing power of the studied GRIN PC as a function of the altered layer number, *N*. A spot size conversion ratio of approximately 11.4 can be attained with *N*=5, 6 or 7 layers. That is to say, a wide Gaussian beam with a full width at half maximum (FWHM) of 6.38λ is focused to a spot of 0.56λ. In the end, the choice of *N*=6 layers prevailed amongst the other options by intensifying the highest amount of electric field at the exit side. As a last remark, the transfer function of the GRIN PC lens differs from that of a conventional lens. It should be noticed in Fig. 7.11(a) that the output of a Gaussian pulse is not a real Gaussian, anymore. This point is going to be essential in the out-coupling of the light from the PCW.

Therefore, a 6-layer GRIN PC is placed in front of the PCW. The insertion loss (*IL*) figures have been numerically calculated and illustrated in Fig. 7.11(c) while varying the spacing between the PCW and the GRIN PC, d_1. The *IL* was calculated by taking the ratio of the following quantities:

$$IL = \frac{\int_{-14\lambda}^{+14\lambda} \mathrm{Re}\left\{E \times H^*\right\}_{\mathrm{GRIN+PCW}}\, dx}{\int_{-14\lambda}^{+14\lambda} \mathrm{Re}\left\{E \times H^*\right\}_{\mathrm{Free\ Space}}\, dx} \tag{7.8}$$

where a numerical integration scheme was applied to the calculated Poynting vectors at the same distance from the Gaussian excitation, along the simulation domain of 28λ in the x direction. The denominator gives the total incident power launched from the excitation source, whereas the numerator is equal to the coupled power to the exit side of the PCW. *IL* values as small as -1.35 *dB* have been observed. Another noteworthy consequence of this calculation is the invulnerability of the coupling mechanism to the abrupt changes in d_1 such that over 70% of the total power is coupled to the exit side as long as $0.5a_1 \le d_1 \le 1.0a_1$. This feature is quite handy for the experimental realization of the GRIN PCs as input couplers. Then, d_1 is set to $1.0a_1$. These parameters for N and d_1 are consistent with the previous studies in Ref. 132.

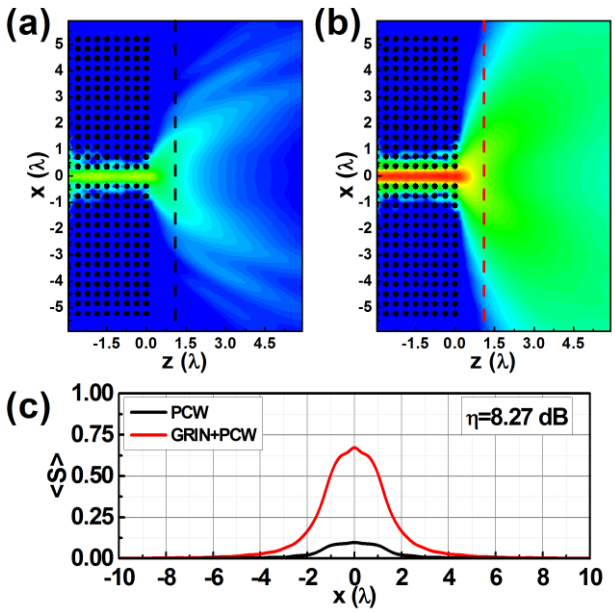

Figure 7.12: Time-averaged intensity maps at the exit of the PCW for the cases (a) without GRIN PC and (b) with GRIN PC at *f*=17.7 GHz. Intensity maps are plotted in logarithmic scale. (c) The distribution of the Poynting vectors along the *x* axis for the cases without GRIN PC (black line) and with GRIN PC (red line). The cross sections are shown with dashed lines in (a) and (b), which are located 1.0λ away from the PCW.

The GRIN enhanced coupling to the PCW is demonstrated in Fig. 7.12 in order to fully appreciate the efficiency of the GRIN PC as an input coupler. Figure 7.12(a) depicts the case without the GRIN PC, whereas the GRIN PC

aided coupling is shown in Fig. 7.12(b). The intensity maps have been plotted in the same scale. The Poynting vectors are once again integrated at the cross sections that are displayed in the regarding figures. The distribution of the calculated Poynting vectors at the cross sections can be found in Fig.7.12(c). The ratio of the two numerical integrals determines the coupling efficiency which is represented by η, following a similar formalism given in Eq. (7.8). Subsequently, there is an improvement of more than 6 times in terms of the coupled power at the exit side. The experimental validation of the improved coupling had been presented in our previous study [132].

Bethe had put forward theoretically in the mid 40s that the transmission of the light through tiny apertures was bound by the diffraction limit [33]. Once the higher-order effects coming from the finite thickness of the aperture are neglected, the aperture can be modeled as a combination of the equivalent magnetic and electric dipole moments parallel and perpendicular to the aperture, respectively. As a consequence, the light emanating from such subwavelength apertures would undergo a strong angular spread to fill out the whole 2π solid angle. In most of the cases, the defect site of the PCW can also be categorized as a subwavelength opening. Thus, the functionality of the GRIN PC as an output coupler is going to be discussed in this section. Intelligent ways of directing the outgoing radiation are going to be considered. The simulations are going to be supported with the experimental results.

The radiation profile is required to follow a narrow divergence angle at the exit side of the PCW in order to process the information effectively in the succeeding devices. Yet, the physical size of the PCW aperture is on the order of $\lambda/2$ (at 17.7 GHz), which turns the task into a challenging problem. The difficulty of confining the outgoing beam at the PCW exit can be seen in Figs. 7.12(a) and (b). So far, researchers have exploited the interference patterns of the induced surface waves and other resonators located in the vicinity of the PCW exit for the purpose of controlling the radiation of the PCW. Alternatively, we make use of a second GRIN PC positioned at the back side of the PCW to

alleviate the beaming of the out-propagating wave into a narrow divergence angle.

The trivial parameters that the divergence angle depends on are the wavelength and the aperture width. In addition to these ones, the shape of the wave front is critical. The planar fronts are more resistant to diffraction than circularly diverging wave fronts. Ideal plane waves and Bessel beams retain their spatial distribution transverse to the propagation direction. Hence, they have wave-front normals parallel to the propagation direction and they are known as the non-divergent waves. Accordingly, the GRIN PC structure enables us to transform the wave front into flat ones and allows the beam to couple to free space with a larger beam width. As a result, the radiated field is directed within a narrow divergence angle.

Several phase components were excited in order to facilitate the focusing behavior in the GRIN PC, as it is described in the previous section. The incident beam's wave front experienced a transformation that could be noticed in Fig. 7.8(a). Likewise, the GRIN PC is assigned to an inverse problem as an output coupler. The focused beam that is available at the PCW exit is expected to be reconstructed to a larger beam with plane-wave like features before being released to the air. FDTD simulations have been performed in order to determine the exact number of GRIN PC layers that would yield the best results. The following scheme has been practiced. For the equivalent problem in $z \geq 0$, the PCW radiation is modeled with a current source (in y direction) that has a subwavelength width of $w_0=0.2\lambda$. The electric field distribution map is shown in Fig. 7.13(a) in which the PCW is substituted with the predefined source. The current source results in spherical wave fronts and presents the worst-case scenario where the beam is spread out to the whole 2π solid angle by inducing an isotropic radiation. However, the divergence angle is significantly reduced with the inclusion of the GRIN PC. The results are plotted in Fig. 7.13(b). A 5-layer GRIN PC confined the out-going beam into a much smaller radiation cone. The relevant divergence angles have been found by fitting the out-going beam to

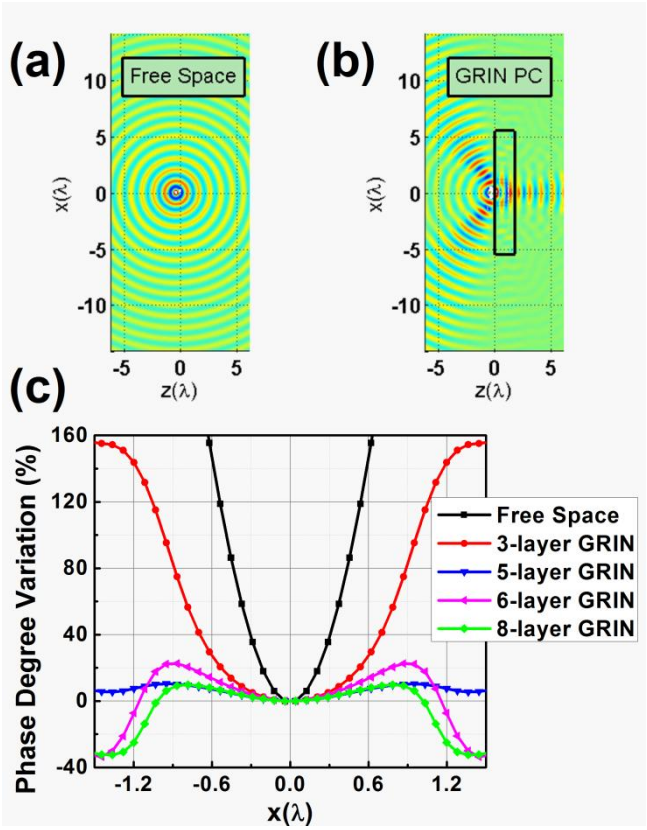

Figure 7.13: The electric field distribution map at f=17.7 GHz for a current source (a) in free space (video 1), (b) that is incorporated with a 5-layer GRIN PC (video 2). The illumination is handled with a current source that is 0.41λ away from the origin and has a width of w_0=0.2λ. (c) The phase variation with respect to the phase value at x=0 for different N values of GRIN PC. The phase fronts for different N values are inspected at 1.0λ away from the GRIN PC.

a Gaussian profile. These divergence angle values are estimated by finding the arithmetic mean of the instantaneous divergence angle values of the radiated field in z direction. Then, it can be deduced that a reduction of $\Delta\theta_0 \approx 40^o$ in the divergence angle is possible with the addition of the 5-layer GRIN PC, roughly. The wave fronts are plotted at a distance of 1.0λ away from the GRIN PC as the next step. The phase variation with respect to the phase value attained at x=0 point at the planar cross section is depicted in Fig. 7.13(c). The spherical wave fronts of the free-space radiation (black line) portray the maximum amount of phase variation at the planar cross section, as expected. The 3-layer GRIN (red line) can only pull down this variation to some extent. Yet, the 5-layer GRIN structure (blue line) promises the most planar wave fronts at the designated

location [the results for the remaining layer numbers are not plotted on the same figure for visualization purposes]. On the other hand, side lobes start to get noticeable in the field maps and multi humps appear for higher number of layers. This is the main reason of the deviations in the phase values along the planar cross section for higher number of layers.

In conclusion, the PCW is terminated with a 5-layer GRIN PC which offers planar wave fronts and a high divergence angle reduction at the same time. The 5-layer GRIN PC has the same b_0, n, Δb and a_1 parameters of the 6-layer GRIN PC at the input side. The overall schematic is given in Fig. 7.14. The separation between the PCW and the 5-layer GRIN PC is labeled as d_2. This quantity is going to be important in the process of out-coupling the light from the PCW and spatially confining the radiated beam.

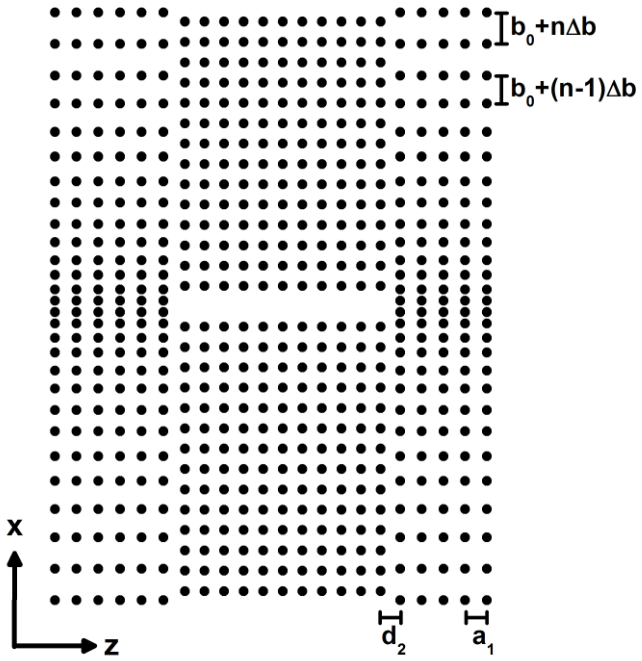

Figure 7.14: The overall schematic of the configuration (1st GRIN PC+PCW+2nd GRIN PC)

It had been shown in Ref. 186 that the width of the incident beam was one of the key factors that determined the trajectory of the incident beam in the quadratic GRIN PC. For large and small beam widths the incoming field converged or diverged, respectively. With that in mind, a similar behavior is

observed in our study. In contrast to the focusing action in the 1st GRIN PC, the beam width reached a larger value in the 2nd GRIN PC, intentionally. The spatially widened beam with plane-wave like features suffered much less from the broadening effects in air. Then, the choice of d_2 is critical because it automatically affects the beam width that is present at the input of the 2nd GRIN PC. The intensity maps have been plotted for a variety of d_2 values in Fig. 7.15. The case without the 2nd GRIN PC is shown as a reference in Fig. 7.15(a). The intensity distributions are exhibited at a cross section that is 6λ away from the surfaces for every configuration. As it can be seen in Fig. 7.15(d), the beam is once again focused at the exit side since a relatively large beam impinges on the 2nd GRIN PC. For $d_2=1.3a_1$, the spacing between the PCW and the 2nd GRIN PC starts to act as a waveguide, inadvertently. The beams are allowed to expand and enter the 2nd GRIN PC with a considerably large beam width. Consequently, the 2nd GRIN PC attempts to refocus this spread-out beam and focuses this irregular field confidently within the region $z\leq3\lambda$. However, the out-coupled beam does not possess plane-wave characteristics and its shape is altered as it propagates. This resembles the case in Fig. 7.15(b). The PCW and the 2nd GRIN PC is very close to each other. The beam enters the 2nd GRIN PC with the smallest width as opposed to the other scenarios. One could expect the largest divergence inside the 2nd GRIN PC, accordingly. However, several of the higher order modified Hermite-Gaussian modes are not excited at the outer shells at the same time. Then, it is not possible to reconstruct a planar wave front that will endure the broadening effects in air. On the contrary, the range $0.9a_1\leq d_2\leq1.0a_1$ presented the best results in Fig. 7.15(c) by yielding beams with shapes that are preserved as much as possible throughout the calculation domain. The beam's energy is in a way transferred more to the direction that is transverse to the propagation.

The need for a larger beam width at the entrance of the 2nd GRIN PC can also be inferred from our earlier claims. A Gaussian beam with a relatively large width had been focused in Fig. 7.11(a). Yet, the side lobes had also been observed around the focal point. For a bilateral system like our GRIN PC, we would need the contributions from the side lobes in order to accomplish the

inverse problem of the in-coupling case. However, the PCW mode is confined to a narrow region in Fig. 7.11(c). Then, it is apparent that the beam is required to expand in the lateral direction before being fed to the 2nd GRIN PC. Consequently, d_2 is a crucial parameter that controls the spatial distribution of the beam that is present at the input side of the 2nd GRIN PC.

We have defined a confinement factor in Fig. 7.15(e), which is a measure of the spatial confinement within a region of λ. First, I_0 is calculated at a λ distance away from the boundary of the 2nd GRIN PC, as depicted in Fig. 7.15(c). I_0 is the numerical integration of the intensity at the specified cross section. Then, the integral of the intensity within λ width [$I(z)$] is divided to I_0 in order to find out the confinement ratio as a function of z, which is also given in Eq. (7.9),

$$I_0 = \int_{-14\lambda}^{+14\lambda} \left|E(x, z=\lambda)\right|^2 dx,\ I(z) = \int_{-\lambda/2}^{\lambda/2} \left|E(x,z)\right|^2 dx, \ldots$$
$$\ldots \text{Confinement (\%)} = \frac{I(z)}{I_0} \times 100 \tag{7.9}$$

As far as the confinement factors are concerned, there is not a significant distinction between the cases presented in Figs. 7.15(b) and (c). Yet, the confinement factor conceals certain aspects. Although the energy percentage that is delivered within λ is almost the same, FWHM values of the profiles at 6λ are 2.76λ and 3.16λ for $d_2=0.9a_1$ and $d_2=0.5a_1$, respectively. The out-coupled beam stretches out more in Fig. 7.15(b). Furthermore, the peak value of the calculated intensity is 75% higher for $d_2=0.9a_1$ in comparison to the case with $d_2=0.5a_1$. One can extract more power from the PCW when the spacing is adjusted to $d_2=0.9a_1$. The superior out-coupling efficiency stems from the impedance matching at the PCW-2nd GRIN PC interface, which in turn reduces the reflections. The out-coupled beam sees a denser region for $d_2=0.5a_1$, whereas the same beam is tolerated to expand in the oblique direction for $d_2=0.9a_1$ and it perceives a relatively lower effective index with the addition of the outer regions. The figures have been plotted on the same scale. Then, the

reflections can be spotted in Fig. 7.15(b). The standing-wave formations are more pronounced inside the PCW owing to the back reflections occurring at the entrance of the 2nd GRIN PC.

The other observation concerns the transmission efficiency values, which are estimated to be the peak values of the intensity profiles at the cross sections. Then, it can be figured out that the transmission efficiency of the overall system is also elevated by 300% with the inclusion of the 5-layer GRIN PC, when we examine the calculated intensity values in Figs. 7.15(a) and (c). This value is comparable to the reported value in Ref. 173.

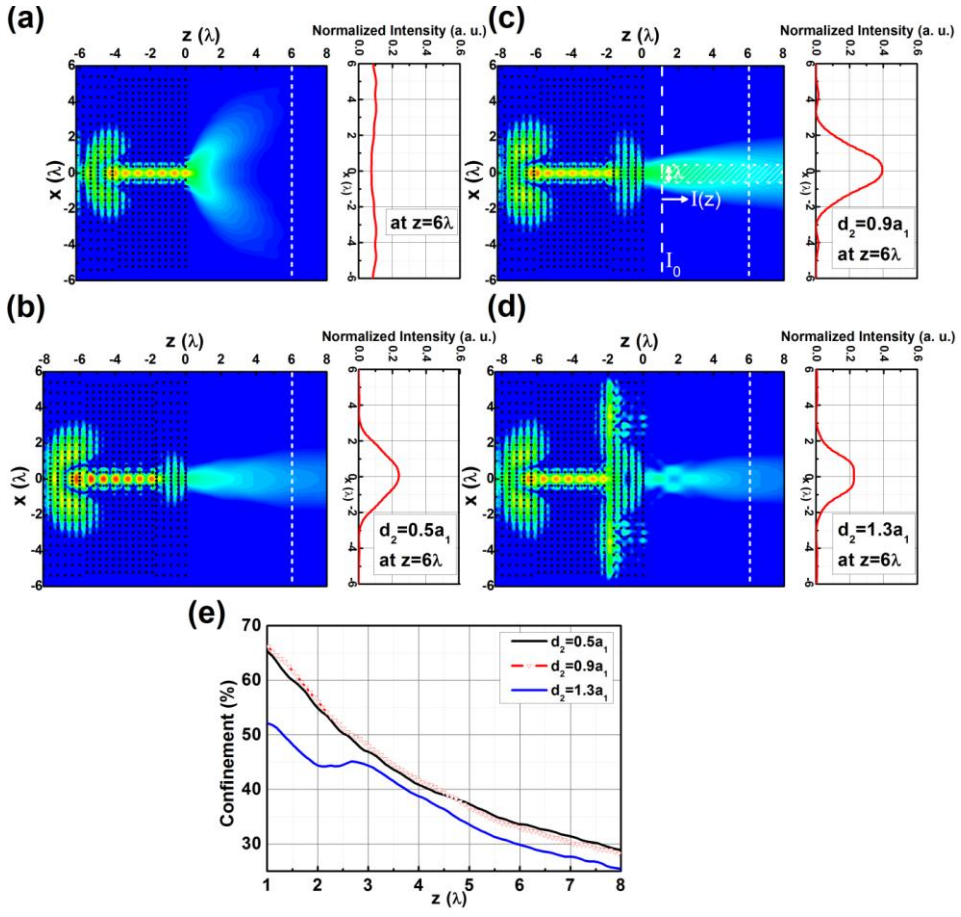

Figure 7.15: Time-averaged intensity maps at f=17.7 GHz in logarithmic scale when (a) the 2nd GRIN PC is not present, (b) d_2=0.5a_1, (c) d_2=0.9a_1 and (d) d_2=1.3a_1. The regarding intensities are plotted at slices 6λ away from the boundary of each configuration. (e) The confinement percentile of the intensities restricted to a width of λ have been shown for d_2=0.5a_1 (black line), d_2=0.9a_1 (marked red line) and d_2=1.3a_1 (blue line) as function of the propagation direction.

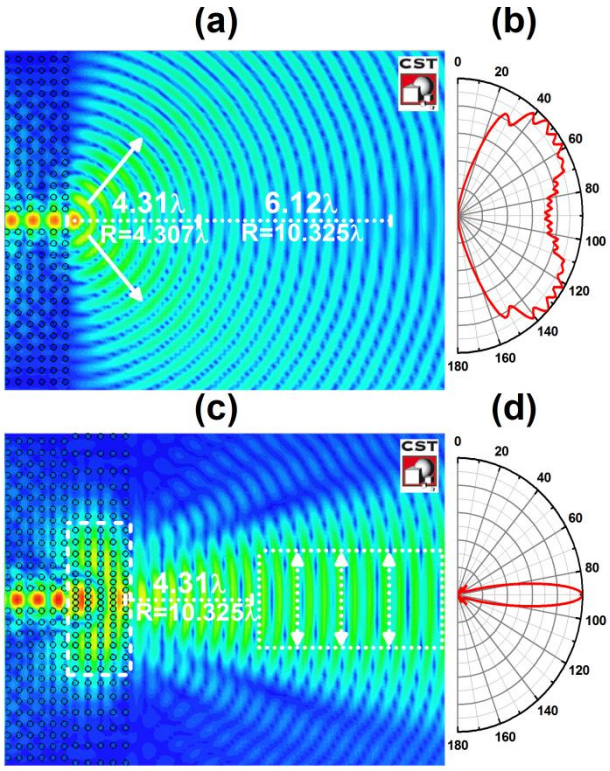

Figure 7.16: The absolute values of the electric field distribution maps at f=17.7 GHz for the case (a) without the 2nd GRIN PC and (c) the case with the 2nd GRIN PC. The corresponding far-field plots of the E-field are shown in (b) and (d) in linear scale. The arrows in (a) indicate the dominant plane-wave components of the outgoing beam. The radius of curvatures of the beams are inspected at 4.31λ and 10.43λ. The thick white-dotted region in (c) carries the significant portion of the out-coupled power while the wave fronts are comparatively planar, as implied by the arrows perpendicular to the propagation direction.

Figure 7.16 summarizes the issues that were covered in the previous paragraphs by illustrating the phase fronts. The far-field patterns are also depicted by employing a near-field to far-field transformation. The PCW radiates circularly diverging beams with a divergence angle $\theta_0 \approx 70^o$ [corresponding to the e^{-1} or in other words 36% of the fields in the radiation pattern in Fig. 7.16(b)], which is a spread-out beam like the modeled source in Fig. 7.13(a). The dominant wave vectors are heading to the directions equivalent to the radiation angles 45^o and 135^o, as indicated by the arrows in Fig. 7.16(a). As soon as the 2nd GRIN PC which comprises 5 layers with a spacing $d_2=0.9a_1$ from the PCW is employed, the radiation patterns are altered. The half-power beamwidth (*HPBW*) of the PCW emission is $HPBW=2\times67^o$ for the two lobes

centered around the 45^{o} and 135^{o}. On the other hand, *HPBW* is 14^{o} for the case with the 2nd GRIN PC. The emission is squeezed to a narrower region in the angle domain with the help of the 2nd GRIN PC which flattened the impinging circular wave fronts into more planar counterparts. There is almost 90% reduction in *HPBW* values. These values bring an improvement on top of the attained *HPBW* value in Ref. 181 and the *HPBW* reduction value in Ref. 180, in which the *HPBW* value was reported as 16^{o} and a 75% reduction in *HPBW* with respect to the PCW emission was realized, respectively.

The reversed action of the in-coupling problem takes place in the dashed area shown in Fig. 7.16(c). The phase retardation occurs by exciting several orders of the modified Hermite-Gaussian modes inside the 2nd GRIN PC. Then, the phase velocities of the lower order Hermite-Gaussian modes are trimmed down, as the dispersion diagrams and the analogous analytical solutions for the quadratic GRIN medium suggest. Consequently, the wave fronts lose their convex shape and become planar before departing the overall structure. The wave fronts naturally tend to get more planar as they propagate in the free space such that they can be treated as plane waves in the far field, whose radius of curvature (R) approaches infinity. Conversely, R of the beams emanating from the PCW at a distance of 4.31λ is $R=4.307\lambda$ and grows to be $R=10.327\lambda$ after having propagated for another 6.12λ. Yet, the case with the 2nd GRIN PC acquires the same value only after having traveled a distance of 4.31λ away from the surface. In a manner of speaking, the function of the 2nd GRIN PC is to carry the out-coupled beam more rapidly to the far-field zone without allowing it to spatially diverge.

The experimental setup contained a two-port Agilent 8720B Network Analyzer (NA) and two reciprocal standard pyramidal horn antennas with an operational frequency range from 12 GHz to 20 GHz. Alumina rods with a length of 15.4 cm were assembled in order to form the PC structures. The length of the rods was more than 8λ within the band of our interest (16–19 GHz),

which secured our case as a two-dimensional problem. Two sets of experimental setups have been utilized in the measurements.

The radial scans have been performed using the setup in Fig. 7.17(a). The transmitter antenna is placed 8 cm away from the GRIN PC, which is very close to the assigned value in the simulations. The transmitter antenna is located at such a close distance in order to prevent the unwanted contributions of the diffractions from the corners of the PC. The receiver antenna travels along two semicircular paths while recording the angular distribution in the *x*-*z* plane. Both of the antennas are carefully aligned with respect to the main axis of the overall structure. The area of the horn antenna aperture is 6.5×4.6 cm^2. Then, the Fresnel number (N_F) for the receiver antenna becomes $N_F = A_{\max}^2 / L\lambda < 0.8$ for every measurement distance and frequency, which implies that our receiver antenna is close to the Fraunhofer zone of the horn antenna [187]. Therefore, the collected radiation patterns are expected to be comparable to the calculated *H*-plane far-field patterns, as it is going to be discussed in the following sections. On the other hand, the PC acts as an antenna with a considerable effective aperture size [see Fig. 7.16(c)] while the beam abandons the overall structure and we are obliged to stay inside the Fresnel zone for a couple of meters.

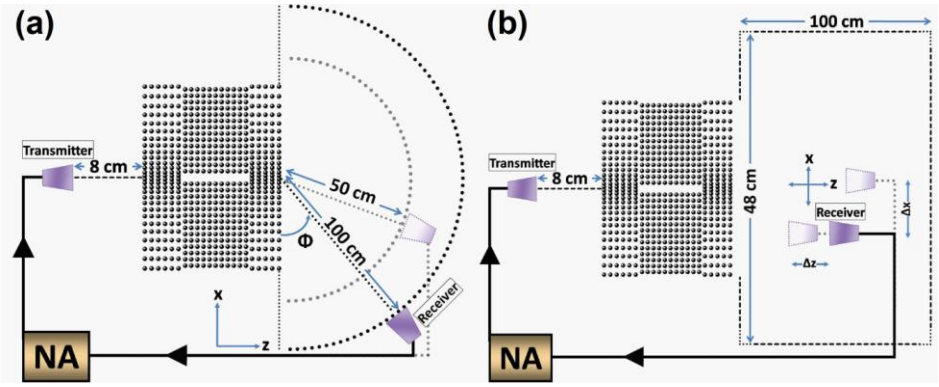

Figure 7.17: Schematic of the experimental setups, NA: Network Analyzer. (a) The radial scanning experiment, (b) *x*-*z* plane scanning experiment.

An *x*-*z* plane scanning has also been carried out. The near-fields are recorded with increments Δx=5 mm and Δz=15 mm. These two quantities are

smaller than λ for every frequency in our band of interest and thereby offer adequate resolution of the field distributions inside an area of 48×100 cm^2.

The radial scans within the frequency band of our interest are depicted as a function of the varied angle Φ in Figs. 7.18(a) and (b) at the measurement distances of 50 cm and 100 cm, respectively. In fact, both of the measurement distances reside in the Fresnel zone and the results of the measurement distance 100 cm are expected to be the Fractional Fourier Transform of the results at 50 cm. Indeed, the angular distribution of the beam has not dramatically changed its characteristics in Fig. 7.18(b) in comparison to Fig. 7.18(a). A refocusing at the output stage at the regarding distances is quite unlikely but still has to be taken into consideration for our configuration. Since the angular distributions are recorded in the near field, one cannot immediately distinguish the focusing and beaming phenomena just by considering the patterns at a single measurement distance. Figures 7.18(a) and (b) are presented in order to spot the beaming instantly. Then, the bands that are depicted in Fig. 7.18 as A, B, C and D are identified as the possible beaming frequencies.

Figure 7.18(c) illustrates the confined power within the angular distribution $\Phi=90^o\pm5^o$ (with respect to the z-axis) at each frequency. The confined normalized power is estimated by dividing the integral of the intensities within $\Phi=90^o\pm5^o$ in Figs. 7.18(a) and (b) to the whole summation of the intensities for each frequency slice. More than 60% of the power is confined inside 10^o at band A and C, which is comparable to the numerical findings presented in the corrugation assisted PCW in Ref. 178. The transmitted power values are slightly higher than the values reported by the research community [173,177,188]. Furthermore, there is a very good consistency between the confined power levels at 50 cm and 100 cm. The field patterns have not spread out or refocused even after having traveled for another 50 cm. These characteristics are not monitored at band B. Figure 7.18(c) discovers that the intensity patterns lose their conformity by making a comparison between the confined levels detected at 50 cm and 100 cm at band B. Then, the main

attention is paid to the bands A, C and D. The simulation results are shown on the same plot. There is a very good agreement between the experiments and simulations. Most of the features are also recognizable in the simulation results. Then, the corresponding beaming bands are labeled as A^*, C^* and D^* based on the simulation results. There is less than 100 MHz deviation between the peaks observed at the experiments and simulations. A, B, C and D are at 17.62 GHz, 18.05 GHz, 18.25 GHz and 18.44 GHz, respectively. Accordingly, A^*, C^* and $D^*$are calculated precisely at 17.7 GHz, 18.33 GHz and 18.4 GHz, in that order. A peak that can correspond to band B does not exist in the numerical results. The calibration processes of the simulation and experimental results are different. The intensity values of the calculated results are given with respect to the peak value of the launched beam from the source, which is 1 arbitrary unit. On the other hand, the magnitudes of the measured intensities are calibrated with respect to the free-space transmission results when the transmitter and receiver antennas are separated by a certain calibration distance, which is not the same value for the experimental setups shown in Fig. 7.17. The total length of the overall configuration is around 14 cm. Then, the calibration distance is approximately 22 cm for the setup in Fig. 7.17(b), whereas it is 72 cm and 122 cm for the radial measurements in Fig. 7.17(a) at 50 cm and 100 cm, respectively. As a result, the experimentally acquired intensity values are automatically higher than the obtained numerical counterparts. Therefore, a direct comparison of the magnitudes of the measured and calculated intensities does not provide an insight in the following sections. We have rather preferred to compare the overall characteristics, instead. The remaining discrepancies between the experimental and numerical results are attributed mainly to the difference in the excitation sources. A rather wide Gaussian beam that can cover the frequency band of our interest has been utilized in the simulations whereas the radiated fields of the horn antenna are expressed with complicated Fresnel Integrals [92]. Then, the impinging fields have quite different radius of curvature values, widths and intensity distributions. The other underlying distinctions originate from the difficulty of the manual alignment of the alumina

rods in the experiments and the proper adjustment of d_2 spacing whose electrical size directly affects the beaming phenomena [see Fig. 7.15]. It was already pointed out in Fig. 7.15 that the actual value of d_2 had a tolerance of less than 0.7 mm variation in the simulations at 17.7 GHz to sustain the high power collimation of the out-coupled beam.

The field patterns are depicted in Figs. 7.18(d) and (e) at bands A and C, respectively. The calculated far-field patterns of the horn antenna are given as a reference. The horn antennas that have been used in the experiments have directivity figures of $D\approx 11.3$ *dBi* (at 17.62 GHz) and $D\approx 11.57$ *dBi* (at 18.25 GHz) in the *H*-plane. The similar directivity figures confirm the bandwidth and suitability of our antennas for the investigation of the beaming in the frequency of interest. The measured free-space field patterns of the employed horn antennas at 100 cm are also given in the regarding figures. The measured angular distributions are very close to the calculated far-field patterns, which verify that the antennas are located near the Fraunhofer zone. It is apparent that the beam is confined within narrow angular distributions for these two bands. However, the characteristics of the evolution of the beam as it propagates are different. The angular resolution of the measurements is 1^o. Having said that, $HPBW\approx 12^o$ at 50 cm and stays almost constant for the measurement at 100 cm for band A, whereas *HPBW* shrinks down to 7^o at 100 cm for band C. The measured *HPBW* values at band A are consistent with the far-field patterns in Fig. 7.16(d). The beam travels with the same angular confinement in band A while yielding a constant directivity in the *x*-*z* plane. On the other hand, the spatial confinement is sustained in band C. The beam propagates with a smaller divergence. The measured *HPBW* value at band A still brings an additional improvement on top of the attained results in the literature [180,181] and it is comparable to the reported values in the experimental studies which also tackle the problem of out-coupling the wave from the PCW [173,189,190]. Consequently, the measured *HPBW* value at band C is a significant enhancement of the beaming in contrast to the previous studies, whose physical mechanism is going to be discussed in the following sections.

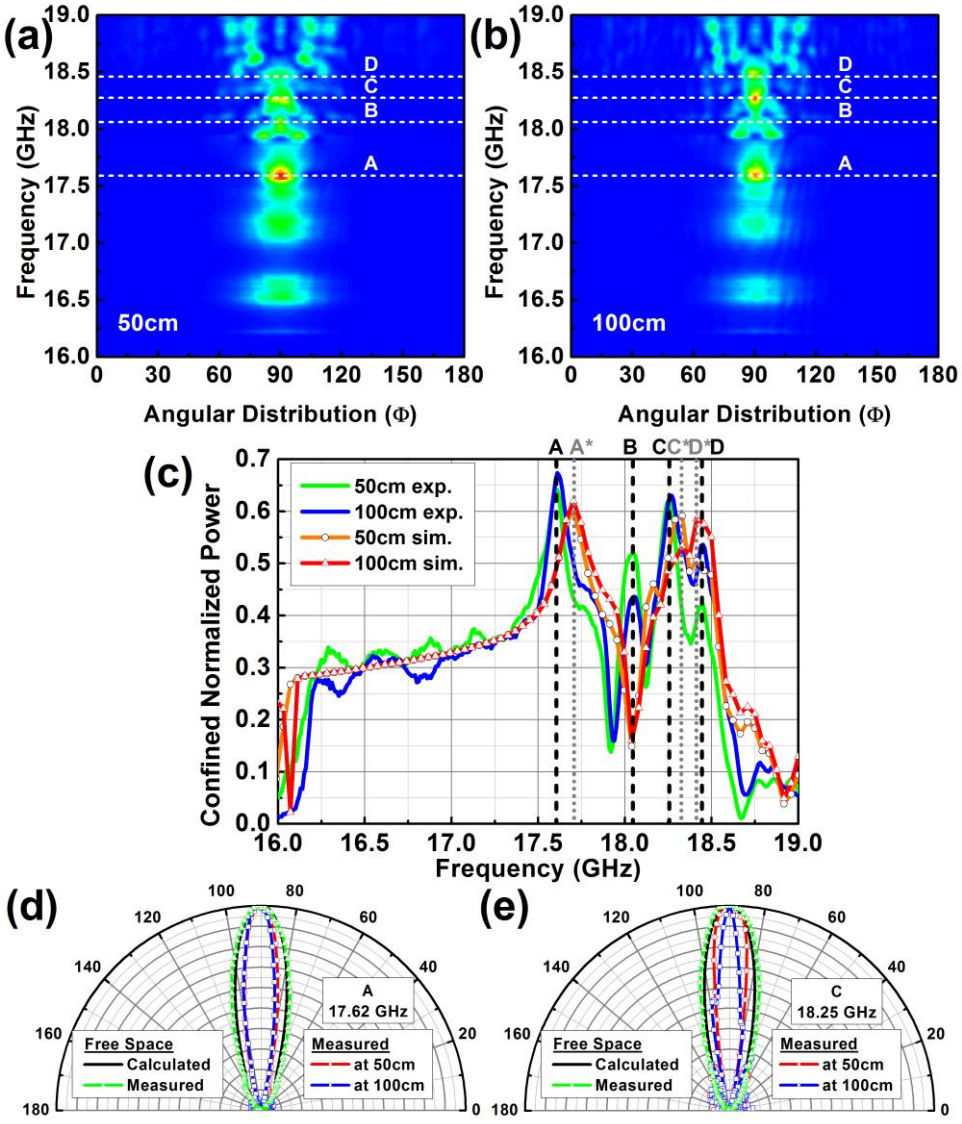

Figure 7.18: The angular distribution maps of the measured intensity profiles within the frequency of our interest (a) at 50 cm, (b) at 100 cm. The designated bands are A, B, C and D. (c) Confined Normalized Power inside $\Phi=90^{o}\pm5^{o}$. The experimental results for the measurements at 50 cm (light-green line), 100 cm (blue line) are shown together with the numerical results at 50 cm (orange line with markings) and 100 cm (red line with markings). The corresponding bands that are numerically calculated are labeled as A^{*}, C^{*} and D^{*}. The radiation patterns in the *H*-plane of the horn antennas for band (d) A and (e) C. The calculated far-field patterns of the horn antenna (black patterns) are given as a reference. The measured patterns of the horn antenna (light-green patterns) at 100 cm, the measured patterns of the out-coupled beam at 50 cm (red pattern with markings) and at 100 cm (blue pattern with markings) are also shown.

Figure 7.19 illustrates the numerical and experimental results of the out-coupled beams for bands A^{*} and A, respectively. The experimental results are

obtained by the scanning experiments. The FWHM of the intensity profiles are depicted in Figs. 7.19(b) and (e) for the regarding bands. The FWHM values of both the experimentally and numerically obtained intensities increase with a constant slope. The slopes are calculated as $\alpha^* \approx 13^o$ and $\alpha \approx 15.7^o$ for the numerical and experimental results, respectively. Even though the excitation sources are different, as it was mentioned earlier, the out-coupled radiation obeyed similar divergence courses, which underlines the harmony between the experimental and numerical results. The intensity profiles are plotted in Figs. 7.19(c) and (f). These profiles are the extracted results from the cross sections that are shown on the intensity maps. According to the demonstrated results, the out-coupled beam does not change its Gaussian shape. From one perspective, the patterns remind one of the Fresnel diffraction from a Gaussian aperture, for which the divergence angle is expressed as $\theta_0 = \tan^{-1}(\lambda / \pi w_{eff})$ beyond the Rayleigh distance. Here, w_{eff} is the effective aperture size of the emitted beam at the exit side of the 2nd GRIN PC. The divergence angle value for the experiments is found to be θ_0=15^o at band A, whereas the simulations yielded θ_0=11^o at band A*. This again points out to the agreement between the experimental and simulation results. The divergence angle had also turned out to be θ_0=11^o as indicated by the far-field patterns in Fig. 7.16(d), which is the same as the proposed value of the design examined in Ref. 174. Nonetheless, such comparisons should be made with caution since the divergence angle strongly depends on the operating wavelength for distinct devices. The main task of converting the diverging beam at the PCW exit to a wider beam has been accomplished. Accordingly, the beam emanating from the subwavelength opening of the PCW is transformed into a beam with a width that is equal to w_{eff}=1.64λ at band A* owing to the contributions of the modified Hermite-Gaussian modes. The original beam width was 0.51λ again at band A* for the PCW mode depicted in Fig. 7.11(c).

Special schemes had been adapted in Refs. 191 and 192 in order to generate a Bessel beam and the difficulty had arisen from the infinite *rms* width

of the Bessel beam. Hence, it had been shown that it was possible to transmit the incident beam up to 10 times distance further away with the configuration given in Ref. 191. The realized Bessel beams were resilient to the diffractions in accordance with the Helmholtz equation whose solutions implied planar phase fronts for such waves. Thus, Ref. 193 concentrates on the feasibility of controlling the radiation in 2D rather than 3D schemes [191,192] and mentions the consequences of the dimension reduction. A pseudo non-diffracting beam had been presented in Ref. 193, which is similar to the case considered in Ref. 194. Quasi-Bessel beams were produced in 2D, which preserved their shapes over long distances. Unlike the Gaussian-beam diffraction, the side lobes carried a significant portion of the power and shared the power of the central lobe. This prospect has been proven to be useful within the framework of the attainment of the reduced diffractive spreading of the beams emanating from the PCWs, as well. Similarly, it was emphasized in Ref. 180 that the side lobes with small amplitudes were needed for directional beaming at the exit of the PCW. Yet, the diffraction phenomenon depicted in Fig. 7.19 had a Gaussian nature at band A and lacked such side lobes. Consequently, we have detected the formation of the relevant side lobes at higher frequencies in our configuration (at bands C and D) and the spatial confinement was sustained successfully, as anticipated from the earlier discussions.

Figure 7.20 shows the calculated and experimental results for bands D^* and C, respectively. The extent of the spatial confinement of this slowly expanding beam can be immediately noticed by inspecting the variations in the FWHM values [Figs. 7.20(b) and (e)] or the intensity profiles taken from the designated slices [Figs. 7.20(c) and (f)]. The α and α^* values are dramatically reduced in contrast to the Gaussian diffraction portrayed in Fig. 7.19. The oscillatory contributions of the side lobes to the intensity profiles are evident at these higher frequencies. One explanation of this phenomenon could be constituted based on the dispersion results. The PCW starts to become a leaky waveguide with a worsened confinement factor at around 18 GHz. Then, the walls of the PCW can no longer be treated as perfect mirrors. This fact allows a

certain amount of the wave to propagate in the defect-free zones of the PCW. These waves are permitted to retain k components parallel to the propagation direction and impinge on the outer shells of the 2nd GRIN PC. Meanwhile, several additional higher-order modified Hermite-Gaussian modes are supported at higher frequencies in the GRIN PCs [see Fig. 7.9(b)]. Consequently, a good deal of the power is carried by the outer segments of the GRIN PC.

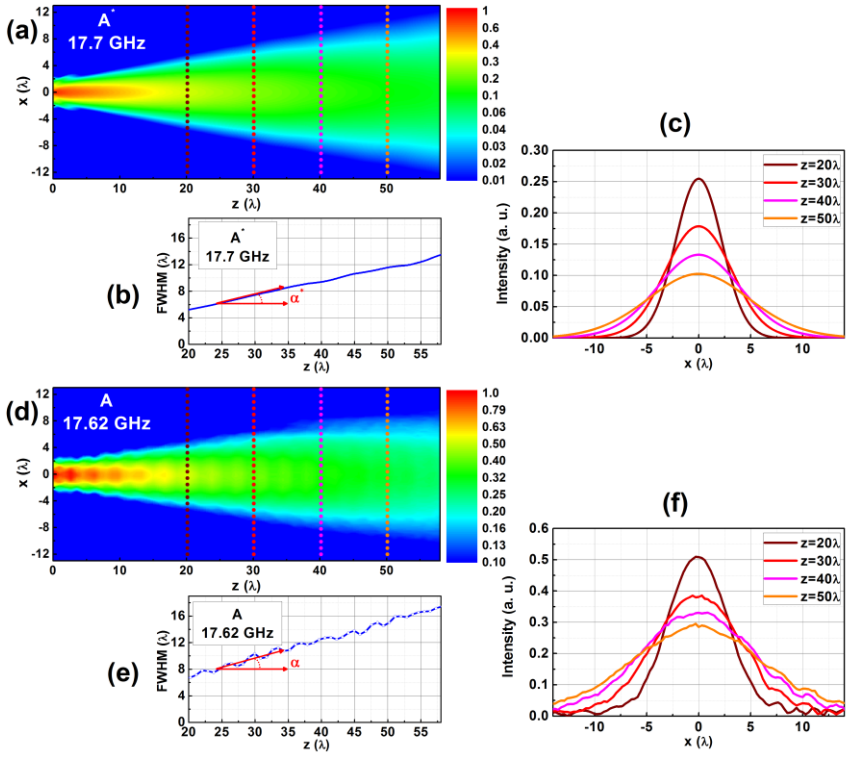

Figure 7.19: The numerical results of the out-coupled beam for band A*. (a) The intensity map of the out-coupled beam in logarithmic scale. (b) The FWHM values of the propagating beam. (c) The intensity profiles for the designated slices. The experimental results of the out-coupled beam for band A. (d) The intensity map of the out-coupled beam in logarithmic scale. (e) The FWHM values of the propagating beam. (f) The intensity profiles for the designated slices.

The 1st GRIN PC attempts to focus the incident beam. However, the electrical sizes of d_1 and the 1st GRIN PC are now altered and a beam with a wider profile enters the leaky PCW. There are three factors that play a part in the formation of a relatively wider beam at the entrance of the PCW. First of all, the pitch length of the GRIN PC differs from the case at band A, which is related to the electrical length of the GRIN PC. The beam follows a quite

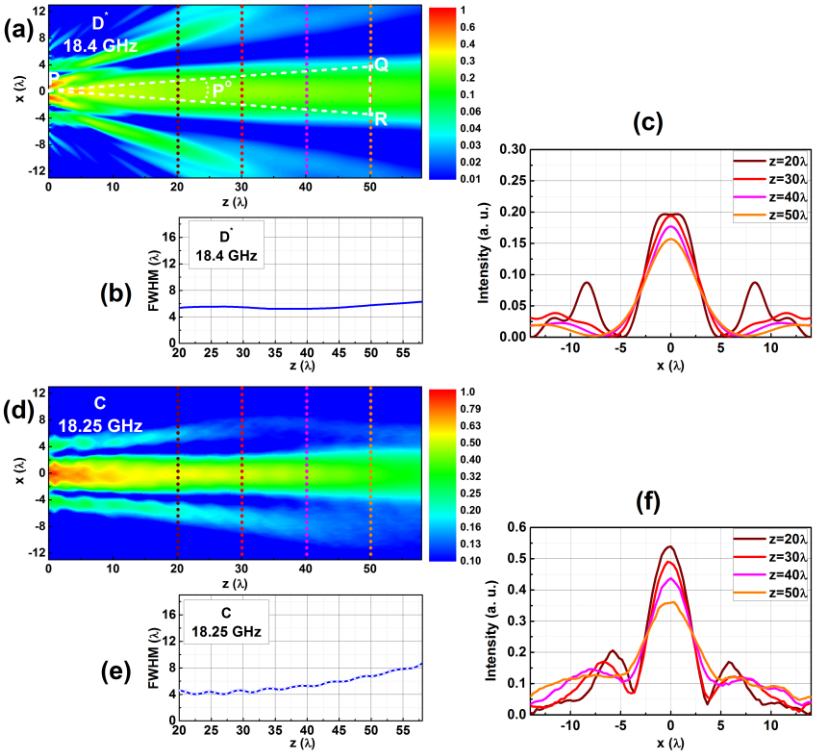

Figure 7.20: The numerical results of the out-coupled beam for band D*. (a) The intensity map of the out-coupled beam in logarithmic scale. (b) The FWHM values of the propagating beam. (c) The intensity profiles for the designated slices. The experimental results of the out-coupled beam for band C. (d) The intensity map of the out-coupled beam in logarithmic scale. (e) The FWHM values of the propagating beam. (f) The intensity profiles for the designated slices.

different trajectory. A bigger separation distance, d_1 (in electrical size) at the PCW entrance allows the beam to diverge further before being fed into the PCW. Lastly, the beam penetrates the outer shells of the GRIN PC at higher frequencies. The weakly confined beam is transmitted to the exit of the PCW. The electrical size of d_2 is also enlarged. Furthermore, the beam is diffused to the outer fractions of the 2nd GRIN PC. The majority of the beam power is emitted from the outer segments of the 2nd GRIN PC. The side lobes are created due to this fact. As a result, the observed limited diffraction phenomenon is a consequence of the special interference mechanism of the beam emanating from the 2nd GRIN PC, which is an analogue of placing resonant defects in the vicinity of the exit of the PC structure, as implemented in Ref. 180 and 181. Accordingly, the measured beam preserves almost half of the maximum

intensity at 30λ, which is an improvement over the recorded value at band A [compare Fig. 7.19(f) and Fig. 7.20(f)].

In the end, the configuration offers two bands of operation that possess different characteristics. The directivity figures stay constant and the angular distribution of the out-going beam remains the same at around band A. The 2nd GRIN PC has immensely decreased the divergence angle of the out-coupled beam by flattening the emitted wave fronts and widening the beam waist before being radiated into the free space. On the other hand, the spatial confinement is enhanced at around band C. The mechanism depends on the contribution of the side lobes in contrast to the wave-front retardation method employed at band A. These two bands can be explicitly seen in Fig. 7.21. P^o is defined in Fig. 7.20(a) as the angle that is associated with the side *QR* in the triangle *QPR*. Then, the normalized power that lies inside *QR* can experimentally take values as high as 0.76 at bands A and D, which is slightly better than the numerically attained values in Ref. 184 when $P^o=10^o$. This quantity is identified as the efficiency of the directional emission in Ref. 184 while the calculations are carried out at around 8λ away from the PC structure. Conversely, *QR* is located 50λ away from the 2nd GRIN PC, which brings a significant improvement over the presented results in Ref. 184. Additionally, the numerical results are depicted on the same plot. The simulation results are calculated at frequency intervals of 0.05 GHz. Conversely, the experimental results have been measured at frequency steps of 0.01 GHz. Even though there exist discrepancies between the experimental and numerical results due to the aforementioned reasons in the preceding sections, the general characteristics of the experimental and simulation based results are in agreement with each other. We accept the same formalism in Ref. 184 and define the acceptable bandwidth as within that the efficiency of the directional emission is greater than the 80% of the maximum efficiency. In that case, the bandwidth turns out to be 17.55 GHz<f<17.76 GHz around band A and 18.31 GHz<f<18.44 GHz around band D when $P^o=10^o$. The measured directional emission efficiency is approximately 35% even when

$P^{o}=4^{o}$, which implies that 35% of the total power can still collected at 50λ away by a receiver with a width of 3.5λ.

We have begun by inspecting the enhancement of the in-coupling figures with the addition of the 1st GRIN PC. We have recognized the important structural parameters such as the GRIN PC width and distance between the GRIN PC and the PCW. The GRIN PC promised a spot size conversion ratio of 11.4 and the utilization of the GRIN PC as an input coupler yielded insertion losses as small as -1.35 *dB*, while producing a coupling efficiency of 8.27 *dB* on top of the arrangement without the GRIN PC. Then, the out-coupling mechanism has been explored. It has been found out that the wave fronts of the beam are flattened before being radiated from the structure such that the divergence angle is dramatically reduced from 70^{o} to 11^{o}, while sustaining a 90% decrease in the *HPBW* values of the far-field results with the inclusion of the 2nd GRIN PC in contrast to the PCW radiation, solely. The transmission efficiency has been shown to improve 300% as soon as the 2nd GRIN PC is employed as the output coupler. The performance characteristics of the GRIN PC aided in/out-coupling has been compared with the reported topologies in the literature and it has been argued that the GRIN PC leads to superior features from certain perspectives. Finally, the simulation results are backed up by the experimental findings. The enhanced confinement of either the angular or the spatial distribution for the out-going beam has been confirmed by the experimental results at the associated frequency bands. The distinct physical mechanisms behind the directional beaming at these distinguished bands have been discussed. The significance of the side lobes has been underlined in order to accomplish a successful spatial confinement at higher frequencies. A directional beaming efficiency of 0.76 has been achieved experimentally at 50λ away. The *HPBW* values have shrunk down to 7^{o} while confining more than 60% of the total power inside $\pm5^{o}$.

Eventually, the in/out-coupling processes happen due to the wave-front transformation capability of the graded-index materials. The flexibility of

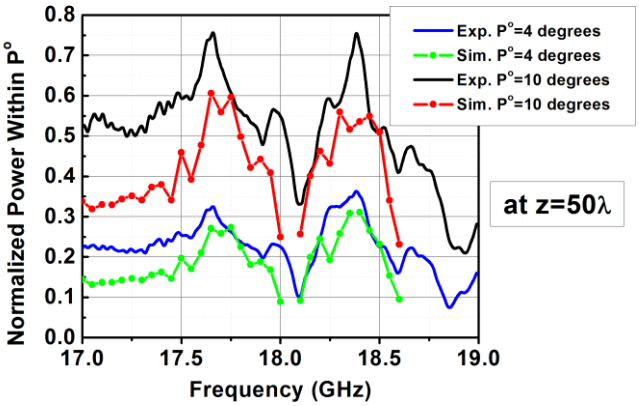

Figure 7.21: The measured (solid lines) and calculated (plots with markers) normalized power levels within the angle of P^o at 50λ measurement distance for the band of interest. The experimental results for P^o=4^o (solid blue line) and P^o=10^o (solid black line). The simulation results for P^o=4^o (green line with markers) and P^o=10^o (red line with markers).

producing large index gradient and the flat surfaces of the GRIN PC are the glaring properties of these materials as compared with the traditional lens-like medium. The GRIN concept shows potential for the negative-index lenses, too. A comprehensive study of the GRIN PC as input and output couplers at microwave frequencies have been the main focus of the presented paper. Yet, the feature sizes can be scaled up to optical frequencies at which such optical couplers can be realized with the conventional fabrication technologies. Nonetheless, the experimental complexities are likely to manifest themselves at optical frequencies in comparison to the microwave experiments. Several of these difficulties are going to be related to the alignment problems. Thus, future theoretical studies are going to address the problems that can be caused by the misalignment of the GRIN PC couplers with respect to the PCW in the lateral direction. The challenges originating from the non-idealities in the fabrication processes are going to be attended. It has already been shown in the present paper that the coupling mechanism is not strongly sensitive to the changes in d_1, whereas the out-coupling procedure dictated a narrower acceptable margin for d_2. The numerical aperture of the GRIN PC couplers is going to be determined precisely. Essentially, the PCW might already be dedicated for any particular purpose within the framework of optical signal processing. The PCW might be a

channel-drop filter, a waveguide bend or it might include resonant defects for slow-light applications. The fabricated GRIN PCs can be integrated with these PCWs to minimize losses, since GRIN PC formalism offers an advanced control over the trajectories of the electromagnetic waves. Finally, it is worth mentioning once again that a PC based GRIN relieves the restrictions on the compatibility issues with the PCWs and proposes a larger bandwidth of operation.

7.3 Cavity formation in graded-index photonic crystals along the transverse direction

So far, we have only investigated the transmission for the GRIN PCs along the lateral direction in the previous sections. Then, the propagation direction is automatically orthogonal to the grading, i.e. lattice modulation. However, the propagation in the transverse direction also offers promising results.

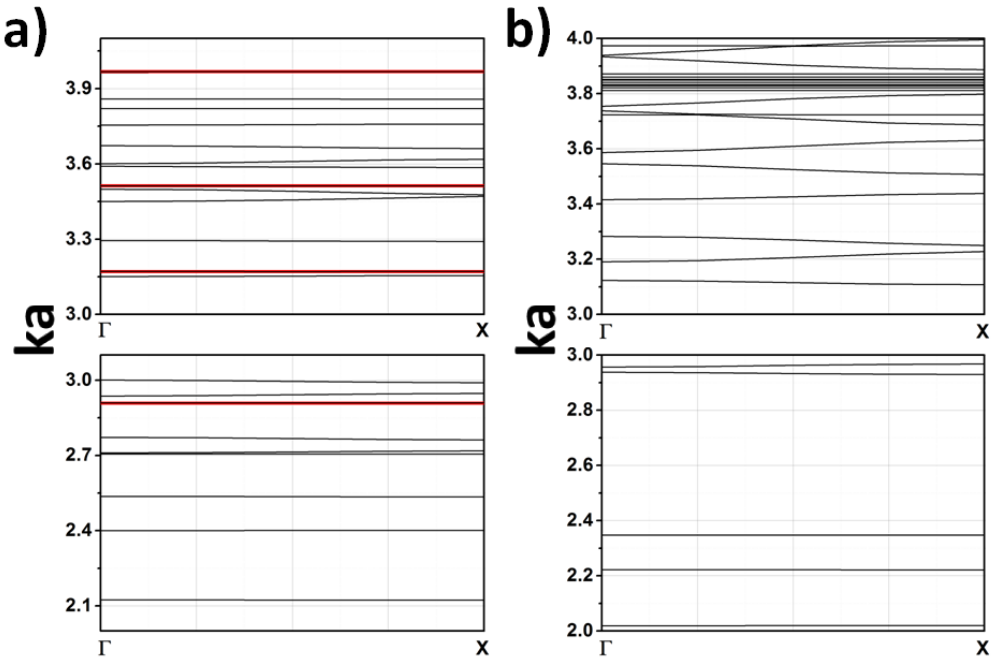

Figure 7.22: The dispersion graphs for the GRIN PC (a) (configuration A), (b) (configuration B). *y*-axis denotes the frequency values in the units of *ka*. (*a* is the unit lattice, *k* is the wave vector)

The dispersion graphs in the transverse direction are plotted in Fig. 7.22. It can be seen that the bands are extremely flat, which is a direct signature of the slow or cavity modes. These dispersion plots are computed for a supercell of 11x1 rods. Consequently, the structure is illuminated with a plane wave in FDTD simulations and the transmission results are shown in Fig. 7.23. The flat dispersion bands give rise to narrow peaks in the transmission spectrum. The locations of these transmission peaks coincide well with the flat bands in the dispersion graph.

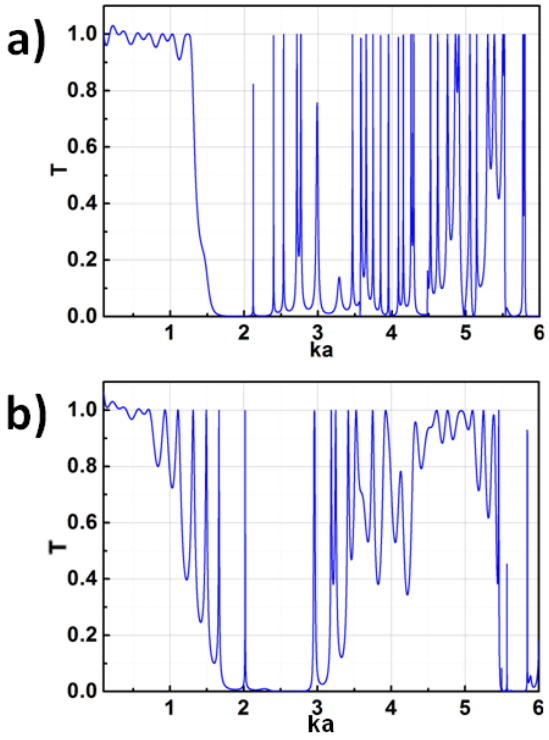

Figure 7.23: The computed plane wave transmission results for the GRIN PC (a) configuration A and (b) configuration B.

The field maps are shown in Fig. 7.24 for couple of the cavity like modes that are shown in the transmission spectrum.

The cavity-like modes are localized inside the inner regions of configuration A and B which are realized by modulating the filling factor in the transverse direction through either playing with the radii of the dielectric rods

(configuration A) or lattice spacing (configuration B). Once again, the alumina rods are utilized.

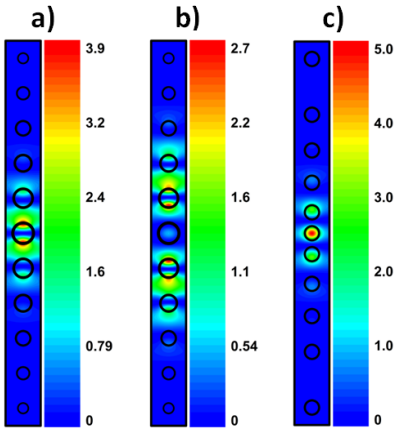

Figure 7.24: Field maps (electrical field) of the cavity-like GRIN PC (a) configuration A at *ka*=2.123, (b) configuration A at *ka*=2.4 and (c) configuration A at *ka*=2.019.

The cavity-like modes yield almost complete transmission in Fig. 7.23. The convergence problem of the simulation results is addressed in Fig. 7.25. The FDTD simulations converge to unity transmission with increased total simulation times. Hence, we can conclude that these modes enable total transmission, at least theoretically.

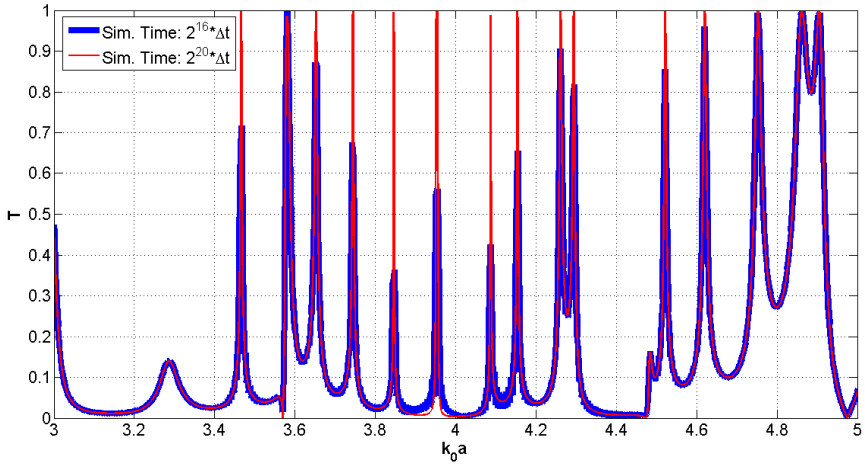

Figure 7.25: The convergence problem of the calculated transmitted values with FDTD for cavity-like modes in the GRIN PC (configuration A). The results of the exemplary two total simulation times ($2^{16}\Delta t$ – blue line and $2^{20}\Delta t$ – red line) are compared.

The quality factors for the first two peaks in configuration A's transmission spectrum were calculated using the decay of the energy inside the cavity and directly using the FHA (full harmonic analysis which is supported by RSoft). The peaks are so narrow that it is impossible to simply find out the Q factors using the frequency spectrum ($f_0/\Delta f$).

Then, the Q factor is extracted roughly by fitting it to an exponential function, as shown in Fig. 7.26. The quality factors, Q_1 and Q_2 are found to be 9336 and 3597, respectively for the regarding peaks. However, a FHA method is already provided by RSoft which gives better converged results for the Q factors. When they were used Q_1 and Q_2 turned out to be 8970 and 2936, respectively.

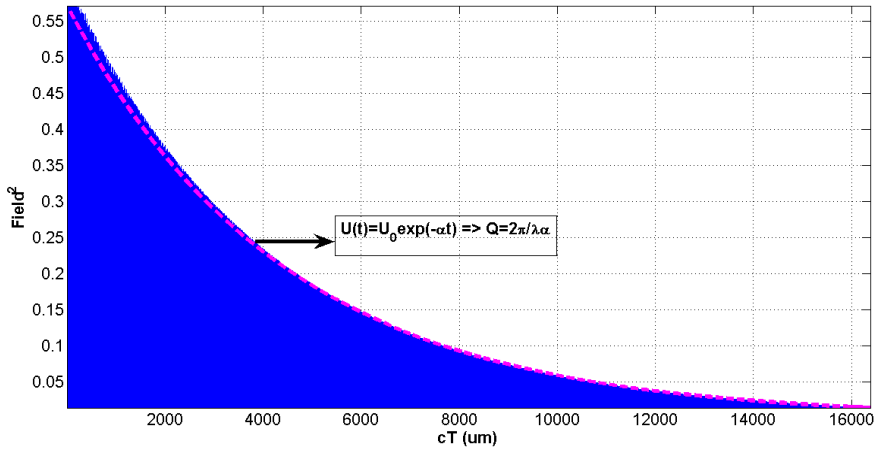

Figure 7.26: The energy decay for the cavity-like modes in GRIN PC (configuration A) *ka*=2.123. The energy decay is fitted to an exponential in order to figure out the Q factor.

7.4 Unidirectional transmission with photonic crystal gratings

This paper was published in Optics Express and is made available as an electronic reprint with the permission of OSA. The paper can be found at the following URL on the OSA website: http://dx.doi.org/10.1364/OE.18.022283

Systematic or multiple reproduction or distribution to multiple locations via electronic or other means is prohibited and is subject to penalties under law.

Realization of various functions in the optical and microwave frequency ranges leads to the demand in the devices with strong directional selectivity. In the limiting case of the directional selectivity such a device would allow (nearly) total transmission in one direction and no transmission in the opposite direction within the same propagation channel, which can be considered as the electromagnetic counterpart of a diode. The conventional approach to achieve the unidirectional transmission in passive devices is based on the use of the anisotropic [195-197] or nonlinear [198] materials. In particular, the strongly pronounced unidirectional transmission has been demonstrated for the one-dimensional photonic crystals (PCs) [199,160] and for the stacks of the two-dimensional PCs [195], in which anisotropic materials were utilized. Directional waveguides have been realized in PCs with broken time-reversal symmetry [196].

In the last years, the interest has been directed towards the potential of the structures, which are made of purely isotropic materials, in achieving strong directional selectivity. This directional selectivity might be similar, but not exactly the same as those achievable due to the anisotropy. In particular, it has been demonstrated that at a fixed angle of incidence most part of the energy of the incident plane wave can be transmitted from half space 1 to half space 2, while no transmission occurs from half space 2 to half space 1, provided that a PC grating is located in between so that the interface bounding half space 1 is only corrugated [200]. The transmission mechanism studied therein is based on exploiting the dispersion features of the PCs, which facilitate that the zero (reciprocal) order is not coupled to a Floquet-Bloch wave of the PC at a proper choice of the angle of incidence, while several higher diffraction orders may exist due to the effect of corrugations and may be coupled as long as the grating is illuminated from the side of corrugations.

The unidirectional transmission can be obtained for different types of dispersion of the PCs, which also include that corresponding to the ultralow-index media [201]. Therefore, it is not surprising to observe that the same unidirectional effect can be obtained in purely metallic non-symmetric gratings, as well as in the gratings comprising dielectric and metallic layers [202]. When we compare the results presented in [200,202-204], it can be inferred that the unidirectional transmission is also obtainable for the metallic slabs with the periodic branched slits at non-zero angles of incidence, which have been studied at normal incidence in [204]. Hence, the effect of the unidirectional transmission in non-symmetric gratings is rather general and can be obtained for various grating performances, provided that the corrugations, the dispersion, and the angle of incidence are properly chosen. In addition to the above-mentioned structures, the unidirectional transmission may appear, for example, in non-symmetric gratings based on one- and three-dimensional PCs. The unidirectional transmission can also be achieved in the specially designed combination of the two dielectric gratings, which enable the dramatic reduction of the contribution of the zero order [205]. Moreover, the asymmetric excitation of the surface plasmons on the metallic corrugated surfaces has been studied in [206,207]. Recently, another mechanism for the unidirectional transmission has been suggested, which is based on the excitation of the surface plasmons on the corrugated surfaces of the non-symmetric metallic gratings with a single slit [208].

In this study, we investigate the directional selectivity in the PC gratings in the microwave regime at beam-type illumination. In contrast to our earlier theoretical studies of the higher-order related unidirectional transmission, in which the consideration had been restricted to the plane-wave illumination, we focus on the validation of this mechanism for Gaussian-beam and horn antenna illuminations in the present study. The geometry of the gratings is similar to one of those studied in [200], but shows some differences in the shape and depth of the corrugations. The simulations and the microwave experiments are performed for a wide frequency range that involves the first five PC bands (Floquet-Bloch

waves), which are distinguished in terms of their respective dispersion features. The presented results include the transmission spectra of the examined structures for the plane-wave illumination, the frequency response of the transmittance for Gaussian-beam and horn antenna illuminations, and the angular distributions of the transmittance, at a proper value of the angle of incidence.

The PC grating has been designed by taking into account our previous experience with such structures, availability of the materials, and the existing experimental facilities. Since the studied mechanism is relatively new, it is worth while performing the first experiments by using horn antennas at the microwave frequencies. It is expected to be scalable down to much smaller frequencies. For the purposes of comparison, simulations for the Gaussian-beam and the plane-wave illuminations have been scaled to match the same frequency range. We decided in favor of the performance that is based on the square-lattice PC composed of alumina rods with a relative permittivity ε=9.61 and a diameter d=3.1mm. The lattice constant is a=7mm. The grating is assembled as an 8x100 array. Some of the cells were left empty by removing the rods at specific locations in order to obtain the corrugations at one of the interfaces.

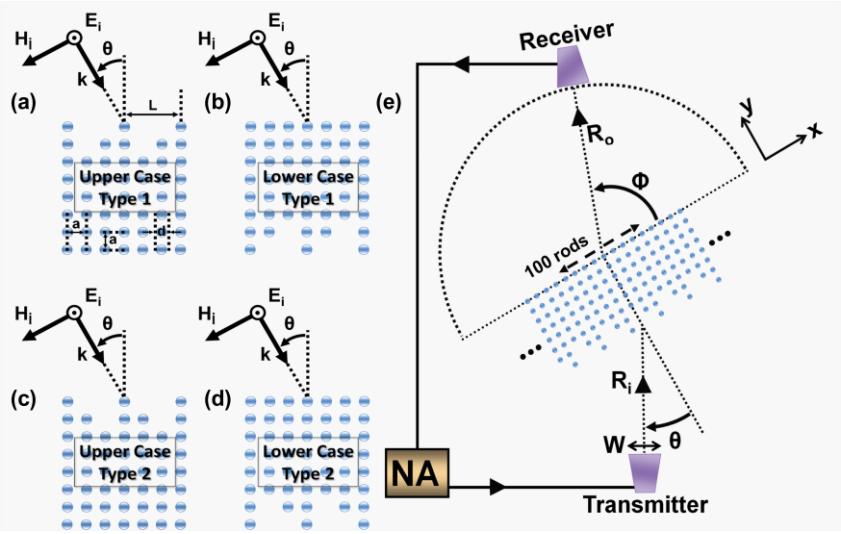

Figure 7.27: The geometry of the PC grating under study (two lateral periods are shown) – illustrations (a)-(d) and the schematic of the experimental setup – illustration (e). NA stands for the Network Analyzer, W represents the aperture size of the horn antenna.

Figures 7.27(a)-(d) schematically show the cases that will be studied in this study. Contrary to the PC gratings considered in [200], for which the grating period was $L=4a$, here we take $L=3a$. A reduction in the grating period assures obtaining a desired strong directional selectivity at smaller values of kL (k is the free-space wavenumber) while illuminating a smaller area of the input interface. Furthermore, the corrugations in Fig. 7.27 are placed asymmetrically with respect to the interface normal, which is also distinguished from the PC gratings studied in [200]. The grating that is seen from the side of the interface is associated with a *structured echelette*. Its asymmetry with respect to the interface normal offers two transmission regimes by switching between the two orientations of the interface "triangle", which can be handled by changing the sign of the incidence angle.

The experimental setup is schematically shown in Fig. 7.27(e). It contains an Agilent two-port 8510C Network Analyzer, and two standard pyramidal horn antennas with an operational frequency range starting from 16 GHz up to 30 GHz. The distances R_i=20cm and R_0=1m were used in the experiment. In this case, the input (illuminated) interface of the grating is located in the near zone of the transmitter antenna, while the incident wavefronts possess a significant curvature and the angular plane-wave spectrum of the incident wave is relatively wide. In fact, the transmitter antenna can be considered as a model of an optical source with a moderate directivity. Our study is restricted to the case when the electric field vector is parallel to the rod axes.

For the sake of definiteness, we refer to the PC interface without echelette-type corrugations as the non-corrugated interface throughout the study. In turn, the interface showing such corrugations is referred to as the corrugated interface. Strictly speaking, the non-corrugated interface represents itself as a periodic structure with a period of a. However, the non-zero diffraction orders may appear in this case at $ka>\pi$, which corresponds to $kL>3\pi$ and, hence, this range is beyond our main interest. At intermediate values of the angle of

incidence (θ), which are expected to be the most appropriate for obtaining a single-beam unidirectional transmission, the higher orders can be generated by the non-corrugated interface starting from even larger values of kL (e.g. at $kL>4\pi$ for $\theta<60^{o}$), so that the suggested terminology is quite reasonable for most of the considered cases.

First of all, the plane-wave transmission has been studied in order to justify the choice of the geometrical and the material parameters of the gratings in Fig. 7.27, and to provide a connection to the results obtained for the PC gratings in [200]. According to the general theory of diffraction gratings [209], transmittance is determined as follows:

$$T = \sum_{M}^{N} t_n \tag{7.10}$$

where t_n is n^{th} order partial transmittance, and M and N are the smallest and the largest indices of the propagating orders, respectively. Throughout the study, the transmittance is denoted with $T^{\rightarrow}$ for the cases when the corrugated interface is illuminated (upper cases in Fig. 7.27), and the notation $T^{\leftarrow}$ is used for the cases when the non-corrugated interface is illuminated (lower cases in Fig. 7.27). For all of the finite-thickness diffraction gratings, $t_0^{\rightarrow} = t_0^{\leftarrow}$ (reciprocal component) and $t_n^{\rightarrow} \neq t_n^{\leftarrow}$ (non-reciprocal components), if θ=const, $M \leq n \leq N$, and $n \neq 0$. At some special frequency values, the situation can be realized such that $t_n^{\rightarrow} = t_n^{\leftarrow}$ at $n \neq 0$. For the PC gratings [200] and the gratings containing metallic layers [202], the non-reciprocity of the non-zero (higher) orders can manifest itself so that $t_n^{\rightarrow} \neq 0$ but $t_n^{\leftarrow} = 0$ within a wide frequency range, while θ is kept constant. Therefore, if the zero order is not coupled to a Floquet-Bloch wave of the PC, the unidirectional transmission may be obtained, i.e., simultaneously $T^{\rightarrow} \neq 0$ and $T^{\leftarrow} = 0$, for a wide frequency range.

According to [200,202], a non-zero θ is required for obtaining a single-beam unidirectional transmission. Figure 7.28 presents an example of the

transmission spectra which are characterized by relatively large values of $T^{\rightarrow} \neq 0$ over relatively wide bandwidths. Five *kL*-ranges can be spotted in Fig.

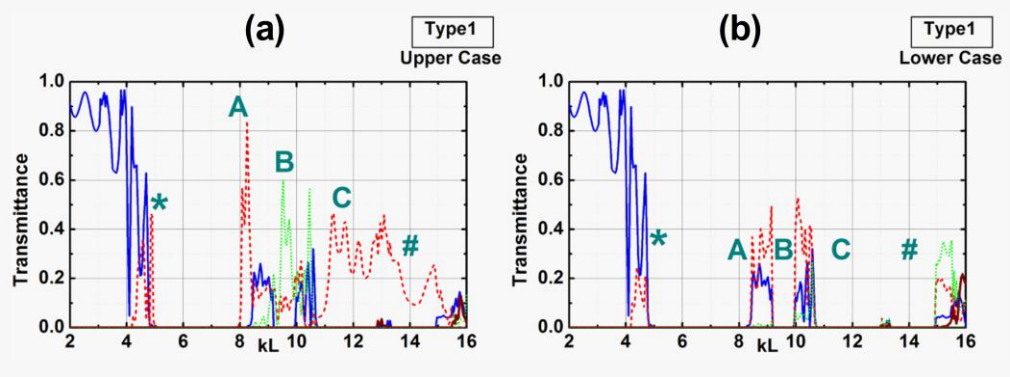

Figure 7.28: The transmittance for the cases shown in Fig. 7.27(a) – plot (a) and Fig. 7.27(b) – plot (b); solid blue line – zero order, dashed thicker red line – first negative order, dotted green line – second negative order, solid wine-colored line – first positive order; θ=30°.

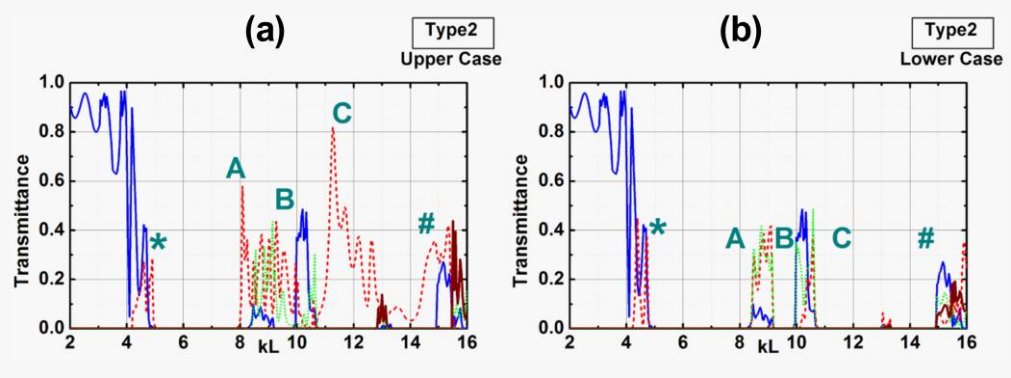

Figure 7.29: Same as in Fig. 7.28 but for the cases shown in Fig. 7.27(c) – plot (a), and Fig. 7.27(d) – plot (b).

7.28, where $T^{\rightarrow} \neq 0$ and $T^{\leftarrow} \approx 0$. They are centered nearly at *kL*=4.9, 8.1, 9.6, 11.8, and 14.1, i.e., for all of them $ka<2\pi$. Consequently, they can be labeled as the unidirectional passbands. The bandwidths of the regarding passbands are 3.5%, 4.1%, 7.8%, 18.2%, and 11.3%, respectively. Then, we have a single-beam unidirectional transmission $T^{\rightarrow} = t_{-1}$ except for the third lowest range. Based on the obtained results, we select the ranges of variation of *kL*, which are particularly interesting for the experimental study. The ranges which will be studied in detail are denoted by A, B, and C in Fig. 7.28. Among them, only the

ranges A and C correspond to the single-beam transmission. The range denoted by * is narrower than the range A, and it is characterized by smaller values of $T^{\rightarrow}$. Besides, the transmittance is weaker in the range denoted by # than in the range C. Moreover, the operational frequency range of our horn antennas for the specified PC parameters is most suitable for the ranges A, B and C, which mainly relates our main scope to these unidirectional bands.

In Fig. 7.29, the transmission spectra are shown at the same parameters as in Fig. 7.28, but the difference is that now the other side of the interface "triangle" is illuminated. It is seen that changing the illumination in such a way can result in a significant modification of the transmission within the ranges A, B and C, but does not lead to new unidirectional passbands. In particular, the maximal value of $T^{\rightarrow} = 0.82$ is obtained inside the range C at kL=11.26. This value is comparable with those obtained earlier for the two-dimensional PC gratings [200] and the special combination of the two dielectric gratings [205]. The location and, hence, the width of the unidirectional passbands are slightly different as compared to Fig. 7.28 owing to the different strengths of the diffraction and the different contributions of the individual diffraction orders. The results presented in Figs. 7.28 and 7.29 are obtained by using an integral equation method.

Figure 7.30 presents the isofrequency dispersion contours (IFCs) for the corresponding infinite PC with periods $a_x=a_y=a$, at several typical values of kL taken from for the ranges A and C. The horizontal dashed lines are assumed to be parallel to the non-corrugated interface. The signs "**+**" and "**–**" at the top depicts whether a diffraction order is coupled to a Floquet-Bloch wave or not in the upper case as in Figs. 7.27(a) and (c). On the other hand, the signs "**–**" and "**x**" at the bottom signify whether a diffraction order is not coupled to a Floquet-Bloch wave, or cannot exist at all in the lower case as in Figs. 7.27(b) and (d).

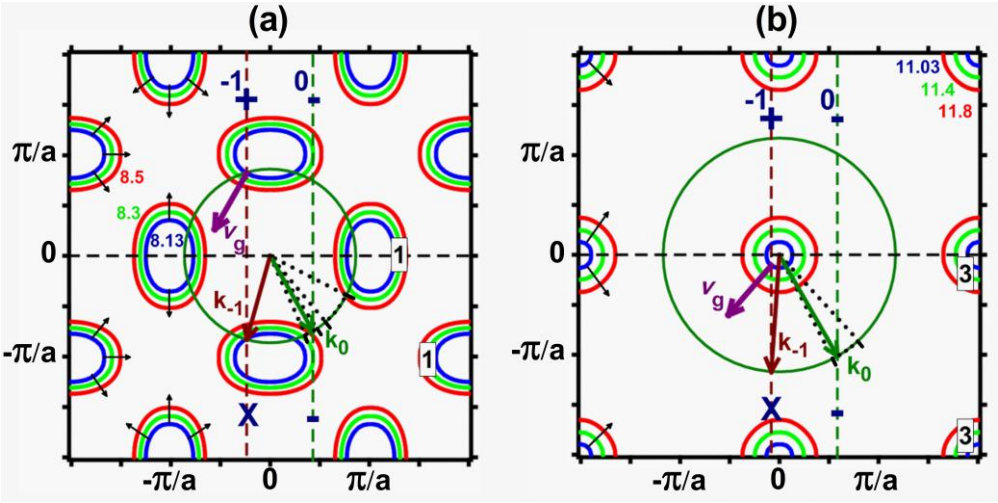

Figure 7.30: IFCs of the PC on the (k_x,k_y)-plane in the vicinity of kL=8.3 – plot (a), and in the vicinity of kL=11.4 – plot (b). The numbers of the PC bands (Floquet-Bloch wave numbers start from 0) are shown in the boxes. Thin arrows show the possible directions of the gradients that indicate the directions of the group velocity, v_g. The air IFCs (green circles), the construction lines (vertical dashed lines), the wave vectors of the diffraction orders, k_0 and k_{-1} (intermediately thick arrows) and the directions of v_g (thick arrows) correspond to kL=8.13 in plot (a) and kL=11.03 in plot (b). The vectors k_0 and k_{-1} and the directions of v_g are shown here at θ=30° and at the illumination direction depicted in Figs. 7.27(a) and (c). The dotted lines show the ranges of k_0, where the unidirectional transmission is expected to appear.

In Fig. 7.30(a), the dispersion is non-isotropic with the IFCs located around X point ($k_x=\pi/a$, $k_y=0$) of the irreducible Brillouin zone. Then, the zero order is not coupled if

$$k_{\min}^{(2)} > k_{\|} > k_{\max}^{(1)} \tag{7.11}$$

where $k_{\|}$ is the tangential component of the incident wave vector, $k_{\max}^{(1)}$ and $k_{\min}^{(2)}$ are the maximal k_x for the IFCs near $k_x=0$ and the minimal k_x for the IFCs near $k_x=\pi/a$, provided that $k_{\|} > 0$. At kL=8.13, Eq. (7.11) is satisfied nearly within the range 24°<θ<63°. In this range, $t_{-1}^{\rightarrow}$ may be non zero. Moreover, only the first negative order is coupled to a Floquet-Bloch wave at 24°<θ<33° and 40°<θ<63°, while the first and second negative orders both contribute to the transmission at 33°≤θ≤40°. In Fig. 7.30(b), the dispersion is nearly isotropic with 0<n_{eff}<1, i.e., the IFC for the PC is centralized around Γ point ($k_x=k_y=0$)

and it is narrower than the IFC for air. In particular, n_{eff} =0.11 at kL=11.03. In this case, Eq. (7.11) is satisfied already at θ>27°, while $k_{\min}^{(2)}$ is formally equal here to $2\pi/a - k_{\max}^{(1)}$. However, the range of θ where $t_{-1}^{\rightarrow} \neq 0$ and $t_{-1}^{\leftarrow} = 0$ is much narrower, because the IFC is very narrow. Here, it occurs within the range 27°<θ<47°.

Therefore, regardless of the differences in the IFC shape, the zero order cannot be coupled to a Floquet-Bloch wave at θ=30°. If the first negative order may exist in this case due to the shape of the input interface, it is the only coupled order in the upper case at kL=8.13 and kL=11.03. This is also true for the other kL values from the ranges A and C. The negative refraction is mimicked at the input interface in Fig. 7.30 by the only coupled order, i.e. by the first negative order, since $\mathrm{sgn}(\mathbf{v_g}\cdot\hat{x}) \neq \mathrm{sgn}(\mathbf{k_0}\cdot\hat{x})$. It is interesting that in contrast to the PCs with non-corrugated interfaces, e.g., see [210,211], the negative refraction can be achieved in the presently studied PC gratings not only without a left handedness, but also with a positive effective index of refraction, as seen in Fig. 7.30(b). Furthermore, the single outgoing beam must be negatively deflected because $\mathrm{sgn}(\mathbf{k_0}\cdot\hat{x}) \neq \mathrm{sgn}(\mathbf{k_{-1}}\cdot\hat{x})$. On the other hand, neither the negative refraction at the input interface nor the negative deflection of the transmitted beam appear when only the zero order is coupled, as it occurs for small positive θ. Note that the IFCs in Fig. 7.30 are analogous to those in Figs. 3 and 13 in [200], where they are presented for a PC with similar parameters. In turn, the IFCs for the range B (not shown here) are similar to those in Fig. 7.33 in [200]. In this case, they are nearly flat and located around Γ and M points, where M point corresponds to $k_x=k_y=\pi/a$. Furthermore, in accordance with our earlier claims concerning Figs. 7.27 and 7.28, the second negative order is also coupled together with the first negative order in range B. Thus, we do not observe a single-beam unidirectional transmission regime around these kL values at θ=30°.

The Gaussian-beam illumination is considered in this section, which is in some sense an intermediate step between a plane-wave and a horn antenna

illumination. We utilize a Gaussian beam with a width of 10a, whose source is located R_i=20cm away from the input interface, while the transmittance is calculated at a distance R_0=1m away from the output interface, see Fig. 7.27(e). For the chosen beam width and distances, the plane-wave nature of the incident wavefronts is still strongly pronounced. Nevertheless, we should still take into account the effect coming from the finite-width angular plane-wave spectrum of the incident Gaussian beam, which implies the contribution of the other angular components associated with an angle different from θ.

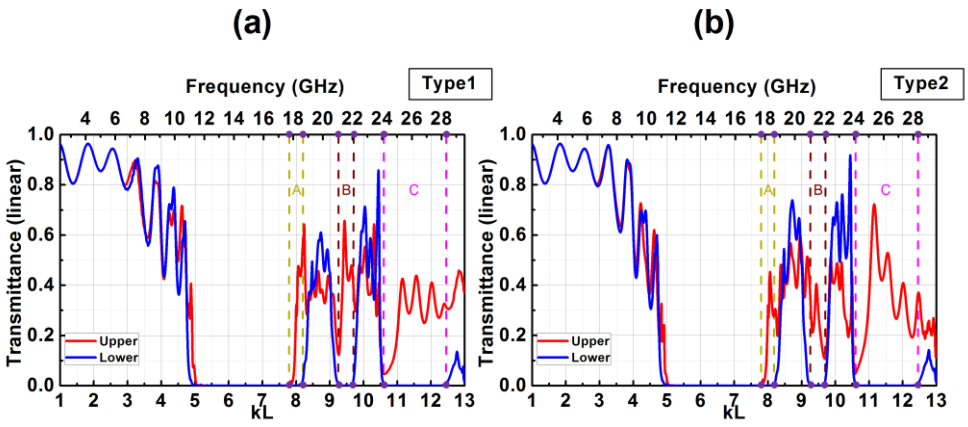

Figure 7.31: The integral transmittance at the Gaussian-beam illumination: left plot corresponds to Figs. 7.27(a) and 7.27(b), right plot corresponds to Figs. 7.27(c) and 7.27(d); solid blue line - the illumination is from the non-corrugated interface (Lower), red line – the illumination is from the corrugated interface (Upper); θ=30°.

An FDTD code has been used for the simulations. In Fig. 7.31, the integral transmittances, $\tau^{\rightarrow}$ and $\tau^{\leftarrow}$ are presented as a function of kL for all four cases from Figs. 7.27(a)-7.27(d). They are calculated as follows:

$$\tau^{\rightarrow} = \frac{1}{\pi}\int_0^{\pi} T^{\rightarrow}(\Phi)d\Phi, \text{ and } \tau^{\leftarrow} = \frac{1}{\pi}\int_0^{\pi} T^{\leftarrow}(\Phi)d\Phi\,. \qquad (7.12)$$

In fact, if $\tau^{\rightarrow}$ (red lines) and $\tau^{\leftarrow}$ (blue lines) are calculated in the far zone, they represent analogs of $T^{\rightarrow}$ and $T^{\leftarrow}$ at a beam-type illumination. In contrast with Figs. 7.28 and 7.29, the contribution of the individual orders cannot be specified here. However, the basic features are the same in Figs. 7.28,

7.29 and 7.31. The ranges of the unidirectional transmission, A, B, and C, are centered now nearly at kL=8, 9.46, and 11.5 in both Fig. 7.31(a) and Fig. 7.31(b), i.e., they show nearly the same locations as the plane-wave illumination in Figs. 7.28 and 7.29 suggests.

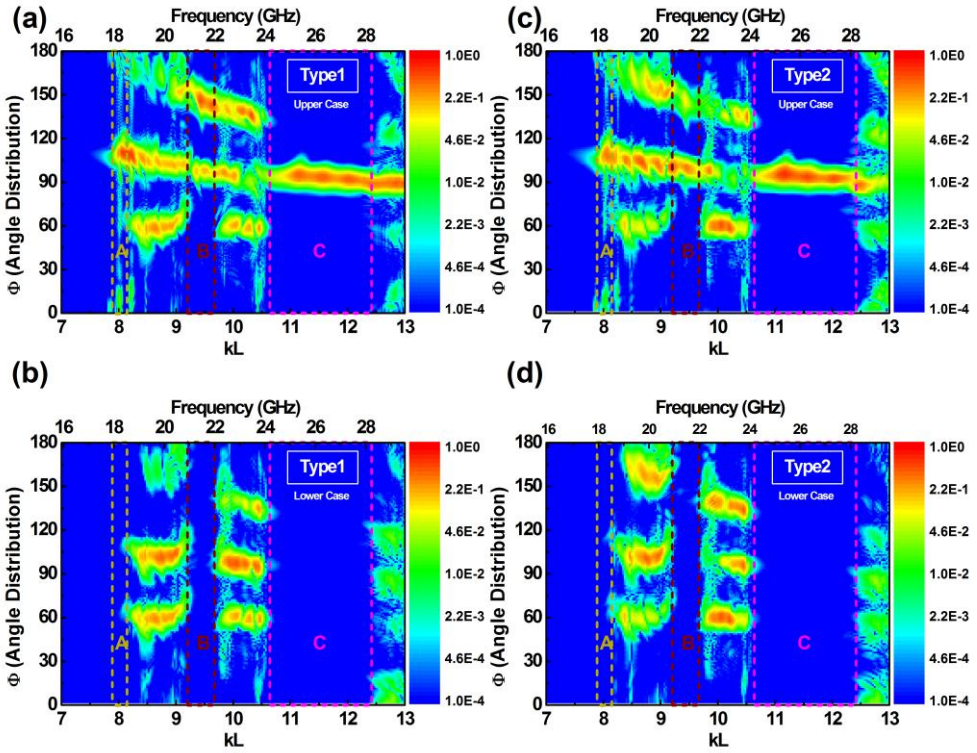

Figure 7.32: Transmittance (in logarithmic scale) at the Gaussian-beam illumination on (kL,Φ)-plane: plots (a), (b), (c) and (d) correspond to Figs. 7.27(a), (b), (c) and (d), respectively; θ=30°.

Figure 7.32 presents $T^{\rightarrow}$ and $T^{\leftarrow}$ on the (kL,Φ)-plane, at the same Gaussian-beam illumination as in Fig. 7.31. Here, Φ is the observation angle that is defined in Fig. 7.27. This type of a presentation of the results allows us to associate the basic transmission features with the contribution of the individual diffraction orders. One can immediately distinguish the areas where the transmission is strong in the upper case but very weak in the lower case by comparing Figs. 7.32(a) with 7.32(b) and Fig. 7.32(c) with 7.32(d). These areas are located inside the ranges A, B, and C, which are bounded here at the same kL values as in Fig. 7.31. The angle of diffraction of the n^{th} order in the transmission half-space is determined from the following equation:

$$\phi_n = \sin^{-1}(\sin\theta + 2\pi n / kL) \tag{7.13}$$

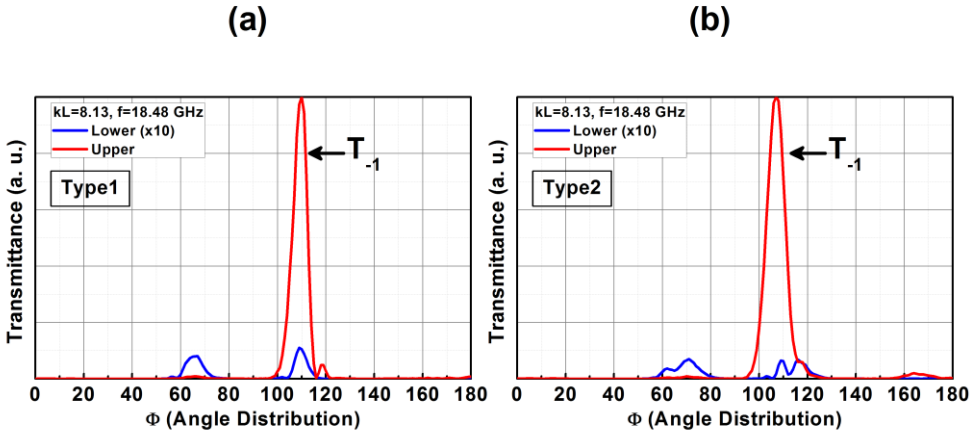

Figure 7.33: Angular dependence of the transmittance at a frequency value from the range A: plot (a) corresponds to Figs. 7.27(a) and (b), plot (b) corresponds to Figs. 7.27(c) and (d); blue line – the non-corrugated interface is illuminated, red line – the corrugated interface is illuminated; R_i=20cm; θ=30°.

The diffraction angle, ϕ_n in Eq. (7.13) is measured in the clockwise direction from the *y*-axis, it is connected to the observation angle, Φ, as ϕ_n=-Φ+π/2. Then, one can easily see that the lowest-Φ areas of significant transmission in Fig. 7.32 should be associated with the zero order (Φ=60° corresponds to ϕ_n=30°). In turn, the middle (85°<Φ<120°) and the most upper (Φ>130°) areas correspond to the first-negative-order and the second-negative-order transmission. Although the boundary between the areas of the strong and weak transmission is blurred, the appearance of the strong directional selectivity is well demonstrated. In Fig. 7.32, the range C seems to be the most promising candidate for the experimental verification of the unidirectional transmission not only because it is wider than the ranges A and B, but also because of the better isolation from the weaker transmission coming from the adjacent areas. Note that the absolute transmission values are depicted in Fig. 7.32. A pulse function in the time domain has been employed as the source in order to attain the transmission values over a wide frequency range. The monitored intensity values that are collected 1m away from the exit side of the PC are normalized

with respect to the free space transmission results for each *kL* value, and thereby the problem originating from the inefficiency of the pulse function to excite a relatively wide frequency range in a balanced manner is overcome.

Figure 7.33 presents *T* vs Φ, which has been calculated at a selected frequency value that is taken from the range A. The strong contrast between the forward and backward transmittance is well seen by comparing the blue and red lines. Next, we focus our attention to the location of the peaks of *T*. It is noteworthy that a peak arising at $\Phi=\pi/2$ would correspond to $\phi_n=0$, i.e., to the case when the n^{th}-order transmitted beam propagates along the *y*-axis so that $\mathbf{k_n}\cdot\hat{x}=0$. At least at large distances away from the grating, the cases of $\phi_n>0$ and $\phi_n<0$ correspond to the transmitted beams with $\mathbf{k_n}\cdot\hat{x}>0$ and $\mathbf{k_n}\cdot\hat{x}<0$, respectively. Furthermore, a significant lateral beam shift can appear at the output interface. If $\Phi-\pi/2+\phi_n>0$, the negative shift should manifest itself in angular location of the maximum of *T*. If $\Phi-\pi/2+\phi_n<0$, the positive shift takes place. According to Eq. (7.13), $\phi_{-1}=-15.8°$. In turn, at the maxima of *T* in Figs. 7.33(a) and 7.33(b), we obtain Φ=110° and Φ=107°, respectively. Hence, the angular deviation for the beam-type illumination turns out to be $\zeta_{-1}=\Phi-\pi/2+\phi_{-1}=4.2°$ in Fig. 7.33(a) and $\zeta_{-1}=1.2°$ in Fig. 7.33(b). The observed negative shift qualitatively coincides with the predictions based on the wave vector diagram in Fig. 7.30(a). The effect of the corrugation shape and the orientation of the interface on the value of ζ_{-1} and on the lateral shift at the output interface will be studied in a forthcoming study.

In Fig. 7.34, the angular distribution is presented at the same *kL*-value from the range C, for which the wave vector diagram was plotted in Fig. 7.30(b). Here, $\phi_{-1}\approx-4°$, so that the outgoing beam should propagate in the direction that is nearly normal to the output interface. In turn, Φ=95° and $\zeta_{-1}\approx1°$ in both Fig. 7.34(a) and Fig. 7.34(b). Thus, the obtained results are in qualitative agreement with the wave vector diagram. In this case, both the mimicking of the negative refraction at the input interface and the negative deflection of the

transmitted beam take place. Moreover, the transmission contrast is very strong. In particular, at the maximum of $T^{\rightarrow}$ (red line), we obtain $T^{\rightarrow}/T^{\leftarrow} = 1.75\times10^{4}$ in Fig. 7.34(a) and $T^{\rightarrow}/T^{\leftarrow} = 2.07\times10^{4}$ in Fig. 7.34(b).

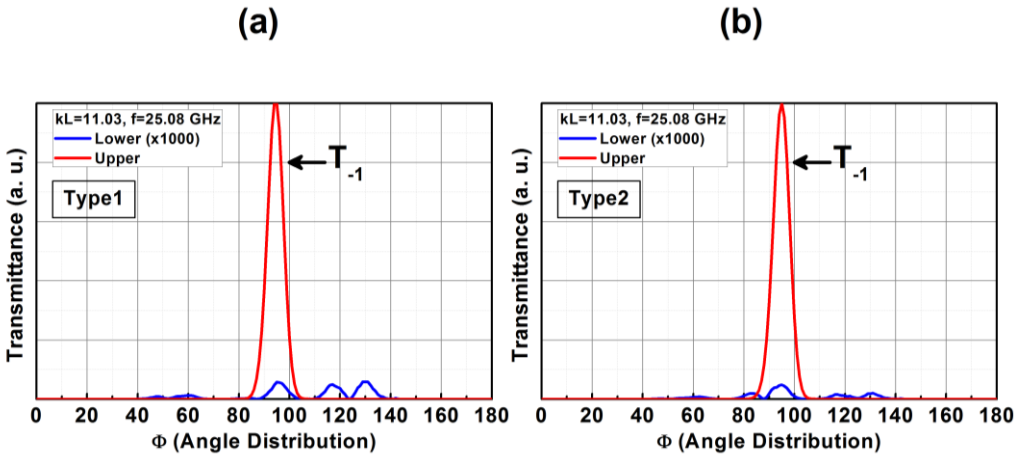

Figure 7.34: Same as Fig. 7.33 but for a frequency value taken from the range C.

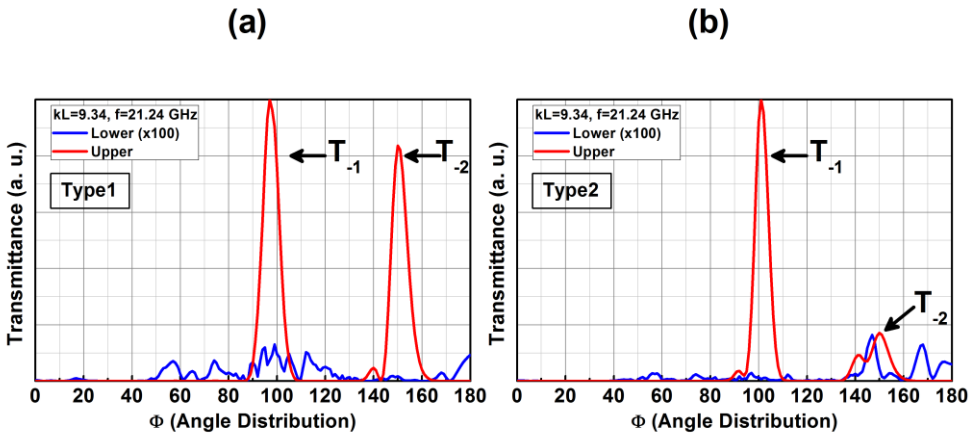

Figure 7.35: Same as Fig. 7.33 but for a frequency value taken from the range B.

For the comparison, Fig. 7.35 shows the angular distribution for the *kL*-value taken from the range B. Here, in contrast to Figs. 7.33 and 7.34, two higher orders are coupled to a Floquet-Bloch wave at the input (corrugated) interface, and thus two beams appear in the transmission. According to Eq. (7.13), ϕ_1=-9.95° and ϕ_2=-57.7°. In turn, from the simulation results, we obtain Φ=97° and Φ=150° for the first and second peaks of *T* shown by the red line in

Fig. 7.35(a), and Φ=101° and Φ=150° for the first and second peaks of T shown by red line in Fig. 7.35(b). Correspondingly, $T^{\rightarrow}/T^{\leftarrow}=1.34\times10^{3}$ and $T^{\rightarrow}/T^{\leftarrow}=5.42\times10^{3}$ for the first and second peaks in Fig. 7.35(a), and $T^{\rightarrow}/T^{\leftarrow}=1.43\times10^{4}$ and $T^{\rightarrow}/T^{\leftarrow}=192$ for the first and second peaks in Fig. 7.35(b). The extent to which the second negative order contributes to the transmission can be varied due to changing the sign of θ. It is noteworthy that the first negative order corresponds to the square-like IFC located around Γ point, while the second negative order corresponds to the square-like IFC surrounding M point.

The first series of the measurements have been performed while placing the transmitter antenna at a distance R_i=25cm away from the input interface, and the receiver antenna at the distance R_o=1m away from the output interface. The effect of the incident wave's angular spectrum width is expected to be more prominent in the case of the horn antenna illumination than in the Gaussian-beam illumination case. In addition, the curvature of the wavefronts that reach the PC interface still keeps the strong non-planar features. The results are presented in Fig. 7.36 on the (kL,Φ)-plane for the ranges A and C. Here and in the other similar figures, the dashed lines approximately show the areas, within which the transmission is significant only for the upper case.

The unidirectional transmission can be clearly seen from the comparison of Fig. 7.36(a) with Fig. 7.36(b), and Fig. 7.36(c) with Fig. 7.36(d). The same advantages of the range C are recognized here as for the Gaussian-beam illumination, i.e., weak transmittance in adjacent larger and smaller Φ ranges, larger bandwidth, and stronger contrast between the upper case and the lower case. The transmission results were calibrated with respect to the free space measurements.

The locations of the areas shown by the dashed lines quite well coincide with the predictions, which are based on the dispersion results and the transmission results for the plane-wave and Gaussian-beam illuminations. In particular, the corner points of the mentioned areas correspond to Φ=98° and

Φ=110° at f=17.4 GHz, and to Φ=98° and Φ=116° at f=18.43 GHz in Figs. 7.36(a) and 7.36(b), respectively. In Figs. 7.36(c) and 7.36(d), the corner points correspond to Φ=80° and Φ=93° at f=23.78 GHz, and Φ=80° and Φ=109° at f=28.6 GHz. The contrast $T^{\rightarrow}/T^{\leftarrow}$ exceeds 200 for the transmission data in Figs. 7.36(a) and 7.36(b) and 900 for those in Figs. 7.36(c) and 7.36(d).

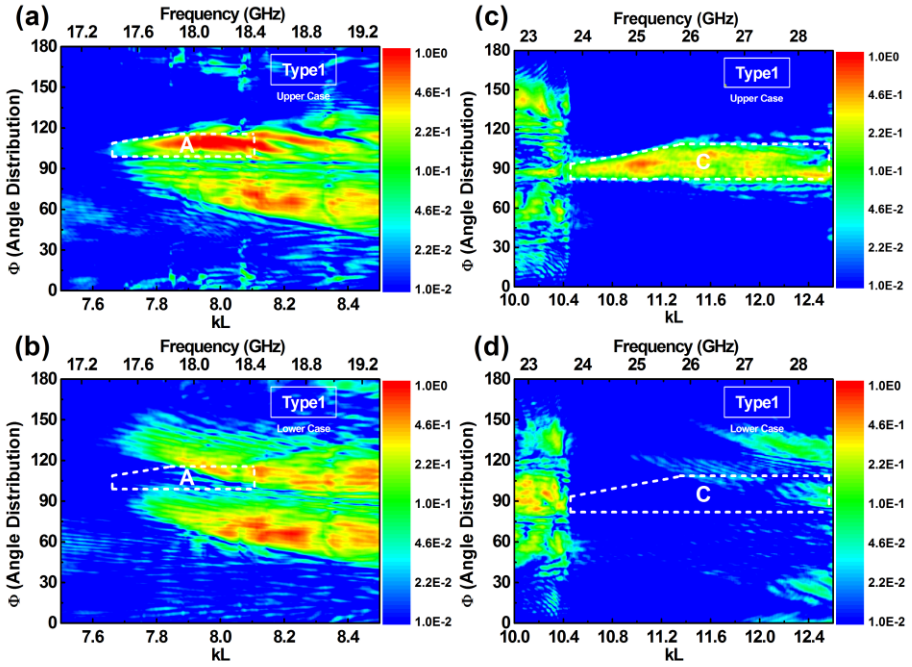

Figure 7.36: The measured transmittance (in arbitrary units, in logarithmic scale) on the (kL,Φ)-plane for the range A in the upper case as in Fig. 7.27(a) – plot (a), for the range A in the lower case in Fig. 7.27(b) – plot (b), for the range C in the upper case as in Fig. 7.27(a) – plot (c), and for the range C in the lower case as in Fig. 7.27(b) – plot (d); R_i=25cm.

Figure 7.37 presents the measured transmittance maps, which differ from those in Figs. 7.36(c) and 7.36(d) in that now the input (corrugated) interface is illuminated from the other side of the interface "triangles". Here, the uppermost and lowest points of the ellipse that is shown by the dashed line correspond to Φ=116° and Φ=74°, respectively, while f=25.89 GHz. The leftmost and rightmost points correspond to f=23.84 GHz and f=27.95 GHz while Φ=95°. The maximal contrast for the data in Fig. 7.37 is nearly the same as for those in Fig. 7.36. Based on the plane-wave and Gaussian-beam results obtained for the

range C, one could expect a stronger transmission in the upper case in the vicinity of kL=11 for Type 2 than for Type 1. Indeed, from the comparison of Fig. 7.36(c) with 7.32(a), one can see that this feature is preserved at the horn antenna illumination, too.

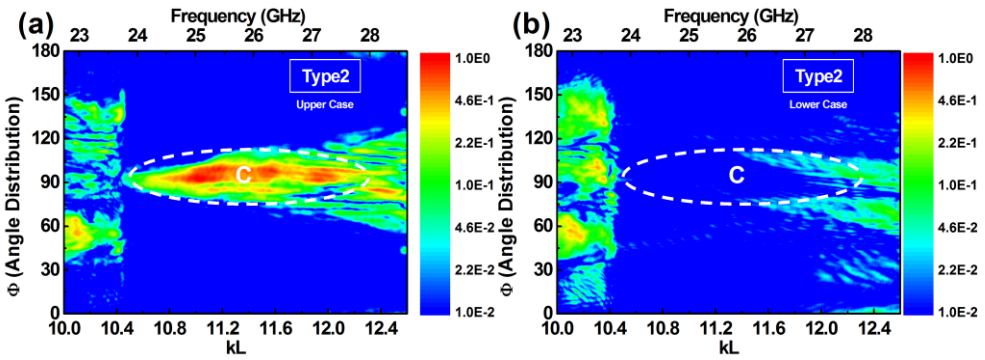

Figure 7.37: The measured transmittance (in arbitrary units, in logarithmic scale) on the (kL,Φ)-plane for the range C in the upper case as in Fig. 7.27(c) – plot (a), and for the range C in the lower case as in Fig. 7.27(d) – plot (b); R_i=25cm.

The second series of the experiments have been carried out by placing the transmitter antenna further away from the grating, i.e., at R_i=60cm while R_o=1m is kept. The main goal was to estimate the extent, to which the above-discussed features could be modified, and detect the factors, which might be dominant for such a modification. Among such factors, one should mention the possible diffraction at the grating edges, variations in the angular plane-wave spectrum of the incident wave, and the curvature of the incident wavefronts that varies with the distance from the input interface. An example is presented in Fig. 7.38. The basic features remain the same, but significant transmission appears now within those areas where it was typically near-zero for R_i=25cm. In particular, relatively weak but not negligible transmission appears within rather wide ranges that are in the vicinity of Φ=60° at f<17.6 GHz in Figs. 7.38(a) and 7.38(b), and at 24 GHz<f<27 GHz in Figs. 7.38(c) and 7.38(d). One could deduce that the effect of the zero order is pronounced here by comparing the values of Φ with those of $\pi/2$-ϕ_0, and also by judging the fact that these ranges appear in both the lower case and the upper case. This might indicate, in

particular, that the angular spectrum of the incident wave become wider for a larger R_i, so that the contribution of the spectral components, which correspond to the plane waves incident at the angles that allow coupling of the zero order to a Floquet-Bloch wave, become more significant.

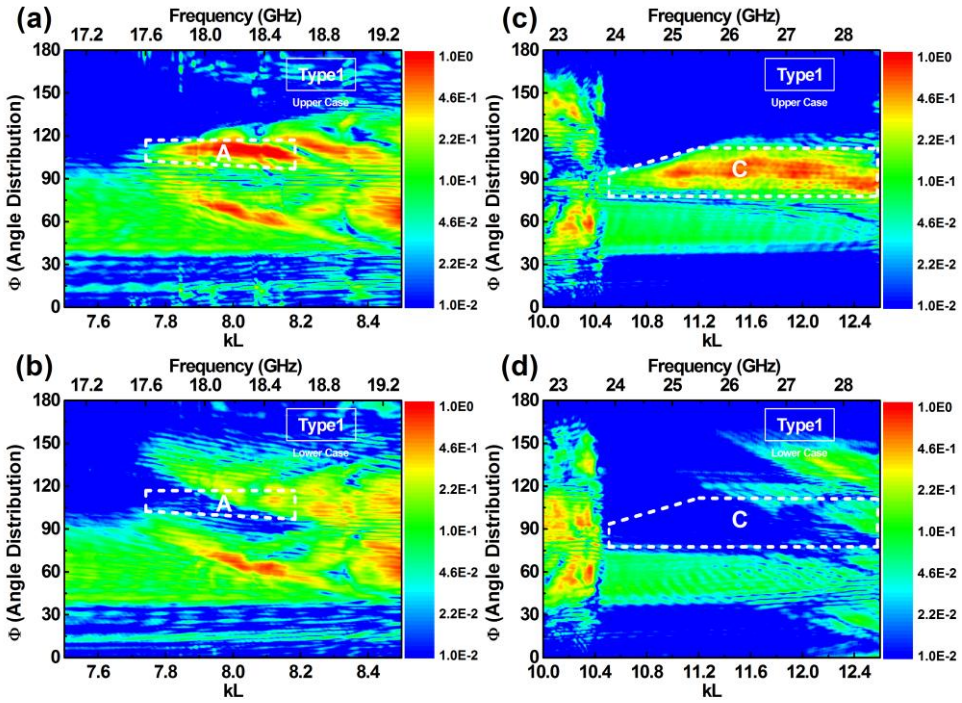

Figure 7.38: Same as Fig. 7.36 but for R_i=60cm.

In Figs. 7.38(a) and (b), the corner points of the area bounded by the dashed line are located at Φ=100° and Φ=117° for f=17.6 GHz, and at Φ=95° and Φ=117° for f=18.6 GHz. In Figs. 7.38(c) and (d), they are located at Φ=77° and Φ=100° for f=23.84 GHz, and at Φ=77° and Φ=112° for f=28.66 GHz. In other words, they show nearly the same locations as in Figs. 7.36(a)-(d). In fact, now we have a *combination of two-way and one-way transmission regions* for both A and C ranges. Despite this, the transmission contrast for the areas bounded by the dashed line remains within the same range of variation as in Figs. 7.36 and 7.37.

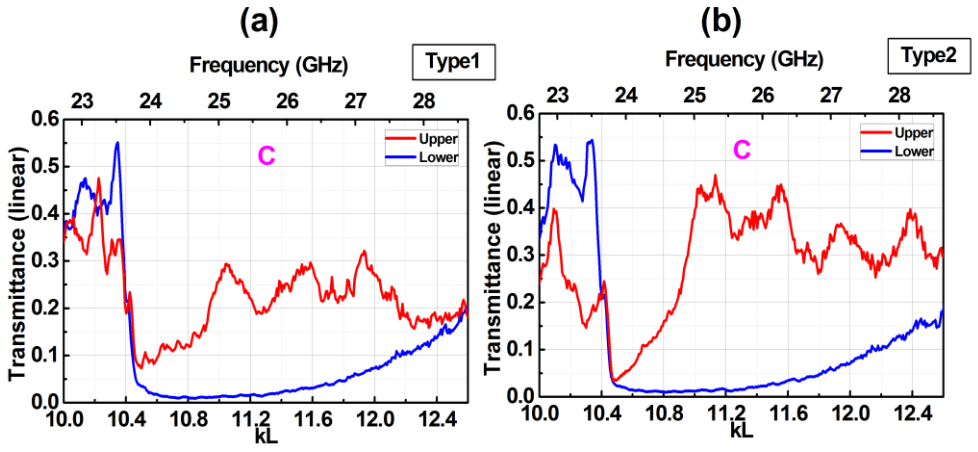

Figure 7.39: The integral transmittance in the *kL* range, which includes the range C: plot (a) corresponds to Figs. 7.27(a) and (b), plot (b) corresponds to Figs. 7.27(c) and (d); R_i=25cm.

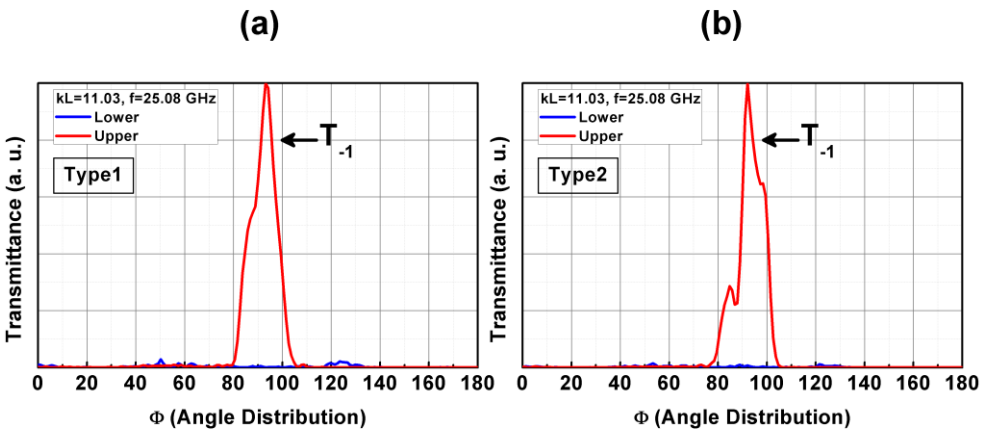

Figure 7.40: The measured angular distribution of the transmittance for a *kL* value taken from the range C: plot (a) corresponds to Figs. 7.27(a) and (b), plot (b) corresponds to Figs. 7.27(c) and (d); R_i=25cm.

Figure 7.39 presents the experimental variation of $\tau^{\rightarrow}$ (red lines) and $\tau^{\leftarrow}$ (blue lines) as a function of *kL*, which correspond to Figs. 7.36(c), 7.36(d), 7.37(a), and 7.37(b). The presented results differ from those in Fig. 7.31 only in the type of the incident wave. Although the one-way transmission in Fig. 7.39 is weaker pronounced, and the boundaries of the corresponding *kL*-range are blurred, the same basic features can be recognized. In particular, we again observe (i) a maximum of transmission in the vicinity of *kL*=11, (ii) a stronger

transmission for Type 2 than for Type 1, and (iii) a strong local minimum of transmission in the vicinity of kL=10.5 in Fig. 7.39(b) [compare with Figs. 7.31(a) and 7.31(b)].

The measured angular distributions of $T^{\rightarrow}$ and $T^{\leftarrow}$ are presented at kL=11.03 (range C) in Fig. 7.40. The maxima of $T^{\rightarrow}$ occurs at Φ=93° in Fig. 7.40(a) and at Φ=92° in Fig. 7.40(b). These values are in good coincidence with those in Figs. 7.34(a) and (b), and also with the corresponding value of $\phi_1 \approx -4°$. The contrast at the peaks is 2.98×10^3 in Fig. 7.40(a) and 850 in Fig. 7.40(b). Hence, the transmittance can be vanishing for all Φ values in the lower case also at horn antenna illumination, at least if R_i is relatively small.

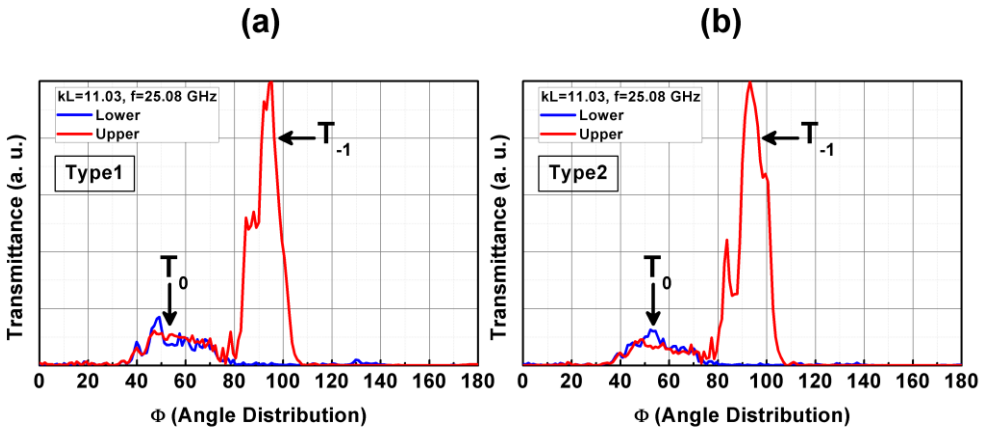

Figure 7.41: Same as Fig. 7.40 but for R_i=60cm

It has been observed in Figs. 7.36 and 7.38 that non-negligible two-way transmittance can start to appear at Φ<90° at those values of kL for which it was negligibly small at R_i=25cm, as we increase R_i. An example of the manifestation of this effect in the angular dependence at a fixed kL is presented in Fig. 7.41. It is mainly associated with the zero order, since Φ=60° corresponds to ϕ_0=30° and $t_0^{\rightarrow} = t_0^{\leftarrow}$ at the plane-wave illumination. Here, it appears nearly at 35°<Φ<80°. At the same time, the strong one-way transmission remains within the range of variation of Φ, which is associated with the first negative order. The maxima are located here at Φ=95° in Fig. 7.41(a) and at Φ=93° in Fig. 7.41(b), respectively.

These values are in good coincidence with those in Fig. 7.40 and with the value of $\phi_1 \approx -4°$. The contrast is equal to 730 at the maximum in Fig. 7.41(a) and 1.04×10^3 at the maximum in Fig. 7.41(b). In fact, this regime is similar to the one studied for the metallic slabs with the branched slits [204]. Indeed, we obtain nearly reciprocal transmission within one range of the Φ variation, and simultaneously the strongly pronounced unidirectional transmission within another range of the Φ variation.

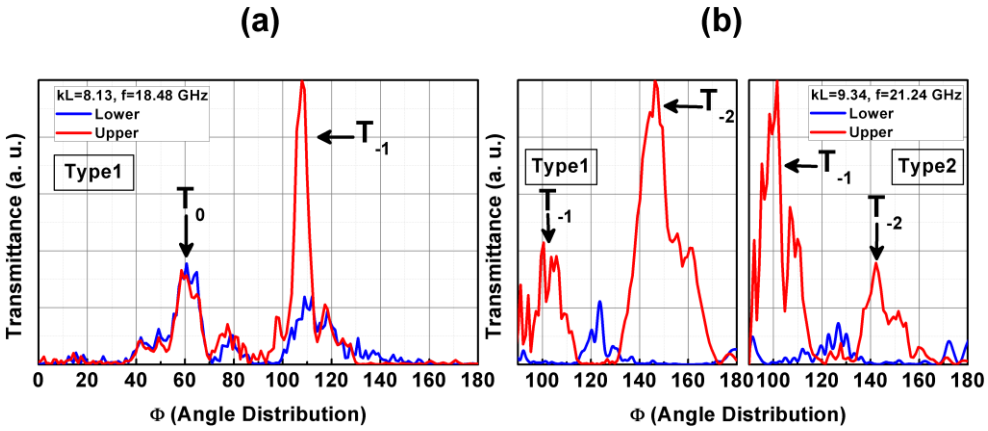

Figure 7.42: The measured angular distribution of the transmittance for *kL* values taken from the range A – plot (a), and range B – plot (b); plot (a) and left panel of plot (b) correspond to Figs. 7.27(a) and (b), right panel in plot (b) corresponds to Figs. 7.27(c) and (d); R_i=60cm.

Finally, let us check whether the strong directional selectivity remains at R_i=60cm in the ranges A and B. Figure 7.42 presents the measured transmittance for the same values of *kL* as in Figs. 7.33 and 7.35. In Fig. 7.42(a), the maximal transmittance is observed at Φ=107°. It is associated with the first negative order since $\pi/2 - \phi_1 = 105.8°$. However, the one-way transmission that is pronounced here is much weaker than in Fig. 7.41. At the maximum, we obtain $T^{\rightarrow} / T^{\leftarrow} = 5.6$. Furthermore, the transmission associated with the zero order is stronger compared to Fig. 7.41. As a result, $T^{\leftarrow} = 0$ cannot be obtained, at least for those values of Φ where $T^{\rightarrow}$ takes large values. It is noteworthy that the

zero-order related maximum appears in the upper case at Φ=59° while $\pi/2-\phi_{-1}$=60°.

In Fig. 7.42(b), one can see that although $T^{\leftarrow}$ cannot vanish in the lower case for all values of Φ, strong directional selectivity remains within particular Φ-ranges, which are associated with the first and second negative orders. The corresponding maxima appear at Φ=100.5° and Φ=146.3° in the left panel in Fig. 7.42(b), and at Φ=101.5° and Φ=142° in the right panel in Fig. 7.42(b), while $\pi/2-\phi_{-1}$=100° and $\pi/2-\phi_{-2}$=147.7°. The contrasts are $T^{\rightarrow}/T^{\leftarrow}=44$ and $T^{\rightarrow}/T^{\leftarrow}=140$ for the maxima associated with the first and second negative orders in the left panel, and $T^{\rightarrow}/T^{\leftarrow}=170$ and $T^{\rightarrow}/T^{\leftarrow}=180$ for the maxima associated with the first and second negative orders in the right panel. Besides, notice the "inverse" unidirectional effect, i.e., when $T^{\rightarrow}\approx 0$ but $T^{\leftarrow}>0$, as observed in the left panel in Fig. 7.42(b) at Φ=120°. Similar effect is observed for example in Figs. 7.36(a) and 7.36(b) at Φ>120° in the vicinity of *kL*=7.8. Among others, this effect will be a subject of the future studies.

To summarize, we have demonstrated unidirectional transmission in the PC gratings with one-side echelette-type corrugations at beam-type illumination. Simulation results obtained for the plane-wave and Gaussian-beam illuminations, and the experimental results for the microwave horn antenna illumination were presented and analyzed. They indicate that the existence of the unidirectional transmission itself does not depend on the type of dispersion. In contrast, the appearance of this regime strongly depends on the dispersion features, which determine the width of the unidirectional transmission range and affect the behavior of the transmission within the neighboring ranges of the observation and incidence angles. For the studied mechanism, all the waves have linear polarization, while strong directional selectivity is obtained due to the different conditions of coupling of higher diffraction orders at the corrugated and non-corrugated interfaces. We have observed a good connection between the features detected at plane-wave, Gaussian-beam and horn antenna

illuminations. For a wide Gaussian beam, all basic features of the transmission inferred from the plane-wave analysis remain, so that the ranges of the unidirectional transmission appear within nearly the same frequency bands. On the other hand, a wider angular spectrum of the incident wave and a variation in the distance from the source to the input interface lead to the transformation in the ranges of the unidirectional transmission, so that one-way and two-way transmissions can co-exist for the horn antenna illumination. The future studies will be dedicated, in particular, to the effect of the angular spectrum of the incident wave and the curvature of the incident wavefronts on the unidirectional transmission, as well as to the effect of the corrugation shape on the lateral beam shift and the possible reduction of the reflections at the unidirectional transmission.

7.5 Diffraction relevant total transmission in the optical diodes made with photonic crystals

This paper was published in Optics Express and is made available as an electronic reprint with the permission of OSA. The paper can be found at the following URL on the OSA website: http://dx.doi.org/10.1364/OE.20.014980 Systematic or multiple reproduction or distribution to multiple locations via electronic or other means is prohibited and is subject to penalties under law.

Diode-like optical transmission is usually associated with the use of anisotropic [195,196,199,212] or nonlinear [198,213] materials. Single-channel diffraction-free unidirectional transmission is expected to require the simultaneous breaking of time-reversal and spatial inversion symmetries [214]. For example, strongly pronounced unidirectional transmission has been observed in a stack of two two-dimensional photonic crystals (PCs) that are made of gyromagnetic materials [195,212]. On the other hand, searching for asymmetric reciprocal (in sense of the Lorentz Lemma) transmission, i.e., that obtainable without breaking time-reversal symmetry has been a focus of interest for a long time. Chiral structures are known to enable a well pronounced

asymmetry in transmission [215] and isolation for certain polarization states [216,217]. Complete optical isolation can also be achieved dynamically due to the temporal modulation of the refractive index in a linear photonic system [218]. Nonmagnetic optical isolators can be obtained in the structures that contain two modulators, in which a desired phase shift for co- and counter-propagating waves is achieved due to temporal modulation of bias voltages [219].

On the other hand, PCs made of isotropic linear materials show a rich variety of dispersion types, which are associated with the intriguing phenomena like negative refraction, focusing, superprism, and collimation [220]. Recently, it has been suggested to utilize the combination of some of the dispersion features with the effect of curvilinear interface(s) of the PC in order to obtain one-way transmission regimes [200]. In particular, it has been demonstrated that strong directional selectivity, i.e., strong forward-to-backward transmission contrast can be obtained in the gratings based on square-lattice dielectric PCs, whose spatial inversion symmetry is broken due to that the corrugations are either different at the two sides, or placed at one of the sides only. It needs a proper combination of the *umklapp* scattering relevant asymmetry in coupling and dispersion, creating new transmission channels that might be open in a one-way manner. For this mechanism, the forward transmission, i.e., from half space I, which is bounded by the corrugated interface, to half space II, which is bounded by the noncorrugated interface, can be significant (transmittance $T^{\rightarrow} < 1$ and reflectance $R^{\rightarrow} \leq 1$), while backward transmission is blocked ($T^{\leftarrow} = 0$ and $R^{\leftarrow} = 1$) at the same angle of incidence, $\theta = \theta^{\rightarrow} = \theta^{\leftarrow}$, which is measured in the same, e.g., clockwise direction with respect to the normal to the incidence side. Hence, an extremely strong asymmetry in transmission can be achieved.

According to [200], for this diode-like asymmetric transmission mechanism, the dispersion in the PC has to ensure that the specular (zero) order is not coupled to a Floquet-Bloch (FB) wave of the PC. This is a key condition

that is required for its existence. In turn, *umklapp* scattering is responsible for the *multichannel* nature of this mechanism. At least one higher order must propagate in air and must be coupled to a FB wave, but only if the corrugated side is illuminated. Hence, at least two propagation channels are required to be open in air half spaces, each being connected with a certain diffraction order. At the same time, all the orders (zero and higher) are uncoupled at the noncorrugated-side illumination. In terms of the *n*th-order diffraction efficiencies in transmission (partial transmittances), $t_n^{\rightarrow}$ and $t_n^{\leftarrow}$, a nonsymmetric dielectric grating allows one obtaining a partially asymmetric transmission, because $t_n^{\rightarrow} \neq t_n^{\leftarrow}$ at $|n| > 0$ (asymmetric component) and $t_0^{\rightarrow} = t_0^{\leftarrow}$ (symmetric component) at $\theta = \theta^{\rightarrow} = \theta^{\leftarrow}$. However, wideband suppression of the symmetric component cannot be achieved in the general case. Using a PC instead of a dielectric, one can obtain extreme asymmetry in transmission, i.e., unidirectionality with $t_0^{\rightarrow} = t_0^{\leftarrow} = 0$, while $t_n^{\leftarrow} = 0$ for all n in wide ranges of variation in frequency and angle of incidence. Thus, $T^{\leftarrow} = 0$, but $T^{\rightarrow} > 0$ due to extreme conversion of the incident wave energy into that of higher diffraction orders ($|n| > 0$), which are efficiently coupled to a FB wave. For the diffraction inspired mechanism of asymmetric transmission, all the waves keep linear polarization.

The first experimental results have been obtained to validate this mechanism in PC gratings in the microwave regime [221]. Later, the same idea has been utilized in sonic crystals at $\theta \neq 0$, for which the experimental validation has also been done [222]. Recently, the structures with the diffraction relevant asymmetric transmission have been reported that are designed to operate at optical frequencies [223]. In fact, it does not matter whether one-dimensional, two-dimensional, or three-dimensional PC is taken to obtain a PC grating. For example, similar transmission features have been found in the structures that comprise a slab of one-dimensional PC and a dielectric grating placed at one of the interfaces [224]. Unidirectional transmission that exploits

the combination of the dispersion and diffraction effects has been demonstrated in the compact (less than one free-space wavelength thick) structure that is based on the stacked hole arrays with one-side corrugations [225]. Similar unidirectional transmission in the beaming regime has been obtained in the nonsymmetric gratings with a single subwavelength slit, where it is connected with the asymmetry in excitation of spoof surface plasmons at the input and exit interfaces [226,227]. The *exactly* diode regime, i.e., that with total transmission in one direction has not been reported yet.

In this section, we will show that *total* unidirectional diode-like transmission, with $T^{\rightarrow}=1$ and $T^{\leftarrow}=0$, can be obtained in the nonsymmetric PC gratings owing to the *umklapp* scattering relevant coupling, for *s*-polarized incident light at the plane-wave approximation. It can occur at some angles of incidence and frequencies taken from a wide range, for which $T^{\rightarrow}\leq 1$ and $T^{\leftarrow}=0$, at least in case of (near-)square-shaped isofrequency dispersion contours (IFCs) like those known from the studies of negative refraction, imaging and spatial filtering in PCs [210,228,211]. A different number of the propagating beams can be involved in the transmission also at $T^{\rightarrow}=1$ and $T^{\leftarrow}=0$, leading to various regimes of asymmetric transmission, e.g., two-beam unidirectional splitting and single-beam unidirectional deflection. In contrast with the earlier studies, similar regimes but with $T^{\leftarrow}=1$ and $T^{\rightarrow}=0$ will also be demonstrated at some frequencies, at which zero order is coupled to a FB wave at the input side, but zero-order transmission is suppressed in the exit half space due to the peculiar diffractions. Consideration is restricted here to the square-lattice PCs composed of circular dielectric rods. The diffraction angles, $\phi_n^{\rightarrow}$ and $\phi_n^{\leftarrow}$, are measured in the counter-clockwise direction with respect to the normal to the incidence side for the reflected waves, and in the clockwise direction with respect to the normal to the exit side for the transmitted waves. Diffraction results have been obtained by using Coupled Integral Equation Technique [229]. CST Microwave Studio [230] has been used for the calculations of the dispersion of FB waves.

First, let us review the coupling scenarios which are associated with the different coupling conditions at the interfaces of a nonsymmetric grating. The condition of the uncoupled zero order limits the appropriate values of θ and determines PC IFC shapes. One more condition that is required for the unidirectional transmission is that the higher order may be coupled to a Floquet-Bloch wave at one of the interfaces only. Four typical coupling scenarios, which fulfill these conditions, are demonstrated in Fig. 7.43 by using the repeated zone diagram and construction lines, also see Refs. [200,221]. IFCs of PC are assumed to be around (a) Γ point, (b) X point, (c) M point, and (d) Γ and M points. Locations of the construction lines correspond to

$$k_x^{(n)} = (\omega / c)\sin\theta + 2\pi n / L, \tag{7.14}$$

where n is the order index and L is the grating period. Coupling occurs when a construction line crosses an IFC, so that k_x is conserved. Only those crossing points may contribute to the transmission, which satisfy the causality principle.

Figure 7.43(a) demonstrates the coupling scenario in the case of circular IFC of PC. In fact, it corresponds to an isotropic material with the refractive index $0 < N < 1$, e.g., a Drude metal above the plasma frequency, or a wire medium above the effective plasma frequency [9,201,202]. The construction lines are plotted in Figs. 7.43(a), 7.43(b), and 7.43(d) for a value of $\theta = \theta^{\rightarrow} = \theta^{\leftarrow} \neq 0$, at which the beam of the order $n = -1$ is only coupled to a FB wave. In Fig. 7.43(c), the construction lines correspond to $\theta = \theta^{\rightarrow} = \theta^{\leftarrow} = 0$, so that the both beams with $n = -1$ and $n = +1$ are coupled. In turn, there is no coupling at the noncorrugated-side illumination. The IFC shapes, which are similar to but distinguished from those in Fig. 7.43, e.g., those for anti-cutoff media [30], are also appropriate. This mechanism of unidirectional transmission cannot appear in the nonsymmetric dielectric gratings, since if a higher order ($|n| > 0$) is coupled to a wave propagating in the grating material, then zero order ($n = 0$) is always coupled, too.

In order to obtain the *unidirectional deflection regime* at $\theta \neq 0$, at least one higher order must propagate in air due to the corrugated interface [200], that can be considered as a compensation for the lack of anisotropic or nonlinear constituents in the proposed performances, see Figs. 7.43(a), 7.43(b), and 7.43(d).

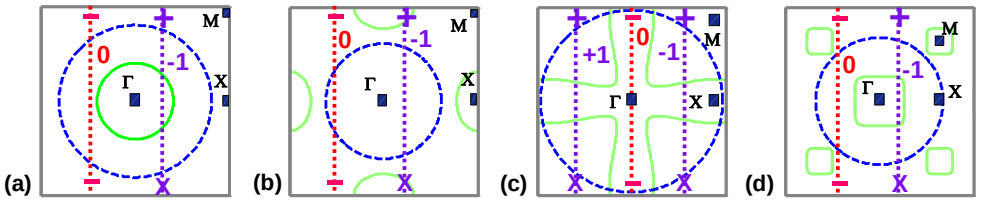

Figure 7.43: Coupling scenarios, at which the unidirectional transmission can be obtained: green solid line – IFC of PC; blue dashed circle – IFC in air; dotted lines – construction lines; "0" , "-1" and "+1" denote *n*; "+" and "–" at the plot top indicate that the corresponding order that propagates in air is coupled or not coupled to a FB wave, if the corrugated side is illuminated; "–" and "X" at the plot bottom indicate that the corresponding order may propagate in air but is not coupled or evanescent, if the noncorrugated side is illuminated; IFCs of PC are loated around (a) Γ point, (b) X point, (c) M point, and (d) Γ and M points.

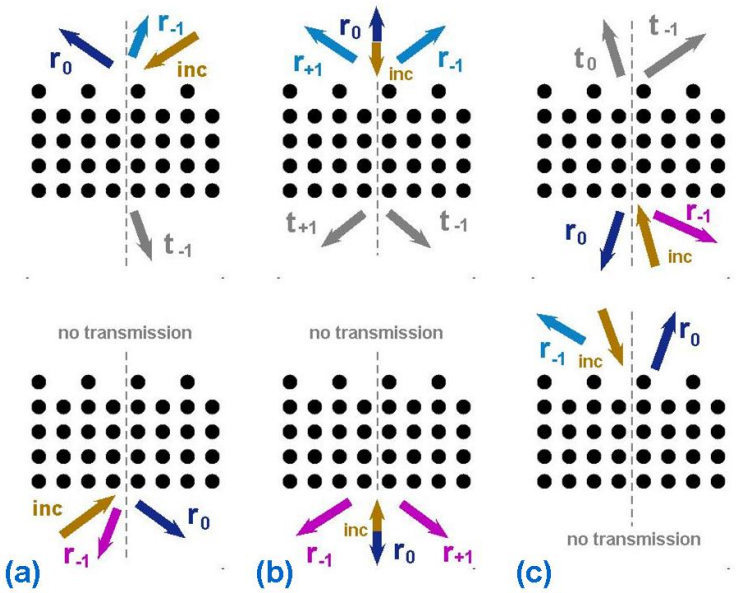

Figure 7.44: Diffraction scenarios corresponding to unidirectional transmission in nonsymmetric PC gratings: (a) deflection and (b) splitting in the direct (forward) transmission regime, and (c) splitting in the inverse (backward) transmission regime.

If more than two orders may propagate in air, splitting with non-equal transmittances can appear in this regime. At $\theta = 0$, deflection occurs in the *unidirectional splitting regime*, where any pair of the symmetrically deflected higher-order beams shows the equal transmittances, see Fig. 7.43(c). In order to obtain $T^{\leftarrow} = 0$, the noncorrugated interface should not allow the unwanted higher orders to propagate in air. Since all the constituents are isotropic and linear, transmission has to be reciprocal according to the Lorentz Lemma [232]. To observe the reciprocity, the PC grating could be illuminated from the noncorrugated side at $\theta^{\leftarrow} = \phi_n^{\rightarrow}$, where $\phi_n^{\rightarrow}$ is the diffraction angle of the *n*th-order transmitted beam at the corrugated-side illumination, which is given by

$$\phi_n^{\rightarrow} = \sin^{-1}[\sin\theta^{\rightarrow} + 2\pi n / kL] \tag{7.15}$$

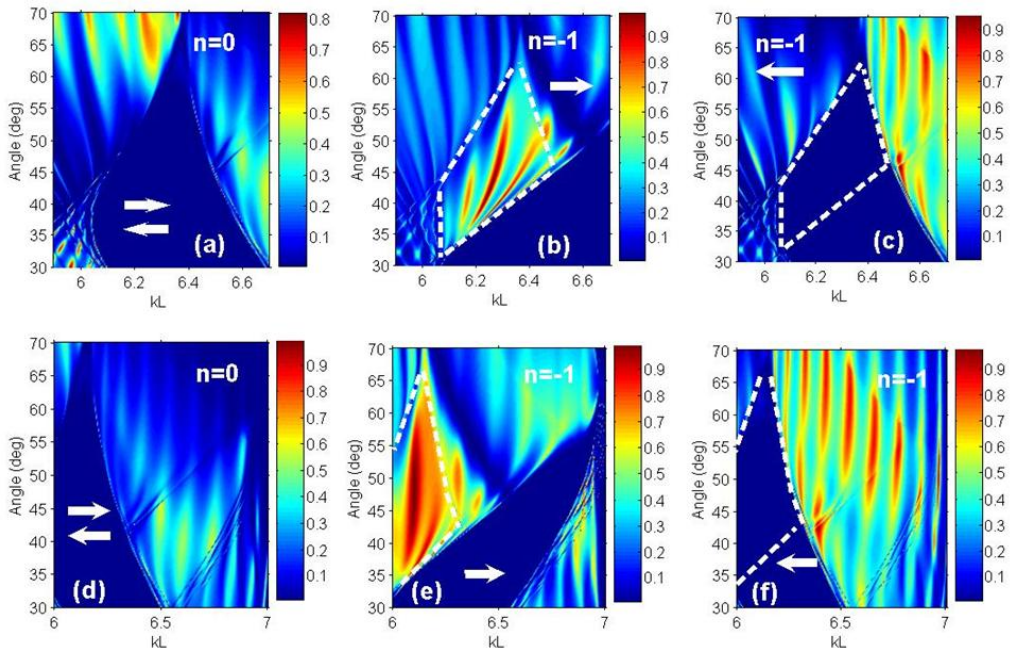

Figure 7.45: Transmittance $t_0 = t_0^{\rightarrow} = t_0^{\leftarrow}$ (a), $t_{-1}^{\rightarrow}$ (b), and $t_{-1}^{\leftarrow}$ (c) at $P = 12$, $\varepsilon_r = 11.4$, and $d/a = 0.4$; $t_0 = t_0^{\rightarrow} = t_0^{\leftarrow}$ (d), $t_{-1}^{\rightarrow}$ (e), and $t_{-1}^{\leftarrow}$ (f) at $P = 12$, $\varepsilon_r = 9.61$, $d/a = 0.45$, and benchmark corrugations, direct regime.

If $T^{\rightarrow} = t_{-1}^{\rightarrow} = \tilde{T}$ and $R^{\rightarrow} = 1 - \tilde{T}$ at $\theta = \theta^{\rightarrow}$, single-beam unidirectional deflection should also appear in the inverse regime, i.e., $T^{\leftarrow} = t_{-1}^{\leftarrow} = \tilde{T}$ and

$R^{\leftarrow} = 1 - \tilde{T}$ at $\theta = \theta^{\leftarrow} = \phi_n^{\rightarrow}$. The beam diagrams are presented in Fig. 7.44 for the coupling scenarios that correspond to Fig. 7.43. The following cases are schematically illustrated: single-beam unidirectional deflection (a) and two-beam unidirectional splitting (b) in the direct regime (transmission is nonzero only if the corrugated interface is illuminated), and (c) unidirectional deflection in the inverse regime (transmission is nonzero only if the noncorrugated interface is illuminated). One can see that the scenario presented in Fig. 7.44(a) needs asymmetry in coupling like that in Figs. 7.43(a), 7.43(b), and 7.43(d). In turn, the scenario in Fig. 7.44(b) corresponds to Fig. 7.43(c). Finally, the scenario in Fig. 7.44(c) cannot be predicted by using IFCs. It is expected to appear as a consequence of the reciprocity, as has been discussed above.

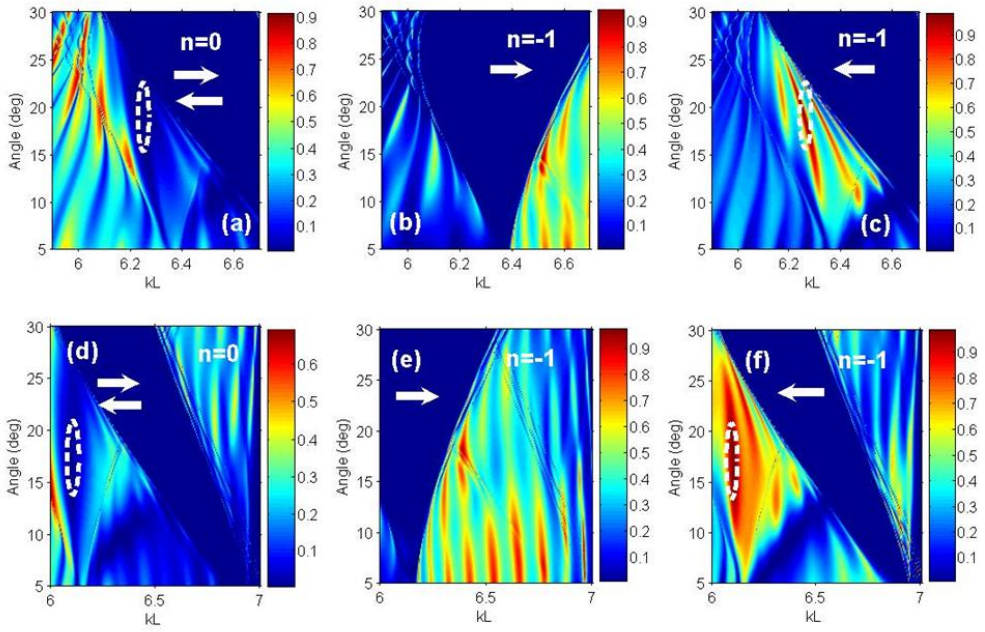

Figure 7.46: Same as Fig. 7.45 but for another range of θ variation, inverse regime.

Comparison of the unidirectional transmission efficiency for different IFC shapes (not presented) shows that for the purposes of realizing a single-beam unidirectional total transmission, the (near-)square-shaped IFCs, as in Figs. 7.43(c) and 7.43(d), are most appropriate. Figure 7.45 shows t_0, t_{-1}, and t_{+1} for the two twelve-layer structures ($P = 12$), in the ranges of kL and θ

variation, where *single-beam unidirectional deflection* is observed in the direct regime, i.e., when strong higher-order transmission occurs if the corrugated side is illuminated, while transmission is vanishing if the noncorrugated side is illuminated. ε_r and *d/a* denote the relative permittivity of the rods and the ratio of rod diameter to PC lattice constant, respectively. Corrugations are obtained by removing every second rod from one of the interface layers of the noncorrugated *P*-layer PC, which we refer to as the *benchmark corrugations* ($L = 2a$). Such non-deep corrugations are expected to be more preferable than those used in [200], since the transmission features associated with the Fabry-Perot resonances should be better pronounced. Right and left arrows in Fig. 7.45 and in all the next figures indicate that the corrugated side and the noncorrugated side are illuminated, respectively. At the same time, smaller *L/a* than in [200] should make the suggested structures less sensitive to the incident beam width.

A broadband diode-like transmission is observed in Fig. 7.45 within the area that is approximately bounded by a white dashed line. Here, $T^{\rightarrow} = t_{-1}^{\rightarrow} \le 1$ but $T^{\leftarrow} = 0$, since $t_0^{\leftarrow} = t_0^{\rightarrow} = 0$. Adjusting lattice parameters, one can vary width and location of the mountain of $t_{-1}^{\rightarrow}$, for which the incident plane-wave energy can be *entirely* converted to that of the first-negative-order transmitted beam, i.e., $T^{\rightarrow} = t_{-1}^{\rightarrow} = 1$. This possibility is very important for practical applications. The obtained simulation results show that this regime is realizable while PC lattice parameters are taken from a rather wide range, e.g., $5 < \varepsilon_r < 12$. The range of variation of *d/a* from 0.25 to 0.55 is recommended to consider first in order to find a unidirectional transmission regime. Usually, $P \ge 5$ is required. However, using an arbitrary combination of ε_r , *d/a*, and *P* does not ensure the existence of the regime with $T^{\rightarrow} = 1$ and $T^{\leftarrow} = 0$.

In Fig. 7.45, the unidirectional transmission can be predicted by the analysis of the IFCs and construction lines, which are similar to those in Fig. 7.43(d). The single transmitted beam ($n = -1$) is *negatively deflected*, i.e.,

$\operatorname{sgn}\phi_{-1} \neq \operatorname{sgn}\phi_0$. The corresponding transmission channel is open due to the coupling of the FB wave, for which the IFCs are the near-square shaped and located around Γ point. In our case, they indicate the left handedness ($\mathbf{S}\cdot\mathbf{k}^{\mathbf{PC}} < 0$ where $\mathbf{S}$ is Poynting vector and $\mathbf{k}^{\mathbf{PC}}$ is wave vector of a FB wave), while positive refraction is *mimicked* at the corrugated (here - incidence) interface. In order to estimate the range of ϕ_{-1} variation that corresponds to the strong unidirectional transmission, we use Eq. (7.15). For the data in Fig. 7.45(b), we obtain $\phi_{-1}^{\rightarrow} \approx -26^{\circ}$ at $kL = 6.2$ and $\theta = 35^{\circ}$, and $\phi_{-1}^{\rightarrow} \approx -10.3^{\circ}$ at $kL = 6.3$ and $\theta = 55^{\circ}$. For Fig. 7.45(e), Eq. (7.15) yields $\phi_{-1}^{\rightarrow} \approx -21^{\circ}$ at $kL = 6.09$ and $\theta = 42^{\circ}$, and $\phi_{-1}^{\rightarrow} \approx -12^{\circ}$ at $kL = 6.12$ and $\theta = 55^{\circ}$. The alternating mountains and valleys observed in the transmittance maps appear owing to the Fabry-Perot type resonances. Here, the regime of $T^{\rightarrow} = 1$ might be connected with *hybridization* of one of the resonances and peculiar diffractions.

The Lorentz reciprocity [232] forces the unidirectional transmission to appear at a fixed θ in the inverse regime, e.g., when $T^{\leftarrow} = t_{-1}^{\leftarrow} = 1$ and $T^{\rightarrow} = 0$. Figure 7.46 presents the transmittance maps obtained at the same parameters as in Fig. 7.45, except for the used range of θ variation. As expected, the unidirectional transmission in plots (a), (c), (d), and (f) occurs inside the area bounded by white line. The Lorentz reciprocity relevant *similarity* of the maps of $t_{-1}^{\rightarrow}$ in Fig. 7.45(b) and $t_{-1}^{\leftarrow}$ in Fig. 7.46(c) is clearly seen. It is observed also for $t_{-1}^{\rightarrow}$ in Fig. 7.45(e) and $t_{-1}^{\leftarrow}$ in Fig. 7.46(f). In particular, $T^{\leftarrow} = t_{-1}^{\leftarrow} = 1$ is achieved in Fig. 7.46(c) at $\theta^{\leftarrow} = \phi_{-1}^{\rightarrow}$, where $\phi_{-1}^{\rightarrow}$ is the angle of diffraction of the first negative order at the mountain of $T^{\rightarrow} = t_{-1}^{\rightarrow}$ in Fig. 7.45(b), for the *kL* value at which $t_{-1}^{\rightarrow} = 1$. The same remains true for the regimes with $t_{-1}^{\rightarrow} = 1$ in Fig. 7.45(e) and $t_{-1}^{\leftarrow} = 1$ in Fig. 7.46(f). It is noteworthy that zero order is coupled now to the FB wave at the incidence interface in the inverse regime. Then, the corresponding transmission regime can be interpreted in terms of a two-way

Fabry-Perot resonance relevant transmission in a single *curvilinear (bended)* transmission channel. If one has a higher-order transmittance map that corresponds to the direct single-beam transmission regime, the map can immediately be plotted for the same order in the inverse regime by solving Eq. (7.15) for the values of $\theta^{\leftarrow}$. At the same time, the studied PC gratings are nonreciprocal in a wider sense, since forward and backward transmittances are not equal.

According to the obtained results, the effect of the corrugated exit interface manifests itself in the *superefficient*, i.e., entire transformation of the energy of the wave(s), which propagate in the PC due to the ideal coupling of zero order to a FB wave at the noncorrugated input interface, into the first-order transmitted beam. In contrast with the direct regime of unidirectional transmission where $t_0 = 0$ in a rather wide *kL* range around the *kL*-value at which $t_{-1}^{\rightarrow} = 1$, now $t_0 \neq 0$ around the *kL*-value at which $t_{-1}^{\leftarrow} = 1$. As a result, the unidirectional transmission "point" appears in the inverse regime instead of a unidirectional transmission band, as it occurs in the direct regime. Thus, the latter should be preferable to fulfill requirements to the practical devices. The inverse regime may occur but has not yet been studied in various structures with the broken spatial inversion symmetry, which are suggested to operate at the frequencies from acoustic to optical ones, e.g., see [221-225]. One should note in Figs. 7.45 and 7.46 that $t_{-1}^{\leftarrow}$ can be substantially larger than t_0 and $t_{-1}^{\rightarrow}$ beyond the unidirectional transmission range.

To better illustrate the basic transmission features of the *single-beam unidirectional deflection* regime, Fig. 7.47 presents the transmittance as a function of *kL* for the corrugated-side [plots (a), (d), (g)] and noncorrugated-side [plots (b), (e), (h)] illumination, and reflectance for the noncorrugated-side illumination [plots (c),(f)], at fixed θ. Here, the lattice and corrugation parameters are the same as in Figs. 7.45 and 7.46. In Figs. 7.47(a) and 7.47(b), the unidirectional transmission is observed in the vicinity of $kL = 6.25$, i.e.,

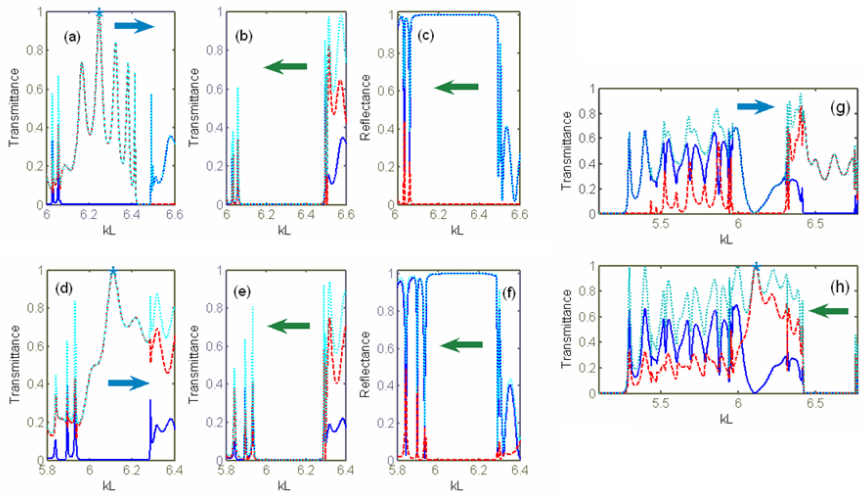

Figure 7.47: Transmittances $t_n^{\rightarrow}$ and $T^{\rightarrow}$ (a,d,g), $t_n^{\leftarrow}$ and $T^{\leftarrow}$ (b,e,h), and reflectances $r_n^{\leftarrow}$ and $R^{\leftarrow}$ (c,f) at $P=12$ and benchmark corrugations; (a)-(c): $\varepsilon_r=11.4$, $d/a=0.4$, and $\theta=43^{\circ}$; (d)-(f): $\varepsilon_r=9.61$, $d/a=0.45$, and $\theta=47^{\circ}$; (g,h): $\varepsilon_r=9.61$, $d/a=0.45$, and $\theta=-17.3^{\circ}$; blue solid line – $n=0$, red dashed line – $n=-1$, cyan dotted line – $T^{\rightarrow}$ (a,d,g), $T^{\leftarrow}$ (b,e,h), and $R^{\leftarrow}$ (c,f); asterisk denotes the cases of $T^{\rightarrow}=1$ (a,d) and $T^{\leftarrow}=1$ (h).

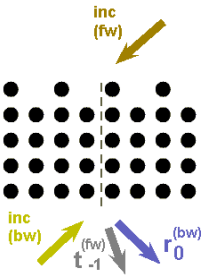

Figure 7.48: Diffraction scenario with the two beams that are simultaneously incident from the corrugated and noncorrugated sides in the opposite directions; fw and bw stand for the forward and backward cases, respectively.

when $ka\approx\pi$. At $kL=6.25$, $T^{\rightarrow}=t_{-1}^{\rightarrow}=1$ and $T^{\leftarrow}=0$ in the direct regime, while the angle between the incident and outgoing beams is $\Omega^{\rightarrow}=\pi-\theta^{\rightarrow}+\phi_{-1}^{\rightarrow}\approx 118^{\circ}$. In Figs. 7.47(d) and 7.47(e), it occurs in the vicinity of $kL=6.1$, i.e., when $ka<\pi$. At $kL=6.11$, $T^{\rightarrow}=t_{-1}^{\rightarrow}=1$ and $T^{\leftarrow}=0$ in the direct regime, while $\Omega^{\rightarrow}\approx 116^{\circ}$. Figures 7.47(g) and 7.47(h) demonstrate unidirectional deflection in the inverse regime at $\theta=\theta^{\rightarrow}=\theta^{\leftarrow}$, where

$\theta^{\leftarrow} = -17.3^{\circ}$ is the same as $\phi_{-1}^{\rightarrow}$ at $kL = 6.11$ in Fig. 7.47(d). The Lorentz reciprocity [232] results in that $T^{\leftarrow} = t_{-1}^{\leftarrow} = 1$ and $T^{\rightarrow} = 0$ at $kL = 6.11$, but t_0 remains quite large in the vicinity of this unidirectional "point".

In addition to the unidirectional transmission, the *isolation* takes place here, which is understood in the sense of the lack of interference between the two diffraction processes that is observed at the *simultaneous* illumination of the PC grating from the two sides being opposite to each other. The existence of this regime is clearly seen from the comparison of Figs. 7.47(a) and 7.47(c), and Figs. 7.47(d) and 7.47(f). In the former case, this occurs at $6.09 < kL < 6.49$, where $T^{\rightarrow} = t_{-1}^{\rightarrow}$, $R^{\leftarrow} = r_0 = 1$, and $R^{\rightarrow} = r_0 + r_{-1}^{\rightarrow}$, so that all the transmitted and reflected beams propagate in different directions. In Figs. 7.47(d) and 7.47(f), this occurs at $5.94 < kL < 6.29$. Inside this range, i.e., at $kL = 6.11$, there are only two outgoing beams – one transmitted and one reflected, while the angle between them is 30°. Similarly, there are only two beams at $kL = 6.25$ in Figs. 7.47(a) and 7.47(c). To demonstrate the main idea of the isolation regime, Fig. 7.48 presents a diagram that schematically shows the corresponding diffraction scenario.

High transmittance can be obtained in the direct and inverse regimes also for the *two-beam unidirectional splitting* which occurs at $\theta = 0$. Three examples are presented in Fig. 7.49. In Fig. 7.49(a), $T^{\rightarrow} = t_{-1}^{\rightarrow} + t_{+1}^{\rightarrow}$ at $8.44 < kL < 9.38$, while $T^{\leftarrow} < 5 \times 10^{-3}$ Here, $\max T^{\rightarrow} = 0.95$ at $kL = 9.15$ where $\phi_{\pm 1}^{\rightarrow} \approx \pm 43^{\circ}$. In this case, the IFCs and construction lines are similar to those in Fig. 7.43(c), and diffraction scenario is the same as in Fig. 7.44(b). Although $T^{\rightarrow} = 1$ is not achieved, the unidirectional transmission with $T^{\rightarrow} \geq 0.9$ is now more broadband and, thus, the PC grating should be weaker sensitive to the possible nanofabrication inaccuracies than those in Figs. 7.45 and 7.46. Unidirectional transmission with $T^{\rightarrow} = 1$ and $T^{\leftarrow} \approx 0$ can be obtained in the direct regime at the edge of the range of $T^{\rightarrow} \neq 0$, as shown in Fig. 7.49(b). Here,

$T^{\rightarrow} = t_{-1}^{\rightarrow} + t_{+1}^{\rightarrow} \neq 0$ at $11.3 < kL < 12.4$, while $T^{\leftarrow} < 4.5 \times 10^{-4}$ However, there is no wide unidirectional range with high transmission, e.g., with $T^{\rightarrow} > 0.75$. Thus, a compromise between the maximum value of $T^{\rightarrow}$ and unidirectional range width is required, being dependent on the peculiarities of a certain application. In the inverse regime, one can obtain $T^{\leftarrow} = t_{-1}^{\leftarrow} + t_{+1}^{\leftarrow} = 1$ and $T^{\rightarrow} \approx 0$ at a certain *kL* value (unidirectional "point"), while zero-order transmission is well suppressed around this *kL* value, see Fig. 7.49(c). For this performance, the total-transmission peak is even wider than in the direct regime in Fig. 7.49(b), making it a promising candidate for practical applications.

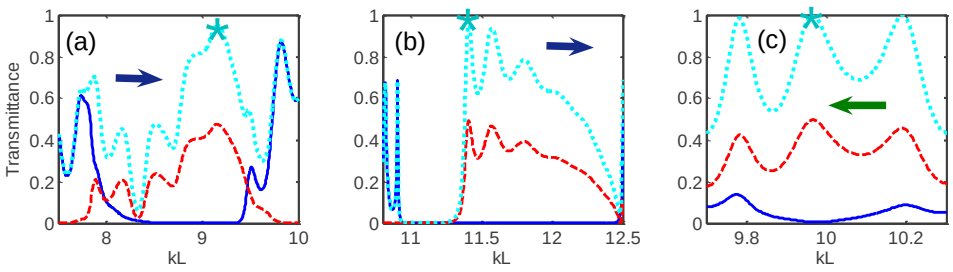

Figure 7.49: Transmittances $t_n^{\rightarrow}$ and $T^{\rightarrow}$ [plots (a),(b)], and $t_n^{\leftarrow}$ and $T^{\leftarrow}$ [plot (c)] for the PC grating with corrugations obtained by removing every second rod from all of the eight layers (a) and one layer (b) that are adjacent to the corrugated (here - illuminated) interface, and (c) from all of the four layers that are adjacent to the corrugated (here - exit) interface, $L = 2a$; $\varepsilon_r = 5.8$, $P = 12$, $\theta = 0$, (a,c) $d/a = 0.4$, (b) $d/a = 0.31$; blue solid line – $n = 0$, red dashed line – $n = -1$, cyan dotted line – $T^{\rightarrow}$ [plots (a),(b)] and $T^{\leftarrow}$ [plot (c)]; asterisk denotes (a) $\max T^{\rightarrow} > 0.9$, (b) $T^{\rightarrow} = 1$, and (c) $T^{\leftarrow} = 1$.

To summarize, strongly asymmetric transmission with a high forward-to-backward transmission contrast can be obtained by using conventional linear isotropic materials, provided that at least one additional transmission channel is open that differs from that is directly associated with the incident wave. In this paper, we demonstrated that the unidirectional diffraction relevant total optical transmission can be obtained in the PC gratings with the broken spatial inversion symmetry that are made of linear isotropic materials. The basic mechanism of the strongly asymmetric transmission, which is studied here, is connected with the *umklapp* scattering at the corrugated input interface that can

result in the appearance of one-way transmission channel(s). In contrast with the earlier studies, it was shown that the *total* transmission can be achieved at the corrugated-side illumination in both diode-like regimes, which we focused on, i.e., single-beam unidirectional deflection and two-beam unidirectional splitting. For the both regimes, total transmission is obtainable also at the noncorrugated-side illumination, provided that the single (in fact, two-way) transmission channel in the PC is connected with zero order, but zero-order transmission is suppressed in the exit half space. For the second regime mentioned, a higher transmittance with a relatively wide maximum occurs at the noncorrugated-side illumination, while a broader band was obtained at the corrugated-side illumination. Studies are in progress, which are aimed to infer the dominant physics of the unidirectional total transmission in order to develop a design oriented semi-analytical model. Finding PC grating performances with a broadband unidirectional total transmission will be a subject of future studies. The suggested operation regimes are promising for the design of new diode-type devices in a wide frequency range that includes not only optical but also microwave and acoustic frequencies.

7.6 Dispersion irrelevant asymmetric transmission in photonic crystal gratings

This section has been submitted in the form of a journal paper to Optics Letters. A.E. Serebryannikov, Evrim Colak, A. Ozgur Cakmak, and Ekmel Ozbay, "Dispersion irrelevant wideband asymmetric transmission in dielectric photonic crystal gratings," submitted to Optics Letters.

Among the approaches enabling partial analogs of diode-like directional selectivity which is usually associated with the use of anisotropic [160,195] and/or nonlinear [198,213] materials, the diffraction [200,204,221] and polarization conversion [233] relevant mechanisms of reciprocal asymmetric transmission should be mentioned. They can be realized in the structures with the broken axial symmetry, which are made of linear isotropic materials and,

thus, are reciprocal in sense of the Lorentz Lemma. However, they could be considered as nonreciprocal in a wider sense, since forward and backward transmissions are strongly distinguished for two opposite directions of incidence [200,223]. In particular, the diffraction relevant asymmetry in transmission originates from asymmetry in the coupling conditions at the incidence (input) and the exit interface, leading to the substantially different contributions of certain higher diffraction orders at the two opposite directions of incidence.

Metallic gratings [204,234] and especially photonic crystal (PhC) gratings [200,235,236] with different periods of the input and the exit interface are the perfect candidates for obtaining the asymmetric transmission. The latter look more promising because the merging effects of the dispersion of Floquet-Bloch (FB) modes of the PhC and diffractions can result in the desired diffraction orders, which may propagate in the incidence half-space, but originally are not coupled into FB waves. Thus, they do not appear in transmission in wide frequency and incidence angle ranges, provided that the exit interface may not create new orders propagating in the exit half-space at a proper choice of the periods of the interfaces. Nonsymmetric PhC gratings have been suggested less than decade ago [237] and then studied with the emphasis put on asymmetric transmission at zero [200,235] and arbitrary [200] angles of incidence, see Fig. 7.50. Later, the advanced performances have been proposed and some of them experimentally validated in various frequency ranges from acoustic to optical ones [221-223,237].

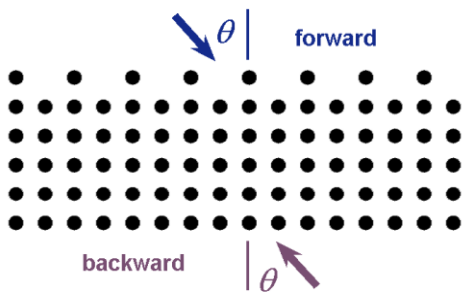

Figure 7.50: Geometry of PhC grating with one-side corrugations.

The wideband unidirectional transmission with high forward-case transmittance (corrugated-side illumination), $T^{\rightarrow} \neq 0$, and vanishing backward-case transmittance (noncorrugated-side illumination), $T^{\leftarrow} = 0$, appears while zero-order transmission is suppressed, $t_0^{\rightarrow} = t_0^{\leftarrow} = 0$. It is referred to as the direct regime [236]. This is probably the most interesting regime of asymmetric transmission realizable in the nonsymmetric PhC gratings due to the common effect of diffraction and dispersion of FB modes.

Very recently, it has been shown that the inverse regime of unidirectional transmission, i.e., that with $T^{\leftarrow} \neq 0$ and $T^{\rightarrow} \approx 0$ can appear in the same structures as the direct one at a certain frequency ("unidirectional point") due to the Lorentz reciprocity [236]. In this scenario, zero order is coupled to a FB wave for both of the (opposite) illumination directions, but extreme conversion into higher-order transmitted beams occurs at the corrugated exit interface. The question remains open whether zero order and the associated symmetric transmission component can be suppressed in wide ranges of variation in frequency and angle of incidence θ.

An attempt to obtain the reversible unidirectional transmission, i.e., that with $T^{\leftarrow} = 0$ and $T^{\rightarrow} \neq 0$ in one, and that with $T^{\rightarrow} = 0$ and $T^{\leftarrow} \neq 0$ in the other among the two adjacent frequency or/and angle ranges should be the next step to achieve new functionalities. However, wideband suppression of t_0 cannot be achieved due to the merging diffraction and dispersion effects in both of the ranges simultaneously. This means that the suppression of t_0 should be realized in one of these ranges solely due to the diffractions (i.e., not due to dispersion effects), if only linear anisotropic constituents are utilized. Such a wideband regime has not yet been found.

In this letter, we demonstrate that the strongly pronounced, wideband asymmetric transmission can be obtained in the inverse regime, including the case when the transmission is vanishing in one of the two opposite directions. It can be obtained using peculiar diffractions obtainable at a proper adjustment of

the lattice and corrugation parameters. In contrast to the direct regime, which is usually studied for the PhC gratings, the suppression of certain diffraction orders is not connected with the restrictions dictated by the dispersion of FB modes and wave vector diagrams. We focus in this study on the cases when not only zero order (symmetric transmission component), but also some of the higher orders (contributing to the asymmetric component), can be suppressed in the forward transmission, even if the wave vector diagram formally allows them to couple to a FB wave at the input and the exit interface. We consider the diffraction on PhC gratings, which are based on the square-lattice PhCs consisting of the dielectric rods of diameter d and permittivity ε_r. Totally, there are P layers of the rods. Since one of the interface layers has a larger lateral period ($L = 2a$) than all the other layers whose lattice constant is a as in Fig. 7.50, the grating is axially nonsymmetric. Illumination is assumed to be a plane wave with the electric field vector along the rods. Simulations have been performed by using an integral equation technique [229].

Figure 7.51 presents n-order forward ($t_n^{\rightarrow}$) and backward ($t_n^{\leftarrow}$) transmittances vs kL (k stands for the free-space wave number) for the PhC grating which has similar parameters as one of the recently studied gratings [221,236]. In the general case, the exit interface with a larger period in comparison to that of the input one can provide the contribution of diffraction orders to the transmission, which have been either evanescent or propagating but have not been coupled at the input interface. In turn, a smaller exit period than the input one cannot close the transmission channels that are open due to the input interface. In case of the backward transmission, the orders with $n = 0$ and $n = -2$ are coupled to one of the FB waves at the input (here - noncorrugated) interface, at least at $7.8 < kL < 8.4$, i.e., in the large portion of the observed asymmetric transmission range. In turn, $t_{-1}^{\leftarrow}$ can contribute to $T^{\leftarrow}$ only due to the effect of the exit (here - corrugated) interface. Variation in d/a allows one controlling the strength of the conversing action of the exit interface. $t_{-1}^{\leftarrow}$ can dominate in $T^{\leftarrow}$, as in Fig. 7.51(a). In case of the forward transmission, the

orders with $n=0$, -1, and -2 may be coupled to the same FB wave in this *kL*-range at the input (now - corrugated) interface, according to the wave vector diagram (not shown). However, only one of the associated three opened transmission channels actually contributes to $T^{\rightarrow}$. Thus, we obtain a wide *kL*-range, in which $T^{\rightarrow} \approx t_{-1}^{\rightarrow}$ and $T^{\leftarrow} \approx t_{-1}^{\leftarrow} + t_{-2}^{\leftarrow}$, while zero order is suppressed.

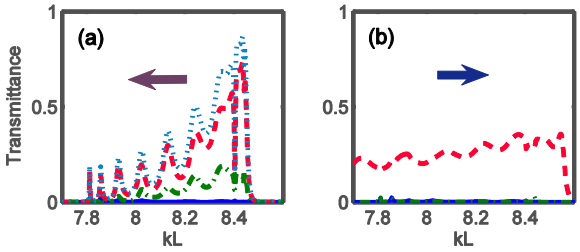

Figure 7.51: Backward (a) and forward (b) transmittance at $d/a=0.53$, $\varepsilon_r=9.61$, $P=12$ **, and** $\theta=60^{o}$**; blue solid line -** $t_0=t_0^{\leftarrow}=t_0^{\rightarrow}\approx 0$**, red dashed line -** $t_{-1}^{\leftarrow}$ **(a) and** $t_{-1}^{\rightarrow}$ **(b), green dash-dotted line -** $t_{-2}^{\leftarrow}$ **(a) and** $t_{-2}^{\rightarrow}\approx 0$ **(b), cyan dotted line -** $T^{\leftarrow}$ **(a).**

This asymmetric transmission range can be thought as a partial analog of the known one-way bands with $T^{\rightarrow} \approx t_0$ and $T^{\leftarrow} \approx t_0 + t_{-1}^{\leftarrow} + t_{+1}^{\leftarrow}$ that have been demonstrated at $\theta=0^{o}$ in the nonsymmetric PhC gratings [200,235] and nonsymmetric metallic gratings [204,234]. The first negative order in Fig. 7.51 plays the role similar to that of zero order in the regimes studied in [200,235], because of contributing to both $T^{\rightarrow}$ and $T^{\leftarrow}$. However, in contrast to [200,204,234,235], the two-way transmission component, which is associated now with the order with $n=-1$ shows different efficiencies in the forward and backward cases. Besides, in Fig. 7.51(b) one can observe the merging of the ranges of $T^{\rightarrow} \approx t_{-1}^{\rightarrow}$ which have different origins, that are associated with the exit-interface relevant suppression of zero order nearly at (i) $7.8<kL<8.4$, on one hand, and the uncoupling of zero order to a FB wave at the input interface at (ii) $kL<7.8$ and (iii) $kL>8.4$, on the other hand. Such a merging can be observed in a wide range of parameter variation. Roughly, these three regimes correspond – within transition ranges - to the isofrequency contours (IFCs)

located (ii) around Γ point (being narrower than in air), (i) around Γ and M points, and (iii) around X point.

The presented results above show that the wideband suppression of zero order and the relevant asymmetric transmission can be obtained without the blocking effect occurring due to the specific dispersion of the FB mode, as in [200,236]. However, this does not guarantee that $T^{\rightarrow} \approx 0$ as required for obtaining of a diode-like operation regime. Further adjustment is $kL = 8.5$ needed to obtain $T^{\rightarrow} = 0$ and $T^{\leftarrow} \neq 0$ in a wide kL-range.

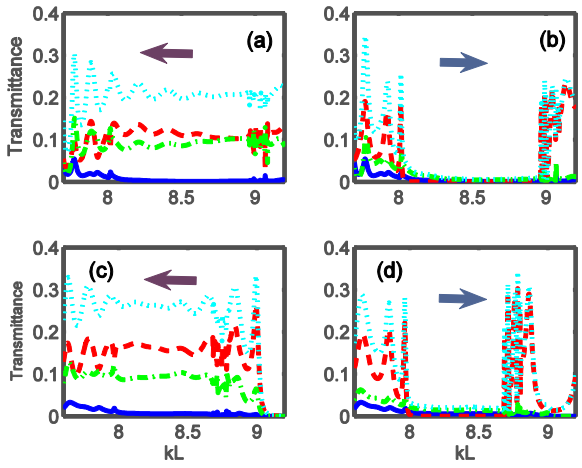

Figure 7.52: Backward (a,c) and forward (b,d) transmittance at $d/a = 0.4$ (a,b) and $d/a = 0.43$ (c,d), $\varepsilon_r = 5.8$, $P = 12$, and $\theta = 60^{\circ}$; blue solid line - $t_0 = t_0^{\leftarrow} = t_0^{\rightarrow}$, red dashed line - $t_{-1}^{\leftarrow}$ (a,c) and $t_{-1}^{\rightarrow}$ (b,d), green dash-dotted line - $t_{-2}^{\leftarrow}$ (a,c) and $t_{-2}^{\rightarrow}$ (b,d), cyan dotted line - $T^{\leftarrow}$ (a,c) and $T^{\rightarrow}$ (b,d).

Two examples are presented in Fig. 7.52. Here, the lattice parameters are either the same as or close to those of some performances studied in Ref. 221. One can see the range of unidirectional transmission with $T^{\rightarrow} \approx 0$ and $T^{\leftarrow} \approx t_{-1}^{\leftarrow} + t_{-2}^{\leftarrow}$ in the vicinity of . In both of the forward and backward cases, the orders with $n = 0$ and $n = -2$ may be coupled to the FB wave at the input interface. Now, the IFCs are located around M point and show a nearly square shape, as those used earlier for band-pass spatial filtering [228] and direct regime of unidirectional transmission [200]. In turn, the order with $n = -1$ contributes to $T^{\leftarrow}$ due to the coupling at the exit (here – corrugated) interface.

Furthermore, although the order with $n=-2$ is itself coupled to the FB wave in a two-way manner, we obtain $t_{-2}^{\leftarrow} >> t_{-2}^{\rightarrow}$. Hence, the effect of the corrugated interface can manifest itself also in the actual contribution of the formally coupled orders. Another adjustment would be required for increasing $T^{\leftarrow}$ when $T^{\rightarrow} \approx 0$, and obtaining the switching between the regimes with $T^{\leftarrow} \neq 0$ and $T^{\rightarrow} \approx 0$, and $T^{\leftarrow} = 0$ and $T^{\rightarrow} \neq 0$.

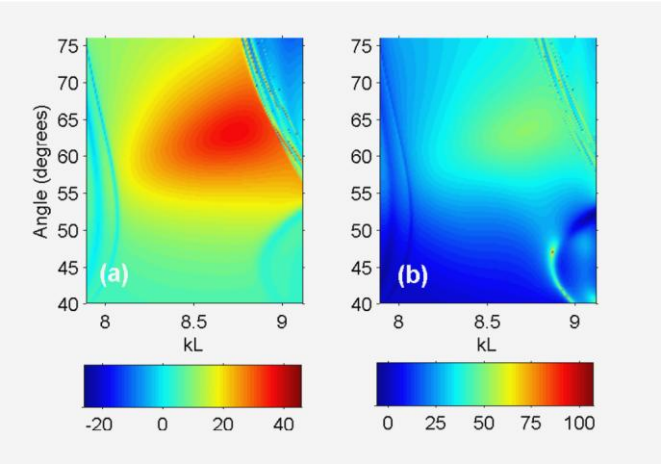

Figure 7.53: Maps of (a) backward-to-forward transmittance contrast, $C_1 = T^{\leftarrow}/T^{\rightarrow}$, and (b) higher-to-zero-order transmittance contrast in the backward case, $C_2 = (t_{-1}^{\leftarrow} + t_{-2}^{\leftarrow})/t_0$, in dB, for the same PhC grating as in Fig. 7.52.

For practical applications, it is important to estimate the extent to which the studied asymmetric transmission regime is sensitive to variations in *d/a* and θ. An important feature that follows from the obtained results (not shown) is the existence of the inverse unidirectional regime, as that in Fig. 7.52, in a wide range of *d/a*-variation, i.e., at least from $d/a = 0.27$ to $d/a = 0.43$. In order to demonstrate the band width and effect of θ, Fig. 7.53 presents the two contrasts, C_1 and C_2, which characterize the asymmetry in transmission, at the simultaneous variation of *kL* and θ. Both of the contrasts are mostly quite high in the considered ranges of *kL* and θ variation. Furthermore, there is strong correlation between C_1 and C_2. They are the highest in the vicinity of $\theta = 63^{o}$. Here, the band width is about 11%. The obtained results show that the inverse regime of unidirectional transmission can appear in a wide range of parameter

variation. This gives one significant freedom in choice of the parameters of PhC and beam-type illumination. In this concern, the inverse regime might be even more preferable than the direct regime, although higher efficiency can be obtained for the latter.

To summarize, we demonstrated that the wideband asymmetric transmission which can be obtained in a nonsymmetric PhC grating in the inverse regime as a purely diffraction effect. The obtained asymmetric transmission results include the case in which the transmission vanishes for one of the two opposite incidence directions. This is distinguished from the direct regime which appears due to the merging of diffraction and dispersion effects. It is shown that zero order being responsible for the symmetric transmission may be coupled to a FB wave at the incidence interface in both of the forward and backward cases but its contribution to the transmission is negligible. In turn, the contributions of the higher orders, which are asymmetric due to the structural (axial) asymmetry, can be significant and strongly dependent on the choice of the incidence direction. The studied mechanism is quite tolerant with respect to the variations in the angle of incidence and rod-diameter-to-lattice-constant ratio. The obtained results confirm the principal possibility of switchable diode-like devices in which the directions of the nonvanishing transmission are opposite for the two neighbouring wide frequency ranges, one of the ranges corresponds to the direct regime, while the second does to the inverse regime.

Chapter 8

Conclusion

At the end of this thesis I would like to make a brief summary of the important outcomes. First of all, the subwavelength resonators that are in the vicinity of the single subwavelength aperture are shown to drastically enhance the transmission. Unlike the counterparts in the literature, the transmission enhancement phenomenon is demonstrated for a single aperture. It is clearly illustrated that a periodic aperture arrangement is not mandatory in order to witness the transmission enhancement and the transmission enhancement stems from the excitation of the dipoles of the subwavelength resonator. On the other hand, the contribution of the secondary diffractions at the edges of the finite metallic screen is shown to obstruct the transmission enhancement phenomenon. It is concluded that antennas with relatively high directivity figures are needed to observe the transmission enhancement phenomenon through single subwavelength apertures in the microwave experiments in order to tackle the problem of the secondary diffractions. Of course, other conventional methods to reduce the contribution of the diffractions (rearranging the position of the subwavelength hole with respect to the edges, smoothing the edges, etc.) can be adapted.

The waves at the exit side of the metallic screen are evanescent. The resonator incorporated aperture yielded a subwavelength focusing, typically on the order of $\lambda/20$. Hence, such a confined wave in the near field could be employed in devices where the resolution really matters, e.g. in nano lithography, sensing applications, etc.

It was also pointed out that the subwavelength resonator needs to be considered together with the aperture in certain cases, i.e. when the plane of the resonator is parallel to the screen. Hence, an optimum value for the area of the aperture can be attained for a specific resonator. Image currents are formed

inside the overlapping regions of the metallic screen and the subwavelength resonator, which in turn causes the shifts in the transmission enhancement frequency. The subwavelength resonator does not interact with the subwavelength aperture that much as soon as the subwavelength resonator is located in an orthogonal fashion with respect to the screen. Yet, the highest transmission enhancement factors are observed for the prior case. Finally, the connecting bars between two resonators on each half space of the screen enable a broadband transmission enhancement that is almost independent of the size of the subwavelength aperture.

The origin of the transmission enhancement is also discussed for the aperture arrays. The enhanced transmission is connected to the diffraction mechanisms and the coupling of the artificial (surrounding) waveguide's modes to the subwavelength aperture arrays below the cutoff frequency of the holes owing to the periodic boundary conditions for sparsely separated apertures. On the other hand, the resonator nature of the hybridized unit lattices was shown to be the main reason behind the extraordinary transmission band for the dense configurations. The structures are shown to be scalable to optical wavelengths. The left handed behavior has been numerically demonstrated at infrared regime, which coincided with the extraordinary transmission phenomenon.

The coupling mechanism between the lattices along the propagation direction becomes important as the separation gets smaller values. Thus, elevated transmission results are observed as a consequence of the coupling mechanism. A wedge shaped arrangement has been constructed in order to study the negative refraction. The negative refraction has been spotted in the wedge experiments at the left handed transmission frequency band of the single layer fishnet, whereas the usual positive refraction has been observed for the right handed transmission frequency band of the same single layer. The origin of the negative refraction is shown to be caused by the zero order transmission rather than the higher negative diffraction orders. Furthermore, the performance characteristics of the wedge configuration have been examined by working with

different lattice spacing values along the propagation direction. It has been emphasized that the validity of the homogenization of the wedge arrangement at normal incidence is a controversial issue. The wedge can be treated as a composition of several 1-D transmission line columns with slightly different propagation constants. The inherent losses of the wedge configuration come into play in the negative refraction but the overall phenomenon is governed by the interference mechanism of the outgoing beam from these 1-D transmission lines. Consequently, the outgoing beam loses its coherency for certain values of lattice separation and the negative refraction does not appear. The wedge arrangement has been offered as a candidate for a wavelength demultiplexing process in a communication channel.

Later on, photonic crystal based designs have been under investigation. The graded index photonic crystals are shown to operate as input and output couplers to photonic crystal waveguides. The proposed graded index photonic crystal is studied at smaller wavelength regime unlike the previous examples in the literature. It is demonstrated that modified versions of the Gauss Hermite modes are supported inside the graded index photonic crystals such that a phase retardation mechanism is still applicable out of the metamaterial regime. Large spot size conversion ratios can be attained when the graded index photonic crystal is functionalized as a lens. The input coupling efficiency of the photonic crystal waveguide is drastically altered positively with the incorporation of the graded index photonic crystal as the input coupler. Likewise, the phase fronts of the exiting wave from the photonic crystal waveguide are reengineered by utilizing the graded index photonic crystal as an output coupler. Hence, the power is confined within a small angle at the far field and beaming is achieved with the aid of the graded index photonic crystal at the output side.

Furthermore, the photonic crystal gratings have been studied with the intention of achieving a diode like behavior. The incident wave is coupled to the different diffraction orders on opposite sides. The asymmetry of the index distribution enables the coupling of higher order diffractions from one side,

whereas the zero order transmission is suppressed. Extremely high contrast ratios have been attained as the transmission ratio of the forward and backward propagating waves. The phenomenon has been explained with the dispersion plots of the bulk photonic crystals. The unidirectional transmission is shown to obey the reciprocity rule. Moreover, the unidirectional transmission has also been illustrated as a result of the peculiar diffractions at the exit surface of the photonic crystal in another study. Hence, it is demonstrated that the unidirectional transmission could also exist independent of the dispersion effects as well.

Now, I have to make some critiques regarding the research fields of metamaterials and photonic crystals for those junior researchers who are about to enter the research areas. Both of these research areas are still attracting a lot of attention and several papers are being published every year. Particularly, the field of metamaterials has undergone lots of changes in the recent years. The main focus was about the negative refraction and subwavelength imaging at the beginning of the century. The main motivation behind the metamaterial based research and its funding used to be projected towards these research items. Nevertheless, either the disappointments arising from the fabrication and realization difficulties or the innovations in neighboring research areas compelled the field of metamaterials to shift its main course. The main topics that are covered in the conferences present a clue about this shift in interest. Nowadays, the metamaterials are commonly spelled out with non-linear phenomena and nano plasmonics. Tunable metamaterials and THz metamaterials are still active areas of research, but the major portion of the efforts are transferred to metasurfaces, transformation optics (cloaking), chirality, photovoltaic applications (light trapping) and sensing. Considering that, I have been involved actively in the research area since 2005 and I might be one of the last examples in the research community to investigate the metamaterials in the old style, i.e. within the context of left handedness and negative refraction. Likewise, I might be one of the last graduating Ph.D. students with this particular research focus.

Finally, the photonic crystal research has also been saturated over the last 20 years. Commercial applications of the photonic crystal are readily available. It is rumored that the photonic crystal research will still be active at least for another 5 years. However, it has started to be extremely difficult to publish new results in photonic crystals. Nonetheless, the research has been mainly led by certain research items like slow wave phenomenon, nonlinear effects and cavity interaction with light.

Bibliography

[1] V. Veselago, "The electrodynamics of substances with simultaneously negative values of ε and μ," *Soviet Physics Uspekhi*, vol. 10, no. 4, pp. 509-514, 1968.

[2] L. I. Mandelshtam, "Lecture on some problems of the theory of oscillations," *Complete Collection of Works*, vol. 5, pp. 428-467, 1944.

[3] L. I. Mandelshtam, "Group velocity in a crystal lattice," *Zhurnal Eksperimentalnoi i Teoreticheskoi Fiziki*, vol. 15, no. 9, pp. 476-478, 1945.

[4] D. V. Sivukhin, "The energy of electromagnetic waves in dispersive medi," *Opt. Spektrosk.*, vol. 3, pp.308-312, 1957.

[5] R. A. Silin, "Waveguiding properties of two-dimensional periodical slow-wave systems," *Voprosy Radioelectroniki Electronika*, vol. 4, pp. 11-33, 1959.

[6] L. Brillouin, *Wave Propagation in Periodic Structures*, McGraw-Hill, 1946.

[7] D. R. Smith, W. J. Padilla, D. C. Vier, S. C. Nemat-Nasser, and S. Schultz, "Composite medium with simultaneously negative permeability and permittivity," *Phys. Rev. Lett.*, vol. 84, no. 18, pp. 4184-4187, 2000.

[8] R. A. Shelby, D. R. Smith, and S. Schultz, "Experimental verification of a negative index of refraction," *Science*, vol. 292, pp. 77-79, 2001.

[9] J. B. Pendry, A. J. Holden, W. J. Stewart, and I. Youngs, "Extremely low frequency plasmons in metallic mesostructure," *Phys. Rev. Lett.*, vol. 76, no. 25, pp. 4773-4776, 1996.

[10] J. B. Pendry, A. J. Holden, D. J. Robbins, and W. J. Stewart, "Low frequency plasmons in thin-wire structures," *J. Phys. Condens. Matter*, vol. 10, pp. 4785-4809, 1998.

[11] A. H. Sihvola, A. J. Viitanen, I. V. Lindell, and S. A. Tretyakov, *Electromagnetic Waves in Chiral and Bi-Isotropic Media*, Artech House, 1994.

[12] S. A. Schelkunoff and H. T. Friis, *Antennas: Theory and Practice*, John Wiley & Sons, 1952.

[13] E. Yablonovitch, "Inhibited spontaneous emission in solid-state physics and electronics," *Phys. Rev. Lett.*, vol. 58, no. 20, pp. 2059-2062, 1987.

[14] Ltd Samsung Electronics Co, Us patent 7064886: Light regulating device and photonic crystal display utilizing photonic bandgap controls, 2006.

[15] Alex Scherer and Marko Loncar, Us patent 7079240: Photonic crystal laser sources for chemical detection, 2006.

[16] Philip St. John Russell, Timothy Adam Birks, and Jonathan Cave Knight, Us patent 6631234: Photonic crystal fibers, 2003.

[17] Jan Lipson, Hongyu Deng, and Thomas Lenosky, Us patent 6810056: Single mode vertical cavity surface emitting laser using photonic crystals with a central defect, 2004.

[18] S. Tretyakov, S. I. Maslovski, "Veselago Materials: What is Possible and Impossible about the Dispersion of the Constitutive Parameters," *IEEE Ant. And Prop. Mag.*, vol. 49, no. 1, pp. 37-43, 2007.

[19] L. D. Landau and E. M. Lifshits, *Electrodynamics of Continuous Media*, 2nd Edition, Oxford, Pergamon Press, 1984.

[20] N. Engetha, "Is Foster's Reactance Theorem Satisfied in Double Negative and Single-Negative Media?," *Microw. Opt. Tech. Lett.*, vol. 39, no. 1, pp. 11-14, 2003.

[21] S. Tretyakov, "Meta-materials with wideband negative permittivity and permeability," *Microw. Opt. Tech. Lett.*, vol. 31, no. 3, pp. 163-165, 2001.

[22] T. J. Yen, W. J. Padilla, N. Fang, D. C. Vier, D. R. Smith, J. B. Pendry, D. N. Basov, and X. Zhang, "Terahertz Magnetic Response from Artificial Materials," *Science*, vol. 303, no. 5663, pp. 1494-1496, 2004.

[23] S. Linden, C. Enkrich, M. Wegener, J. Zhou, T. Koschny, and C. M. Soukoulis, "Magnetic Response of Metamaterials at 100 Terahertz," *Science*, vol. 306, no. 5700, pp. 1351-1353, 2004.

[24] C. Enkrich, M. Wegener, S. Linden, L. Zschiedrich, F. Schmidt, J. F. Zhou, T. Koschny, and C. M. Soukoulis, "Magnetic Metamaterials at Telecommunication and Visible Frequencies," *Phys. Rev. Lett.*, vol. 95, no. 20, 203901, 2005.

[25] H. O. Moser, B. D. F. Casse, O. Wilhelmi, B. T. Saw, "Terahertz Response of a Microfabricated Rod–Split-Ring-Resonator Electromagnetic Metamaterial," *Phys. Rev. Lett.*, vol. 94, no. 6, 063901, 2005.

[26] V. M. Shalaev, W. Cai, U. K. Chettiar, Hsiao-Kuan Yuan, A. K. Sarychev, V. P. Drachev, and A. V. Kildishev, "Negative index of refraction in optical metamaterials," *Opt. Lett*., vol. 30, no. 24, pp. 3356-3358, 2005.

[27] G. Dolling, C. Enkrich, M. Wegener, J. F. Zhou, C. M. Soukoulis, and S. Linden, "Cut-wire pairs and plate pairs as magnetic atoms for optical metamaterials,"*Opt. Lett.*, vol. 30, no. 23, pp. 3198-3200, 2005.

[28] J. Zhou, L. Zhang, G. Tuttle, T. Koschny, and C. M. Soukoulis, "Negative index materials using simple short wire pairs," *Phys. Rev. B*, vol. 73, no. 4, 041101, 2006.

[29] S. Zhang, W. Fan, N. C. Panoiu, K. J. Malloy, R. M. Osgood, and S. R. J. Brueck, "Experimental Demonstration of Near-Infrared Negative-Index Metamaterials," *Phys. Rev. Lett.*, vol. 95, 137404, 2005.

[30] K. Aydin, K. Guven, M. Kafesaki, L. Zhang, C. M. Soukoulis, and E. Ozbay, “Experimental observation of true left-handed transmission peak in metamaterials,” *Opt. Lett.*, vol. 29, no23, pp. 2623-2625, 2004.

[31] C. Genet and T. W. Ebbesen, “Light in tiny holes,” *Nature*, vol. 445, pp. 39-46, 2007.

[32] T. Matsui, A. Agrawal, A. Nahata, and Z. V. Vardeny, “Transmission resonances through aperiodic arrays of subwavelength apertures,” *Nature*, vol. 446, pp. 517-521, 2007.

[33] H. A: Bethe, “Theory of Diffraction by Small Holes,” *Phys. Rev.*, vol. 66, pp. 163-182, 1944.

[34] T. W. Ebbesen, H. J. Lezec, H. F. Ghaemi, T. Thio, and P. A. Wolff, “Extraordinary optical transmission through sub-wavelength hole arrays,” *Nature*, vol. 391, pp. 667-669, 1998.

[35] L. M. Moreno, F. J. G. Vidal, H. J. Lezec, K. M. Pellerin, T. Thio, J. B. Pendry, and T. W. Ebbesen, “Theory of Extraordinary Optical Transmission through Subwavelength Hole Arrays,” *Phys. Rev. Lett.*, vol. 86, no. 6, pp. 1114-1117, 2001.

[36] W. L. Barnes, W. A. Murray, J. Dintinger, E. Devaux, and T. W. Ebbesen, “Surface Plasmon Polaritons and Their Role in the Enhanced Transmission of Light through Periodic Arrays of Subwavelength Holes in a Metal Film,” *Phys. Rev. Lett.*, vol. 92, no. 10, 107401, 2004.

[37] J. B. Abad, A. Degiron, F. Pryzbilla, C. Genet, F. J. G. Vidal, L. M. Moreno, and T. W. Ebbesen, “How light emerges from an illuminated array of subwavelength holes,” *Nature Phys.*, vol. 2, pp. 120-123, 2006.

[38] A. Alu, F. Bilotti, N. Engetha, and L. Vegni, “Metamaterial covers over a small aperture,” *IEEE Trans. Antennas Propag.*, vol. 54, no. 6, pp. 1632-1643, 2006.

[39] N. Katsarakis, M. Kafesaki, I. Tsiapa, E. N. Economou, and C. M. Soukoulis, "High transmittance left-handed materials involving symmetric split-ring resonators," *Photonics Nanostruct. Fundam. Appl.*, vol. 5, no. 4, pp. 149-155, 2007.

[40] R. Marques, F. Mesa, J. Martel, and F. Medina, "Comparative analysis of edge- and broadside- coupled split ring resonators for metamaterial design - theory and experiments," *IEEE Trans. Antennas Propag*., vol. 51, no. 10, pp. 2572-2581, 2003.

[41] K. Aydin, A. O. Cakmak, L. Sahin, Z. Li, F. Bilotti, L. Vegni, and E. Ozbay, "Split-Ring-Resonator-Coupled Enhanced Transmission through a Single Subwavelength Aperture," *Phys. Rev. Lett.*, vol. 102, no. 1, 013904, 2009.

[42] J. A. Porto, F. J. Garcia-Vidal, and J. B. Pendry, "Transmission resonances on metallic gratings with very narrow slits," *Phys. Rev. Lett.*, vol. 83, pp. 2845-2848, 1999.

[43] K. G. Lee and Q.-H. Park, "Coupling of surface plasmon polaritons and light in metallic nanoslits," *Phys. Rev. Lett.*, vol. 95, 103902, 2005.

[44] Y. Xie, A. R. Zakharian, J. V. Moloney, and M. Mansuripur, "Transmission of light through periodic arrays of sub-wavelength slits in metallic hosts," *Opt. Express*, vol. 14, pp. 6400-6413, 2006.

[45] F. J. Garcia de Abajo, J. J. Saenz, I. Campillo, and J. S. Dolado, "Site and lattice resonances in metallic hole arrays," *Opt. Express*, vol. 14, pp. 7-18, 2006.

[46] F. Marquier, J.-J. Greffet, S. Collin, F. Pardo, and J. L. Pelouard, "Resonant transmission through a metallic film due to coupled modes," *Opt. Express*, vol. 13, pp. 70-76, 2005.

[47] H. F. Schouten, N. Kuzmin, G. Dubois, T. D. Visser, G. Gbur, P. F. A. Alkemade, H. Blok, G. W. 't Hooft, D. Lenstra, and E. R. Eliel,

"Plasmon-assisted two-slit transmission: Young's experiment revisited," *Phys. Rev. Lett.*, vol. 94, 053901, 2005.

[48] A. Dogariu, T. Thio, L. J. Wang, T. W. Ebbesen, and H. J. Lezec, "Delay in light transmission through small apertures," *Optics Lett.*, vol. 26, pp. 450-452, 2001.

[49] Q.-j. Wang, J.-q. Li, C.-p. Huang, C. Zhang, and Y.-y. Zhu, "Enhanced optical transmission through metal films with rotation-symmetrical hole arrays," *Appl. Phys. Lett.*, vol. 87, 091105, 2005.

[50] K. J. K. Koerkamp, S. Enoch, F. B. Segerink, N. F. v. Hulst, and L. Kuipers, "Strong influence of hole shape on extraordinary transmission through periodic arrays of subwavelength holes," *Phys. Rev. Lett.*, vol. 92, 183901, 2004.

[51] H. F. Ghaemi, T. Thio, D. E. Grupp, T. W. Ebbesen, and H. J. Lezec, "Surface plasmons enhance optical transmission through subwavelength holes," *Phys. Rev. B*, vol. 58, pp. 6779-6782, 1998.

[52] F. J. Garcia de Abajo, "Light transmission through a single cylindrical hole in a metallic film," *Opt. Express*, vol. 10, pp. 1475-1484, 2002.

[53] A. R. Zakharian, M. Mansuripur, and J. V. Moloney, "Transmission of light through small elliptical apertures," *Opt. Express*, vol. 12, pp. 2631-2648, 2004.

[54] F. J. Garcia-Vidal, E. Moreno, J. A. Porto, and L. Martin-Moreno, "Transmission of light through a single rectangular hole," *Phys. Rev. Lett.*, vol. 95, 103901, 2005.

[55] L. Yin, V. K. Vlasko-Vlasov, A. Rydh, J. Pearson, U. Welp, S.-H. Chang, S. K. Gray, G. C. Schatz, D. B. Brown, and C. W. Kimball, "Surface plasmons at single nanoholes in Au films," *Appl. Phys. Lett.*, vol. 85, pp. 467-469, 2004.

[56] A. Degiron and T. W. Ebbesen, "Analysis of the transmission process through single apertures surrounded by periodic corrugations," *Opt. Express*, vol. 12, pp. 3694-3700, 2004.

[57] F. J. Garcia-Vidal, L. Martin-Moreno, H. J. Lezec, and T. W. Ebbesen, "Focusing light with a single subwavelength aperture flanked by surface corrugations," *Appl. Phys. Lett*., vol. 83, pp. 4500-4502, 2003.

[58] H. Caglayan, I. Bulu, and E. Ozbay, "Plasmonic structures with extraordinary transmission and highly directional beaming properties," *Microw. Opt. Techn. Lett*., vol. 48, pp. 2491-2496, 2006.

[59] S. S. Akarca-Biyikli, I. Bulu, and E. Ozbay, "Enhanced transmission of microwave radiation in one-dimensional metallic gratings with subwavelength aperture," *Appl. Phys. Lett*., vol. 85, pp. 1098-1100, 2004.

[60] S. S. Akarca-Biyikli, I. Bulu, and E. Ozbay, "Resonant excitation of surface plasmons in one-dimensional metallic grating structures at microwave frequencies," *J. Opt. Pure Appl. Opt*., vol. 7, pp. S159-S164, 2005.

[61] L. Martin-Moreno, F. J. Garcia-Vidal, H. J. Lezec, A. Degiron, and T. W. Ebbesen, "Theory of highly directional emission from a single subwavelength aperture surrounded by surface corrugations," *Phys. Rev. Lett*., vol. 90, 167401, 2003.

[62] H. J. Lezec, A. Degiron, E. Devaux, R. A. Linke, L. Martin-Moreno, F. J. Garcia-Vidal, and T. W. Ebbesen, "Beaming light from a subwavelength aperture," *Science*, vol. 297, pp. 820-822, 2002.

[63] G. Gbur, H. F. Schouten, and T. D. Visser, "Achieving superresolution in near-field optical data readout systems using surface plasmons," *Appl. Phys. Lett*., vol. 87, 191109, 2005.

[64] T. Ishi, J. Fujikata, K. Makita, T. Baba, and K. Ohashi, "Si nano-photodiode with a surface plasmon antenna," *Jpn. J. Appl. Phys*., vol. 44, pp. L 364-L 366, 2005.

[65] C. Liu, V. Kamaev, and Z. V. Vardeny, "Efficiency enhancement of an organic light-emitting diode with a cathode forming two-dimensional periodic hole array," *Appl. Phys. Lett.*, vol. 86, 143501, 2005.

[66] X. Luo and T. Ishihara, "Sub-100-nm photolithography based on plasmon resonance," *Jpn. J. Appl. Phys*. vol. 43, pp. 4017-4021, 2004.

[67] D. B. Shao and S. C. Chen, "Surface-plasmon-assisted nanoscale photolithography by polarized light," *Appl. Phys. Lett*., vol. 86, 253107, 2005.

[68] P. R. H. Stark, A. E. Halleck, and D. N. Larson, "Short order nanohole arrays in metals for highly sensitive probing of local indices of refraction as the basis for a highly multiplexed biosensor technology," *Methods*, vol. 37, pp. 37-47, 2005.

[69] S. M. Williams, K. R. Rodriguez, S. Teeters-Kennedy, S. Shah, T. M. Rogers, A. D. Stafford, and J. V Coe, "Scaffolding for nanotechnology: extraordinary infrared transmission of metal microarrays for stacked sensors and surface spectroscopy," *Nanotechnology*, vol. 15, pp. S495-S503, 2004.

[70] H. Rigneault, J. Capoulade, J. Dintinger, J. Wenger, N. Bonod, E. Popov, T. W. Ebbesen, and P.-F. Lenne, "Enhancement of single-molecule fluorescence detection in subwavelength apertures," *Phys. Rev. Lett*., vol. 95, 117401, 2005.

[71] J. B. Pendry, L. Martin-Moreno, and F. J. Garcia-Vidal, "Mimicking surface plasmons with structured surfaces," *Science*, vol. 305, pp. 847-848, 2004.

[72] F. J. Garcia-Vidal, L. Martin-Moreno, and J. B. Pendry, "Surfaces with holes in them: new plasmonic metamaterials," *J. Opt. Pure Appl. Opt.*, vol. 7, pp. S97-S101, 2005.

[73] A. O. Cakmak, K. Aydin, E. Colak, Z. Li, F. Bilotti, L. Vegni, and E. Ozbay, "Enhanced transmission through a subwavelength aperture using metamaterials," *Appl. Phys. Lett.*, vol. 95, 052103, 2009.

[74] K. B. Alici, F. Bilotti, L. Vegni, and E. Ozbay, "Optimization and tunability of deep subwavelength resonators for metamaterial applications: complete enhanced transmission through a subwavelength aperture," *Opt. Express*, vol. 17, pp. 5933-5943, 2009.

[75] F. Bilotti, L. Scorrano, E. Ozbay, and L. Vegni, "Enhanced transmission through a sub-wavelength aperture: resonant approaches employing metamaterials," *J. Opt. Pure Appl. Opt.*, vol. 11, 114029, 2009.

[76] M. Beruete, M. Sorolla, I. Campillo, J. S. Dolado, L. Martin-Moreno, J. Bravo-Abad, and F. J. Garcia-Vidal, "Enhanced millimeter wave transmission through quasioptical subwavelength perforated plates," *IEEE Trans. on Anten. and Propag.*, vol. 53, no. 6, pp. 1897- 1903, 2005.

[77] F. J. Garcia-Vidal, H. J. Lezec, T. W. Ebbesen, and L. Martin-Moreno, "Multiple Paths to Enhance Optical Transmission through a Single Subwavelength Slit," *Phys. Rev. Lett.*, vol. 90, 213901, 2003.

[78] E. Ozbay, "Plasmonics: Merging Photonics and Electronics at Nanoscale Dimensions," *Science*, vol. 311, no. 5758, pp. 183-193, 2006.

[79] D. Ates, A. O. Cakmak, E. Colak, R. Zhao, C. M. Soukoulis, and E. Ozbay, "Transmission enhancement through deep subwavelength apertures using connected split ring resonators," *Opt. Express*, vol. 18, pp. 3952-3966, 2010.

[80] X. Jiang and C.M. Soukoulis, “Time dependent theory for random lasers,” *Phys. Rev. Lett.*, vol. 85, pp. 70-73, 2000.

[81] X. Jiang and C. M. Soukoulis, “Localized random lasing modes and a path for observing localization,” *Phys. Rev. E*, vol. 65, 025601, 2002.

[82] S. Kao, F. M. Huang, Y. Chen, E. T. F. Rogers, and N. I. Zheludev, “Metamaterial as a controllable template for nanoscale field localization,” *Appl. Phys. Lett.*, vol. 96, 041103, 2010.

[83] S. Savo, N. Papasimakis, and N. I. Zheludev, “Observation of slow-light in a metamaterials waveguide at microwave frequencies,” *Quant. Elect. and Laser Sci. Conference*, OSA, 2011.

[84] T. S. Kao, S. D. Jenkins, J. Ruostekoski, and N. I. Zheludev, “Coherent Control of Nanoscale Light Localization in Metamaterial: Creating and Positioning Isolated Subwavelength Energy Hot Spots,” *Phys. Rev. Lett.*, vol. 106, 085501, 2011.

[85] H. Caglayan, I. Bulu, M. Loncar, and E. Ozbay, “Experimental observation of subwavelength localization using metamaterial-based cavities,” *Opt. Lett.*, vol. 34, pp. 88-90, 2009.

[86] M. Bayindir, B. Temelkuran, and E. Ozbay, “Tight-Binding Description of the Coupled Defect Modes in Three-Dimensional Photonic Crystals,” *Phys. Rev. Lett*. vol. 84, 2140, 2000.

[87] J. B. Pendry, “Negative refraction makes a perfect lens,” *Phys. Rev. Lett.*, vol. 85, 3966, 2000.

[88] N. Fang and X. Zhang, “Imaging properties of a metamaterial superlens,” *Appl. Phys. Lett.*, vol. 82, 161, 2003.

[89] A. Grbic, and G. V. Eleftheriades, “Overcoming the Diffraction Limit with a Planar Left-Handed Transmission-Line Lens,” *Phys. Rev. Lett.*, vol. 92, 117403, 2004.

[90] K. Aydin, I. Bulu, and E. Ozbay, "Focusing of electromagnetic waves by a left-handed metamaterial flat lens," *Opt. Express*, vol. 13, pp. 8753-8759, 2005.

[91] S. Ramo, J. R. Whinnery, and T. Van Duzer, *Fields and Waves in Communication Electronics*, John Wiley & Sons Inc., 1994.

[92] C. A. Balanis, *Antenna theory Analysis and Design*, John Wiley & Sons Inc., 2005.

[93] R. Marques, F. Mesa, L. Jelinek, and F. Medina, "Analytical theory of extraordinary transmission through metallic diffraction screens perforated by small holes," *Opt. Express*, vol. 17, no. 7, pp. 5571-5579, 2009.

[94] F. Medina, F. Mesa, and R. Marques, "Extraordinary Transmission Through Arrays of Electrically Small Holes From a Circuit Theory Perspective," *IEEE Trans. Microw. Theory Tech.*, vol. 56, no. 12, pp.3108-3120, 2008.

[95] M. Beruete, I. Campillo, M. Navarro-Cia, F. Falcone, and M. S. Ayza, "Molding Left- or Right-Handed Metamaterials by Stacked Cutoff Metallic Hole Arrays," *IEEE Trans. on Anten. and Propag.*, vol. 55, no. 6, pp. 1514-1521, 2007.

[96] G. Dolling, M. Wegener, C. M. Soukoulis, and S. Linden, "Negative-index metamaterial at 780 nm wavelength," *Opt. Lett*., vol. 32, no. 1, pp. 53-55, 2007.

[97] G. Dolling, C. Enkrich, M. Wegener, C. M. Soukoulis, S. Linden, "Simultaneous Negative Phase and Group Velocity of Light in a Metamaterial," *Science*, vol. 312, pp. 892-894, 2006.

[98] M. Beruete, M. Sorolla, and I. Campillo, "Left-handed extraordinary optical transmission through a photonic crystal of subwavelength hole arrays," *Opt. Express*, vol. 14, no. 12, pp. 5445-5455, 2006.

[99] M. Beruete, M. Navarro-Cia, F. Falcone, I. Campillo, and M. Sorolla, "Connection between extraordinary transmission and negative refraction in a prism of stacked sub-wavelength hole arrays," *J. Phys. D: Appl. Phys*., vol. 42, no. 16, 165504, 2009.

[100] C. Menzel, T. Paul, C. Rockstuhl, T. Pertsch, S. Tretyakov, and F. Lederer, "Validity of effective material parameters for optical fishnet metamaterials," *Phys. Rev. B*, vol. 81, no. 3, 035320, 2010.

[101] L. Jelinek, R. Marques, and J. Machac, "Fishnet Metamaterials-Rules for Refraction and Limits of Homogenization," *Opt. Express*, vol. 18, no. 17, pp. 17940-17948, 2010.

[102] G. V. Eleftheriades, O. Siddiqui, and A. K. Iyer, "Transmission Line Models for Negative Refractive Index Media and Associated Implementations Without Excess Resonators," *IEEE Microw. Wirel. Compon. Lett.*, vol. 13, no. 2, pp. 51-53, 2003.

[103] M. Beruete, M. Sorolla, I. Campillo, and J. S. Dolado, "Increase of the Transmission in Cut-Off Metallic Hole Arrays," *IEEE Microw. Wirel. Compon. Lett.*, vol. 15, no. 2, pp. 116-118, 2005.

[104] M. Beruete, M. Sorolla, I. Campillo, J. S. Dolado, L. Martin-Moreno, J. Bravo-Abad, and F. J. Garcia-Vidal, "Enhanced millimeter-wave transmission through subwavelength hole arrays," *Opt. Lett*., vol. 29, no. 21, pp. 2500-2502, 2004.

[105] K. B. Alici, and E. Ozbay, "A planar metamaterial: Polarization independent fishnet structure," *Photon. Nano. Fund. Appl*., vol. 6, pp. 102-107, 2008.

[106] K. B. Alici, and E. Ozbay, "Characterization and tilted response of a fishnet metamaterial operating at 100 GHz," *J. Phys. D: Appl. Phys*. vol. 41, no. 13, 135011, 2008.

[107] N. –H. Shen, G. Kenanakis, M. Kafesaki, N. Katsarakis, E. N. Economou, and C. M. Soukoulis, "Parametric investigation and analysis of fishnet metamaterials in the microwave regime," *J. Opt. Soc. Am. B*, vol. 26, no.12, pp. B61-B67, 2009.

[108] K. Aydin, Z. Li, L. Sahin, and E. Ozbay, "Negative phase advance in polarization independent, multi-layer negative-index metamaterials," *Opt. Express*, vol. 16, no. 12, pp. 8835-8843, 2008.

[109] M. Kafesaki, I. Tsiapa, N. Katsarakis, Th. Koschny, C. M. Soukoulis, and E. N. Economou, "Left-handed metamaterials: The fishnet structure and its variations," *Phys. Rev. B*, vol. 75, no. 23, 235114, 2007.

[110] R. Ortuno, C. Garcia-Meca, F. J. Rodriguez-Fortuno, J. Marti, and A. Martinez, "Role of surface plasmon polariton on extraordinary optical transmission through double-layer metallic hole arrays," *Phys. Rev. B*, vol. 79, no. 7, 075425, 2009.

[111] R. Marques, L. Jelinek, F. Mesa, and F. Mediana, "Analytical theory of wave propagation through stacked fishnet metamaterials," *Opt. Express*, vol. 17, no. 14, pp. 11582-11592, 2009.

[112] H. Caglayan, I. Bulu, M. Loncar, and E. Ozbay, "Experimental observation of cavity formation in composite metamaterials," *Opt. Express*, vol. 16, no. 15, pp. 11132-11140, 2008.

[113] M. Beruete, M. Navarro-Cia, S. A. Kuznetsov, and M. Sorolla, "Circuit Approach to the minimal configuration of terahertz anomalous extraordinary transmission," *Appl. Phys. Lett.*, vol. 98, no. 1, 014106, 2011.

[114] M. Beruete, M. Navarro-Cia, M. Sorolla, "Understanding Anomalous Extraordinary Transmission From Equivalent Circuit and Grounded Slab Concepts," *IEEE Trans. Microw. Theory Tech.*, vol. 59, no. 9, pp. 2180-2188, 2011.

[115] M. Beruete, M. Sorolla, M. Navarro-Cia, F. Falcone, I. Campillo, and V. Lomakin, "Extraordinary transmission and left-handed propagation in miniaturized stacks of doubly periodic subwavelength hole arrays," *Opt. Express*, vol. 15, no. 3, pp. 1107-1114, 2007.

[116] J. Zhou, Th. Koschny, M. Kafesaki, and C. M. Soukoulis, "Size dependence and convergence of the retrieval parameters of metamaterials," *Photon. Nano. Fund. Appl.*, vol. 6, pp. 96-101, 2008.

[117] M. Beruete, M. Navarro-Cia, and M. Sorolla, "Strong lateral displacement in polarization anisotropic extraordinary transmission metamaterial," *New J. Phys*., vol. 12, 063037, 2010.

[118] B. A. Munk, *Metamaterials: Critique and Alternatives*, The USA: John Wiley & Sons, Inc., 2009.

[119] R. C. Hansen, "Negative refraction without negative index," *IEEE Trans. Antennas Propag.*, vol. 56, 402, 2008.

[120] C. Gomez-Reino, M. V. Perez, C. Bao, *Gradient-Index Optics: Fundamentals and Applications*, Springer, 2002.

[121] P. S. J. Russell, and T. A. Birks, "Hamiltonian Optics of Nonuniform Photonic Crystals," *J. Lightwave Technol*., vol. 17, pp. 1982- 1988, 1999.

[122] K. Q. Le, and P. Bienstman, "Padé approximate solution for wave propagation in graded-index metamaterials," *J. Opt*., vol. 13, 024015, 2011.

[123] J.-H. Park, W. S. Choi, H. Y. Koo, and D.-Y. Kim, "Colloidal Photonic Crystal with Graded Refractive-Index Distribution," *Adv. Mater*., vol.17, pp. 879-885, 2005.

[124] H. Kurt, and D. S. Citrin, "Graded index photonic crystals," *Opt. Express*, vol. 15, pp. 1240-1253, 2007.

[125] Q. Wu, J. M. Gibbons, and W. Park, “Graded negative index lens by photonic crystals,” *Opt. Express*, vol. 16, pp. 16941-16949, 2008.

[126] F. S. Roux, and I. D. Leon, “Planar photonic crystal gradient index lens, simulated with a finite difference time domain method,” *Phys. Rev. B*, vol. 74, 113103, 2006.

[127] H. Kurt, and D. S. Citrin, “A Novel Optical Coupler Design With Graded-Index Photonic Crystals,” *IEEE Photon. Technol. Lett*., vol. 19, pp. 1532-1534, 2007.

[128] E. Centeno, and D. Cassagne, “Graded photonic crystals,” *Opt. Lett*., vol. 30, pp. 2278-2280, 2005.

[129] E. Centeno, D. Cassagne, and J.-P. Albert, “Mirage and superbending effect in two-dimensional graded photonic crystals,” *Phys. Rev. B*, vol. 73, 235119, 2006.

[130] E. Akmansoy, E. Centeno, K. Vynck, D. Cassagne, and J.-M. Lourtioz, “Graded photonic crystals curve the flow of light: An experimental demonstration by the mirage effect,” *Appl. Phys. Lett*., vol. 92, 133501, 2008.

[131] E. Centeno, E. Akmansoy, K. Vynck, D. Cassagne, and J.-M. Lourtioz, “Light bending and quasi-transparency in metallic graded photonic crystals,” *Photonics Nanostruct. Fundam. Appl*. vol.8, pp. 120-124, 2010.

[132] A. O. Cakmak, E. Colak, H. Caglayan, H. Kurt, and E. Ozbay, “High efficiency of graded index photonic crystal as an input coupler,” *J. Appl. Phys*., vol. 105, 103708, 2009.

[133] S.-C. S. Lin, T. J. Huang, J.-H. Sun, and T.-T. Wu, “Gradient-index phononic crystals,” *Phys. Rev. B*, vol. 79, 094302, 2009.

[134] B. K. Juluri, S.-C. S. Lin, T. R. Walker, L. Jensen, and T. J. Huang, "Propagation of designer surface plasmons in structured conductor surfaces with parabolic gradient index," *Opt. Express*, vol. 17, pp. 2997-3006, 2009.

[135] G. Lubkowski, R. Schuhmann, and T. Weiland, "Extraction of Effective Metamaterial Parameters by Parameter Fitting of Dispersive Models," *Microwave Opt. Technol. Lett.*, vol. 49, pp. 285-288, 2007.

[136] B. D. F. Casse, W. T. Lu, Y. J. Huang, and S. Sridhar, "Nano-optical microlens with ultrashort focal length using negative refraction," *Appl. Phys. Lett.*, vol. 93, 053111, 2008.

[137] C. G. Parazzoli, R. B. Greegor, J. A. Nielsen, M. A. Thompson, K. Li, A. M. Vetter, M. H. Tanielian, and D. C. Vier, "Performance of a negative index of refraction lens," *Appl. Phys. Lett.*, vol. 84, pp. 3232-3234, 2004.

[138] T. Driscoll, D. N. Basov, A. F. Starr, P. M. Rye, S. Nemat-Nasser, D. Schurig, and D. R. Smith, "Free-space microwave focusing by a negative-index gradient lens," *Appl. Phys. Lett.*, vol. 88, 081101, 2006.

[139] R. B. Greegor, C. G. Parazzoli, J. A. Nielsen, M. A. Thompson, M. H. Tanielian, and D. R. Smith, "Simulation and testing of a graded negative index of refraction lens," *Appl. Phys. Lett*., vol. 87, 091114, 2005.

[140] D. R. Smith, J. J. Mock, A. F. Starr, and D. Schurig, "Gradient index metamaterials," *Phys. Rev. E*, vol. 71, 036609, 2005.

[141] O. Paul, B. Reinhard, B. Krolla, R. Beigang, and M. Rahm, "Gradient index metamaterial based on slot elements," *Appl. Phys. Lett*., vol. 96, 241110, 2010.

[142] R. Liu, X. M. Yang, J. G. Gollub, J. J. Mock, T. J. Cui, and D. R. Smith, "Gradient index circuit by waveguided metamaterials," *Appl. Phys. Lett*., vol. 94, 073506, 2009.

[143] R. Lui, Q. Cheng, J. Y. Chin, J. J. Mock, T. J. Cui, and D. R. Smith, "Broadband gradient index microwave quasi-optical elements based on non-resonant metamaterials," *Opt. Express*, vol. 17, pp. 21030-21041, 2009.

[144] U. Levy, M. Nezhad, H.-C. Kim, C.-H. Tsai, L. Pang, and Y. Fainmann, "Implementation of a graded-index medium by use of subwavelength structures with graded fill factor," *J. Opt. Soc. Am. A*, vol. 22, pp. 724-733, 2005.

[145] U. Levy, M. Abashin, K. Ikeda, A. Krishnamoorthy, J. Cunningham, and Y. Fainman, "Inhomogenous Dielectric Metamaterials with Space-Variant Polarizability," *Phys. Rev. Lett.*, vol. 98, 243901, 2007.

[146] M. Lu, B. K. Juluri, S.-C. S. Lin, B. Kirally, T. Gao, and T. J. Huang, "Beam aperture modifier and beam deflector using graded-index photonic crystals," *J. Appl. Phys.*, vol. 108, 103505, 2010.

[147] H.-W. Wang, and L.-W. Chen, "High transmission efficiency of arbitrary waveguide bends formed by graded index photonic crystals," *J. Opt. Soc. Am. B*, vol. 28, pp. 2098-2104, 2011.

[148] H.-W. Wang, and L.-W. Chen, "A cylindrical optical black hole using graded index photonic crystals," *J. Appl. Phys*., vol. 109, 103104, 2011.

[149] M. Yin, X. Y. Tian, H. X. Han, and D. C. Li, "Free-space carpet-cloak based on gradient index photonic crystals in metamaterial regime," *Appl. Phys. Lett*., vol. 100, 124101, 2012.

[150] B. Vasic, G. Isic, R. Gajic, and K. Hingerl, "Controlling electromagnetic fields with graded photonic crystals in metamaterial regime," *Opt. Express*, vol. 18, pp. 20321-20333, 2010.

[151] Z. L. Mei, J. Bai, and T. J. Cui, "Gradient index metamaterials realized by drilling hole arrays," *J. Phys. D: Appl. Phys*., vol. 43, 055404, 2010.

[152] B. Vasic, R. Gajic, and K. Hingerl, "Graded photonic crystals for implementation of gradient refractive index media," *J. Nanophoton*., vol. 5, 051806, 2011.

[153] B. Vasic, and R. Gajic, "Self-focusing media using graded photonic crystals: Focusing, Fourier transforming and imaging, directive emission, and directional cloaking," *J. Appl. Phys*., vol. 110, 053103, 2011.

[154] E. Cassan, K.-V. Do, C. Caer, D. Marris-Morini, and L. Vivien, "Short-Wavelength Light Propagation in Graded Photonic Crystals," *J. Lightwave Technol*. vol. 29, pp. 1937-1943, 2011.

[155] V. K. Do, X. L. Roux, C. Caer, D. Marris-Morini, N. Izard, L. Vivien, and E. Cassan, "Wavelength Demultiplexer Based on a Two-Dimensional Graded Photonic Crystal," *IEEE Photon. Technol. Lett*., vol. 23, pp. 1094-1096, 2011.

[156] C. Tan, T. Niemi, C. Peng, and M. Pessa, "Focusing effect of a graded index photonic crystal lens," *Opt. Comm*., vol. 284, pp. 3140-3143, 2011.

[157] M. Notomi, "Manipulating light with strongly modulated photonic crystals," *Rep. Prog. Phys*., vol. 73, 096501, 2010.

[158] M. Notomi, "Theory of light propagation in strongly modulated photonic crystals: Refractionlike behavior in the vicinity of the photonic band gap," *Phys. Rev. B,* vol. 62, pp. 10696-10705, 2000.

[159] B. Lombardet, L. A. Dunbar, R. Ferrini, and R. Houdré, "Fourier analysis of Bloch wave propagation in photonic crystals," *J. Opt. Soc. Am. B,* vol. 22, pp. 1179-1190, 2005.

[160] A. Figotin, and I. Vitebskiy, "Electromagnetic unidirectionality in magnetic photonic crystals," *Phys. Rev. B,* vol. 67, 165210, 2003.

[161] J. T. Verdeyen, *Laser Electronics 3rd Edition,* Prentice-Hall, 1995.

[162] D. Mendlovic, and H. M. Ozaktas, “Fractional Fourier transforms and their optical implementation: I,” *J. Opt. Soc. Am. A*, vol. 10, pp. 1875-1881, 1993.

[163] H. M. Ozaktas, and D. Mendlovic, “Fractional Fourier transforms and their optical implementation. II,” *J. Opt. Soc. Am. A*, vol. 10, pp. 2522-2531, 1993.

[164] I. D. Leon, and F. S. Roux, “Fourier analysis of reflection and refraction in two-dimensional photonic crystals,” *Phys. Rev. B*, vol. 71, 235105, 2005.

[165] R. D. Meade, A. Devenyi, J. D. Joannopoulos, O. L. Alerhand, D. A. Smith, and K. Kash, “Novel applications of photonic band gap materials: Low-loss bends and high Q cavities,” *J. Appl. Phys*., vol. 75, pp. 4753-4755, 1994.

[166] B. Temelkuran, and E. Ozbay, “Experimental demonstration of photonic crystal based waveguides,” *Appl. Phys. Lett*., vol. 74, pp. 486-488, 1999.

[167] J. Bauer, and S. John, “Broadband optical coupling between microstructured fibers and photonic band gap circuits: Two-dimensional paradigms,” *Phys. Rev. A*, vol. **77**, 013819, 2008.

[168] P. Sanchis, J. Garcia, J. Marti, W. Bogaerts, P. Dumon, D. Taillaert, R. Baets, V. Wiaux, J. Wouters, and S. Beckx, “Experimental Demonstration of High Coupling Efficiency Between Wide Ridge Waveguides and Single-Mode Photonic Crystal Waveguides,” *IEEE Photon. Technol. Lett.*, vol. 16, pp. 2272-2274, 2004.

[169] A. Mekis, and J. D. Joannopoulos, “Tapered Couplers for Efficient Interfacing Between Dielectric and Photonic Crystal Waveguides,” *J. Lightwave Technol.*, vol. 19, 861-865, 2001.

[170] A. Hakansson, P. Sanchis, J. Sanchez-Dehesa, and J. Marti, "High-Efficiency Defect-Based Photonic-Crystal Tapers Designed by a Genetic Algorithm," *J. Lightwave Technol.*, vol. 23, pp. 3881-3888, 2005.

[171] P. Bienstman, S. Assefa, S. G. Johnson, J. D. Joannopoulos, G. S. Petrich, and L. A. Kolodziejski, "Taper structures for coupling into photonic crystal slab waveguides," *J. Opt. Soc. Am. B*, vol. 20, pp. 1817-1821, 2003.

[172] D. W. Prather, J. Murakowski, S. Shi, S. Venkataraman, A. Sharkawy, C. Chen, and D. Pustai, "High-efficiency coupling structure for a single-line-defect photonic-crystal waveguide," *Opt. Lett.*, vol. 27, pp. 1601-1603, 2002.

[173] I. Bulu, H. Caglayan, and E. Ozbay, "Beaming of light and enhanced transmission via surface modes of photonic crystals," *Opt. Lett.*, vol. 30, pp. 3078-3080, 2005.

[174] E. Moreno, F. J. Garcia-Vidal, and L. Martin-Moreno, "Enhanced transmission and beaming of light via photonic crystal surface modes," *Phys. Rev. B*, vol. 69, pp. 121402, 2004.

[175] E. Moreno, L. Martin-Moreno, and F. J. Garcia-Vidal, "Efficient coupling of light into and out of a photonic crystal via surface modes," *Photonics Nanostruct. Fundam. Appl.*, vol. 2, pp. 97-102, 2004.

[176] J. N. Winn, R. D. Meade, and J. D. Joannopoulos, "Two-dimensional Photonic Band-gap Materials," *J. Modern Opt.*, vol. 41, pp. 257-273, 1994.

[177] Q. Wang, Y. Cui, C. Yan, L. Zhang, and J. Zhang, "Highly efficient directional emission using a coupled multi-channel structure to a photonic crystal waveguide with surface modification," *J. Phys. D*, vol. 41, 105110, 2008.

[178] P. Kramper, M. Agio, C. M. Soukoulis, A. Birner, F. Müller, R. B. Wehrspohn, U. Gösele, and V. Sandoghar, "Highly Directional Emission from Photonic Crystal Waveguides of Subwavelength Width," *Phys. Rev. Lett.*, vol. 92, 113903, 2004.

[179] S. K. Morrison, and Y. S. Kivshar, "Engineering of directional emission from photonic-crystal waveguides," *Appl. Phys. Lett.*, vol. 86, 081110, 2005.

[180] H. Kurt, "Theoretical Study of Directional Emission Enhancement From Photonic Crystal Waveguides With Tapered Exits," *IEEE Photon. Technol. Lett.*, vol. 20, pp. 1682-1684, 2008.

[181] C.-C. Chen, T. Pertsch, R. Iliew, F. Lederer, and A. Tünnermann, "Directional emission from photonic crystal waveguides," *Opt. Express*, 14, pp. 2423-2428, 2006.

[182] W. R. Frei, D. A. Tortorelli, and H. T. Johnson, "Topology optimization of a photonic crystal waveguide termination to maximize directional emission," *Appl. Phys. Lett.*, 86, 111114, 2005.

[183] J.-M. Park, S.-G. Lee, H. Y. Park, and J.-E. Kim, "Efficient beaming of self-collimated light from photonic crystals," *Opt. Express*, vol. 16, pp. 20354-20367, 2008.

[184] Y. Zhang, Y. Zhang, and B. Li, "Highly-efficient directional emission from photonic crystal waveguides for coupling of freely propagated terahertz waves into Si slab waveguides," *Opt. Express*, vol. 15, pp. 9281-9286, 2007.

[185] W. Y. Liang, J. W. Dong, G. Q. Liang, and H. Z. Wang, "Highly collimated emission from a left-handed photonic crystal with a quasi-cavity," *Appl. Phys. B*, vol. 96, pp. 781-785, 2009.

[186] H. Kurt, and D. S. Citrin, "Graded index photonic crystals," *Opt. Express*, vol. 15, pp. 1240-1253, 2007.

[187] B. E. A. Saleh, and M. C. Teich, *Fundamentals of Photonics 2nd Edition*, Wiley, 2007.

[188] D. Tang, L. Chen, and W. Ding, "Efficient beaming from photonic crystal waveguides via self-collimation effect," *Appl. Phys. Lett.*, vol. 89, 131120, 2006.

[189] H. Caglayan, I. Bulu, and E. Ozbay, "Off-axis beaming from subwavelength apertures," *J. Appl. Phys.*, vol.104, 073108, 2008.

[190] H. Caglayan, I. Bulu, and E. Ozbay, "Off-axis directional beaming via photonic crystal surface modes," *Appl. Phys. Lett.*, vol. 92, 092114, 2008.

[191] J. Durnin, J. J. Miceli, and J. H. Eberly, "Diffraction-Free Beams," *Phys. Rev. Lett.*, vol. 58, pp. 1499-1501, 1987.

[192] Z. Li, K. B. Alici, H. Caglayan, and E. Ozbay, "Generation of an Axially Asymmetric Bessel-Like Beam from a Metallic Subwavelength Aperture," *Phys. Rev. Lett.*, vol. 102, 143901, 2009.

[193] J. Rosen, B. Salik, A. Yariv, and H.-K. Liu, "Pseudonondiffracting slitlike beam and its analogy to the pseudonondispersing pulse," *Opt. Lett.*, vol. 20, pp. 423-425, 1995.

[194] H. Kurt, "Limited-diffraction light propagation with axicon-shape photonic crystals," *J. Opt. Soc. Am. B*, vol. 26, pp. 981-986, 2009.

[195] Z. Wang, Y. D. Chong, J. D. Joannopoulos, and M. Soljacić, "Reflection-free one-way edge modes in gyromagnetic photonic crystals," *Phys. Rev. Lett*., vol. 100, no. 1, 013905, 2008.

[196] F. D. M. Haldane, and S. Raghu, "Possible realization of directional optical waveguides in photonic crystals with broken time-reversal symmetry," *Phys. Rev. Lett*. vol. 100, 013904, 2008.

[197] Z. Yu, Z. Wang, and S. Fan, “One-way total reflection with one-dimensional magneto-optical photonic crystals,” *Appl. Phys. Lett.*, vol. 90, no. 12, 121133, 2007.

[198] M. Scalora, J. P. Dowling, C. M. Bowden, and M. J. Bloemer, “The photonic band edge optical diode,” *J. Appl. Phys.*, vol. 76, no. 4, 2023, 1994.

[199] A. Figotin, and I. Vitebskiy, “Electromagnetic unidirectionality and frozen modes in magnetic photonic crystals,” *J. Magn. Magn. Mater.*, vol. 300, no. 1, pp. 117–121, 2006.

[200] A. E. Serebryannikov, “One-way diffraction effects in photonic crystal gratings made of isotropic materials,” *Phys. Rev. B*, vol. 80, no. 15, 155117, 2009.

[201] B. T. Schwartz, and R. Piestun, “Total external reflection from metamaterials with ultralow refractive index,” *J. Opt. Soc. Am. B*, vol. 20, no. 12, 2448, 2003.

[202] A. E. Serebryannikov, and E. Ozbay, “Unidirectional transmission in non-symmetric gratings containing metallic layers,” *Opt. Express*, vol. 17, no. 16, pp. 13335–13345, 2009.

[203] A. E. Serebryannikov, and E. Ozbay, “Isolation and one-way effects in diffraction on dielectric gratings with plasmonic inserts,” *Opt. Express*, vol. 17, no. 1, pp. 278–292, 2009.

[204] M. J. Lockyear, A. P. Hibbins, K. R. White, and J. R. Sambles, “One-way diffraction grating,” *Phys. Rev. E Stat. Nonlin. Soft Matter Phys.*, vol. 74, no. 5, 056611, 2006.

[205] W.-M. Ye, X.-D. Yuan, C.-C. Guo, and C. Zen, “Unidirectional transmission in non-symmetric gratings made of isotropic material,” *Opt. Express*, vol. 18, no. 8, pp. 7590–7595, 2010.

[206] N. Bonod, E. Popov, L. Li, and B. Chernov, "Unidirectional excitation of surface plasmons by slanted gratings," *Opt. Express*, vol. 15, no. 18, pp. 11427–11432, 2007.

[207] I. P. Radko, S. I. Bozhevolnyi, G. Brucoli, L. Martín-Moreno, F. J. García-Vidal, and A. Boltasseva, "Efficient unidirectional ridge excitation of surface plasmons," *Opt. Express*, vol. 17, no. 9, pp. 7228–7232, 2009.

[208] S. Cakmakyapan, A. E. Serebryannikov, H. Caglayan, and E. Ozbay, "One-way transmission through the subwavelength slit in nonsymmetric metallic gratings," *Opt. Lett*., vol. 35, no. 15, pp. 2597-2599, 2010.

[209] R. Petit, *Electromagnetic theory of gratings*, Springer, Berlin, 1980.

[210] R. Moussa, S. Foteinopoulou, L. Zhang, G. Tuttle, K. Guven, E. Ozbay, and C.M. Soukoulis, "Negative refraction and superlens behavior in a two-dimensional photonic crystal," *Phys. Rev. B*, vol. 71, no. 8, 085106, 2005.

[211] C. Luo, S. G. Johnson, J. D. Joannopoulos, and J. B. Pendry, "All-angle negative refraction without negative effective index," *Phys. Rev. B*, vol. 65, no. 20, 201104 2002.

[212] C. He, X.–L. Chen, M.-H. Lu, X.-F. Li, W.-W. Wan, X.-S. Qian, R.-C. Yin, and Y.-F. Chen, "Tunable one-way cross-waveguide splitter based on gyromagnetic photonic crystal," *Appl. Phys. Lett.*, vol. 96, no. 11, 111111, 2010.

[213] M. Soljacic, C. Luo, J. D. Joannopoulos, and S. Fan, "Nonlinear photonic microdevices for optical integration," *Opt. Lett.*, vol. 28, no. 8, pp. 637-639, 2003.

[214] C. E. Rüter, K. G. Makris, R. El-Ganainy, D. N. Christodoulides, M. Segev, and D. Kip. "Observation of parity–time symmetry in optics," *Nat. Phys*., vol. 6, no. 2, pp. 192-195, 2010.

[215] C. Menzel, C. Helgert, C. Rockstuhl, E.-B. Kley, A. Tünnermann, T. Pertsch, and F. Lederer, "Asymmetric transmission of linearly polarized light at optical metamaterilas," *Phys. Rev. Lett.*, vol. 104, no. 25, 253902, 2009.

[216] J.-Y. Chen and L.-W. Chen, "Color separating with integrated photonic band-gap optical diodes: a numerical study," *Opt. Express*, vol. 14, no. 22, pp. 10733-10739, 2006.

[217] G. Shvets, "Optical polarizer/isolator based on rectangular waveguide with helical grooves," *Appl. Phys. Lett*., vol. 89, no. 14, 141127, 2006.

[218] Z. Yu and S. Fan, "Complete optical isolation created by indirect interband photonic transitions," *Nat. Phot*., vol. 3, no. 2, pp. 91-94, 2008.

[219]. S. K. Ibrahim, S. Bhandare, D. Sandel, H. Zhang, and R. Noe, "Non-magnetic 30dB integrated opical isolator in III/Vmaterial," *Electron. Lett*., vol. 40, no. 20, pp. 1293-1294, 2004.

[220] K. Inoue and K. Ohtaka, Eds., *Photonic crystals. Physics, fabrication, and applications*, Springer, Berlin, 2004.

[221] A. O. Cakmak, E. Colak, A. E. Serebryannikov, and E. Ozbay, "Unidirectional transmission in photonic-crystal gratings at beam-type illumination," *Opt. Express*, vol. 18, no. 21, pp. 22283-22298, 2010.

[222] X.-F. Li, X. Ni, L. Feng, M.-H. Lu. C. He, and Y.-F. Chen, "Tunable unidirectional sound propagation through a sonic-crystal-based acoustic diode," *Phys. Rev. Lett*., vol. 106, no. 8, 084301, 2011.

[223] C. Lu, X. Hu, and Q. Gong, "Ultrahigh-contrast and wideband nanoscale photonic crystal all-optical diode," *Opt. Lett*., vol. 36, no. 23, pp. 4668-4670, 2011.

[224] X.-B. Kang, W. Tan, Z.-S. Wang, Z.-G. Wang, and H. Chen, "High efficiency one-way transmission by one-dimensional photonic crystals

with graings on one side," *Chin. Phys. Lett.*, vol. 27, no. 7, 074204, 2010.

[225] M. Beruete, A. E. Serebryannikov, V. Torres, M. Navarro-Cia, and M. Sorolla, "Toward compact millimeter-wave diode in thin stacked hole array assisted by a dielectric grating," *Appl. Phys. Lett*., vol. 99, no. 15, 154101, 2011.

[226] S. Cakmakyapan, A. E. Serebryannikov, H. Caglayan, and E. Ozbay, "One-way transmission through the subwavelength slit in nonsymmetric metallic gratings," *Opt. Lett*., vol. 35, no. 15, pp. 2597-2599, 2010.

[227] S. Cakmakyapan, H. Caglayan, A. E. Serebryannikov, and E. Ozbay, "Experimental validation of strong directional selectivity in nonsymmetric metallic gratings with a subwavelength slit," *Appl. Phys. Lett*., vol. 98, no. 5, 051103, 2011.

[228] A. E. Serebryannikov, A. Y. Petrov, and E. Ozbay, "Toward photonic crystal based spatial filters with wide angle ranges of total transmission," *Appl. Phys. Lett*., vol. 94, no. 18, 181101, 2009.

[229] T. Magath and A. E. Serebryannikov, "Fast iterative, coupled-integral-equation technique for inhomogeneous profiled and periodic slabs," *J. Opt. Soc. Am. A*, vol. 22, no. 11, pp. 2405-2418, 2005.

[230] See www.cst.com.

[231] D. Schurig and D. R. Smith, "Spatial filtering using media with indefinite permittivity and permeability tensors," *Appl. Phys. Lett*., vol. 82, no. 14, pp. 2215-2217, 2003.

[232] J. A. Kong, *Electromagnetic Wave Theory*, EMW Publishing, Cambridge, MA, USA, 2005.

[233] M. Mutlu, A. E. Akosman, A. E. Serebryannikov, and E. Ozbay, "Diodelike Asymmetric Transmission of Linearly Polarized Waves

Using Magnetoelectric Coupling and Electromagnetic Wave Tunneling," *Phys. Rev. Lett.*, vol. 108, no. 21, 213905, 2012.

[234] Z. He, S. Peng, Y. Ye, Z. Dai, C. Qiu, and Z. Liu, "Asymmetric acoustic gratings," *Appl. Phys. Lett*. vol. 98, no. 8, 083505, 2011.

[235] A. Mandatori, M. Bertolotti, and C. Sibilla, "Asymmetric transmission of some two-dimensional photonic crystals," *J. Opt. Soc. Am. B*, vol. 24, no. 3, pp. 685-690, 2007.

[236] A. E. Serebryannikov, A. O. Cakmak, and E. Ozbay, "Multichannel optical diode with unidirectional diffraction relevant total transmission," *Opt. Express*, vol. 20, no. 14, pp. 14980-14990, 2012.

[237] A. E. Serebryannikov, T. Magath, and K. Schuenemann, "Bragg transmittance of s-polarized waves through finite-thickness photonic crystals with a periodically corrugated interface," *Phys. Rev. E*, vol. 74, no. 6, 066607, 2006.

Appendix A

Simulation Tools

A.1 Finite Difference Time Domain (FDTD) Solver (RSoft)

RSoft FullWave solver is based on FDTD. RSoft has been utilized especially in electromagnetically large 2-D problems, e.g. photonic crystals simulations. FullWave package offers the transmission results, as well as the field monitors at specific times, since RSoft is a time domain solver. The meshing and total simulations times are optimized for best performance. Generally, these quantaties are assigned to $\Delta x = \Delta y = a/32$ (uniform meshing, a is the unit lattice size of the photonic crystal), $\Delta t_{total} = 2^{16}\Delta t$, where Δt is the time step of the FDTD simulation and is equal to $\Delta t = \Delta x/2c$ (a value that satisfies the stability issue in 2-D FDTD solutions). FullWave package enables continous wave, pulse and impulse excitations with rectangular (mimics plane waves), Gaussian, other possible user-defined waves.

RSoft also presents the BandSolve package, which can make use of the plane wave expansion method, if chosen. This particular package has been heavily functionalized in order to calculate the dispersion graphs and isofrequency contours of the investigated photonic crystal structures.

A.2 Finite Integration Technique (CST Microwave Studio®)

CST comes with many possibilities and packages. However, in this thesis work only the transient solver and eigen solver units have been employed. CST transient solver has been used in 3-D problems, especially those that involve metamaterials. CST transient utilizes periodic boundaries, these periodic boundaries can be used to convert the 3-D problem into a 2-D one. Scattering

parameters can be extracted from the CST transient solver. The convergence of the solutions have to be checked carefully since subwavelength resonators are studied in the thesis.

Eigen solver of CST resembles the BandSolve package of RSoft. Eigen solver is used to find out the dispersion graphs, as well. The advantage of Eigen solver is that 3-D problems with metallic inclusions can be investigated in CST.

Appendix B

Publication list in SSI journals

1. Atilla Ozgur Cakmak, Hamza Kurt, Evrim Colak and Ekmel Ozbay *A study on the electromagnetic wave propagation in graded index photonic crystals out of the metamaterial regime*, Optics Express. June, 2012 (Submitted)

2. Andriy E. Serebryannikov, Evrim Colak, Atilla Ozgur Cakmak and Ekmel Ozbay *Dispersion irrelevant wideband asymmetric transmission in dielectric photonic crystal gratings*, Optics Letters. June, 2012 (Submitted)

3. Atilla Ozgur Cakmak, Evrim Colak and Ekmel Ozbay *Simultaneously opening transmission channels with left- and right-handed behavior for the stacked subwavelength apertures in fishnet metamaterials with hybrid unit lattices*, Journal of Nanophotonics. 2012 (to appear)

4. Andriy E. Serebryannikov, Kamil Boratay Alici, Thore Magath, Atilla Ozgur Cakmak and Ekmel Ozbay *Asymmetric Fabry-Perot type transmission in photonic crystal gratings with one-side corrugations at two-way coupling*, Physical Review A. 2012 (to appear)

5. Andriy E. Serebryannikov, Atilla Ozgur Cakmak and Ekmel Ozbay *Multichannel optical diode with unidirectional relevant total transmission*, Optics Express, 2012. **20**(14): p. 14980-14990.

6. Damla Ates, Atilla Ozgur Cakmak and Ekmel Ozbay *Near-field light localization using subwavelength apertures incorporated with metamaterials*, Optics Communications, 2012. **285**(16): p. 3390-3396.

7. Cumali Sabah, Atilla Ozgur Cakmak, Ekmel Ozbay and Savas Uckun *Transmission measurements of a new metamaterial sample with negative refraction index*, Physica B, 2010. **405**(14): p. 2955-2958.

8. Atilla Ozgur Cakmak, Evrim Colak, Andriy E. Serebryannikov and Ekmel Ozbay *Unidirectional transmission in photonic-crystal gratings at beam-type illumination*, Optics Express, 2010. **18**(21): p. 22283-22298.

9. Damla Ates, Atilla Ozgur Cakmak, Evrim Colak, R. Zhao, Costas M. Soukoulis and Ekmel Ozbay *Transmission enhancement through deep subwavelength apertures using connected split ring resonators*, Optics Express, 2010. **18**(4): p. 3952-3966.

10. Evrim Colak, Atilla Ozgur Cakmak, Andriy E. Serebryannikov and Ekmel Ozbay *Spatial filtering using dielectric photonic crystals at beam-type excitation*, Journal of Applied Physics, 2010. **108**(11), 113106.

11. Evrim Colak, Humeyra Caglayan, Atilla Ozgur Cakmak, A. D. Villa, F. Capolino and Ekmel Ozbay *Frequency dependent steering with backward leaky waves via photonic crystal interface layer*, Optics Express, 2009. **17**(12): p. 9879-9890.

12. Atilla Ozgur Cakmak, Koray Aydin, Evrim Colak, Zhaofeng Li, F. Bilotti, L. Vegni and Ekmel Ozbay *Enhanced transmission through a subwavelength aperture using metamaterials*, Applied Physics Letters, 2009. **95**(5), 052103.

13. Koray Aydin, Atilla Ozgur Cakmak, Levent Sahin, Zhaofeng Li, F. Bilotti, L. Vegni and Ekmel Ozbay *Split-Ring-Resonator-Coupled Enhanced Transmission through a Single Subwavelength Aperture*, Physical Review Letters 2009. **102**(1), 013904.

14. Atilla Ozgur Cakmak, Evrim Colak, Humeyra Caglayan, Hamza Kurt and Ekmel Ozbay *High efficiency of graded index photonic crystal as an input coupler*, Journal of Applied Physics, 2009. **105**(10), 103708.

15. Hamza Kurt, Evrim Colak, Atilla Ozgur Cakmak, Humeyra Caglayan and Ekmel Ozbay *The focusing effect of graded index photonic crystals*, Applied Physics Letters, 2008. **93**(17), 171108.

16. Atilla Ozgur Cakmak, Kaan Guven and Ekmel Ozbay *Planar bilayer metamaterial with left-handed transmission and negative refraction at microwave frequencies*, Physica Status Solidi (b), 2007. **244**(4), p: 1188-1191.

17. Kaan Guven, Atilla Ozgur Cakmak, M. Deniz Caliskan, Tamara Funda Gundogdu, Maria Kafesaki, Costas M. Soukoulis and Ekmel Ozbay *Bilayer metamaterial: analysis of left-handed transmission and retrieval of effective medium parameters*, Journal of Optics A: Pure Applied Optics, 2007. **9**(9), p: S361-S365.

AMERICAN INSTITUTE OF PHYSICS LICENSE TERMS AND CONDITIONS

Aug 15, 2012

All payments must be made in full to CCC. For payment instructions, please see information listed at the bottom of this form.

License Number	2970560554555
Order Date	Aug 15, 2012
Publisher	American Institute of Physics
Publication	Applied Physics Letters
Article Title	Enhanced transmission through a subwavelength aperture using metamaterials
Author	Atilla Ozgur Cakmak, Koray Aydin, Evrim Colak, Zhaofeng Li, et al.
Online Publication Date	Aug 4, 2009
Volume number	95
Issue number	5
Type of Use	Thesis/Dissertation
Requestor type	Author (original article)
Format	Print and electronic
Portion	Figure/Table
Number of figures/tables	5
Title of your thesis / dissertation	Applications of Electromagnetic Phenomena in Periodic Structures
Expected completion date	Aug 2012
Estimated size (number of pages)	325
Total	0.00 USD
Terms and Conditions	

American Institute of Physics -- Terms and Conditions: Permissions Uses

American Institute of Physics ("AIP") hereby grants to you the non-exclusive right and license to use and/or distribute the Material according to the use specified in your order, on a one-time basis, for the specified term, with a maximum distribution equal to the number that you have ordered. Any links or other content accompanying the Material are not the subject of this license.

1. You agree to include the following copyright and permission notice with the reproduction of the Material: "Reprinted with permission from [FULL CITATION]. Copyright [PUBLICATION YEAR], American Institute of Physics." For an article, the copyright and permission notice must be printed on the first page of the article or book chapter. For photographs, covers, or tables, the copyright and permission notice may appear with the Material, in a footnote, or in the reference list.
2. If you have licensed reuse of a figure, photograph, cover, or table, it is your responsibility to ensure that the material is original to AIP and does not contain the copyright of another entity, and that the copyright notice of the figure, photograph, cover, or table does not indicate that it was reprinted by AIP, with permission, from another source. Under no circumstances does AIP, purport or intend to grant permission to reuse material to which it

does not hold copyright.

3. You may not alter or modify the Material in any manner. You may translate the Material into another language only if you have licensed translation rights. You may not use the Material for promotional purposes. AIP reserves all rights not specifically granted herein.
4. The foregoing license shall not take effect unless and until AIP or its agent, Copyright Clearance Center, receives the Payment in accordance with Copyright Clearance Center Billing and Payment Terms and Conditions, which are incorporated herein by reference.
5. AIP or the Copyright Clearance Center may, within two business days of granting this license, revoke the license for any reason whatsoever, with a full refund payable to you. Should you violate the terms of this license at any time, AIP, American Institute of Physics, or Copyright Clearance Center may revoke the license with no refund to you. Notice of such revocation will be made using the contact information provided by you. Failure to receive such notice will not nullify the revocation.
6. AIP makes no representations or warranties with respect to the Material. You agree to indemnify and hold harmless AIP, American Institute of Physics, and their officers, directors, employees or agents from and against any and all claims arising out of your use of the Material other than as specifically authorized herein.
7. The permission granted herein is personal to you and is not transferable or assignable without the prior written permission of AIP. This license may not be amended except in a writing signed by the party to be charged.
8. If purchase orders, acknowledgments or check endorsements are issued on any forms containing terms and conditions which are inconsistent with these provisions, such inconsistent terms and conditions shall be of no force and effect. This document, including the CCC Billing and Payment Terms and Conditions, shall be the entire agreement between the parties relating to the subject matter hereof.

This Agreement shall be governed by and construed in accordance with the laws of the State of New York. Both parties hereby submit to the jurisdiction of the courts of New York County for purposes of resolving any disputes that may arise hereunder.

If you would like to pay for this license now, please remit this license along with your payment made payable to "COPYRIGHT CLEARANCE CENTER" otherwise you will be invoiced within 48 hours of the license date. Payment should be in the form of a check or money order referencing your account number and this invoice number RLNK500839513. Once you receive your invoice for this order, you may pay your invoice by credit card. Please follow instructions provided at that time.

Make Payment To:
Copyright Clearance Center
Dept 001
P.O. Box 843006
Boston, MA 02284-3006

For suggestions or comments regarding this order, contact RightsLink Customer Support: customercare@copyright.com or +1-877-622-5543 (toll free in the US) or +1-978-646-2777.

Gratis licenses (referencing $0 in the Total field) are free. Please retain this printable license for your reference. No payment is required.

AMERICAN INSTITUTE OF PHYSICS LICENSE TERMS AND CONDITIONS

Aug 14, 2012

All payments must be made in full to CCC. For payment instructions, please see information listed at the bottom of this form.

License Number	2967811145644
Order Date	Aug 14, 2012
Publisher	American Institute of Physics
Publication	Applied Physics Letters
Article Title	Enhanced transmission through a subwavelength aperture using metamaterials
Author	Atilla Ozgur Cakmak, Koray Aydin, Evrim Colak, Zhaofeng Li, et al.
Online Publication Date	Aug 4, 2009
Volume number	95
Issue number	5
Type of Use	Thesis/Dissertation
Requestor type	Author (original article)
Format	Electronic
Portion	Excerpt (> 800 words)
Will you be translating?	No
Title of your thesis / dissertation	Applications of Electromagnetic Phenomena in Periodic Structures
Expected completion date	Aug 2012
Estimated size (number of pages)	325
Total	0.00 USD

Terms and Conditions

American Institute of Physics -- Terms and Conditions: Permissions Uses

American Institute of Physics ("AIP") hereby grants to you the non-exclusive right and license to use and/or distribute the Material according to the use specified in your order, on a one-time basis, for the specified term, with a maximum distribution equal to the number that you have ordered. Any links or other content accompanying the Material are not the subject of this license.

1. You agree to include the following copyright and permission notice with the reproduction of the Material: "Reprinted with permission from [FULL CITATION]. Copyright [PUBLICATION YEAR], American Institute of Physics." For an article, the copyright and permission notice must be printed on the first page of the article or book chapter. For photographs, covers, or tables, the copyright and permission notice may appear with the Material, in a footnote, or in the reference list.
2. If you have licensed reuse of a figure, photograph, cover, or table, it is your responsibility to ensure that the material is original to AIP and does not contain the copyright of another entity, and that the copyright notice of the figure, photograph, cover, or table does not indicate that it was reprinted by AIP, with permission, from another source. Under no circumstances does AIP, purport or intend to grant permission to reuse material to which it

does not hold copyright.

3. You may not alter or modify the Material in any manner. You may translate the Material into another language only if you have licensed translation rights. You may not use the Material for promotional purposes. AIP reserves all rights not specifically granted herein.
4. The foregoing license shall not take effect unless and until AIP or its agent, Copyright Clearance Center, receives the Payment in accordance with Copyright Clearance Center Billing and Payment Terms and Conditions, which are incorporated herein by reference.
5. AIP or the Copyright Clearance Center may, within two business days of granting this license, revoke the license for any reason whatsoever, with a full refund payable to you. Should you violate the terms of this license at any time, AIP, American Institute of Physics, or Copyright Clearance Center may revoke the license with no refund to you. Notice of such revocation will be made using the contact information provided by you. Failure to receive such notice will not nullify the revocation.
6. AIP makes no representations or warranties with respect to the Material. You agree to indemnify and hold harmless AIP, American Institute of Physics, and their officers, directors, employees or agents from and against any and all claims arising out of your use of the Material other than as specifically authorized herein.
7. The permission granted herein is personal to you and is not transferable or assignable without the prior written permission of AIP. This license may not be amended except in a writing signed by the party to be charged.
8. If purchase orders, acknowledgments or check endorsements are issued on any forms containing terms and conditions which are inconsistent with these provisions, such inconsistent terms and conditions shall be of no force and effect. This document, including the CCC Billing and Payment Terms and Conditions, shall be the entire agreement between the parties relating to the subject matter hereof.

This Agreement shall be governed by and construed in accordance with the laws of the State of New York. Both parties hereby submit to the jurisdiction of the courts of New York County for purposes of resolving any disputes that may arise hereunder.

If you would like to pay for this license now, please remit this license along with your payment made payable to "COPYRIGHT CLEARANCE CENTER" otherwise you will be invoiced within 48 hours of the license date. Payment should be in the form of a check or money order referencing your account number and this invoice number RLNK500838588. Once you receive your invoice for this order, you may pay your invoice by credit card. Please follow instructions provided at that time.

Make Payment To:
Copyright Clearance Center
Dept 001
P.O. Box 843006
Boston, MA 02284-3006

For suggestions or comments regarding this order, contact RightsLink Customer Support: customercare@copyright.com or +1-877-622-5543 (toll free in the US) or +1-978-646-2777.

Gratis licenses (referencing $0 in the Total field) are free. Please retain this printable license for your reference. No payment is required.

ELSEVIER ORDER DETAILS

Aug 16, 2012

Order Number	500691836
Order Date	Aug 16, 2012
Licensed content publisher	Elsevier
Licensed content publication	Optics Communications
Licensed content title	Near-field light localization using subwavelength apertures incorporated with metamaterials
Licensed content author	Damla Ates,Atilla Ozgur Cakmak,Ekmel Ozbay
Licensed content date	15 July 2012
Licensed content volume number	285
Licensed content issue number	16
Number of pages	7
Start Page	3390
End Page	3396
Type of Use	reuse in a thesis/dissertation
Intended publisher of new work	other
Portion	full article
Format	both print and electronic
Are you the author of this Elsevier article?	Yes
Will you be translating?	No
Order reference number	
Title of your thesis/dissertation	Applications of Electromagnetic Phenomena in Periodic Structures
Expected completion date	Aug 2012
Estimated size (number of pages)	325
Elsevier VAT number	GB 494 6272 12
Permissions price	Not Available
VAT/Local Sales Tax	Not Available
Total	Not Available

JOHN WILEY AND SONS LICENSE TERMS AND CONDITIONS

Aug 16, 2012

This is a License Agreement between Atilla O Cakmak ("You") and John Wiley and Sons ("John Wiley and Sons") provided by Copyright Clearance Center ("CCC"). The license consists of your order details, the terms and conditions provided by John Wiley and Sons, and the payment terms and conditions.

All payments must be made in full to CCC. For payment instructions, please see information listed at the bottom of this form.

License Number	2970590518967
License date	Aug 16, 2012
Licensed content publisher	John Wiley and Sons
Licensed content publication	physica status solidi (b) basic solid state physics
Licensed content title	Planar bilayer metamaterial with left-handed transmission and negative refraction at microwave frequencies
Licensed content author	Atilla Özgür Çakmak,Kaan Guven,Ekmel Özbay
Licensed content date	Mar 20, 2007
Start page	1188
End page	1191
Type of use	Dissertation/Thesis
Requestor type	Author of this Wiley article
Format	Print and electronic
Portion	Full article
Will you be translating?	No
Order reference number	
Total	0.00 USD
Terms and Conditions	

TERMS AND CONDITIONS

This copyrighted material is owned by or exclusively licensed to John Wiley & Sons, Inc. or one of its group companies (each a "Wiley Company") or a society for whom a Wiley Company has exclusive publishing rights in relation to a particular journal (collectively WILEY"). By clicking "accept" in connection with completing this licensing transaction, you agree that the following terms and conditions apply to this transaction (along with the billing and payment terms and conditions established by the Copyright Clearance Center Inc., ("CCC's Billing and Payment terms and conditions"), at the time that you opened your Rightslink account (these are available at any time at http://myaccount.copyright.com)

Terms and Conditions

1. The materials you have requested permission to reproduce (the "Materials") are protected by copyright.

2. You are hereby granted a personal, non-exclusive, non-sublicensable, non-transferable, worldwide, limited license to reproduce the Materials for the purpose specified in the licensing process. This license is for a one-time use only with a maximum distribution equal to the number that you identified in the licensing process. Any form of republication granted by this licence must be completed within two years of the date of the grant of this licence (although copies prepared before may be distributed thereafter). The Materials shall not be used in any other manner or for any other purpose. Permission is granted subject to an appropriate acknowledgement given to the author, title of the material/book/journal and the publisher. You shall also duplicate the copyright notice that appears in the Wiley publication in your use of the Material. Permission is also granted on the understanding that nowhere in the text is a previously published source acknowledged for all or part of this Material. Any third party material is expressly excluded from this permission.

3. With respect to the Materials, all rights are reserved. Except as expressly granted by the terms of the license, no part of the Materials may be copied, modified, adapted (except for minor reformatting required by the new Publication), translated, reproduced, transferred or distributed, in any form or by any means, and no derivative works may be made based on the Materials without the prior permission of the respective copyright owner. You may not alter, remove or suppress in any manner any copyright, trademark or other notices displayed by the Materials. You may not license, rent, sell, loan, lease, pledge, offer as security, transfer or assign the Materials, or any of the rights granted to you hereunder to any other person.

4. The Materials and all of the intellectual property rights therein shall at all times remain the exclusive property of John Wiley & Sons Inc or one of its related companies (WILEY) or their respective licensors, and your interest therein is only that of having possession of and the right to reproduce the Materials pursuant to Section 2 herein during the continuance of this Agreement. You agree that you own no right, title or interest in or to the Materials or any of the intellectual property rights therein. You shall have no rights hereunder other than the license as provided for above in Section 2. No right, license or interest to any trademark, trade name, service mark or other branding ("Marks") of WILEY or its licensors is granted hereunder, and you agree that you shall not assert any such right, license or interest with respect thereto.

5. NEITHER WILEY NOR ITS LICENSORS MAKES ANY WARRANTY OR REPRESENTATION OF ANY KIND TO YOU OR ANY THIRD PARTY, EXPRESS, IMPLIED OR STATUTORY, WITH RESPECT TO THE MATERIALS OR THE ACCURACY OF ANY INFORMATION CONTAINED IN THE MATERIALS, INCLUDING, WITHOUT LIMITATION, ANY IMPLIED WARRANTY OF MERCHANTABILITY, ACCURACY, SATISFACTORY QUALITY, FITNESS FOR A PARTICULAR PURPOSE, USABILITY, INTEGRATION OR NON-INFRINGEMENT AND ALL SUCH WARRANTIES ARE HEREBY EXCLUDED BY WILEY AND ITS LICENSORS AND WAIVED BY YOU.

6. WILEY shall have the right to terminate this Agreement immediately upon breach of this Agreement by you.

7. You shall indemnify, defend and hold harmless WILEY, its Licensors and their respective directors, officers, agents and employees, from and against any actual or threatened claims, demands, causes of action or proceedings arising from any breach of this Agreement by you.

8. IN NO EVENT SHALL WILEY OR ITS LICENSORS BE LIABLE TO YOU OR ANY OTHER PARTY OR ANY OTHER PERSON OR ENTITY FOR ANY SPECIAL, CONSEQUENTIAL, INCIDENTAL, INDIRECT, EXEMPLARY OR PUNITIVE DAMAGES, HOWEVER CAUSED, ARISING OUT OF OR IN CONNECTION WITH THE DOWNLOADING, PROVISIONING, VIEWING OR USE OF THE MATERIALS REGARDLESS OF THE FORM OF ACTION, WHETHER FOR BREACH OF CONTRACT, BREACH OF WARRANTY, TORT, NEGLIGENCE, INFRINGEMENT OR OTHERWISE (INCLUDING, WITHOUT LIMITATION, DAMAGES BASED ON LOSS OF PROFITS, DATA, FILES, USE, BUSINESS OPPORTUNITY OR CLAIMS OF THIRD PARTIES), AND WHETHER OR NOT THE PARTY HAS BEEN ADVISED OF THE POSSIBILITY OF SUCH DAMAGES. THIS LIMITATION SHALL APPLY NOTWITHSTANDING ANY FAILURE OF ESSENTIAL PURPOSE OF ANY LIMITED REMEDY PROVIDED HEREIN.

9. Should any provision of this Agreement be held by a court of competent jurisdiction to be illegal, invalid, or unenforceable, that provision shall be deemed amended to achieve as nearly as possible the same economic effect as the original provision, and the legality, validity and enforceability of the remaining provisions of this Agreement shall not be affected or impaired thereby.

10. The failure of either party to enforce any term or condition of this Agreement shall not constitute a waiver of either party's right to enforce each and every term and condition of this Agreement. No breach under this agreement shall be deemed waived or excused by either party unless such waiver or consent is in writing signed by the party granting such waiver or consent. The waiver by or consent of a party to a breach of any provision of this Agreement shall not operate or be construed as a waiver of or consent to any other or subsequent breach by such other party.

11. This Agreement may not be assigned (including by operation of law or otherwise) by you without WILEY's prior written consent.

12. Any fee required for this permission shall be non-refundable after thirty (30) days from receipt.

13. These terms and conditions together with CCC's Billing and Payment terms and conditions (which are incorporated herein) form the entire agreement between you and WILEY concerning this licensing transaction and (in the absence of fraud) supersedes all prior agreements and representations of the parties, oral or written. This Agreement may not be amended except in writing signed by both parties. This Agreement shall be binding upon and inure to the benefit of the parties' successors, legal representatives, and authorized assigns.

14. In the event of any conflict between your obligations established by these terms and conditions and those established by CCC's Billing and Payment terms and conditions, these terms and conditions shall prevail.

15. WILEY expressly reserves all rights not specifically granted in the combination of (i) the license details provided by you and accepted in the course of this licensing transaction, (ii) these terms and conditions and (iii) CCC's Billing and Payment terms and conditions.

16. This Agreement will be void if the Type of Use, Format, Circulation, or Requestor Type was misrepresented during the licensing process.

17. This Agreement shall be governed by and construed in accordance with the laws of the State of New York, USA, without regards to such state's conflict of law rules. Any legal action, suit or proceeding arising out of or relating to these Terms and Conditions or the breach thereof shall be instituted in a court of competent jurisdiction in New York County in the State of New York in the United States of America and each party hereby consents and submits to the personal jurisdiction of such court, waives any objection to venue in such court and consents to service of process by registered or certified mail, return receipt requested, at the last known address of such party.

Wiley Open Access Terms and Conditions

All research articles published in Wiley Open Access journals are fully open access: immediately freely available to read, download and share. Articles are published under the terms of the Creative Commons Attribution Non Commercial License. which permits use, distribution and reproduction in any medium, provided the original work is properly cited and is not used for commercial purposes. The license is subject to the Wiley Open Access terms and conditions:
Wiley Open Access articles are protected by copyright and are posted to repositories and websites in accordance with the terms of the Creative Commons Attribution Non Commercial License. At the time of deposit, Wiley Open Access articles include all changes made during peer review, copyediting, and publishing. Repositories and websites that host the article are responsible for incorporating any publisher-supplied amendments or retractions issued subsequently.
Wiley Open Access articles are also available without charge on Wiley's publishing platform, **Wiley Online Library** or any successor sites.

Use by non-commercial users

For non-commercial and non-promotional purposes individual users may access, download, copy, display and redistribute to colleagues Wiley Open Access articles, as well as adapt, translate, text- and data-mine the content subject to the following conditions:

- The authors' moral rights are not compromised. These rights include the right of "paternity" (also known as "attribution" - the right for the author to be identified as such) and "integrity" (the right for the author not to have the work altered in such a way that the author's reputation or integrity may be impugned).
- Where content in the article is identified as belonging to a third party, it is the obligation of the user to ensure that any reuse complies with the copyright policies of the owner of that content.
- If article content is copied, downloaded or otherwise reused for non-commercial research and education purposes, a link to the appropriate bibliographic citation (authors, journal, article title, volume, issue, page numbers, DOI and the link to the definitive published version on Wiley Online Library) should be maintained. Copyright notices and disclaimers must not be deleted.
- Any translations, for which a prior translation agreement with Wiley has not been agreed, must prominently display the statement: "This is an unofficial translation of an article that appeared in a Wiley publication. The publisher has not endorsed this translation."

Use by commercial "for-profit" organisations

Use of Wiley Open Access articles for commercial, promotional, or marketing purposes requires further explicit permission from Wiley and will be subject to a fee. Commercial purposes include:

- Copying or downloading of articles, or linking to such articles for further redistribution, sale or licensing;
- Copying, downloading or posting by a site or service that incorporates advertising with such content;
- The inclusion or incorporation of article content in other works or services (other than normal quotations with an appropriate citation) that is then available for sale or licensing, for a fee (for example, a compilation produced for marketing purposes, inclusion in a sales pack)
- Use of article content (other than normal quotations with appropriate citation) by for-profit organisations for promotional purposes
- Linking to article content in e-mails redistributed for promotional, marketing or educational purposes;
- Use for the purposes of monetary reward by means of sale, resale, licence, loan, transfer or other form of commercial exploitation such as marketing products
- Print reprints of Wiley Open Access articles can be purchased from: corporatesales@wiley.com

Other Terms and Conditions:

BY CLICKING ON THE "I AGREE..." BOX, YOU ACKNOWLEDGE THAT YOU HAVE READ AND FULLY UNDERSTAND EACH OF THE SECTIONS OF AND PROVISIONS SET FORTH IN THIS AGREEMENT AND THAT YOU ARE IN AGREEMENT WITH AND ARE WILLING TO ACCEPT ALL OF YOUR OBLIGATIONS AS SET FORTH IN THIS AGREEMENT.

v1.7

If you would like to pay for this license now, please remit this license along with your payment made payable to "COPYRIGHT CLEARANCE CENTER" otherwise you will be

invoiced within 48 hours of the license date. Payment should be in the form of a check or money order referencing your account number and this invoice number RLNK500839526. Once you receive your invoice for this order, you may pay your invoice by credit card. Please follow instructions provided at that time.

Make Payment To:
Copyright Clearance Center
Dept 001
P.O. Box 843006
Boston, MA 02284-3006

For suggestions or comments regarding this order, contact RightsLink Customer Support: customercare@copyright.com or +1-877-622-5543 (toll free in the US) or +1-978-646-2777.

Gratis licenses (referencing $0 in the Total field) are free. Please retain this printable license for your reference. No payment is required.

AMERICAN INSTITUTE OF PHYSICS LICENSE TERMS AND CONDITIONS

Aug 16, 2012

All payments must be made in full to CCC. For payment instructions, please see information listed at the bottom of this form.

License Number	2970640255264
Order Date	Aug 16, 2012
Publisher	American Institute of Physics
Publication	Journal of Applied Physics
Article Title	Spatial filtering using dielectric photonic crystals at beam-type excitation
Author	Evrim Colak, Atilla Ozgur Cakmak, Andriy E. Serebryannikov, Ekmel Ozbay et al.
Online Publication Date	Dec 6, 2010
Volume number	108
Issue number	11
Type of Use	Thesis/Dissertation
Requestor type	Author (original article)
Format	Print and electronic
Portion	Figure/Table
Number of figures/tables	4
Title of your thesis / dissertation	Applications of Electromagnetic Phenomena in Periodic Structures
Expected completion date	Aug 2012
Estimated size (number of pages)	325
Total	0.00 USD

Terms and Conditions

American Institute of Physics -- Terms and Conditions: Permissions Uses

American Institute of Physics ("AIP") hereby grants to you the non-exclusive right and license to use and/or distribute the Material according to the use specified in your order, on a one-time basis, for the specified term, with a maximum distribution equal to the number that you have ordered. Any links or other content accompanying the Material are not the subject of this license.

1. You agree to include the following copyright and permission notice with the reproduction of the Material: "Reprinted with permission from [FULL CITATION]. Copyright [PUBLICATION YEAR], American Institute of Physics." For an article, the copyright and permission notice must be printed on the first page of the article or book chapter. For photographs, covers, or tables, the copyright and permission notice may appear with the Material, in a footnote, or in the reference list.
2. If you have licensed reuse of a figure, photograph, cover, or table, it is your responsibility to ensure that the material is original to AIP and does not contain the copyright of another entity, and that the copyright notice of the figure, photograph, cover, or table does not indicate that it was reprinted by AIP, with permission, from another source. Under no

circumstances does AIP, purport or intend to grant permission to reuse material to which it does not hold copyright.

3. You may not alter or modify the Material in any manner. You may translate the Material into another language only if you have licensed translation rights. You may not use the Material for promotional purposes. AIP reserves all rights not specifically granted herein.
4. The foregoing license shall not take effect unless and until AIP or its agent, Copyright Clearance Center, receives the Payment in accordance with Copyright Clearance Center Billing and Payment Terms and Conditions, which are incorporated herein by reference.
5. AIP or the Copyright Clearance Center may, within two business days of granting this license, revoke the license for any reason whatsoever, with a full refund payable to you. Should you violate the terms of this license at any time, AIP, American Institute of Physics, or Copyright Clearance Center may revoke the license with no refund to you. Notice of such revocation will be made using the contact information provided by you. Failure to receive such notice will not nullify the revocation.
6. AIP makes no representations or warranties with respect to the Material. You agree to indemnify and hold harmless AIP, American Institute of Physics, and their officers, directors, employees or agents from and against any and all claims arising out of your use of the Material other than as specifically authorized herein.
7. The permission granted herein is personal to you and is not transferable or assignable without the prior written permission of AIP. This license may not be amended except in a writing signed by the party to be charged.
8. If purchase orders, acknowledgments or check endorsements are issued on any forms containing terms and conditions which are inconsistent with these provisions, such inconsistent terms and conditions shall be of no force and effect. This document, including the CCC Billing and Payment Terms and Conditions, shall be the entire agreement between the parties relating to the subject matter hereof.

This Agreement shall be governed by and construed in accordance with the laws of the State of New York. Both parties hereby submit to the jurisdiction of the courts of New York County for purposes of resolving any disputes that may arise hereunder.

If you would like to pay for this license now, please remit this license along with your payment made payable to "COPYRIGHT CLEARANCE CENTER" otherwise you will be invoiced within 48 hours of the license date. Payment should be in the form of a check or money order referencing your account number and this invoice number RLNK500839569. Once you receive your invoice for this order, you may pay your invoice by credit card. Please follow instructions provided at that time.

Make Payment To:
Copyright Clearance Center
Dept 001
P.O. Box 843006
Boston, MA 02284-3006

For suggestions or comments regarding this order, contact RightsLink Customer Support: customercare@copyright.com or +1-877-622-5543 (toll free in the US) or +1-978-646-2777.

Gratis licenses (referencing $0 in the Total field) are free. Please retain this printable license for your reference. No payment is required.

Copyright Clearance Center RightsLink®

Home | Account Info | Help

IEEE Requesting permission to reuse content from an IEEE publication

Title: Comparative analysis of edge- and broadside- coupled split ring resonators for metamaterial design - theory and experiments

Author: Marques, R.; Mesa, F.; Martel, J.; Medina, F.

Publication: Antennas and Propagation, IEEE Transactions on

Publisher: IEEE

Date: Oct. 2003

Copyright © 2003, IEEE

Logged in as:
Atilla Cakmak
Account #:
3000561587

LOGOUT

Thesis / Dissertation Reuse

The IEEE does not require individuals working on a thesis to obtain a formal reuse license, however, you may print out this statement to be used as a permission grant:

Requirements to be followed when using any portion (e.g., figure, graph, table, or textual material) of an IEEE copyrighted paper in a thesis:

1) In the case of textual material (e.g., using short quotes or referring to the work within these papers) users must give full credit to the original source (author, paper, publication) followed by the IEEE copyright line © 2011 IEEE.
2) In the case of illustrations or tabular material, we require that the copyright line © [Year of original publication] IEEE appear prominently with each reprinted figure and/or table.
3) If a substantial portion of the original paper is to be used, and if you are not the senior author, also obtain the senior author's approval.

Requirements to be followed when using an entire IEEE copyrighted paper in a thesis:

1) The following IEEE copyright/ credit notice should be placed prominently in the references: © [year of original publication] IEEE. Reprinted, with permission, from [author names, paper title, IEEE publication title, and month/year of publication]
2) Only the accepted version of an IEEE copyrighted paper can be used when posting the paper or your thesis on-line.
3) In placing the thesis on the author's university website, please display the following message in a prominent place on the website: In reference to IEEE copyrighted material which is used with permission in this thesis, the IEEE does not endorse any of [university/educational entity's name goes here]'s products or services. Internal or personal use of this material is permitted. If interested in reprinting/republishing IEEE copyrighted material for advertising or promotional purposes or for creating new collective works for resale or redistribution, please go to http://www.ieee.org/publications_standards/publications/rights/rights_link.html to learn how to obtain a License from RightsLink.

If applicable, University Microfilms and/or ProQuest Library, or the Archives of Canada may supply single copies of the dissertation.

BACK CLOSE WINDOW

Copyright © 2012 Copyright Clearance Center, Inc. All Rights Reserved. Privacy statement.
Comments? We would like to hear from you. E-mail us at customercare@copyright.com